NASA CR - 54704

GPO PRICE $ _____

CFSTI PRICE(S) $ _____

Hard copy (HC) 5.00

Microfiche (MF) 1.00

ff 653 July 65

FACILITY FORM 602

N66-17281	
(ACCESSION NUMBER)	(THRU)
187	1
(PAGES)	(CODE)
CR-54704	26
(NASA CR OR TMX OR AD NUMBER)	(CATEGORY)

BEHAVIOR OF VARIOUS ADSORBATES ON METAL SUBSTRATES

by

C. J. Bennette, R. W. Strayer, L. W. Swanson, E. C. Cooper

prepared for

NATIONAL AERONAUTICS AND SPACE ADMINISTRATION

Lewis Research Center

CONTRACT NAS3-5902

Field Emission Corporation

McMinnville, Oregon

NOTICE

This report was prepared as an account of Government sponsored work. Neither the United States, nor the National Aeronautics and Space Administration (NASA), nor any person acting on behalf of NASA:

A.) Makes any warranty or representation, expressed or implied, with respect to the accuracy, completeness, or usefulness of the information contained in this report, or that the use of any information, apparatus, method, or process disclosed in this report may not infringe privately owned rights; or

B.) Assumes any liabilities with respect to the use of, or for damages resulting from the use of any information, apparatus, method or process disclosed in this report.

As used above, "person acting on behalf of NASA" includes any employee or contractor of NASA, or employee of such contractor, to the extent that such employee or contractor of NASA, or employee of such contractor prepares, disseminates, or provides access to, any information pursuant to his employment or contract with such contractor.

Requests for copies of this report should be referred to

National Aeronautics and Space Administration
Office of Scientific and Technical Information
Attention: AFSS-A
Washington, D.C. 20546

NASA CR-54704

FINAL REPORT
For the Period
3 June 1964 to 18 December, 1965

BEHAVIOR OF VARIOUS ADSORBATES ON METAL SUBSTRATES

by

C. J. Bennette
R. W. Strayer
L. W. Swanson
E. C. Cooper

prepared for

NATIONAL AERONAUTICS AND SPACE ADMINISTRATION
Lewis Research Center

18 February 1966

CONTRACT NAS3-5902

Technical Management
NASA Lewis Research Center
Cleveland, Ohio
Electric Propulsion Office
Y. E. Strausser
John Ferrante

FIELD EMISSION CORPORATION
Melrose Avenue at Linke Street
McMinnville, Oregon

TABLE OF CONTENTS

INTRODUCTION 1
OBJECTIVES AND DESCRIPTION OF WORK 1
SUMMARY OF RESULTS 1
Vacuum Voltage Breakdown Studies 1
Studies of the Surface Kinetics of Adsorbed Layers 2
Sputtering Studies 3
Electron Desorption Studies 4
Studies of Surface Ionization of Tungsten Alloys 4

VACUUM VOLTAGE BREAKDOWN STUDIES 4

THEORY OF THE FIELD EMISSION INITIATED ARC 5
Anode vs Cathode Initiating Processes 5
Space Charge Effects 13
Effect of Electrostatic Stress 14
EXPERIMENTAL PROCEDURES 15
EXPERIMENTAL RESULTS AND DISCUSSION 17
Effect of Pulse Length Variation 20
Effect of Varying Electrode Material 30
Effect of Surface Geometry 34
SUMMARY 38
SURFACE KINETICS OF ADSORBED METALS ON REFRACTORY SUBSTRATES 41
VARIATION IN WORK FUNCTION OF VARIOUS METALS ON CESIUM ADSORPTION 41
Experimental Procedures and Results 41
General Discussion of Results 44
Comparison of Probe Tube Results with Theory 50
Adsorbate Polarizability
Summary 58
SURFACE MIGRATION OF CESIUM ON TUNGSTEN 59
Recent Results on Tungsten 59
Results and Discussion 62
Summary 65
MERCURY ADSORPTION ON MOLYBDENUM 66
Adsorption and Diffusion 66
Thermal Desorption 71
Diffusion and Desorption at Low Coverage 71
COPPER, BERYLLIUM AND CHROMIUM ADSORPTION ON TUNGSTEN 74
Experimental Procedures 74
COPPER ON TUNGSTEN 76
Adsorption 76
Diffusion 79

TABLE OF CONTENTS, Cont'd.

Crystalline Structure 145
Emission Constants for (100) Tungsten 145
Emission Constants for the Flashed Alloy Surfaces 145
Work Functions of the Equilibrated Alloy Surfaces 145
Oxygen in Tungsten - Rhenium Alloys 145

SUMMARY AND CONCLUSIONS 147
Tantalum-Tungsten Alloy 147
Iridium-Tungsten Alloy 147
Osmium-Tungsten Alloy 148
Rhenium-Tungsten Alloy 148

ERRATA 149

REFERENCES 150

LIST OF SYMBOLS 154

TABLE OF CONTENTS, Cont'd.

Thermal Desorption 79
Discussion 81
CESIUM ON COPPER COVERED TUNGSTEN 83
Results 83
Summary 83
BERYLLIUM ON TUNGSTEN 87
CHROMIUM ON TUNGSTEN 87

STUDIES OF ELECTRONIC INTERACTIONS WITH ADSORBATES ON TUNGSTEN 90
EXPERIMENTAL PROCEDURES AND RESULTS 90
DISCUSSION OF RESULTS 96

SPUTTERING OF TUNGSTEN BY CESIUM AND XENON IONS 98
FIELD ION MICROSCOPE STUDY OF XENON ION SPUTTERING OF TUNGSTEN 98
Experimental Tube and Procedure 98
Results 100
FIELD EMISSION INVESTIGATION OF CESIUM ION SPUTTERING OF CLEAN AND CESIUM-COATED TUNGSTEN 105
FEM Sputtering Tube Design 105
Sputtering of Clean Tungsten as a Function of Ion Energy 108
Sputtering of Cesium-Coated Tungsten 112

SURFACE IONIZATION OF CESIUM ON TUNGSTEN ALLOYS 114
INTRODUCTION 114
FIELD EMISSION MEASUREMENTS OF DESORPTION ACTIVATION ENERGIES 116
Formation of Field Emission Cathodes from Tungsten Alloys 116
EXPERIMENTAL PROCEDURES AND RESULTS 116
General Discussion of Results 127
WORK FUNCTIONS OF TUNGSTEN ALLOYS 129
Method of Approach 129
Thermionic Retarding Potential Method of Measuring Work Function 130
Experimental Tube Design 133
Experimental Procedures and Results 135
Determination of the Alloy Work Function 136
Determination of the Alloy Richardson Constants 136
Determination of the Work Function of the Equilibrated Alloy Surface 139
Determination of Crystal Direction and Size 139
Discussion of Results 145

LIST OF TABLES

Table I	Pertinent information related to curves shown in Figures 4 and 5.	26
Table II	For various amounts of surface roughness, indicated by γ, the maximum experimentally attained power at the anode and emitted current can be compared with that calculated for the given electrode to reach a temperature corresponding to a vapor pressure of 10^{-4} torr.	33
Table III	Anode power density W_a and cathode density $G = JR_c$ for various materials to reach a temperature corresponding to a vapor pressure of 10^{-4} torr.	39
Table IV	Yield point and corresponding electrostatic stress for various electrode materials.	40
Table V	Summary of maximum average work function change $\overline{\Delta\phi}_m$, and work function $\overline{\phi}_o$ at $\sigma = 3.2 \times 10^{14}$ atoms/cm^2	46
Table VI	Summary of maximum average work function change $\Delta\phi_m$, apparent monolayer coverage work function ϕ_o, adsorbate work function ϕ_a and predictions of equation (24).	49
Table VII	Constants of Equation (31) obtained from best fit to data of Figure 14.	54
Table VIII	Various constants obtained from Table VII results assuming $z_{110} = 1$ and $\alpha_{110} = \alpha_{100}$.	56
Table IX	Polarizabilities of the adsorbed cesium atoms on two crystallographic planes of tungsten calculated according to Equation (44).	58
Table X	Summary of surface migration data for Cs on tungsten and molybdenum	64
Table XI	Current voltage relationships for electron bombardment beam circuitry of Figure 37.	95
Table XII	Summary of electron induced desorption of Cs on W for 294 volt electrons at a current desnity of 24.0×10^{-3} amps/cm^2.	
Table XIII	Atom count summary	104
Table XIV	Work functions and emission constants of the alloys	121

LIST OF ILLUSTRATIONS

Figure 1. Field enhancement factor $\gamma = F_1/F_o$ at the apex of a small protrusion (i.e., $h \ll d$) of height h and apex radius curvature r, located on one electrode of a plane gap:
solid curve: prolate hemispheroid
dashed curve: cylindrical rod terminated by hemispherical tip 7

Figure 2. Emission from a whisker-type protrusion in a parallel plane gap. Gap: voltage V, spacing d and gross field $F_o = V/d$. Protrusion: height h and tip radius R, apex field F_c and current density J_c. Beam at anode: current density J_a, power density W_a, radius R_a and electron penetration δ. 8

Figure 3. Redesigned variable spacing tube for voltage breakdown studies. 16

Figure 4. Variable gap spacing copper-tungsten diode with the following features: 1) 200 mil diameter disk that is 75 mils thick attached to a 60 mil diameter rod; 2) identical copper electrode; 3) outgassing ring; 4) stannous oxide conductive coating; 5) bellows assembly; 6) field emission microscope and 7) cesium source. 18

Figure 5. Sequence of events showing visible evidence of pre-breakdown electron emission. A - orientation and geometry of the electrodes: B - transition radiation visible on the anode at a cathode current density of approximately 3×10^7 amps/cm^2: C - transition radiation on the anode and also an incandescent spot appears on the cathode at a current density of about 7×10^7 amps/cm^2. 19

Figure 6. Fowler-Nordheim plots of I-V data from clean molybdenum electrodes with various amounts of surface roughness, and several different gap spacings. 21

Figure 7. Fowler-Nordheim plots of I-V data from cesium-covered molybdenum electrodes ($\phi = 1.4$) at different gap spacings and for two different values of enhancement factor. 22

Figure 8. I-V data of Curve 2, Figure 7 plotted as current density $J = I/A$ vs. electrostatic field at the protrusion tip F_o. Curve 1 shows the experimentally recorded values of current divided by the emitting area calculated from the low current density I-V data. Curve 2 shows the same data except that the effect of field and current density have been taken into account in calculating effective emitting area. Curve 3 is the predicted curve if only the original protrusion emits. 24

Figure 9. Shows current density as a function of electrostatic field using the clean molybdenum data of Figure 6. The curve numbers correspond to the respective curve numbers of Figure 6. 25

Figure 10. Electron microscope shadowgraphs (magnification 3000X) of molybdenum electrode surface formed by bringing two thermally cleaned surfaces together in vacuum, then applying an electric field sufficiently high to cause the onset of the runaway condition. No arc took place, although the temperature and fields were very high. 35

Figure 11. The spot pattern at the top of the figure was obtained with the pinhole arrangement shown. The dark circles correspond to emission sites remaining after two arcs--open circles to sites lost and hatched circles to sites formed during the arcs. 36

Figure 12. Fowler-Nordheim plots of the I-V data from the Al cathode: Curve 1 - prior to the arc, Curve 2 - after the first arc, Curve 3 - after the second arc. This data was obtained from the surface whose x-ray output is illustrated in Figure 11

Figure 13. Two-emitter tube results of the work function vs. average cesium atom density on rhenium and molybdenum relative to tungsten. 42

Figure 14. Work function change vs. average cesium atom density for the (110) and (100) planes of tungsten. 45

Figure 15. Empirical relationship between measured maximum work function change and substrate work function 48

Figure 16. Analysis of the data of Figure 14 according to equation (34). 53

Figure 17. Block circuit diagram for measuring pulse voltage V_p and average pulse current I_p. 61

Figure 18. Arrhenius plots of the time required for equilibration of a small dose of cesium for the various underlying coverages of cesium where end points have been determined by the variations in pulse current with time according to the circuitry given in Figure 21. 63

Figure 19. Changes in the field emission pattern of a molybdenum emitter during adsorption of mercury. The relative amount of mercury on the emitter is given by the quantity N. 67

Figure 20. Changes in work function, the Fowler-Nordheim pre-exponential term A, and equilibration temperature as functions of the relative amount of mercury coverage for mercury on molybdenum. 69

Figure 21. Field emission patterns for various coverages of mercury on molybdenum, after equilibration. The relative amount θ is based on the coverage scale of Figure 20. 70

Figure 22. Work function of mercury on molybdenum as a function of desorption temperature to which the emitters had been heated for successive 60-second heating periods. 72

Figure 23. Desorption temperature for successive 60-second heating periods as a function of mercury coverage for mercury on molybdenum. The relative amount θ was obtained by means of Figure 20. 72

Figure 24. Arrhenius plots for a low coverage of mercury on molybdenum.
(a) Surface diffusion between coverages $\theta_i = 0$ and $\theta_f = 0.07$.
(b) Thermal desorption between coverages $\theta_i = 0.07$ and $\theta_f \not\approx 0$. 73

Figure 25. Diagrams of field emission microscopes used in the studies of (a) copper on tungsten and cesium on copper-covered tungsten, and (b) beryllium on tungsten. 75

Figure 26. Changes in work function θ, the Fowler-Nordheim pre-exponential term A, and equilibration temperature T_{eq} as functions of copper atom surface coverage for copper on tungsten. 77

Figure 27. Field emission patterns for various coverage for copper on tungsten 78

Figure 28. Arrhenius plot of copper on tungsten surface diffusion data for coverages between 0 and 0.3×10^{14} atoms/cm^2. 80

Figure 29. Arrhenius plot of copper on tungsten terminal thermal desorption data for coverages between 0.3×10^{14} atoms/cm^2 and 0. 80

Figure 30. Work function of copper on tungsten as a function of desorption temperatures to which the emitter had been heated for 60-second heating periods. 82

Figure 31. Thermal desorption temperature for successive 60-second heating periods as a function of copper-coverage for copper on tungsten. The scale on the right-hand side of the graph is obtained by assuming that the thermal desorption activation energy is proportional to desorption temperature. 82

Figure 32. Field emission patterns of cesium on copper-covered tungsten for various copper coverages and desorption temperatures. 84 and 85

Figure 33. Terminal desorption temperature, heavy coverage cesium work function, and minimum cesium work function as functions of copper coverage. (For reference, the copper on tungsten work function is also graphed.) 86

Figure 34. Field emission patterns of a small amount of beryllium on tungsten for various emitter heating temperatures. Voltage required for obtaining pattern is given. 88

Figure 35. Field emission patterns for chromium on tungsten. The patterns were selected from a sequence by heating the emitter to successively higher temperatures for 60 second heating periods. 89

Figure 36. Electron desorption studies tube. A is a tungsten field emitter, B is a tungsten filament used as the electron source, C is a lens arrangement that can be used either to focus the electron beam or as a Faraday collector, D is a phosphor screen, and E is a collector. 91

Figure 37. Block diagram of the circuitry employed for calibrating the beam characteristics of the electron desorption tube shown in Figure 36. 93

Figure 38. Results of the measured variation in the electron beam at the 15 mil aperture hole as the latter is moved on a line in either direction from its central position. 94

Figure 39. Schematic diagram of field ion microscope used for xenon ion sputtering of tungsten. 99

Figure 40. (a) Typical field ion pattern of a clean and nearly perfect tungsten surface.
(b) Principal planes of a (110)-oriented bcc crystal corresponding to (a). 101

Figure 41. Field ion patterns of xenon ion sputtering of clean tungsten: (a) $N \approx 1200$ ions, $E_p = 500$ v; (b) Impurity pattern corresponding to (c); (c) $N \approx 200$ ions, $E_p = 100$ v; (d) $N \approx 1500$ ions, $E_p = 1300$ v. Ion beam is incident upon left side. 103

Figure 42. Field ion patterns illustrating the depth of damage due to 1300 v sputtering as revealed by the total number of (110) layers removed by field desorption: (a) one, (b) two, (c) four, (d) six. 106

Figure 43. Schematic diagram of field emission microscope tube for the study of cesium-ion sputtering of cesium-covered tungsten. 107

Figure 44. Cesium ion sputtering of clean tungsten ($Q = 6.76$ μcoul, $E_p = 1073$ ev)
(a) Clean and smooth tungsten pattern ($\beta = 10,530$ cm^{-1}, $\phi = 4.52$ ev)
(b) After sputtering ($\beta = 11,120$ cm^{-1}, $\phi = 3.89$ ev)
(c) After partial field desorption of adsorbed cesium layer ($T = 77^{\circ}$K, $F_d = 30$ Mv/cm)
(d) After complete field desorption of adsorbed cesium layer ($T = 77^{\circ}$K, $F_d = 39$ Mv/cm; $\beta = 11,120$ cm^{-1}, $\phi = 4.52$ ev). The spots in the pattern are due to surface roughness. 109

Figure 45. Reduction in surface roughness, as measured by change in β, as a function of emitter temperature. Heating time at each temperature was 60 sec. 110

Figure 46. Surface roughness, as measured by a normalized change in β, as a function of cesium ion energy E_p. 111

Figure 47. Cesium ion sputtering of cesium-coated tungsten.
(a) Before sputtering (= 2.3 x 10^{14} Cs atom/cm^2;
(b) After sputtering with Q = 2.5 μcoul, E_p = 353 ev ions and Cs re-equilibration (= 2.0 x 10^{14} Cs atom/cm^2);
(c) Before sputtering with Q = 2.9 μcoul, E_p = 1073 ev ions and Cs re-equilibration.
(d) After sputtering with Q = 2.9 μcoul, E_p = 1073 ev ions and Cs re-equilibration.
Note roughness is still visible underneath Cs layer 113

Figure 48. Shapes of emitters made from W-Ta alloys at 215x magnification. A, W-5%Ta; B, W-10%; C, W-20%Ta 117

Figure 49. Chart recorder output showing variation of I_p with time at constant V_p. Three types of curve were recorded - (1) ion desorption from W - 20 Ta, W - 1 Ir, and W - 23 Re - (2) ion desorption from remaining alloy surfaces, and (3) neutral desorption 120

Figure 50. Patterns (a), (d) and (g) are psuedo clean tungsten patterns obtained by flash heating; patterns (c), (f) and (h) are obtained by equilibrating at the indicated temperatures 122

Figure 51. Principal pattern changes of (3$\bar{1}$0) oriented osmium alloys 123

Figure 52. Field emission patterns of (4$\bar{1}$1) oriented W - 1 Ir alloy and (310) oriented W - 2 Ir alloy 124

Figure 53. Principal pattern changes of W - 5 Re alloy. (a) and (b) are (411) oriented. The (530) oriented equilibrated alloy shown in (c) was the surface used for the desorption work 125

Figure 54. Pattern changes in a (110) oriented W - 23 Re alloy caused by oxygen diffusing onto the surface from the bulk when the tip is heated at the indicated temperatures 126

Figure 55. Energy barrier to thermionic emission when the current is (a) cathode-limited, or (b) anode-limited 131

Figure 56. Typical plots of the anode current as a function of anode voltage for selected cathode temperatures. The temperatures are obtained from the slopes of the semi-logarithmic portions of the curves 132

Figure 57. Diagram of the electrodes in the work function triode tube. A and G, backplates to prevent electrons from bombarding tube wells; B and F, bombarding filaments; C, cathode; D, center electrode with beam-defining aperture; E, anode 134

Figure 58. Richardson plots of data from lines A, B (both anode-limited emission), and C (cathode-limited emission) of Figure 56 137

Figure 59. Back-scattered Laue patterns of the major low-index planes of tungsten and of the alloy surfaces examined in the work function triode. (a) (110) W, (b) (100)W, (c) (111) W, (d) W - 1% Ir (g) W-2.5% Os, (h) W-5% Os, (i) W-5% Ta 140

Figure 60. Back-scattered Laue patterns of the alloy surfaces examined in the work function triode. (a) W - 10% Ta, (b) W-20% Ta, (c) W-5% Re, (d) W-15% Re before electrolytic etching, (e) W-15% Re before operation in triode, (f) W-15% Re after (g) W-23% Re before operation, (h) W-23% Re after 141

Figure 61. Optical micrographs of electrode surfaces used in work function triodes. (a) (100) W, (b) W-1% Ir, (c) W-2% Ir, (d) W-2.5% Os, (e) W-5% Os, (f) W-5% Ta. Magnification 25x 142

Figure 62. Optical micrographs of alloy surfaces used in work function triodes. (a) W-10% Ta, (b) W-20% Ta, (c) W-5% Re, (d) W-15% Re, (e) W-23% Re before operation in triode, (f) W-23% Re after. Magnification 25x 143

PAPERS AND MEETINGS

The following papers covering portions of work performed under Contracts NASw-458 and NAS3-2596 were published during the present contract period:

"The Effect of Electric Field on Adsorbed Layers of Cesium on Various Refractory Metals", by L. W. Swanson, R. W. Strayer, and F. M. Charbonnier, Surface Science 2, 177 (1964);

"Visible Radiation from Metal Anodes Preceding Electrical Breakdown", by Carol J. Bennette, L. W. Swanson, and R. W. Strayer, communication to the Journal of Applied Physics 35, No. 10, 3054 (Oct. 1964);

"Investigation of the Prebreakdown Gap Currents between Clean and Cesium-Coated Tungsten Electrodes", by Carol J. Bennette, R. W. Strayer, E. C. Cooper, and L. W. Swanson, AIAA Journal 3, No. 2, 284 (Feb. 1965).

Papers were also presented at the following professional meetings:

AIAA Fourth Electric Propulsion Conference, Philadelphia, Pa., 31 Aug. -2 Sept. 1964;

Eleventh International Field Emission Symposium, Cambridge, England, 8-12 Sept. 1964;

International Symposium on Insulation of High Voltage in Vacuum, Massachusetts Institute of Technology, Cambridge, Mass., 19 - 21 Oct. 1964;

Twenty-Fifth Annual Physical Electronics Conference, Massachusetts Institute of Technology, Cambridge, Mass., 24 - 26 Mar. 1965;

Twelfth Field Emission Symposium, Pennsylvania State University, University Park, Pa., 7 - 11 Sept. 1965.

The support given by NASA for the work reported in these papers and the presentation thereof is gratefully acknowledged.

INTRODUCTION

OBJECTIVES AND DESCRIPTION OF WORK

The general objectives of the work being performed on the present contract are to conduct a research program on the electron emission properties of certain selected metals both when clean and when covered with metallic adsorbates, and to apply the knowledge thus gained to problems encountered by ion propulsion systems, in particular, voltage breakdown across vacuum gaps between metal electrodes and the degree of ionization of cesium on various refractory substrates. (The work has been divided into five general areas: (1) an investigation of prebreakdown gap currents and electrical breakdown conditions between clean and cesium-coated metal electrodes as functions ~~of such parameters as applied~~ voltage, surface electric field, cesium coverage, ambient cesium pressure, ~~within the gap~~, and environmental conditions; (2) studies of the surface kinetics and work function changes of various metallic adsorbate/substrate combinations when such ~~parameters as~~ surface temperature and adsorbate coverage are varied; (3) investigation of individual xenon ion sputtering events on clean tungsten ~~by means of field ion microscopy~~ and of cesium ion sputtering of clean and cesium-coated tungsten ~~by field electron microscopy~~; (4) a study of the interaction of low energy electrons with adsorbed layers of cesium on tungsten; and (5) an investigation of the cesium surface ionization properties of several tungsten alloys.)

SUMMARY OF RESULTS

Vacuum Voltage Breakdown Studies

It has been established that the origin of pre-breakdown current between clean and cesium-covered tungsten, molybdenum, copper or aluminum electrodes in vacuum is field emission from microscopic cathode protrusions under the following conditions: gap spacings from 1.0 to 20 mils, cesium coverages corresponding to work functions from 4.52(clean W)to 1.4 ev, (Cs-W) varying degrees of surface roughness related to field enhancement factors from 10 to 600, and both polarities of electric field with voltages applied either continuously or in pulses from 2 to 20 μsec.

On the basis of those results, a theory of field emission initiated vacuum voltage breakdown has been formulated which predicts within certain limits the occurrence of a cathode or anode initiated arc between electrodes with varying degrees of surface roughness. The boundary between anode and cathode initiated breakdown is affected only by the value of the field enhancement factor of localized emitting protrusions. Preliminary experimental results seemed to agree with the general features of the theory, thus a more detailed study in which significant theoretical

parameters could be varied in a controlled manner followed.

The significance of the respective electrode materials in predicting breakdown characteristics is related to the thermal and electrical conductivity of the electrode at a temperature corresponding to a particular vapor pressure. A good conductor such as copper will dissipate heat rapidly so that the electrode surface temperature will rise slowly, and it is difficult for adequate vaporization to take place. However, with a poorer conductor such as tungsten or molybdenum, the surface will heat more readily and reach an adequate vapor pressure more easily. Experimentally and theoretically the boundary value between anode and cathode initiated breakdown is affected in such a way that for a copper-tungsten diode, tungsten is more apt to reach a critical vapor pressure and initiate the arc, while for an aluminum-tungsten diode, aluminum is more likely to become unstable and cause an arc.

In extending the study from the stable pre-breakdown condition into the region of instability leading to the arc, it was found that when the voltage is applied continuously an anode power density was reached at which the current began to increase exponentially with time at a constant applied voltage. The I-V data was often reproducible indicating that the cathode surface geometry was not significantly altered. The dependence on anode power density of the onset of a regenerative instability suggested that this phenomena was related to the thermal properties of the anode material. The best explanation for the observed instability was found to be thermal expansion of the anode due to bombardment heating. In a few cases, particularly when the enhancement factor was high, the instability would terminate in a continuous low voltage, high current discharge, which was apparently limited only by the output impedance of the high voltage power supply in the circuit.

Studies of the Surface Kinetics of Adsorbed Layers

Activation energies of surface diffusion have been performed over a range of cesium coverages on tungsten by utilizing pulsed field emission current variations with time as a measure of the end point. The results confirmed earlier measurements[1] of a similar nature on molybdenum substrates, where it was found that the activation energy for surface diffusion was essentially independent of underlying cesium coverage; however, a variation in the pre-exponential of the rate equation was observed which accounts for the variation of the diffusion rates with coverage in the manner observed earlier.

The variation of work function change with cesium coverage on single crystallographic planes has been completed on the (110) and (100) planes of tungsten. These results have been compared with some of the existing theories, although some problems were encountered when attempting to

establish the absolute coverage since the results suggest a difference in coverage between the two planes. This variation in coverage is such that the (110) plane has greater than average coverage whereas the (100) plane has less than average coverage. An empirical relationship between the maximum work function change and local substrate work function was formulated and appears to have validity for a variety of adsorbate-substrate systems.

The work function variation with coverage for cesium on rhenium and molybdenum has been measured; the shape of the resulting curves are similar to the one for tungsten, but with a slight shift of the minimum toward lower coverages in the case of rhenium.

In an investigation of adsorption and desorption of thin mercury films on molybdenum substrates the work function changes, equilibration temperatures, and desorption temperatures have been measured as functions of relative mercury coverage, and activation energies have been obtained for diffusion and desorption at a low coverage. Some of the more interesting points established are: (1) mercury adsorbed on molybdenum raises the work function; (2) for coverages above a monolayer mercury is mobile at 77°K; (3) applied fields of 25 Mv/cm or greater cause growth of mercury protrusions from the mobile layer at 77°K for certain coverages; and (4) all mercury is completely desorbed from molybdenum at 650°K.

The work function changes, equilibration temperatures, and desorption temperatures have been measured as functions of relative copper coverage for thin copper films on tungsten, and activation energies have been obtained for diffusion and desorption at a low coverage. The results are in general agreement with those obtained elsewhere[2]. Also, cesium desorption from copper-coated tungsten has been investigated, and was found to be similar to cesium desorption from clean tungsten for copper coverages of less than a monolayer, but markedly different for coverages greater than a monolayer.

A preliminary investigation of the adsorption of beryllium and chromium on tungsten has been completed. Surface diffusion of beryllium is accomplished over a range of temperatures (250 to 400°K) and thermal desorption is complete at 1250°K. Chromium appeared to migrate completely across a tungsten substrate at a temperature of 370°K and thermal desorption was complete at 1190°K.

Sputtering Studies

FIM investigation of 100, 500, and 1300 ev Xe^+ sputtering of a W tip has yielded the following results. Sputtering damage was somewhat dependent upon crystallographic direction (being greater on high index planes) for 100 and 500 ev ions, but was not so for 1300 ev ions. Most of the damage occurred

on the side of the tip away from the bombarding ion beam for 100 ev ions and on the side towards the beam for 1300 ev ions. Depth of damage was approximately 1 atom layer for 100 ev ions and 6 atom layers for 1300 ev ions. The FIM patterns also gave some indication of Xe atom burial within the first few atom layers of the tip.

A preliminary FEM investigation of Cs^+ sputtering of clean W has indicated that changes in surface roughness with ion bombardment may be used as an indication of sputtering. Surface roughness increased with ion energy for energies below 300 ev; extrapolation of the data indicated an ion threshold energy for surface roughening of about 20-30 ev. Low energy Cs^+ sputtering of Cs-coated W reduced the Cs coverage and roughened the underlying W substrate for low Cs coverages.

Electron Desorption Studies

A tube designed to study the interaction of low energy electrons with adsorbed layers of cesium and oxygen has been constructed and initial calibration measurements of the electron bombardment beam as a function of total accelerating voltage have been performed. The current density of the bombardment beam at the emitter varies between 7 and 30 ma/cm^2 as the accelerating voltage varies from 23 to 500 volts. The current density should be sufficient to detect electron-adsorbate reactions of moderately low cross section. Measurements of electron desorption cross sections for cesium on clean tungsten over a range of temperatures and coverages for 294-volt electrons show no effect, the data indicate that cross sections for electron desorption of cesium on tungsten are less than 6×10^{-22} cm^2.

Studies of Surface Ionization of Tungsten Alloys

The necessary additional experimental tubes and equipment have been constructed and experimental techniques developed for the measurement of work function, cesium ion and neutral desorption energies for tungsten alloys. Techniques for etching emitters from tungsten-tantalum, tungsten-osmium, and tungsten-iridium alloys have been perfected. Initial data have been obtained from two samples of tungsten-tantalum alloys.

VACUUM VOLTAGE BREAKDOWN STUDIES

The field emission origin of the pre-breakdown current between metal electrodes prior to vacuum voltage breakdown has been established for a wide range of conditions. Under the present contract, the purpose of the investigation has been to gain an understanding of the relationship between the pre-breakdown current and the conditions under which this current can initiate a regenerative process that leads to an arc.

Voltage breakdown is a broad term enveloping a process that begins with the field emitted current from protrusions on the cathode surface,

proceeds from a period of instability in which the emitted current increases with time at constant voltage through a period in which the instability becomes regenerative, and finally into the low impedance discharge or arc in which one or both electrodes undergo significant changes in surface geometry. In the following discussion it will be found that there are several methods in which the breakdown process can be accomplished. The results of our investigation indicate the conditions under which one can predict which path breakdown will follow.

THEORY OF THE FIELD EMISSION INITIATED ARC

In general, the most significant factors limiting the stability of the gap are the following:

1) excessive heating of the cathodic protrusion due to the emitted current;

2) excessive electron beam power density at the anode;

3) excessive ion bombardment of the cathode;

4) excessive electrostatic stress at the electrode surface.

These various factors offer limitations either to the field which can be applied to the cathode protrusion or to the current which can be drawn from it, to an extent dependent upon the experimental conditions. Since all of the work reported was accomplished in very high vacuum the third factor listed is significant only as a contributing factor after significant electrode material has been evaporated into the gap. In the next section relationships are developed which show the conditions under which breakdown will be dominated by anode or cathode processes, followed by a discussion of the conditions under which electrostatic stress becomes significant.

Anode vs Cathode Initiating Processes

As discussed previously[3], field emission from protrusions on the cathode can cause emission induced heating of the protrusion tip at sufficiently high current densities, J. Acceleration of the field emitted electrons across the gap produces in turn local heating of the anode; thus, breakdown can occur when the temperature at either electrode becomes high enough locally to cause enough evaporation of electrode material into the path of the electron beam that the probability of ionization becomes appreciable. Whether it is the cathode or the anode that first reaches this critical condition depends on the geometry of the gap, on the field enhancement factor γ at the apex of the protrusion, on the relative electrode materials, and on whether the gap voltage is continuous or pulsed. The occurrence of high current density field emission does not necessarily lead to breakdown, since in many tests performed at this laboratory dc emission densities in excess of 10^7 amps/cm^2 or pulsed emission

densities in excess of 10^8 amps/cm^2 have been maintained without instability for operating periods of several thousand hours.

Determination of the conditions which lead to either anode initiated or cathode initiated breakdown is of great interest. For the case of a parallel plane gap and a cylindrical whisker-type protrusion, this determination is relatively straightforward if one uses the approximate expressions recently given by Vibrans[4] for the field enhancement factor γ and the spreading of the electron beam. A cylindrical protrusion has been chosen for several reasons. First, cylindrical protrusions exhibit a field enhancement factor appreciably larger than that of a prolate spheroid or conical projection for a given height h and apex radius R_c. This is illustrated in Figure 1 which compares the dependence of γ on $\frac{h}{R_c}$ for the case of a prolate hemispheroidal protrusion to that in the case analyzed by Vibrans of a cylindrical rod terminated by a hemispherical tip. As a result, application of a given microscopic field at the cathode support will lead to a higher apex field and field emitted current in the case of the cylindrical protrusion. Since the cross section of the protrusion is uniform from the apex to the base, the resistively generated heat is greater and the "thermal impedance" at the protrusion apex, is increased. In fact, as first shown by Levine[5] resistive heating causes a long cylindrical protrusion made of some material for which the resistivity increases at least linearly with temperature to heat without limit if the product of current density J and protrusion height h exceeds a critical value (1.4×10^4 amps/cm for tungsten). Thus long cylindrical protrusions are particularly undesirable from the standpoint of high voltage insulation in vacuum. Thus, we have chosen for analysis a protrusion geometry most susceptible to voltage breakdown.

Neglecting space charge effects, the radius R_a of an electron beam at the anode which is emitted from a protrusion tip of radius R_c can be written as[4]

$$R_a \cong 2\sqrt{\gamma R_c d} \tag{1}$$

where d is the gap spacing, as illustrated in Figure 2. Assuming for simplicity that $h \gg R_c$ and $d \gg h$, it follows that $\gamma \cong \frac{h}{R_c}$ (see Figure 1) and the beam power density at the anode W_a can be derived, knowing that

$$W_a = J_a V = F_o d J_a \tag{2}$$

where J_a is the current density at the anode and V is the potential across the gap, and the field across the gap is $F_o = \frac{V}{d}$. At the cathode the field at the tip of a protrusion is:

$$F = \gamma F_o \tag{3}$$

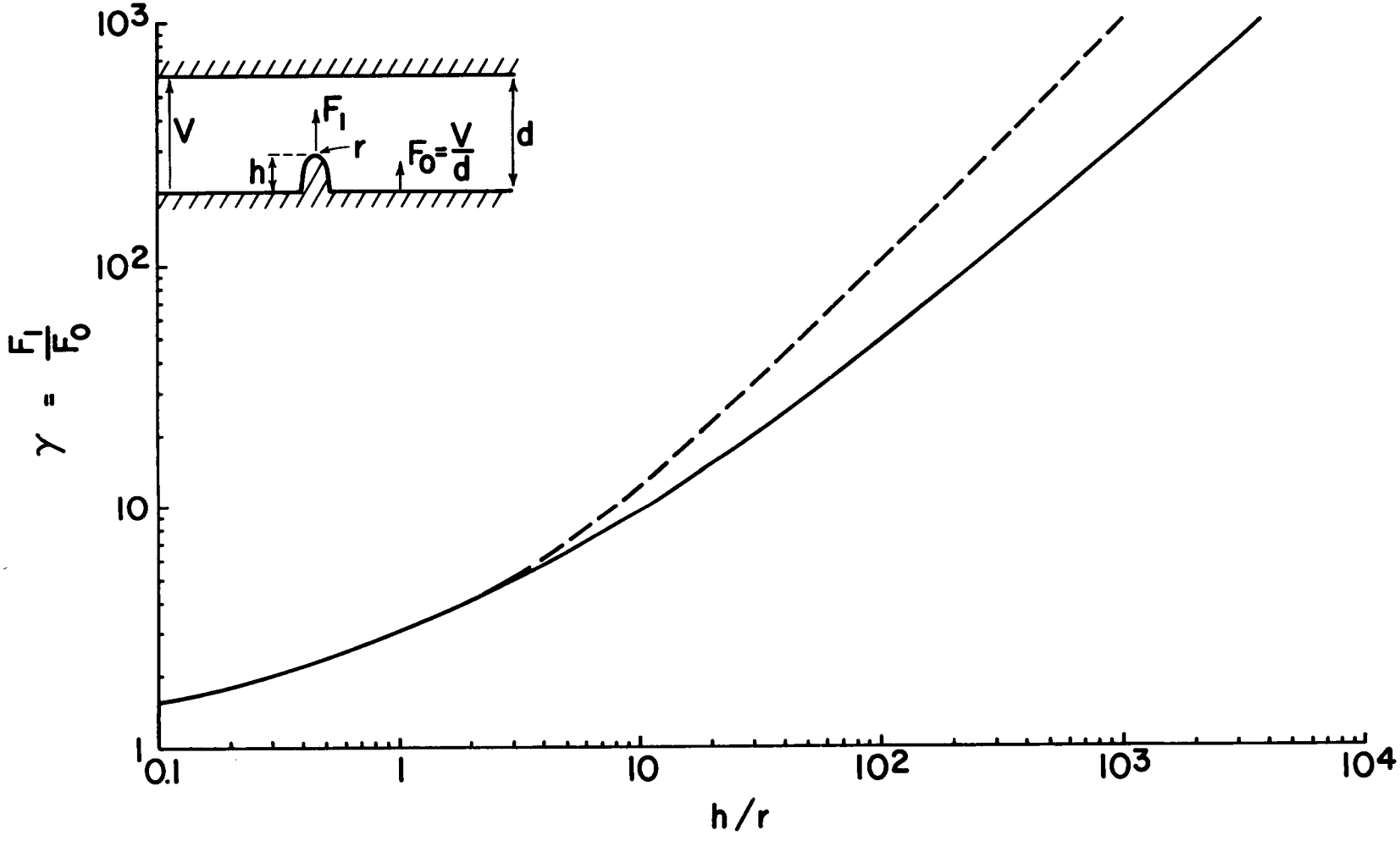

Figure 1. Field enhancement factor $\gamma = F_1/F_o$ at the apex of a small protrusion (i.e., $h \ll d$) of height h and apex radius of curvature r, located on one electrode of a plane gap:

solid curve: prolate hemispheroid

dashed curve: cylindrical rod terminated by hemispherical tip

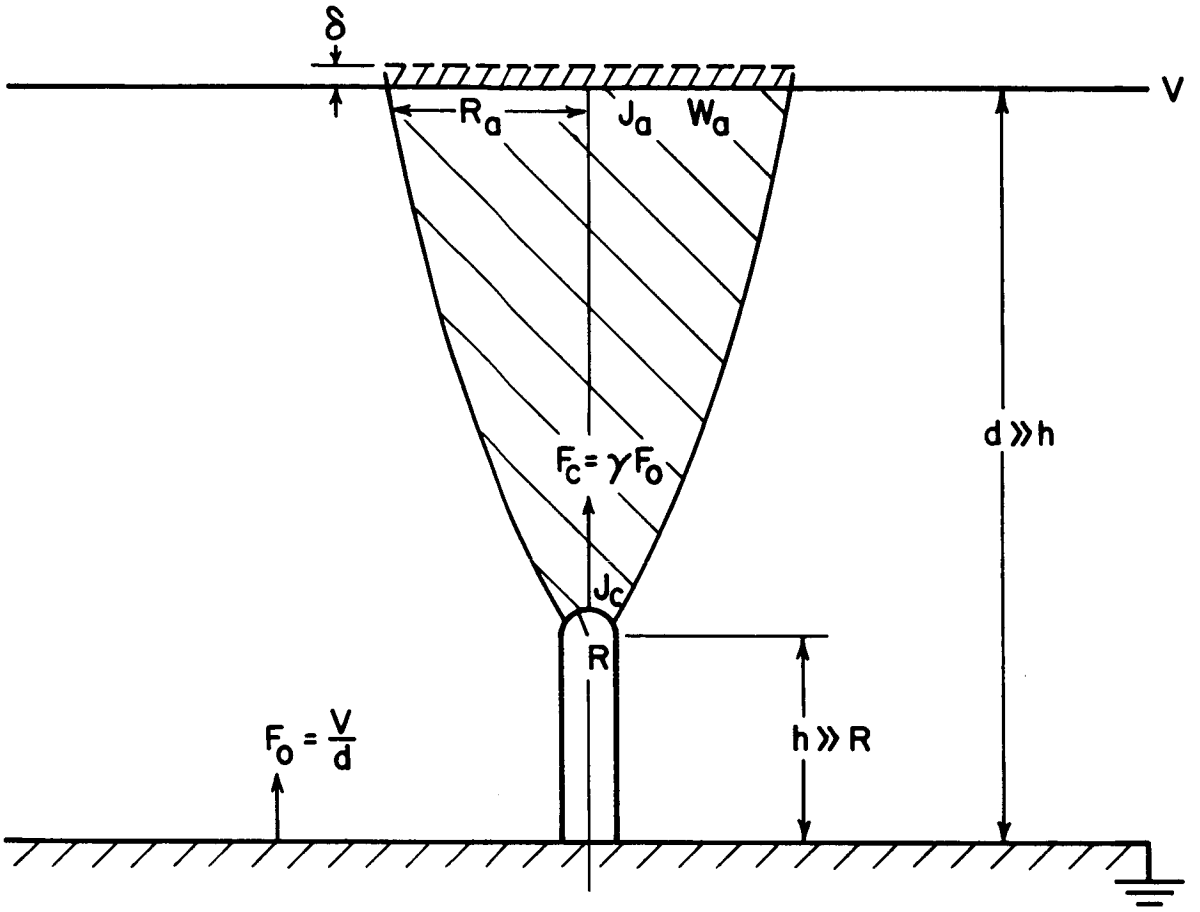

Figure 2. Emission from a whisker-type protrusion in a parallel plane gap. Gap: voltage V, spacing d and gross field $F_o = V/d$. Protrusion: height h and tip radius R, apex field F_c and current density J_c. Beam at anode: current density J_a, power density W_a, radius R_a and electron penetration δ.

which, when combined with Equation (2), yields:

$$W_a = \frac{J_a F d}{\gamma} \tag{4}$$

In addition, the current densities at the cathode and anode are given approximately as:

$$J = \frac{I}{\pi R_c^2} \tag{5}$$

$$J_a = \frac{I}{\pi R_a^2} \tag{6}$$

From Equations (1) through (6) and the assumption that $\gamma \cong \frac{h}{R_c}$, it can be shown that the beam power density at the anode is related to the power density at the cathode protrusion through the single parameter γ as follows:

$$\gamma \cong \left[\frac{h J F}{4 W_a}\right]^{1/3} \tag{7}$$

Equation (7) shows that the key factor in predicting thermal stability of any gap is the field enhancement factor. The fact that the numerator of Equation (7) is related to the properties of the cathode while the denominator is related only to the properties of the anode suggests that there is a boundary value of the surface enhancement factor separating anode from cathode initiated breakdown. A cylindrical cathode protrusion becomes thermally unstable and will be destroyed if the product h J exceeds a critical value[5]. If this critical value of current density at the cathode protrusion J_c is known, the critical field F_c is automatically defined according to the Fowler-Nordheim equation. This means that there is an absolute maximum value of the numerator of Equation (7) which can be uniquely determined for any cathode material. On the other hand, there also is a maximum power density W_{aM} which can be sustained at the anode, its precise value depending on the anode material, on cooling, on pulse duration and also on gap voltage for very short pulses. Whether it will be the cathode or the anode which will initiate breakdown is dependent only on the value of γ with respect to a boundary value of the surface enhancement factor defined by:

$$\gamma_o = \left[\frac{(h J_c F_c)\ \text{Max}}{4 W_{aM}}\right]^{1/3} \qquad \begin{array}{l} \gamma > \gamma_o \text{ (Cathode initiated)} \\ \gamma < \gamma_o \text{ (Anode initiated)} \end{array} \tag{8}$$

If protrusions exist on the cathode with a field enhancement factor greater than γ_o, cathode initiated breakdown will occur at these protrusions before excessive loading is reached at the anode. On the contrary if the cathode protrusions all have enhancement factors smaller than γ_o, then increasing emission from the sharper protrusions will lead to excessive heating of the anode and consequent breakdown before the emission level at the protrusion reaches the level for critical self-heating.

Means by which the numerator of Equation (8) can be determined have been discussed elsewhere.[3, 5, 12-14] In our work where the gap spacing and the electron beam diameters at the anode are small, the critical beam power density W_{aM} is controlled by heat adsorption and diffusion into the bulk of the anode rather than by radiation.

The temperature change in a solid due to an initial input of energy at a time t = 0 is an exponential function of time and distance, hence it is convenient to define a one dimensional thermal time constant $t_c = \frac{c\rho x^2}{4K}$. Here K is the thermal conductivity, ρ is the density, and c is the specific heat of the solid. The significance of this parameter is that at a time t_c 68 % of the initial energy is still within a distance $x = \sqrt{\frac{2K\, t_c}{c\rho}}$ and 99.5% is within 2x. (References 72 and 73).

For purposes of analysis it is convenient to define two characteristic time constants. The first of these is important for pulses that are very long compared to the time required for energy to travel a distance of the order of the electron effective penetration depth. In this case heat is transferred across the anode surface and into the bulk to an extent depending upon the length of the voltage pulse t_o with respect to the time constant t_1:

$$t_1 = \frac{c\rho}{4K} R_a^2 \tag{9}$$

As the pulse length becomes short the significant time constant is that related to the electron effective penetration depth δ:

$$t_2 = \frac{c\rho\delta^2}{4K} \tag{10}$$

If the pulse length t_o is much greater than t_2 two cases must be considered depending upon the pulse length with respect to t_1. Neglecting radiation losses, the temperature change in a homogeneous isotropic solid being bombarded by electrons has been calculated by others.[6, 7, 72, 73] If the temperature distribution in the solid is assumed to be one dimensional (the effective penetration depth δ is small compared to the radius of the bombarded area) the temperature at the center of the bombarded circle is:

$$T = \frac{W_a}{K} \sqrt{4 \frac{K}{c\rho} t} \left[\frac{1}{\sqrt{\pi}} - \text{ierfc} \left(\frac{R_a}{\sqrt{4 \frac{K}{c\rho} t}} \right) \right] \tag{11}$$

where $\text{ierfc}(x) = \frac{1}{\sqrt{\pi e^{-x}}} - x \left[1 - \text{erf}(x)\right]$ is the error function defined by Carslaw and Jaeger[6]. (Tables of values for the standard error function erf(x) are available in handbooks containing various physical, chemical and mathematical data [29]).

<u>Case I</u> - ($t_o >> t_1$) Radial Heat Dissipation

When the gap voltage is continuous or in the form of pulses much longer than t_1, the anode temperature reaches a steady state value which is easily obtained from Equation (11) and the identity:

$$\lim_{x \to o} \left[\text{ierfc}(x) \right] = \lim_{x \to o} \left[\frac{1}{\sqrt{\pi}} - \frac{x^2}{\sqrt{\pi}} \cdots\cdots -x \right] \tag{12}$$

The temperature rise from the initial temperature at t = 0 to the steady state as $t \to \infty$ will be:

$$\Delta T = \frac{R_a W_a}{K} \tag{13}$$

Combining Equations (1), (13), and (8), we can find a value of γ_o:

$$\gamma_o^{5/2} \cong \frac{\left(h\ J_c F_c\right)_{Max}}{2\ K \Delta T_{Max}} (R_c d)^{1/2} \quad \text{or} \quad \gamma_o = \left[\frac{\left(h\ J_c F_c\right)_{Max}}{2\ K \Delta T_{Max}} \right]^{0.4} (R_c d)^{0.2} \tag{14}$$

where ΔT_{Max} refers to the maximum temperature at the anode sufficient to cause instability and a regenerative breakdown. Similarly $\left(h\ J_c F_c\right)_{Max}$ refers to the maximum critical current density and field at the cathode leading to breakdown.

As a numerical example for tungsten protrusions of tip radius R_c between 50 and 2000 A and gap spacing d from 0.005 to 1 cm and arbitrarily assuming T_{Max} to be the melting point ($\Delta T_{Max} \cong 3000\,^oK$) γ_o ranges from about 35 at minimum R_c and d to a maximum of 220. The corresponding value of t_1, the time required for the anode to reach steady state temperature, being ~ 0.1 μsec and 0.003 sec respectively.

Case II - ($t_1 \gg t_o \gg t_2$) No Radial Heat Dissipation

In this case, the voltage pulse duration t_o is too short to permit lateral cooling of the anode spot (i.e., $t_o \ll t_1$), but is sufficiently long ($t_o \gg t_2$) that heat diffuses into the anode to a distance large compared to the electron effective penetration depth δ. In this time range the permissible beam power increases with decreasing pulse length according to the following expression which can be derived from Equation (11) in the limit $t \to o$:

$$W_{aM} = \Delta T_{Max} \sqrt{\frac{\pi}{4} \frac{Kc\rho}{t_o}} \tag{15}$$

which combines with Equation (8) to yield a value of γ_o:

$$\gamma_o \cong \left[\frac{(h\ J_c F_c)_{Max}}{2\ \Delta T_{Max} \sqrt{\pi K c \rho}} \sqrt{t_o} \right]^{1/3} \tag{16}$$

Hence, the shorter the pulse length the smaller the boundary value of γ_o (for example with tungsten electrodes $\gamma_o = 50$ at $t_o = 2\mu$sec).

The electron effective penetration depth is a sensitive function of applied voltage, so that for high voltages ($V > 100$ kv) and short pulse lengths one must consider the case when $t_o \ll t_2 \ll t_1$

This case applies when the pulse length is too short for significant heat diffusion beyond a depth δ in the anode spot, and heat conduction has negligible effect. The maximum permissible temperature at the target T_{Max} will occur at the surface (assuming the electrons have a uniform rate of energy loss at the surface), and will depend on the electron effective penetration depth since t_o is too short for heat dissipation into the volume. This can be considered as the adiabatic case in which the maximum permissible power density W_{aM} is independent of the conductivity of the material [7]

$$W_{aM} = \frac{c\rho\delta\ \Delta T_{Max}}{t_o} \tag{17}$$

substituting Equation (17) into Equation (8) gives a value of γ_o:

$$\gamma_o = \left[\frac{(h J_c F_c)_{Max}\ t_o}{4 c\rho\delta\ \Delta T_{Max}} \right]^{1/3} \tag{18}$$

For example, with tungsten electrodes and a beam gap voltage of 4 Mv for 30 nsec $W_{aM} = 10^{10}$ watts/cm^2, and γ_o is now less than 5.

Thus, cathode initiated breakdown is virtually certain since large surfaces with maximum local field enhancement of less than 10 to 20 are seldom achieved.

From the preceding discussion it has been shown that the boundary value γ_o of the maximum field enhancement factor at the cathode depends significantly on the duration of the voltage pulse applied at the gap, at least when this duration is too short for the anode surface to reach a steady state temperature. The shorter the pulse length, the smaller γ_o, and hence the greater probability of cathode rather than anode processes causing the regenerative instability which will lead to an arc.

The foregoing expressions allow an estimate of γ_o for plane parallel electrodes and various pulse length regions. This can be extended to the case of nonuniform gap geometries and small cathodes where much of the experimental work has been performed.

Space Charge Effects

A serious limitation of the foregoing discussion is that it ignores space charge effects. Early in the development of field emission technology it was noted that as the electric field at the tip of a field emitter became very large, the current increased less rapidly with increasing voltage than the Fowler-Nordheim theory would predict. This was not due to a failure of the theory, but to the onset of space charge effects. The space charge in the beam increases with increasing current and causes the electric field actually present at the emitter surface to be less than the calculated field βV by an amount that increases with increasing emitted current. As a result, space charge can have significant effect because of its magnitude at high current densities.

At the cathode the electron space charge is a contributing factor at high current densities in increasing the effective emitting area, thus the value of current density will be lower than that calculated by assuming that the emitting area remains constant.

In order to see what effect the space charge at the tip of a protrusion will have on the current density at the anode, a calculation must be made to determine how much beam spreading there will be at a distance d from the emitter equal to the gap spacing since $d \gg h$ where h is height of the protrusion. If space charge effects are neglected, the radius of an electron beam at the anode is proportional to the square root of the protrusion tip radius as shown in Equation (1). This expression takes into account the compression of the beam caused by the close proximity to the emitting apex of the supporting plane.

The spreading of an electron beam due to space charge repulsion has been calculated by Vibrans[8] from whose analysis one can obtain a ratio r/r_o which is the ratio of the radius of the beam due to the electron

space charge repulsion r to the initial radius of the beam r_o. A very rough approximation of the beam radius at the anode including the effect of space charge may be made by assuming most of the beam spreading will occur within ten tip radii of the emitting protrusion. The value of R_c in Equation (1) can then be replaced by $r = (r/r_o) R_c$ giving a larger value of R_a thus a smaller value of current density at the anode spot. The effect of space charge is to allow higher gross fields to be sustained across the gap before the onset of thermal instability at either electrode.

Although electron space charge must be considered, ion space charge effects are probably more significant in many practical environments where a limited vacuum leads both to appreciable residual gas pressure and to heavy contamination of electrode surfaces by adsorbates, which often are loosely bound to the substrate and readily release upon energy input by charged particle bombardment. Rapid release of a monolayer of contaminants in a narrow plane gap will cause very high transient gap pressures and, in the presence of a background field emitted electron current from cathode protrusions, will produce large and nonuniform densities of ions which can lead to tightly focused electron beams and local overloading of the anode with resultant breakdown. Release and ionization of surface contaminants with subsequent ion focusing of electron beams and anode overloading probably account in large part for the frequent observation of small craters at the electrode and for the occurrence of anode-initiated breakdown at gap voltages well below those which are predicted by the foregoing analysis in the dc or long pulse situation, where anode initiation predominates.

Effect of Electrostatic Stress

In an earlier report[1] a discussion of the effect of high electric field on the geometry of protrusions was presented. It was shown that when the electrostatic field at the tip of a heated tungsten field emitter exceeded 10^8 v/cm surface protrusions could be nucleated which seemed to increase in length at a rate governed by the temperature, the diffusivity constant and the activation energy for surface migration of the surface atoms. A balance can be achieved between surface tension and field forces when the tip radius and field at a surface are related by the approximate expression:[9]

$$R_c F^2 \cong 16 \pi S \tag{19}$$

where F is the electric field at the apex of the protrusion of tip radius R_c and S is the surface tension of the protrusion material. The fields at which instability will occur for different materials of similar geometry is proportional to the square root of the ratio of their respective surface tension, thus if tungsten becomes unstable at fields of 10^8 v/cm, one would expect copper to become unstable at fields of 6×10^7 v/cm and aluminum at 3×10^7 v/cm. Negative fields of 10^8 v/cm would cause instantaneous destruction of a tungsten protrusion by emission initiated thermal processes, thus one would expect electrostatic stress to be of little significance with tungsten electrodes. However, since both positive and negative fields as high as those quoted are possible with copper or aluminum electrodes, electrostatic stress must be considered as well as thermal effects when these materials are used. Since rates of protrusion growth depend significantly on the surface diffusivity and migration activation energy, more information is

needed concerning these constants before any quantitative analysis predicting growth rates can be made.

The effect of electrostatic stress due to the gross field in the gap has been discussed previously[1]. It has been shown that stress can be responsible for changes in gap spacing that can lead to regenerative processes under certain conditions. For the electrode geometry used in our investigation, calculated values of either electrode movement or surface distortion due to electrostatic stress are not as significant in general as thermal processes.

EXPERIMENTAL PROCEDURES

The molybdenum electrode experimental tube is shown in Figure 3. It was basically a diode consisting of a stationary 30 mil diameter spherical electrode and a moveable 200 mil diameter planar electrode, a cesium source, and a field emission microscope which could be used to monitor conditions within the tube. Both electrodes could be heated to remove surface contaminants and to smooth surface roughness. Observation of events taking place in the gap could be made by means of a flat window directly opposite the gap.

The I-V data was taken in low current ranges (from 10^{-10} to 10^{-6} amps) using only dc voltages but in the higher current range up to the actual arc the voltage could be applied in single pulses of 2 to 10 μsec duration.

From the low current I-V data the work function ϕ, the surface enhancement factor γ, and an effective emitting area could be determined using previously described methods[1]. The radius of the tip of an emitting protrusion is proportional to the square root of the emitting area, the factor of proportionality ranging from 1 - 4 for fields of from 30 - 100 Mv/cm. Knowing the field and the effective emitting area, a value can be calculated for the radius of an emitting protrusion. Using the relationship between the radius of the emitting protrusion and the radius of the anode spot, (Equation (1)) an anode current density could be calculated and thus an anode power density could be assigned for each value of I-V. Since temperature is an important parameter in the theory of field emission initiated voltage breakdown, an independent method was needed to determine the accuracy of the calculations. A very rough check was made experimentally. The diameter of the anode spot was determined by measuring the diameter of the spot from which transition radiation [10] was observed using a telemicroscope with a micrometer eyepiece. After the spot size had been determined in this way, a polaroid filter was placed over the microscope objective positioned so that the plane-polarized transition radiation could not be transmitted to the eye. The onset of thermal radiation could thus be detected at some particular value of current and voltage. Although the small spot size and the low intensity of the radiation made it difficult to use any of the pyrometers available in this laboratory, values were obtained which could be compared with the temperature calculated from Equation (13). The size of the anode spot measured in this way agreed within 30% with that calculated from the relationship between cathode radius and anode radius, the measured radius being the larger. Thermal radiation when the anode power density was such

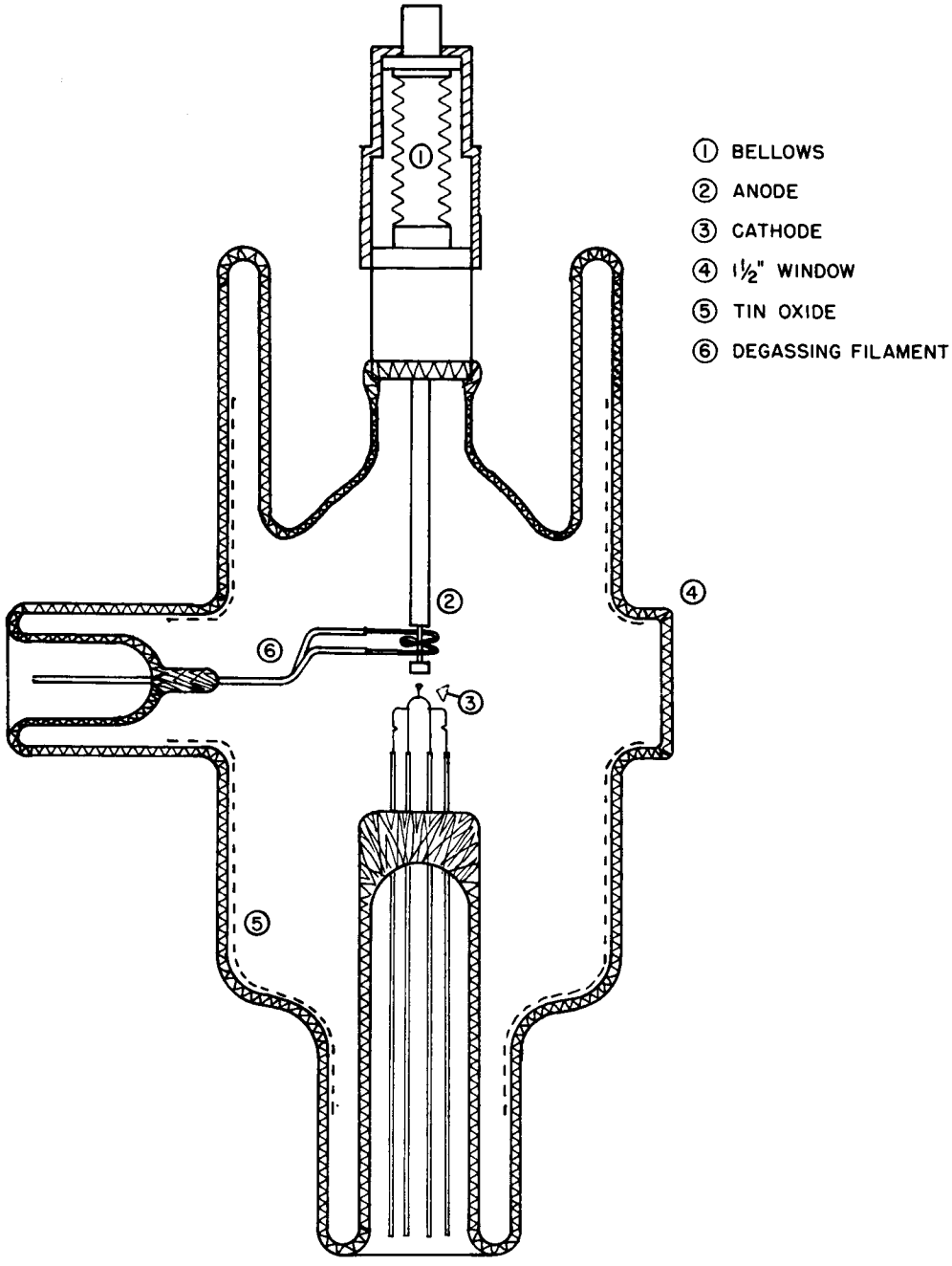

Figure 3. Redesigned variable spacing tube for voltage breakdown studies.

that ΔT was calculated to be 1000°K, that is, the temperature of the anode spot would be ~1300°K was measured by a pyrometer and found to be 1350°K.

In order to determine the effect of the properties of the electrode material on the arc characteristics, two tubes of similar design were built. The tube in Figure 4 is a copper-tungsten diode.

In a similar tube the copper electrode was replaced by an aluminum electrode made from a single crystal 99.995% pure in the form of a cylinder 175 mils in diameter and 3/8 inch in length. The surface of the electrode was polished in a solution of dilute phosphoric acid and glycerol. Before each data run, the aluminum electrode was not heated to a temperature above 450°C. Since it is known that aluminum oxide films form readily at room temperature[11] even when the oxygen supply is limited, there was very likely a thin film (probably less than 30 A thick[11]) of aluminum oxide on the electrode.

EXPERIMENTAL RESULTS AND DISCUSSION

Qualitative experimental agreement with theoretical predictions resulted from early work in which copper electrodes were used in a fixed gap spacing diode whose electrodes consisted of two 30 mil diameter spheres at a gap spacing of 4.5 mils.

As the voltage was increased across the gap, the anode spot became visible due to transition radiation [10] which occurs when electrons impinge upon a metal surface in vacuum. Further increasing the voltage caused the radiation to become sufficiently intense that it could be photographed, as shown in the sequence of photographs in Figure 5. As the field at the cathode was increased until the current density approached 7×10^7 amps/cm^2, a spot of incandescent light became visible on the cathode, as shown in Figure 5, photograph C, and a slight pressure increase was observed. Further increase in gap current caused the blue transition radiation on the anode to become incandescent. However, the spot on the cathode appeared to be at a higher temperature than that on the anode and the current density (7×10^7 amps/cm^2) was sufficient to resistively heat the emitting protrusion. The enhancement factor was calculated from the pre-breakdown field emission I-V data[1] and found to be about 250. The phenomena was reproducible, although the I-V data was quite different after the emitting protrusion had been allowed to heat, indicating that there had been a change in emitter geometry.

The boundary value of the surface enhancement factor which separates anode from cathode initiated thermal processes was calculated from Equation (14). This value of $\gamma_o = 107$ was lower than the actual value of γ hence theory would predict a cathode initiated breakdown in agreement with experimental observation.

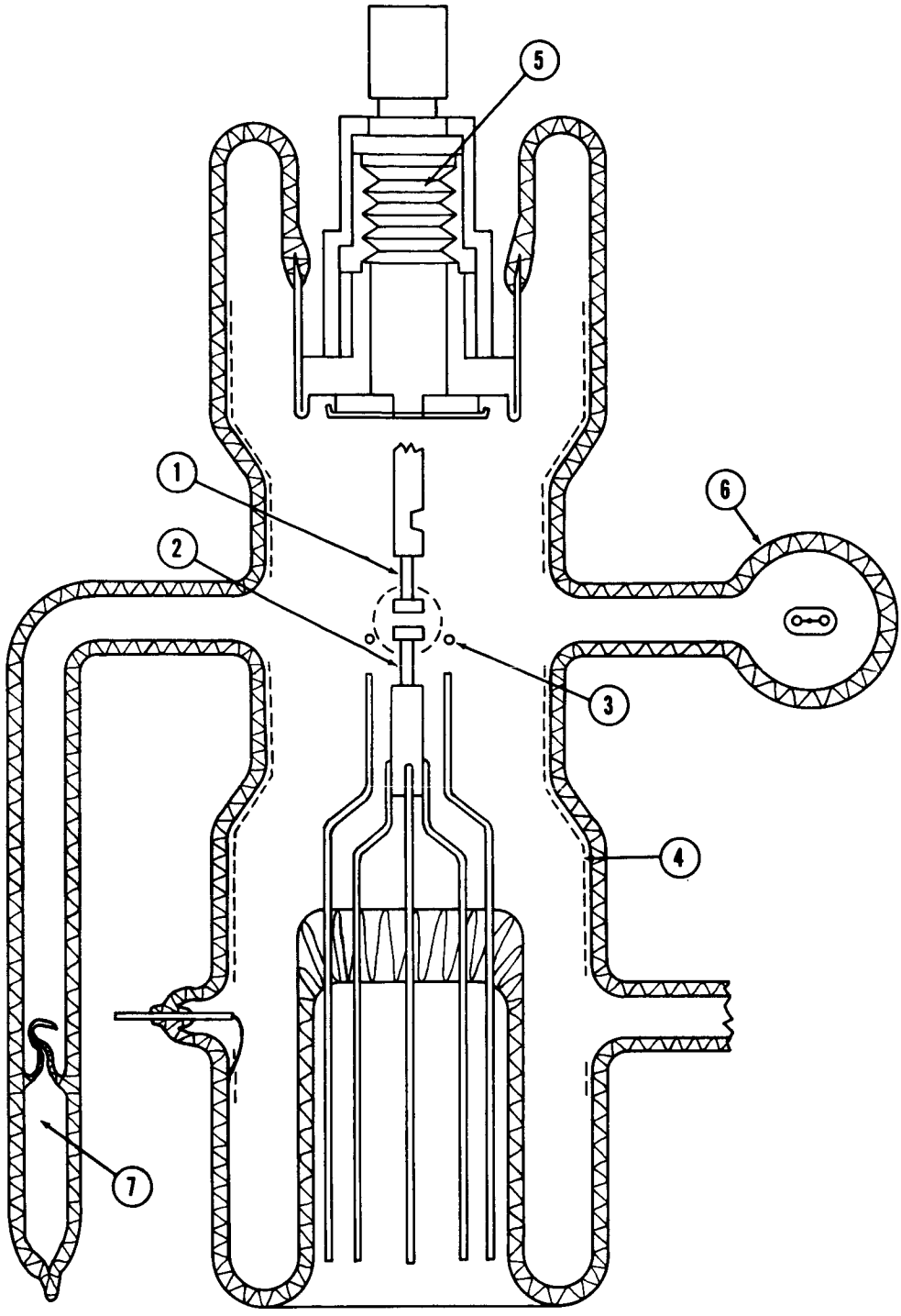

Figure 4. Variable gap spacing copper-tungsten diode with the following features: 1) 200 mil diameter disk that is 75 mils thick attached to a 60 mil diameter rod; 2) identical copper electrode; 3) outgassing ring; 4) stannous oxide conductive coating; 5) bellows assembly; 6) field emission microscope and 7) cesium source.

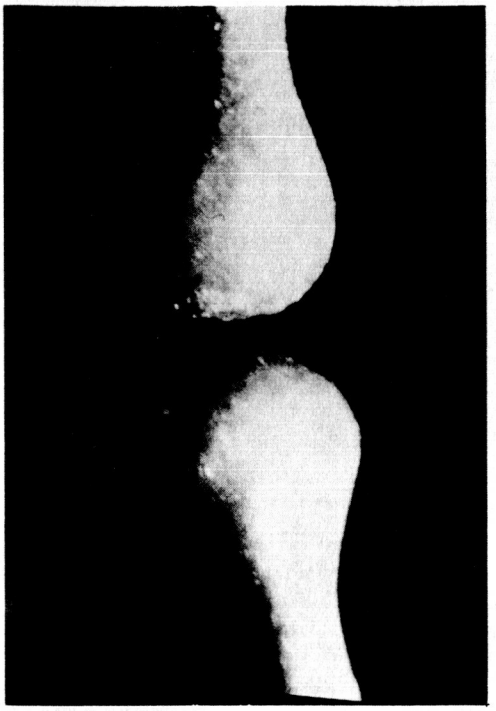

A

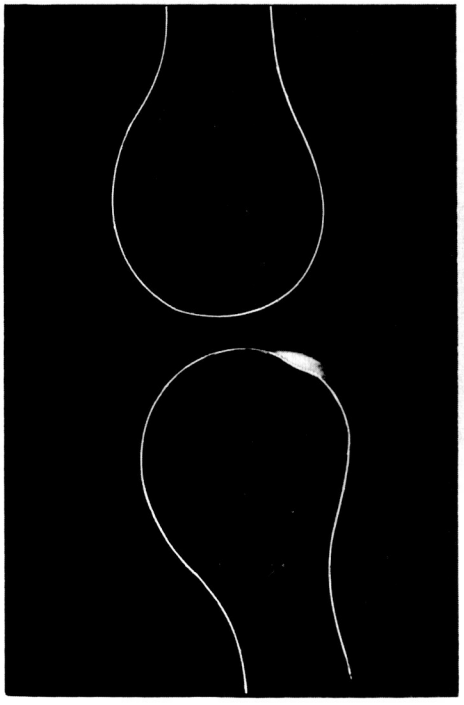

B

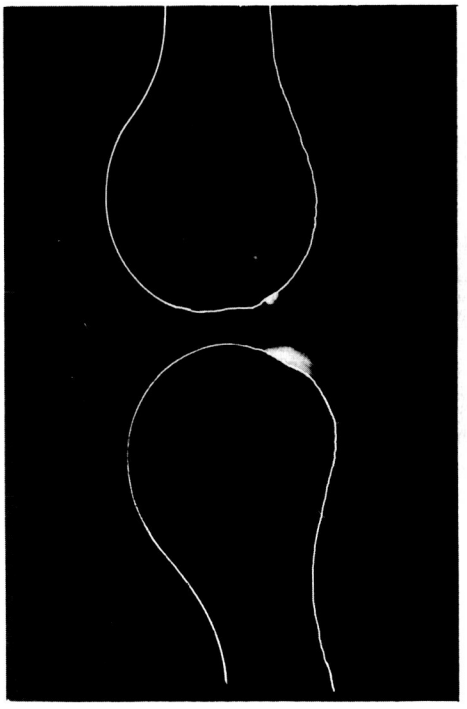

C

Figure 5. Sequence of events showing visible evidence of pre-breakdown electron emission. A - orientation and geometry of the electrodes: B - transition radiation visible on the anode at a cathode current density of approximately 3×10^7 amps/cm^2: C - transition radiation on the anode and also an incandescent spot appears on the cathode at a current density of about 7×10^7 amps/cm^2.

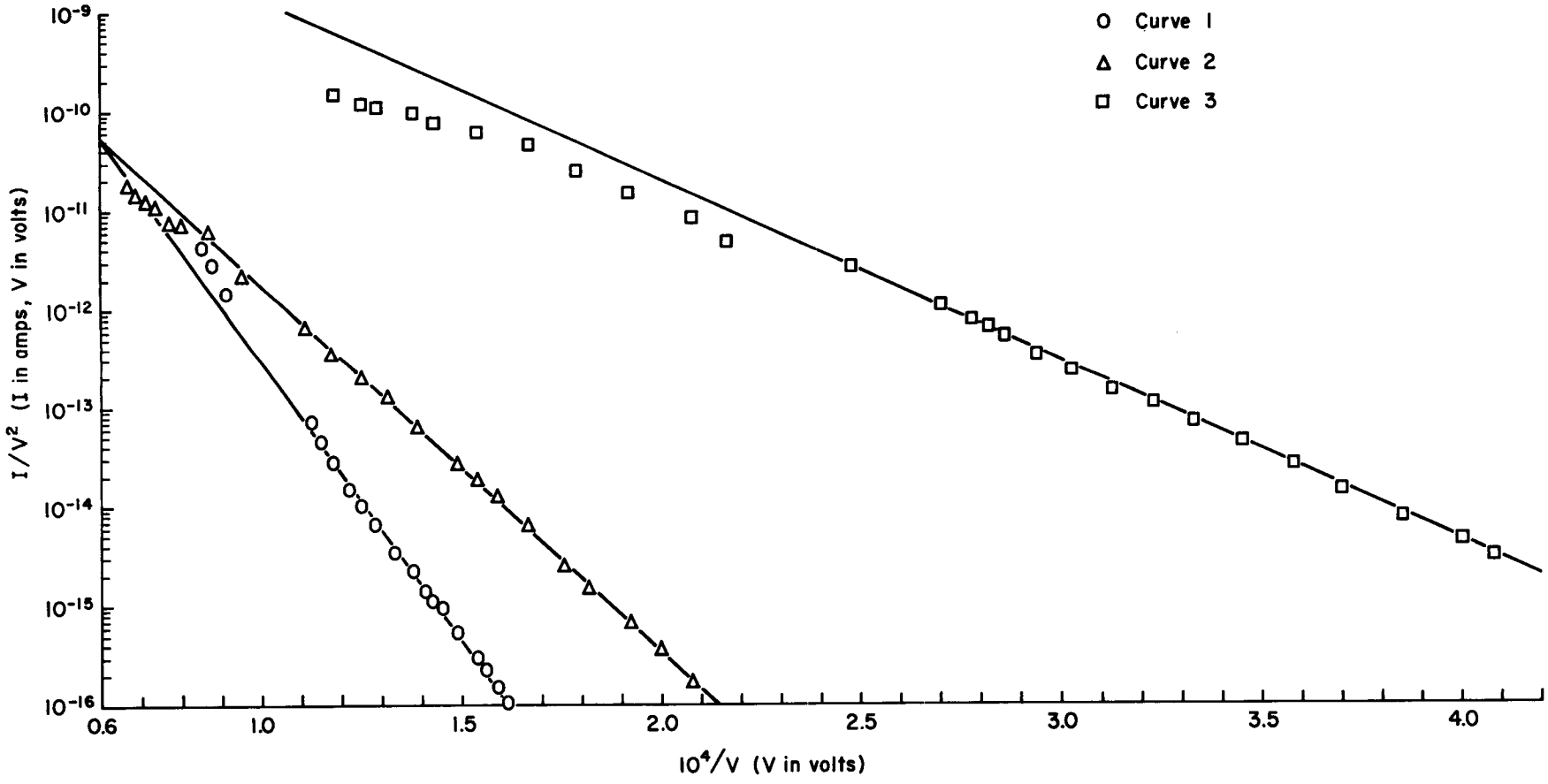

Figure 6. Fowler-Nordheim plots of I-V data from clean molybdenum electrodes with various amounts of surface roughness, and several different gap spacings.

The polarity of the gap was reversed and a new $\gamma_o = 188$ was calculated. No incandescence was now seen on the cathodic electrode although a spot on the anode became incandescent from electron bombardment. For this surface, a γ of 140 was less than γ_o hence an anode initiated breakdown would be predicted. Breakdown did occur at a cathode current density several orders of magnitude lower than would be expected for a cathodic process.

Since these initial observations seemed to agree with theory, a more detailed study was made in which the effect of changing each of the following parameters could be determined: gap spacing, surface enhancement factor, continuous or pulsed voltages, and electrode material.

Effect of Pulse Length Variation

For a voltage pulse length t_o that is greater than the time t_1 required for the anode to reach its steady state temperature, the I-V characteristics for a given electrode surface should simulate the dc condition. According to the preceding discussion breakdown should be anode initiated when the pulse length is very long compared with t_1 unless the surface enhancement factor γ is very large. As the pulse length is shortened the boundary value of the enhancement factor γ_o is lowered until the probability of a cathode initiated arc becomes greater than that of an anode initiated arc. In order to obtain experimental verification pulse lengths t_o varying from 2 to 20μsec were used with varying degrees of surface roughness. Fowler-Nordheim plots of some of the results are shown in Figures 6 and 7 where the curves of Figure 6 are from clean molybdenum at various spacings and γ, while those of Figure 7 are from heavily cesium-covered molybdenum electrodes. Curve 1 of Figure 6 shows the I-V data from a surface with an enhancement factor of 18.4 corresponding to a conical protrusion of tip radius $R_c = 5.5 \times 10^{-6}$ cm. For this surface an anode initiated breakdown would be expected since $t_o = 2\mu$sec and $t_o/t_1 = 3.8$ and γ is 18.4, a value much less than γ_o. Curves 2 and 3 of Figure 6 are for surfaces whose enhancement factors are approximately equal (72 and 71 respectively). However, $t_o = 2$ μsec and $t_o/t_1 = 1.43$ for Curve 3 while $t_o = 20$ μsec and $t_o/t_1 = 11.1$ for Curve 2. The deviation from linearity of both these curves and for Curves 2 and 3 of Figure 7 is due to electron space charge effects, which are quite significant when current densities are high.

The curves of Figure 7 were obtained from a surface heavily cesium coated. The pulse length of 2 μsec gave a value of t_o/t_1 for Curve 1 of only .265, thus the anode was not able to reach its steady state temperature. However, the enhancement factor for this surface was only 10, which is still below the value of $\gamma_o = 50$ so that the theory would predict an anode process to initiate the arc. The cesium coverage decreased during the pulse

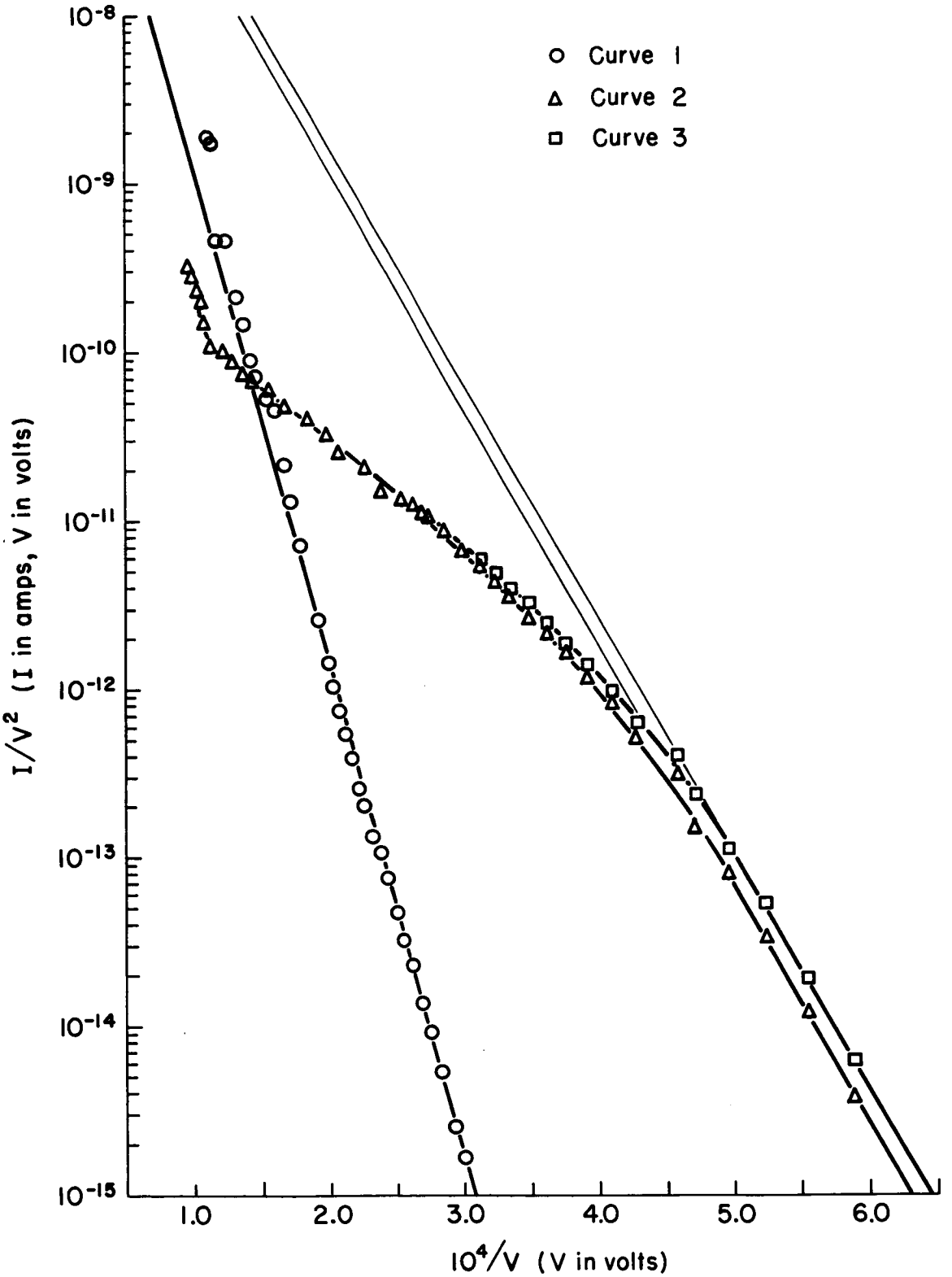

Figure 7. Fowler-Nordheim plots of I-V data from cesium-covered molybdenum electrodes (ϕ = 1.4) at different gap spacings and for two different values of enhancement factor.

interval due to the emission heating of the substrate and the resulting surface migration away from the high field at the protrusion tip and/or to thermal desorption making calculations of $\emptyset$ and T unreliable. Curve 2 of Figure 7 shows the Fowler-Nordheim plot for a surface whose enhancement factor was 47.8, while Curve 3 shows the reproducibility of the data points of Curve 2.

One would predict an anode initiated arc for all cases in the above data except that shown in Curve 3 of Figure 6. The results of analyzing the pulsed voltage data showed that the cathode current density J_M at which breakdown occurred followed trends listed below indicating agreement with theory.

At constant γ:

J_M decreased with increasing pulse length t_o

J_M increased with decreasing t_o

At constant pulse interval t_o:

J_M decreased with decreasing γ

J_M increased with increasing γ

In Figures 8 and 9, the data of Figures 6 and 7 are plotted with the emitted current density as a function of the electrostatic field. The maximum space charge limiting value of current density J_s shown in these figures is that for which the field at the cathode vanishes and is determined by the gap spacing, the apex radius of the emitting protrusion, and the electric field that would exist at the cathode surface in the absence of emission. To calculate R_c from the low J pre-breakdown data and the relationship $I/J = A_c$, some relationship between A_c and R_c must be established. The effective emitting area is not really constant but increases as the anode voltage increases due to the nonlinearity of the field emission response and because of the onset of space charge effects which occur first near the protrusion apex where field and emission are greatest. However, if the effective emitting area is expressed as $A_c = \lambda r^2$ where λ is constant for a given field, it can be shown[12] that λ ranges from 1 to 4 for clean tungsten when the electrostatic field F is between 30 and 100 Mv/cm. Using the value of A_c and λ from the low J pre-breakdown data, a value of R_c can be calculated which will be constant for all values of J and F. For most values of field and current density, $\lambda \sim 2$. Using this average value and assuming that the effective emitting area is constant for all values of current density investigated, Curve 1 of Figure 8 can be obtained for the current density as a function of electrostatic field. If the effect of changing emitting area is considered, the values for current density will be those shown in Curve 2. It can be seen that in the low J region, the two curves are essentially the same but that there is a considerable difference as the current density increases. The

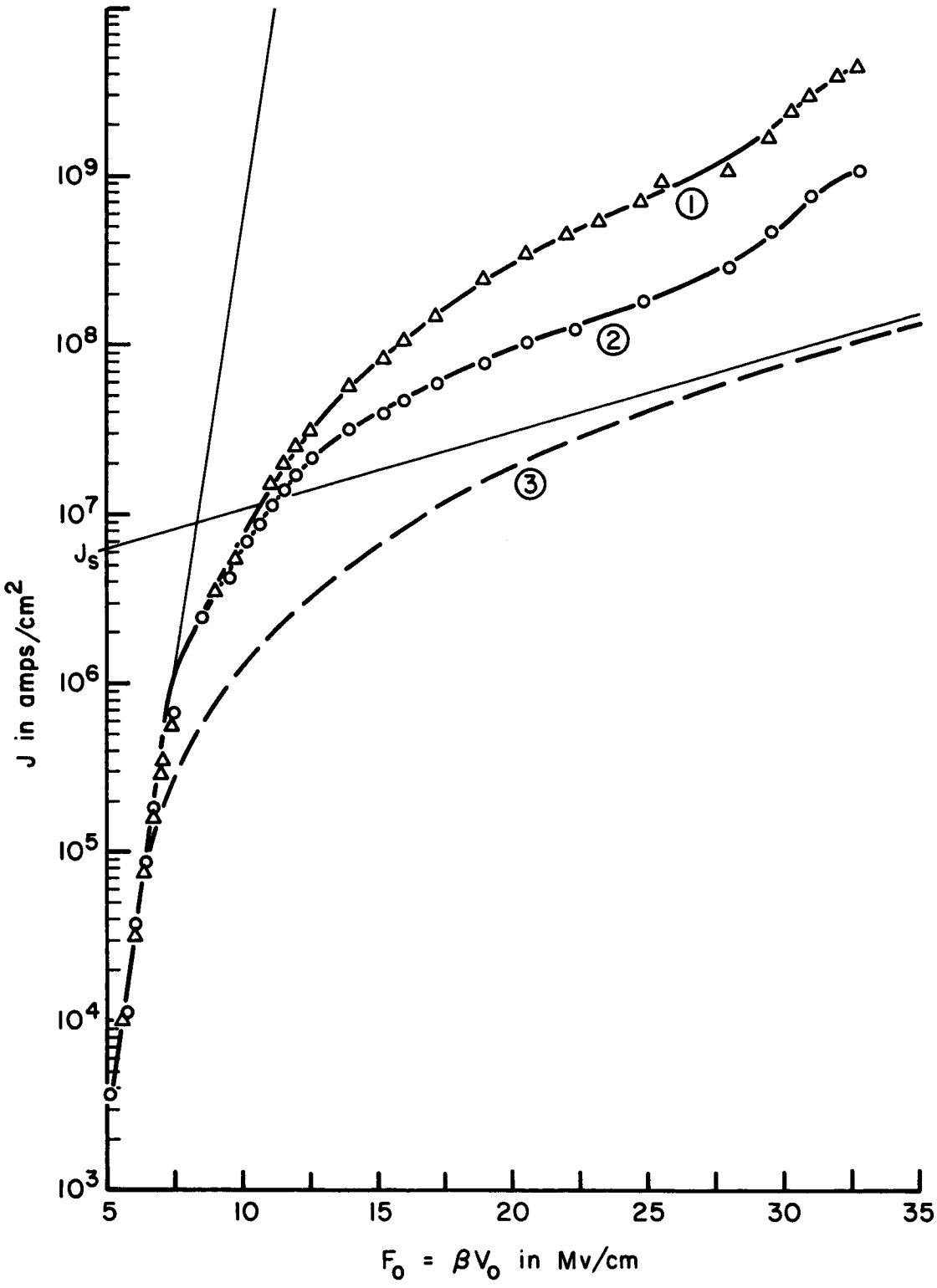

Figure 8. I-V data of Curve 2, Figure 7 plotted as current density $J = I/A$ vs. electrostatic field at the protrusion tip F_0. Curve 1 shows the experimentally recorded values of current divided by the emitting area calculated from the low current density I-V data. Curve 2 shows the same data except that the effect of field and current density have been taken into account in calculating effective emitting area. Curve 3 is the predicted curve if only the original protrusion emits.

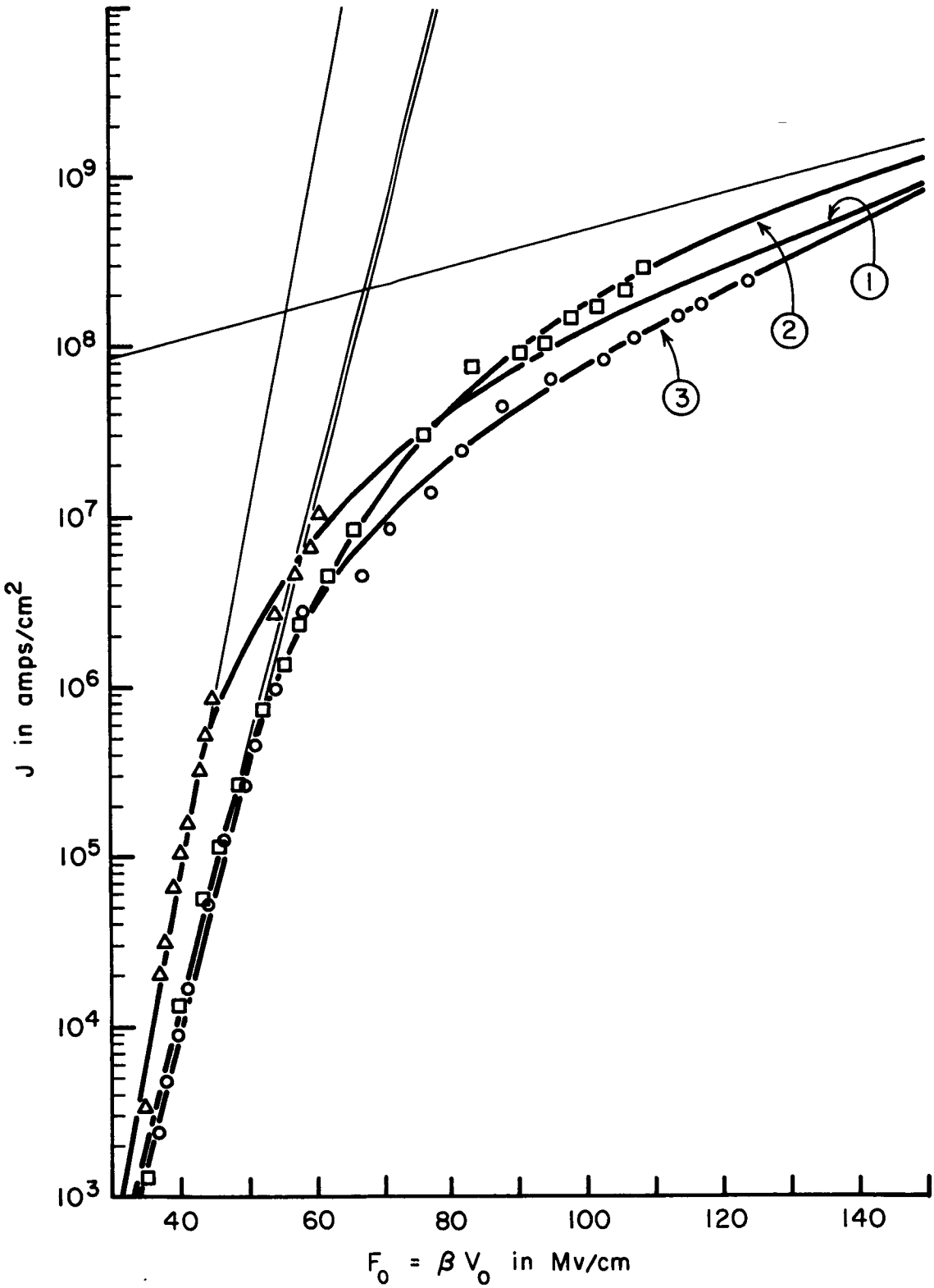

Figure 9. Shows current density as a function of electrostatic field using the clean molybdenum data of Figure 6. The curve numbers correspond to the respective curve numbers of Figure 6.

effect of field on effective emitting area is taken into account when calculating the values of J shown in Figure 9. It is immediately obvious from Figure 8 that the values of J are much too high even when the effect of changing emitting area is taken into account when cesium is on the surface. Thus with cesium present and when the value of γ is high, it seems most likely that as the originally most highly emitting protrusion attains a current density sufficient for a large electron space charge region to form just in front of its apex, emission from this protrusion is suppressed so that it does not become thermally unstable before other protrusions with slightly lower γ are capable of contributing significantly to the total emitted current. Since space charge effects are observed at lower values of J for surfaces with lower work function, one would expect the experimentally observed space charge effects and the occurrence of much higher total currents without an arc for low ϕ surfaces.

The importance of considering space charge repulsion in the beam when calculating anode spot temperature ΔT_a can be seen in Table I where both the anode and the cathode temperatures are calculated from experimental $(IV)_{Max}$. Equation (13) was used to calculate the anode temperature. In order to calculate the cathode temperature, the following approximate equation, derived for an emission heated field emitter[13,14] was used:

$$\Delta T_c = \frac{\eta}{2K} J^2 R_c^2 + J R_c \frac{\pi k T}{K} (\cot \pi p) \tag{20}$$

where η and K are the electrical resistivity and the thermal conductivity at a particular temperature, k is Boltzmann's constant and $p \cong 1.5 \times 10^{-3} \frac{T}{\phi}$. The first term is due to Joule heating and the second term represents the Nottingham effect.

TABLE I

Data	ΔT_c	ΔT_a (neglecting space charge)	ΔT_a (considering space charge)	γ/γ_o	t_1/t_o	d (mils)
Figure 5: (Clean Mo)						
Curve 1	5.7^oK	2900^oK	885^oK	.332	3.8	1.4
Curve 2	404.0^oK	$1.38 \times 10^{4o}K$	1970^oK	.910	11.1	3.9
Curve 3	605.0^oK	$1.64 \times 10^{4o}K$	2480^oK	1.390	1.43	1.9
Figure 4: (Cs on Mo)	69.5^oK	$3.81 \times 10^{6o}K$	2620^oK	.960	.265	5.9

When the voltage across the gap was increased continuously (dc case for which $t_o \rightarrow \infty$) it was found that when the anode power density reached some critical value, the current would increase exponentially with time at a constant voltage until an arc occurred. Changing the work function of the surface so that the voltage required to maintain a constant

current was changed by a factor of five, or changing electrode materials showed that the power density required to initiate the "runaway" condition was constant under these conditions and between 30 and 40 kw/cm^2 in magnitude.

Once the runaway condition had begun two ways were observed in which the condition would terminate, depending on the value of γ. If the initial γ were high, there would be some voltage at which the current would increase rapidly with time. As the current increased the voltage dropped until it had fallen to some fraction of its initial value. When this happened the current which had been increasing rapidly, stabilized at some fairly high value several orders of magnitude higher in some cases than it had been at the onset of the runaway condition. Radiation in the gap offered visual evidence of a continuous glow discharge between the electrodes even though the thermal radiation from the anode indicated that the anode was quite hot ($\sim 1000^{\circ}C$ for tungsten anode as determined by optical pyrometer).

The limiting value of current in the gap appears to be governed by the output impedance of the high voltage power supply in the circuit. This same phenomena was observed using copper, tungsten or molybdenum as the cathode, always occurring when the surface enhancement factor was greater than 100. A similar phenomena has been reported recently by J. Franzen and K. D. Schuy.[15] In a study of the condensed vacuum discharge between stainless steel electrodes, these investigators reported that a short high voltage breakdown spark is followed by a longer low voltage discharge. Since the voltage in their case was applied in single pulses the duration of their low voltage discharge was shown to be proportional to the square root of the primary capacitance in the charging circuit. They report no steady state low voltage discharge condition such as that observed here.

When γ was below 50 the current would continue to increase at a constant voltage until a destructive arc occurred. After the arc the I-V characteristics would be altered in such a way that if the enhancement factor had been below 20 or 30, the surface after the arc would be roughened, whereas if the initial γ were between 30 and 50, γ would be lower after an arc.

Power density is related directly to the temperature of the bombarded surface as given in Equation (13) so that one explanation for the onset of current instability might be that gas atoms on the anode surface are being thermally desorbed or ionized. If this were true, the desorbed atoms could either be ionized in the gap and sputter the emitting protrusion, or contaminate the protrusion and change its work function. Either event would be easily detected as a change in the slope of the Fowler-Nordheim plots before and after the onset of the current instability. However, the reproducibility of the I-V data showed that irreversible alterations of the cathode surface could not cause the increase in current. Further evidence

for this is the fact that the critical anode power density remained constant and independent of the state of cleanliness of the anode surface.

The instability could also be initiated by electrostatic stress, although there was a considerable variation in both the enhanced field and the gross fields at which it was found to occur. If the instability were initiated by electrostatic stress, it would be expected to occur at lower values of field when copper is used as an electrode than when tungsten or molybdenum were used due to the lower yield strength of copper. When both electrodes were molybdenum, the instability began at gross fields of between .115 and 5.3 Mv/cm corresponding to enhanced fields between 39 and 68 Mv/cm, while for the copper tungsten diode, the gross fields were between .093 and .760 Mv/cm, corresponding to enhanced fields from 49 to 80 Mv/cm. Since the data is reproducible after the onset of the instability, the geometry of emitting protrusions is not changed, thus the stress would have to be reversible, resulting in a decrease in gap spacing sufficient to cause the observed increase in current.

A more likely possibility is that the instability is caused by a regenerative decrease in gap spacing caused by the thermal expansion of the anode as it becomes heated by the bombarding electron beam. If one calculates the percent change in length corresponding to the minimum detectable power density at which instability begins, this can be related through the Fowler-Nordheim equation to a percent change in current. The percent change in length due to thermal expansion under conditions at which the instability is first detected corresponds to a change in current of only 1%.

Although a regenerative process initiated by such a slight change in current would take an extremely long time, a slight increase in voltage with the resulting large increase in current would cause an instability which could rapidly lead to an arc. For example, if the voltage is increased only 1%, the current is increased by $\sim 15\%$, which would cause an increase in anode temperature of $\sim 15\%$. If the anode is initially several hundred degrees above room temperature, the resulting change in gap spacing due to expansion could cause an increase in the temperature of the anode spot of one hundred degrees in a few μsec with very narrow gaps.

Very likely the steps in the regenerative process leading to the arc in the dc case are the following: 1) thermal expansion of the anode causes an initial decrease in gap spacing which in turn leads to further heating of the anode and increase in emitted current; 2) as the gap is reduced electrostatic stress can cause further reduction of gap spacing by an amount depending upon the initial spacing and the material of which the electrodes are made; 3) the resulting increase in field causes current density increases at both electrodes so that either the tip of the emitting protrusion becomes thermally unstable and vaporizes material into the gap or the anode spot becomes sufficiently heated that material

is vaporized depending primarily on the magnitude of the surface enhancement factor.

The data suggests that when the electrodes are made of tungsten, copper, or molybdenum, reversible electrostatic stress plays only a secondary part, if any, in generating the arc, but for electrodes made of aluminum one would expect irreversible yield to the electrostatic stress to be significant at much lower fields.

The following experimental facts indicate that with aluminum, stress is important: in the aluminum-tungsten diode no pre-breakdown instability such as that observed for other electrode materials was detected; with either polarity of the gap the local fields at which the arc occurred were roughly the same and almost a factor of two lower than breakdown fields between copper-tungsten or molybdenum electrodes; and the currents at which the arc occurred were too low for thermal processes to be significant.

Effect of Varying Electrode Material

If the electrodes are made of dissimilar materials, the boundary value of surface enhancement factor γ_o predicting whether an arc will be anode or cathode initiated will be different from that given in Equations (14), (16), and (18) by some factor related to the conduction properties of the two electrodes. For example, if ΔT_{Max} is the change in temperature required for a material to reach a particular vapor pressure, γ_o' for a tungsten-copper diode is related to γ_o for a similar tungsten diode in the following way when the copper is the anode:

$$\left.\begin{aligned}
&\text{From Equation (14)}\\
&\text{A)}\quad \gamma_o' = \gamma_o \left[\frac{(K\,\Delta T)_W}{(K\,\Delta T)_{Cu}}\right]^{0.4} = .85\,\gamma_o\\
&\text{From Equation (16)}\\
&\text{B)}\quad \gamma_o' = \gamma_o \left[\frac{(K\,c\,\rho\,\Delta T^2)_W}{(K\,c\,\rho\,\Delta T^2)_{Cu}}\right]^{1/6} = 1.04\,\gamma_o\\
&\text{From Equation (18)}\\
&\text{C)}\quad \gamma_o' = \gamma_o \left[\frac{(c\rho\,\delta\,\Delta T)_W}{(c\,\delta\,\Delta T)_{Cu}}\right]^{1/3} = 1.12\,\gamma_o
\end{aligned}\right\} \qquad (21)$$

where ΔT_W and ΔT_{Cu} correspond to the temperature change required for each of the electrodes to reach a temperature corresponding to a vapor pressure of 10^{-4} torr (just below the melting point for copper) and the physical constants are evaluated at that temperature. From Equation (21) it is apparent that there is a slightly greater tendency for the copper anode to initiate the arc if the voltage is applied in pulses, while for continuously applied voltages there is a slightly greater possibility that the tungsten cathode will initiate the arc.

If the polarity is reversed so that the cathode is copper, a similar computation for the change in γ_o can be made by using Equation (20). The factor by which γ_o will change is now independent of the pulse length since γ_o is proportional to $(J_c F_c)^{1/3}$ in all cases.

If both the resistive heating term and the Nottingham effect term in Equation (20) are considered, one finds that a tungsten cathode at 3000°K (corresponding to a vapor pressure of 10^{-4} torr) is well above the inversion temperature so that there is considerable emission cooling and hence much higher current densities are required to reach this temperature than would be

predicted by resistive heating alone. A copper cathode at the same vapor pressure must be heated to 1300°K, a temperature just below the theoretically predicted inversion temperature so that there is a significant amount of heating of the protrusion tip from the emission process alone, and much lower current densities are therefore required to reach this temperature than would be predicted by considering only resistive heating. This means that although copper is a much better conductor and will tend to dissipate heat rapidly as an anode, as a cathode the gain in conduction properties over a refractory material such as tungsten is balanced by the increased contribution of emission heating at lower temperatures.

If only resistive heating were considered, the effect on γ_o when copper is used as a cathode would be $\gamma'_o = 1.8\gamma_o$, but if both terms are considered as they should be $\gamma'_o = .86\gamma_o$. There is some evidence that γ'_o would be even lower since recent work at this laboratory[16] shows that the inversion temperature for tungsten is even lower than predicted by theory, hence even higher values of current density may be permitted before the required temperature is attained.

Using this method of calculating γ_o comparisons can be made between experiment and theory from Table II which shows the anode power calculated from Equation(13) or (15) and the emitted current according to Equation (20) required for the indicated electrode material to reach a temperature corresponding to 10^{-4} torr. The calculated values can be compared with the maximum values of current and power attained experimentally prior to an arc. In some cases no arc occurred due to external circuitry limitations of $(I)_{max}$. Agreement with theory is indicated in the following way:

1) When $\gamma > \gamma_o$ a cathode initiated process is predicted, hence in Table II, $(IV)_{Max}$ calculated should be greater than $(IV)_{Max}$ experimental, while $(I)_{Max}$ calculated should be the same as $(I)_{Max}$ experimental.

2) When $\gamma < \gamma_o$ an anode initiated process is indicated, thus $(IV)_{Max}$ calculated should be the same as $(IV)_{Max}$ experimental and $(I)_{Max}$ calculated should be greater than $(I)_{Max}$ experimental.

Even in the cases in which the arc was prevented by the external circuitry, comparisons between experiment and theory can be made since the power at the anode will be increased in approximately the same ratio as the current $\frac{\Delta(IV)}{IV} = \frac{\Delta I}{I}$ due to the nonlinearity of field emitted current as a function of applied voltage.

From Table II it is apparent that good agreement exists between experiment and theory for values of $\gamma > 100 > \gamma_o$ for which the cathode should initiate the arc. In all cases in which the maximum current was limited by the external circuitry, the increase in current needed to reach the calculated $(I)_{Max}$ was not sufficient to cause the anode power density to reach the calculated $(IV)_{Max}$. There is also good agreement between experiment and theory for values of $\gamma_o > \gamma$ for which an anode initiated arc would be predicted, since $(I)_{Max}$ experimental is much less than calculated $(I)_{Max}$ but anode power densities are very close to the calculated $(IV)_{Max}$. Here also when the arc was limited or prevented, the required increase in power density would be reached before the current reached $(I)_{Max}$.

Agreement with theory does not exist in Table II when $\gamma_o < \gamma < 100$ for which theory would predict a cathode initiated arc, but for which in every case experiment indicated an anode process. There are two reasons for this. First, in order to calculate a value for γ_o the protrusion was assumed to be a hemispherically capped cylinder. Vibrans[4] has shown that for a constant emitting area and $\gamma = 100$ the temperature of a whisker shaped protrusion would be 1000 times greater than the temperature of a spheroid. Second, the determination of the anode spot radius from the radius of the apex of an emitting protrusion involves simplifications which give a larger value of anode spot size than numerical computations based on electron trajectories by a factor of four for $\gamma = 100$. Hence, our values of γ_o are weighted towards cathode processes from assumptions made at both electrodes. However, for values of $\gamma_o > 100$ both approximations become more valid with increasing γ[4].

TABLE II

For various amounts of surface roughness, indicated by γ, the maximum experimentally attained power at the anode and emitted current can be compared with that calculated for the given electrode to reach a temperature corresponding to a vapor pressure of 10^{-4} torr.

Anode	Cathode	γ (Exp)	γ_o (Calc)	$(IV)_{Max}$ (Calc)	$(IV)_{Max}$ (Exp.)	$(I)_{Max}$ (Calc.)	$(I)_{Max}$ (Exp.)
++ Mo	Mo	990	50	4400 watts	133 watts	.047 amps	.012 amps
Mo	Mo	387	50	236 "	133 "	.012 "	.012 "
Cu	W	195	38	24 "	15 "	.005 "	.005 "
++ W	Cu	172	45	28 "	18 "	.008 "	.007 "
++ Mo	Mo	172	50	240 "	35 "	.033 "	.002 "
Cu	W	110	60	90 "	96 "	.012 "	.012 "
++ Cu	W	93	57	47 "	9 "	.038 "	.001 "
++ Cu	W	91	60	51 "	35 "	.047 "	.005 "
++ W	Cu	84	45	18 "	11 "	.007 "	.001 "
++ W	Cu	79	57	32 "	30 "	.023 "	.005 "
++ Mo	Mo	71	50	288 "	102 "	.051 "	.012 "
++ Mo	Mo	72	77	15 "	14 "	.036 "	.001 "
++ W	Cu	67	82	65 "	35 "	.012 "	.005 "
++ Cu	W	54	47	22 "	3 "	.030 "	.0003 "
++ W	Cu	46	55	31 "	10 "	.076 "	.001 "
Mo	Mo	18	50	11 "	12 "	.090 "	.001 "

++ The maximum current is limited by external circuitry.

Effect of Surface Geometry

In the development of the theory of anode versus cathode field emission initiated breakdown protrusion geometry that was chosen for analysis was that of a hemispherically capped cylindrical whisker. Since the analysis of the data was based on this model, several surfaces with various enhancement factors were examined by electron microscopy as shown in Figure 10. Figure 10 (A) is representative of the types of protrusions found on chemically polished surfaces that have been thermally annealed in vacuum. Figure 10 (B) shows the amount of roughness that can be caused by bringing two electrodes together in vacuum and using an ohmmeter to detect contact. This particular surface was formed by bringing the surfaces together repeatedly. Figure 10 (C) shows how very rough points such as those in Figure 10 (B) can be smoothed by heating. Figure 10 (D) and (E) show a type of protrusion similar to that observed by others,[17,18] but seldom found in our work. The surface shown in these figures exhibited an extremely high enhancement factor, $\gamma \cong 600$, indicating that calculated values were strongly weighted towards such protrusion as in Figure 10 (E).

In order to get meaningful information from the I-V data the effect of more than one emitter needs to be examined[4,18]. In the aluminum-tungsten diode transition radiation from the tungsten anode indicated that a number of sites were emitting from the aluminum cathode although Fowler-Nordheim plots of the I-V data were linear. As the voltage was increased, thermal radiation could be observed localized on the cathode at a particular emission site just prior to a flash of light in the gap associated with the loss of that emitter. In such cases, when a significant contributor to the total current was lost during an arc, changes in surface geometry were associated with changes in the I-V data taken before and after the arc. In other cases when the lost emitter was so small that the only evidence of the arc was the flash of radiation in the gap, the I-V data before and after the arc was essentially reproducible.

In order to obtain evidence of the rearrangement of emitting sites during an arc, a pinhole arrangement similar to one described recently by Singer and Doolittle[19] was used to expose a film to the x-ray output from the bombarding electron beam. The resulting spot pattern, enlarged in the drawing of Figure 11, shows how some sites are lost while others are gained during two successive arcs. The associated I-V data in the Fowler-Nordheim plots of Figure 12 show that the arcs caused γ to be reduced from 100 to 80 even though the total number of emitting sites was increased.

On the basis of these observations, the real surface geometry differs from the model chosen in such a way that for a given γ the results predicted by the theory are weighted towards cathode processes. The total heating of the anode involves electron bombardment from multiple beams rather than from a single electron beam. Although the enhancement factor calculated from the Fowler-Nordheim plot is weighted towards the sharper protrusions,

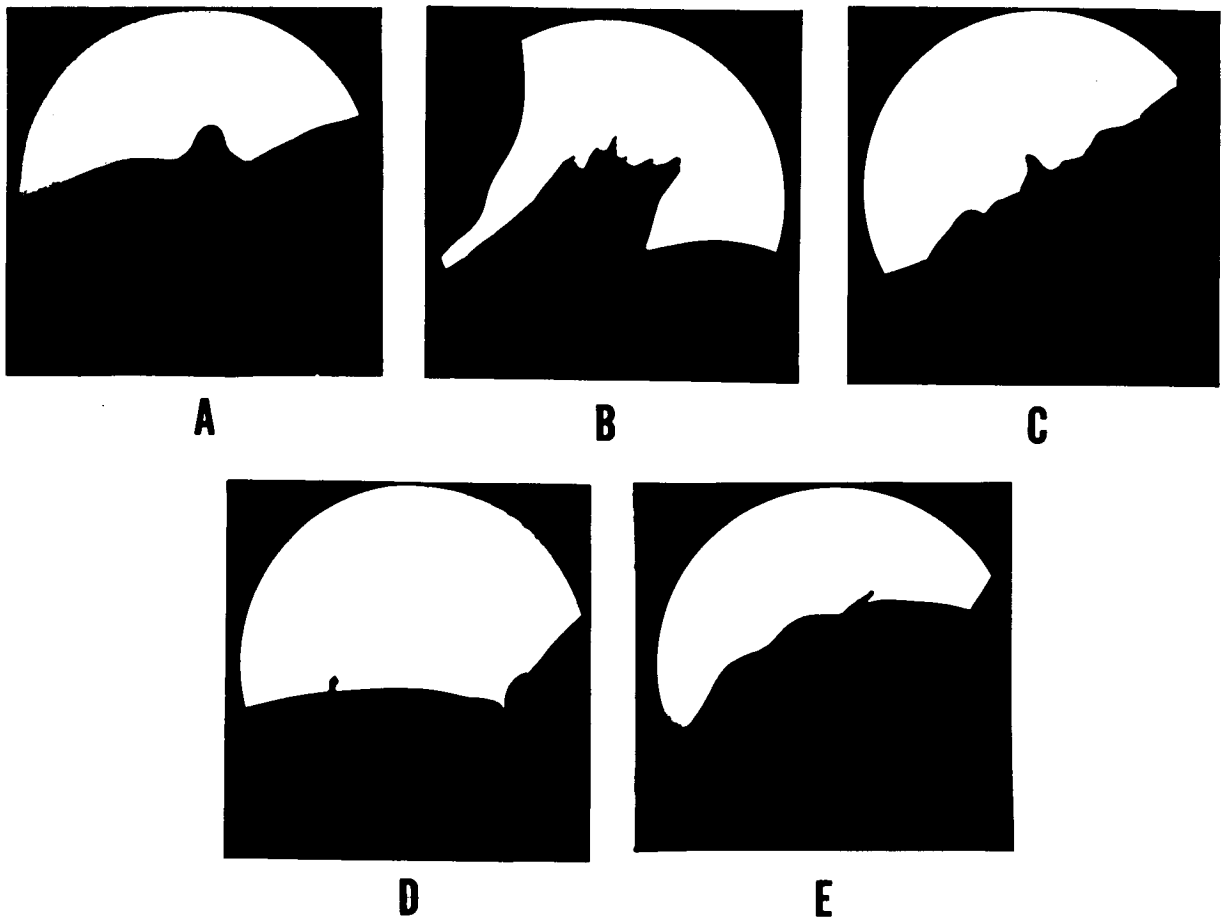

Figure 10. Electron microscope shadowgraphs (magnification 3000X) of molybdenum electrode surface formed by bringing two thermally cleaned surfaces together in vacuum, then applying an electric field sufficiently high to cause the onset of the runaway condition. No arc took place, although the temperature and fields were very high.

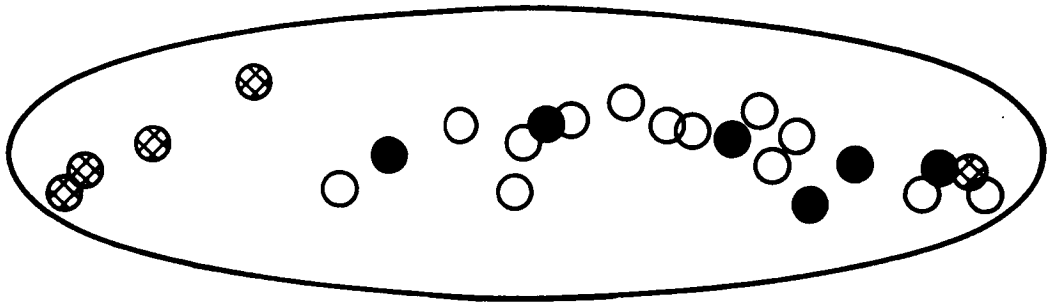

● sites remaining after arc

⊗ sites lost during arc

○ sites gained after arc

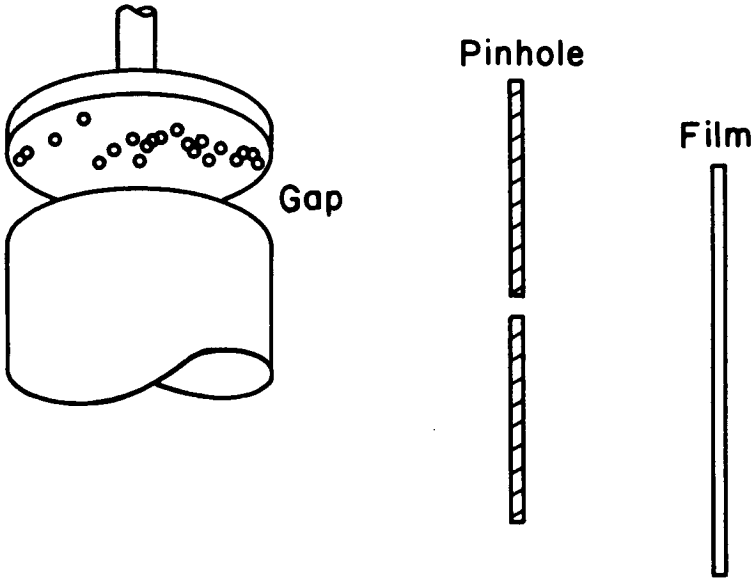

Figure 11. The spot pattern at the top of the figure was obtained with the pinhole arrangement shown. The dark circles correspond to emission sites remaining after two arcs--open circles to sites lost and hatched circles to sites formed during the arcs.

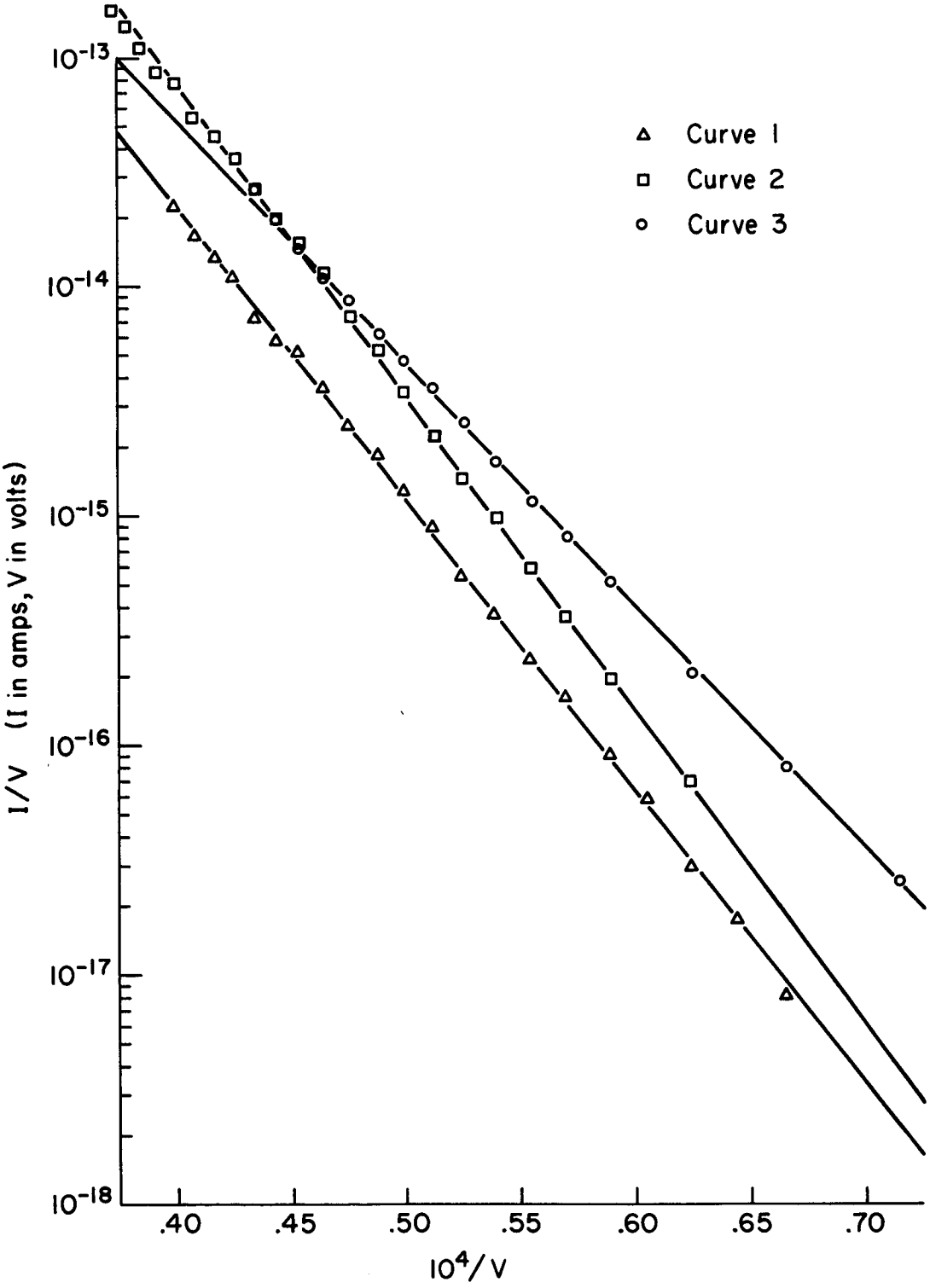

Figure 12. Fowler-Nordheim plots of the I-V data from the Al cathode: Curve 1 - prior to the arc, Curve 2 - after the first arc, Curve 3 - after the second arc. This data was obtained from the surface whose x-ray output is illustrated in Figure 11.

in many cases the cathode can initiate an arc when only that one protrusion reaches a temperature necessary to evaporate sufficient electrode material into the gap to generate a plasma arc by electron impact ionization.

SUMMARY

Pre-breakdown current between clean and cesium coated metal electrodes in vacuum is due to field emission from microscopic protrusions which exist on even the most carefully prepared surfaces. The ways in which this field emitted current can cause voltage breakdown have been investigated both theoretically and experimentally with the following results:

1) Emission induced heating of cathode protrusions or heating of the anode due to bombardment by the field emitted electrons will lead to breakdown when the temperature of one of the electrodes becomes high enough locally to cause significant evaporation of electrode material into the path of the electron beam.

2) There exists a boundary value of surface enhancement factor γ_o which will uniquely determine whether breakdown will be initiated by cathode or anode processes. γ_o is dependent upon the relative electrode materials, the gap geometry, and whether the voltage is applied continuously or in pulses.

3) Knowing γ and γ_o for any set of electrodes, the maximum current and/or power that can be maintained stably can be determined.

For electrode materials of very low yield strength (e.g. aluminum) the experimental results suggest field-stress induced irreversible changes or removal of surface protrusions as the prime initiator of electrical breakdown.

The practical limitations of several electrode materials are indicated in Tables III and IV. In Table III the power density at the anode and the current density at the cathode protrusion tip necessary for the particular material to reach a temperature corresponding to a vapor pressure of 10^{-4} torr are shown. Table IV lists the yield point for various materials and the corresponding value of electrostatic field to reach that stress. The values for the yield point given are for the pure hard drawn metal and may vary due to the general anisotropy of the electrode material, therefore the numbers in Table IV indicate relative strengths of various materials rather than absolute strength.

TABLE IV

Yield point and corresponding electrostatic stress for various electrode materials.

Material	Y.P. + (10^{10} dyne/cm^2)	F_s (Mv/cm)
W	4.100	300
Mo	2.740	249
Ni	.52 - 1.17	108 - 162
Cr	.482	104
Ag	.304 - .352	82.5 - 89
Pt	.241	80.4
Cu	.245	74
Au	.245	74
Al	.110	49.6

+ Values taken from Handbook of Chemistry and Physics (Chemical Rubber Publishing Co., Cleveland, Ohio, 1956), 38th ed., pp 1999 - 2000.

On the basis of this investigation the materials offering optimum properties from the standpoint of both mechanical and thermal stability can be listed. In their order of desirability (best material for the particular situation listed first) these are:

1. Anode materials when dc voltages are to be sustained- Ir, Cu, W, and Ag,

2. Anode materials when pulsed voltages are to be sustained- W, Ir, Re, Mo, Nb, Pt, Cu, Ag, and Ni,

3. Cathode materials - W, Nb, Mo, Hf, Re, Ir, and Cu.

TABLE III

Anode power density W_a and cathode density $G = JR_c$ for various materials to reach a temperature corresponding to a vapor pressure of 10^{-4} torr.

Material	T^oK (at 10^{-4} torr)	$W_a R_a$ dc voltages (kw/cm)	$W_a t_o^{1/2}$ Pulsed Voltages $\frac{kw - sec^{1/2}}{cm^2}$	G (10^6 amp/cm)
W	3000	2.700	5.571	1.1500
Mo	2400	1.620	3.384	.0675
Nb	2550	1.600	3.285	.2200
Ir	2380	2.870	4.282	.0265
Re	2925	1.050	4.163	.0300
Hf	2250	.231	1.100	.0520
Pt	2000	1.030	3.006	.0100
Ni	1550	.780	2.139	.0048
Cr	1400	.665	1.620	.0040
Cu	1300	2.870	2.907	.0165
Au^+	1400	3.020	2.300	.0148
Ag	1100	2.670	2.188	.0144
Al^+	1200	1.030	1.180	.0065

+ Temperature exceeds melting point, hence the calculations are based on a temperature of .9 times the melting temperature.

SURFACE KINETICS OF ADSORBED METALS ON REFRACTORY SUBSTRATES

VARIATION IN WORK FUNCTION OF VARIOUS METALS ON CESIUM ADSORPTION

The average work function change as a function of cesium coverage was reported earlier[1] for cesium on tungsten. Also, results were obtained for the variation of work function with cesium coverage on a single crystallographic plane of tungsten, namely the (100) plane. These results have helped to provide a better understanding of the adsorption process, since they can be compared with available theoretical models more readily than results of measurements on polycrystalline surfaces which in some manner average large differences in local work function. During the past year, these results have been extended to include a measurement of the average work function change for cesium adsorption on molybdenum and rhenium. These results coupled with early results on tungsten provide data for the average work function change vs. cesium coverage for the three refractory metals: tungsten, molybdenum and rhenium. In addition, the variation of work function with cesium coverage on the (110) plane has been obtained.

Experimental Procedures and Results

Two-emitter Tube. - The experimental procedures and method of obtaining the average work function vs. absolute cesium coverage were identical to those described previously[1]. This experiment was implemented by employing tungsten and either molybdenum or rhenium emitters side by side in the two-emitter tube and calculating the average coverage on one emitter relative to that of the tungsten emitter by establishing the beam attenuation and knowing the emitter-to-source distances.

The procedure followed is to dose both emitters from a source in line with the two emitters and measure the work function of each emitter after the cesium has been spread to give an equilibrium coverage over the total emitter surface. The emitters are dosed while at liquid nitrogen temperature so that the assumption of a sticking coefficient of unity is valid; the surface migration is performed at temperatures sufficiently low that thermal desorption is negligible. The results given in Figure 13 show the ϕ vs. σ relationships for the three refractory metals which have been investigated. The data points are given for the most recent results on a molybdenum substrate.

Some difficulty was incurred in attempting to clean the rhenium emitter thermally; it appeared as if a small amount of carbon would diffuse to the surface from the bulk on heating at lower temperatures and alter slightly the emission distribution and work function. After prolonged flashing, however, the surface

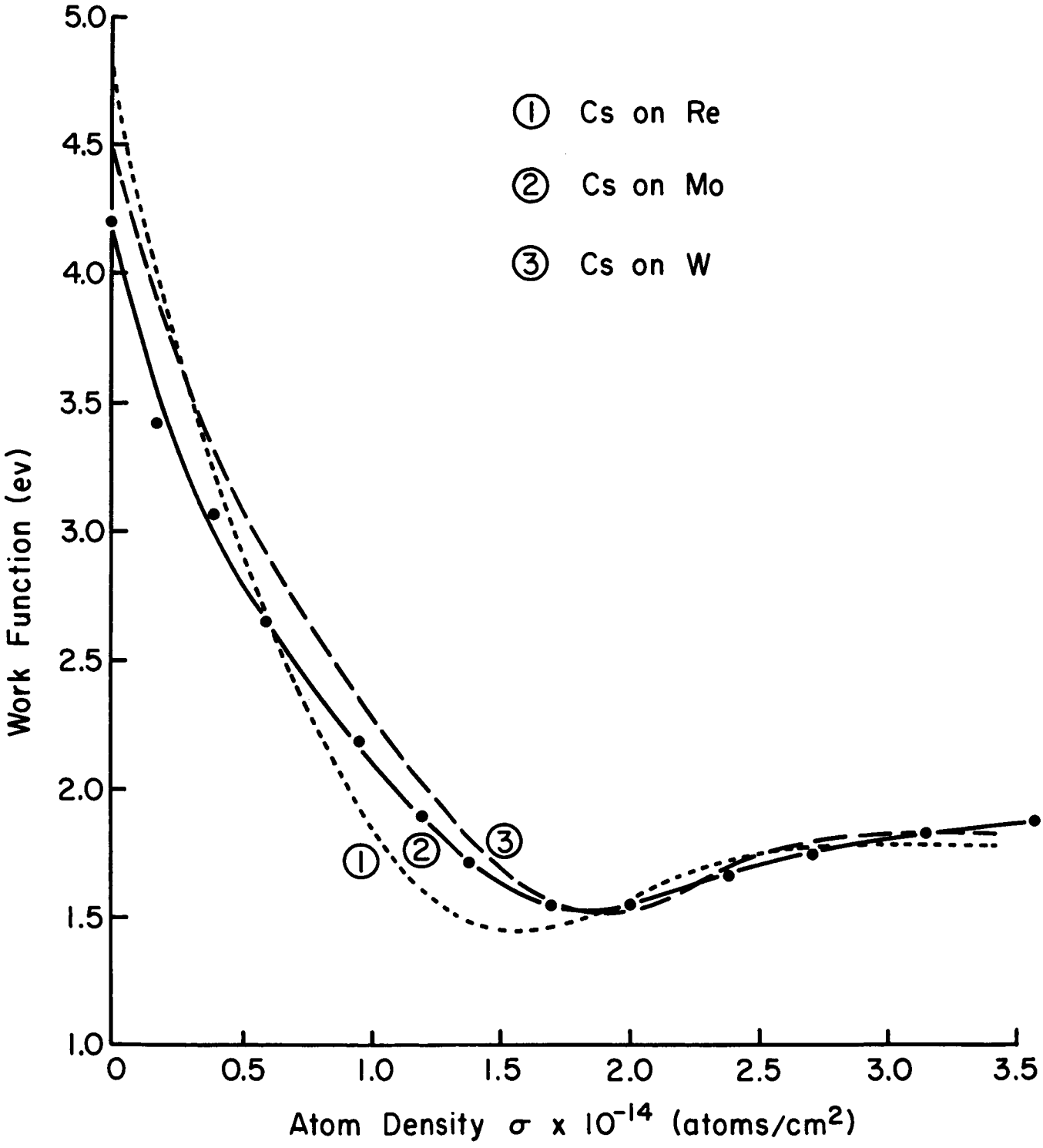

Figure 13. Two-emitter tube results of the work function vs. average cesium atom density on rhenium and molybdenum relative to tungsten.

remained reasonably clean as judged by pattern appearance and the experiment was performed. The results given in Figure 13 show ϕ vs. σ relationship similar to that observed for tungsten with an indication of a slight shift of the work function minimum to lower coverages; in addition, the absolute value of the work function minimum ϕ_m is slightly lower than that observed for tungsten.

Probe Tube. - The probe tube used for this study has been described previously;[1] it is a field emission microscope with a small hole in the anode through which current from a selected portion of the emitter tip may be collected in a Faraday cup arrangement. For the present study zone melted [100] and [110]-oriented emitters were employed. The [110] emitter had an emitter radius of ~2000 A, according to the I-V characteristics of the tube as determined both before and after the work function studies; for this radius the projection of the probe hole back onto the emitter yields a surface area 115 A in diameter. Assuming a perfectly hemispherical tungsten tip 2000 A in radius the uppermost atom layer on the (110) plane can have a diameter as large as 209 A; thus, when the probe is well-centered on the (110) plane of the tip it accepts emission from that plane only. Similarly, for the [100] emitter radius of ~1500 A a projection of the probe hole onto the emitter yields a surface area 94 A in diameter, whereas the uppermost layer on the (100) plane can be as large as 138 A.

The experimental procedure was modified slightly from that used previously because the measured work function of the clean (110) plane of tungsten depends somewhat upon past treatment.[20] If the (110) work function is measured just after the tip is flashed to a high temperature (to clean the emitter surface), the result is lower than if it is measured after the tip is annealed at a lower temperature, because annealing the tip increases the size of the low emitting planes and heals imperfections in the closely packed planes like the (110).[20] Values measured here for the (110) plane include 5.68 ev just after flashing and values between 5.81 and 5.90 ev after annealing at temperatures between 1050 and 1100°K.

The value of the work function ϕ for the clean (100) plane showed a dependency on the annealing temperature similar to that observed earlier for the (110) plane. That is, after flashing at high temperatures, work functions as low as 4.57 ev were obtained, whereas prolonged annealing at approximately 1050°K for several minutes led to work function measurements as high as 4.75 ev.

A second change in procedure involves the direction of coverage change; since the adsorption and desorption processes have been shown to

be completely reversible,[3] it is easier and faster to dose the tip heavily and to obtain the work function changes by desorption.

The experimental procedure used was the following: (1) the total emitted current and the partial current from the single planes were measured as functions of applied voltage for a clean tungsten substrate after the tip had been first flashed clean and then annealed for 300 sec at 1050-1100°K. From the ratio of the slopes of the corresponding Fowler-Nordheim plots and the assumption that the average work function for tungsten is 4.52 ev, the work function of the clean (110) and (100) planes of tungsten were determined by the methods described in earlier reports;[1,3] (2) the tip was covered with a heavy dose of cesium, which was then equilibrated; (3) the tip was heated for 60 sec to a temperature sufficient to cause some desorption, after which work functions of both the total emitting surface and the single plane were determined for the particular cesium coverage from measurements of both total emitted current and the probe current. The average cesium surface concentration σ on the tip was obtained from the known work-function/coverage relationship for the total emitted current from a tungsten emitter.[1] (4) step (3) was repeated for a series of successively higher temperatures, until all cesium was desorbed from the tip.

The results of the probe measurements on the (100) and (110) planes are given in Figure 14 along with the earlier results for the average work function variation. It should be emphasized that the measurement of the atom density σ is based on an assumption of uniform coverage over the hemispherical emitter, so that any deviations from the average σ on a given crystal plane will show up as some sort of a discontinuity in the $\Delta\phi$ vs. σ curve. Such discontinuities can be observed at low cesium coverages on both (100) and (110) planes and are ascribed to anisotropies in the coverage distribution at low coverages. It cannot be determined from the data alone as to what coverage the distribution of cesium becomes uniform over the surface, if it occurs at all.

General Discussion of Results

It is interesting to note that the variation of work function with average cesium coverage shows a similar relationship on all three substrates. Within the accuracy of this measurement, which is probably within 10%, the coverage σ_m at which the minimum in work function occurs is the same for tungsten and molybdenum. This is not unexpected inasmuch as both possess body-centered cubic structures with near identical lattice constants. A summary of the salient features of the results such as the maximum average work function change $\overline{\Delta\phi}_m$, the minimum work function $\overline{\phi}_m$, the average substrate work function $\overline{\phi}_s$ and the value of work function at the highest coverage investigated, $\overline{\phi}_o$ are given in Table V.

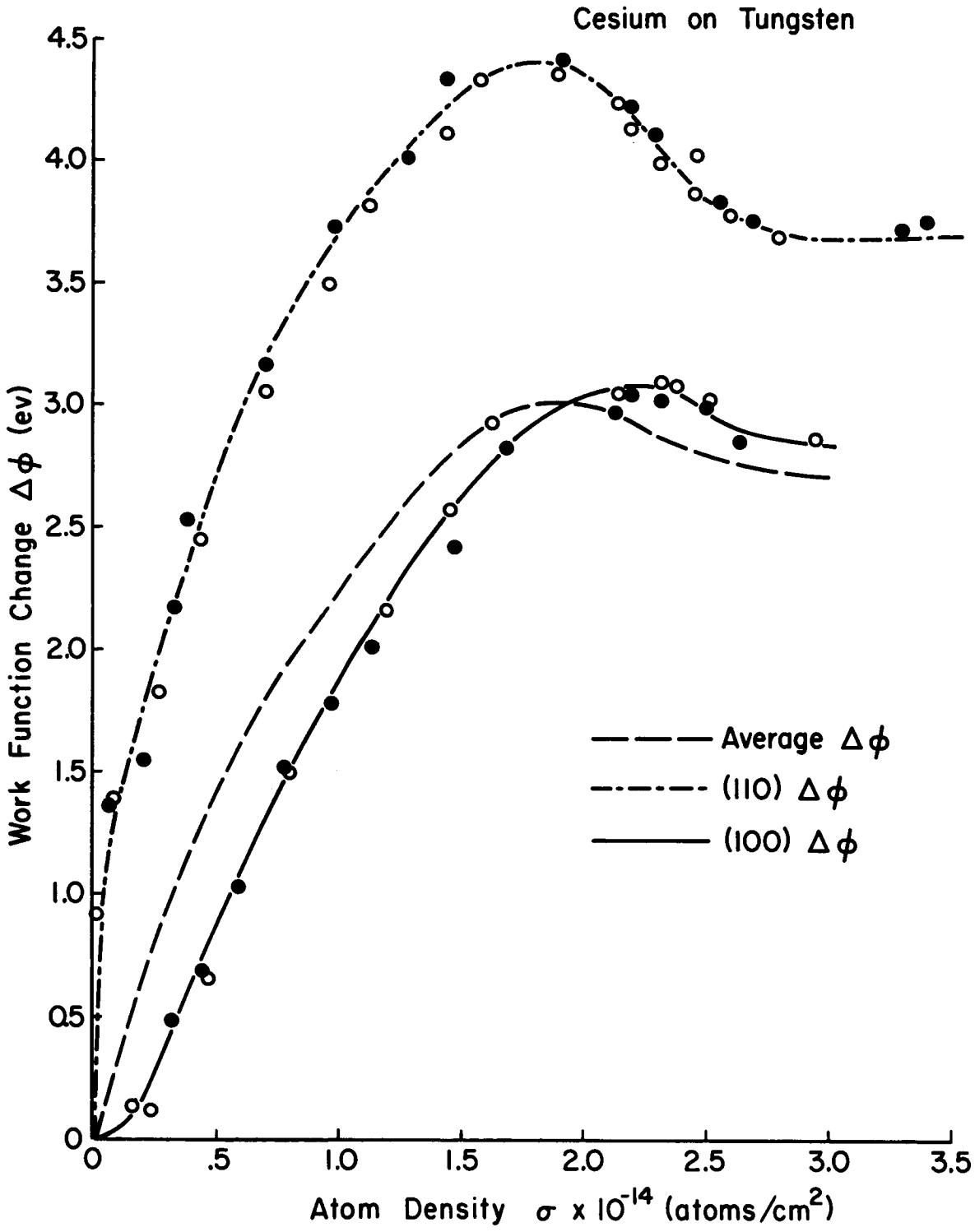

Figure 14. Work function change vs. average cesium atom density for the (110) and (100) planes of tungsten.

TABLE V

Summary of maximum average work function change $\overline{\Delta\phi}_m$ and work function $\overline{\phi}_o$ at σ 3.2 x 10^{14} atoms/cm^2

Substrate	$\overline{\phi}_s$ (ev)	$\overline{\phi}_m$ (ev)	$\overline{\Delta\phi}_m$ (ev)	$\overline{\phi}_o$ (ev)
Mo	4.20	1.55	2.66	1.81
W	4.52	1.52	3.00	1.78
Re	4.85	1.45	3.40	1.82

Comparing the (110) and (100) probe data of Figure 14 points to several interesting features. First, there appears to be a definite break in the (110) curve as $\sigma \rightarrow 0$ such that the slope is greater than the slope of the average work function curve; this change in slope is in the opposite sense of that noted in the results for the (100) plane. Since most theories predict linear relationships between σ and ϕ at low coverages, the discontinuities at low coverages are probably due to local variations in the coverage of these two planes. Thus for σ near zero the $\{110\}$ planes have higher local cesium coverages than average, while the $\{100\}$ planes have lower local cesium coverages than average. Further, it can be noted in Figure 14 that the maxima of the $\Delta\phi_{110}$ and $\Delta\phi_{100}$ curves are shifted from the maximum of the $\overline{\Delta\phi}$ curve in the opposite directions of coverage; addition of a constant coverage increment $\Delta\sigma$ to the σ_{110} values and subtraction of $\Delta\sigma$ from the σ_{100} values will cause the maxima of the $\Delta\phi_{110}$ and $\Delta\phi_{100}$ curves to coincide with the maximum of the $\overline{\Delta\phi}$ curve, and in addition will also remove the low coverage slope discontinuities of the two curves. This suggests that the differences in coverage of the two planes at low coverage are partially maintained through the coverage range $\sigma < \sigma_m$.

In view of the uncertainty in the absolute cesium coverage at a given work function in the single plane studies, there is still some difficulty incurred when one tries to fit these curves to various theories of work function change. We have suggested earlier [1, 3, 21] that several factors seem to indicate the occurrence of the monolayer condition at the knee in the ϕ vs σ curves where ϕ no longer varies appreciably with coverage. This would be approximately 2.8 and 2.7 x 10^{14} atoms/cm^2 for the (100) and (110) planes, respectively. On the basis of geometric considerations only, the cesium monolayer coverage on the (100) plane should be 2.5 x 10^{14}, whereas the monolayer coverage on the (110) plane should be 3.56 x 10^{14} atoms/cm^2. At this juncture there are two points of view which can be taken regarding the work function change with cesium

coverage on the two planes: one, the obvious shifting necessary to cause the two curves to extrapolate linearly to zero coverage (which, according to Figure 14, is roughly plus and minus 0.2×10^{14} atoms/cm^2 for the (110) and (100) planes respectively in the low coverage range) must be such at high coverage to cause a monolayer coverage of $\sigma_o^{110} = 3.6 \times 10^{14}$ and $\sigma_o^{100} = 2.5 \times 10^{14}$ atoms/cm^2; the other view is to assume that the monolayer condition is in fact nearly identical on both planes, namely $\sigma_o = 2.7 \times 10^{14}$ atoms/cm^2 and the anisotropy in the coverage distribution apparent at low σ disappears as σ approaches σ_o. There is no doubt that the discontinuity apparent at the low coverage region in the two curves of Figure 14 is due to anisotropies in the coverage distributions, since dipole moments calculated from the slopes of the curves at near zero coverage would be inexplicably high for the (110) plane, and low for the (100) plane.

The likely explanation for the anisotropy in the coverage distribution is the greater site density and binding energy for cesium on the (110) plane. For example, if the adsorbed layer comes to two-dimensional equilibrium, the distribution of cesium between two regions of different site density and binding energy would be given by the following approximate expression:

$$\frac{\sigma^{110}}{\sigma^{100}} = \left(\frac{\sigma_o^{110}}{\sigma_o^{100}}\right) \exp\left[(H_{110} - H_{100})/kT\right] \tag{22}$$

where $H_{110} - H_{100} = \Delta H$ is approximately equal to the difference in binding energy between the two planes. The amount of shifting of the curves in Figures 14 at low coverage (e.g., $\sigma = 0.3 \times 10^{14}$ atoms/cm^2) suggest $\sigma^{110}/\sigma^{100} = 5$; if it is further assumed that the ratio of site densities is according to the geometric model, then at $T = 250^oK$, $\Delta H = 0.027$ ev. On the other hand, if the ratio of site densities is that suggested by the results given in Figure 14, namely $\sigma^{110}/\sigma^{100} = 1$, then $\Delta H = 0.035$ ev in the same coverage range. Additional experimental results will be needed to establish the absolute coverages on the particular planes and hence the correct value of ΔH.

From the work function data obtained with cesium on various substrates and various single crystallographic planes of a particular substrate, an interesting empirical relation between $\Delta\phi_m$ and ϕ_s has been obtained which is shown in Figure 15 and suggests a relationship between $\Delta\phi_m$ and ϕ_s of the following form:

$$\Delta\phi_m = 1.09\,(\phi_s - 1.78) \tag{23}$$

We observe that the term in brackets in Equation 23 is very nearly equal to $\phi_s - \phi_a$ where ϕ_a is the average work function of bulk cesium. Assuming a relationship of the form,

$$\Delta\phi_m = 1.09\,(\phi_s - \phi_a), \tag{24}$$

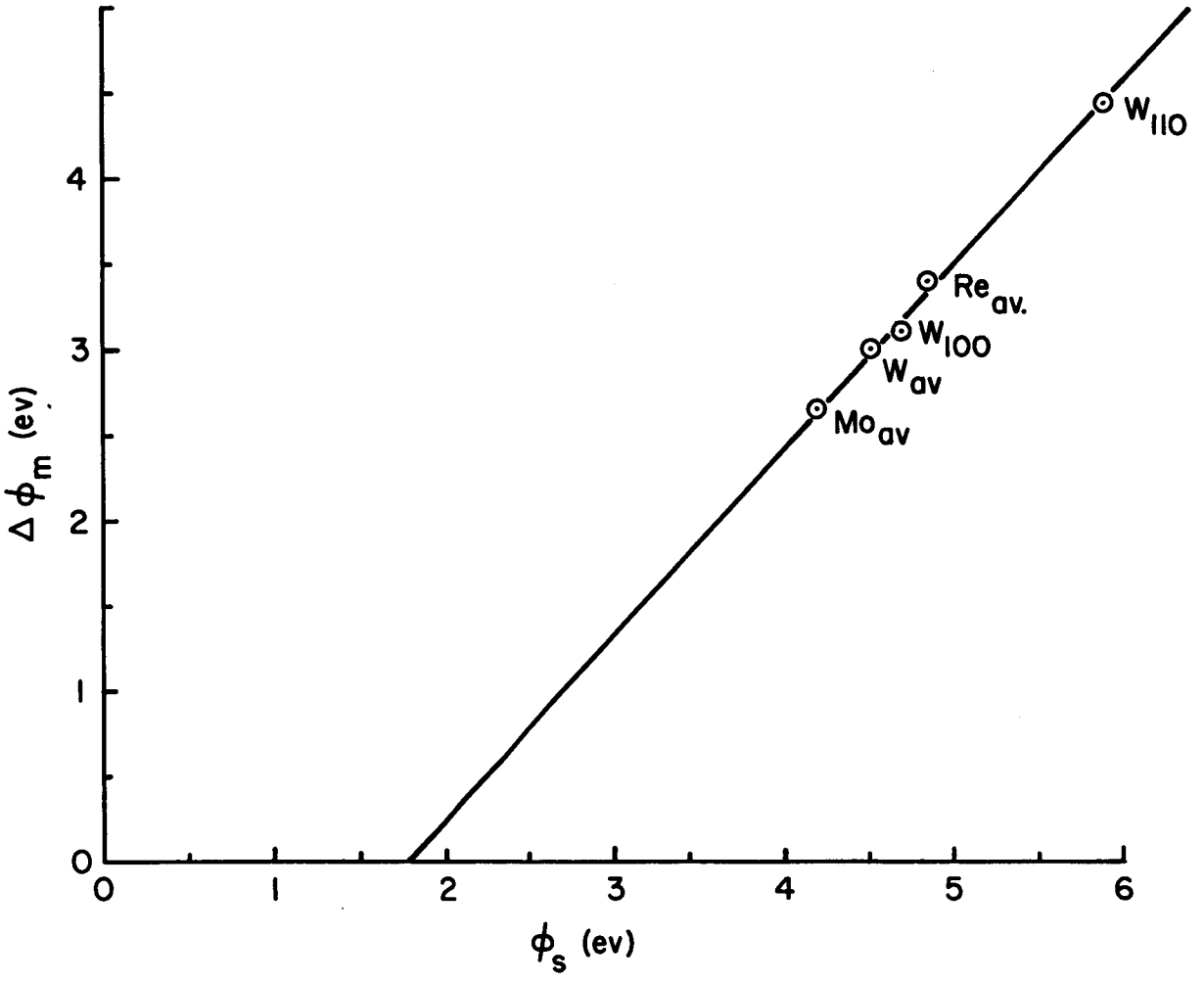

Figure 15. Empirical relationship between measured maximum work function change and substrate work function.

might have some universal applicability for metallic electro-positive adsorption, the work function coverage data for other systems was analyzed according to equation (24), the results of which are given in Table VI. The agreement

TABLE VI

Summary of maximum average work function change $\Delta\phi_m$, apparent monolayer coverage work function ϕ_o, adsorbate work function ϕ_a and predictions of equation (24)

Substrate	ϕ_s(ev)	ϕ_m(ev)	ϕ_o(ev)	Adsorbate	ϕ_a(ev)	$\Delta\phi_m$(exp.)	$\Delta\phi_m$(calc.)
W	4.52	2.10[a]	2.50[a]	Ba	2.40[b]	-2.42	-2.31
"	"	1.78[c]	2.10[c]	K	2.15[e]	-2.74	-2.58
"	"	3.15[d]	3.30[d]	Th	3.38[e]	-1.37	-1.28
"	"	3.65[f]	3.77[f]	Mg	3.67[b]	-0.87	-0.93
"	"	2.30[f]	2.60[f]	Sr	2.35[e]	-2.22	-2.36
"	"	1.74[g]	2.00[g]	Na	2.27[e]	-2.78	-2.45
"	"	2.72[g]	2.82[g]	Ca	2.71[b]	-1.80	-1.97
"	"	3.69[h]	---	Zr	3.84[e]	-0.83	-0.74
Re	4.85	3.15[i]	3.30[i]	Th	3.35[e]	-1.70	-1.63

a) Ref. 26; b) Ref. 27; c) Ref. 34; d) Ref. 28; e) Ref. 29;
b) Ref. 30; g) Ref. 31; h) Ref. 32; i) Ref. 33

between the various experimental and calculated $\Delta\phi_m$ is remarkably good, and therefore lends support to the general validity of Equation (24) in predicting the magnitude of the work function change for certain adsorbate-substrate combinations. Inasmuch as the empirical relation of Equation (24) appears to be valid for several substrate-adsorbate systems, it would be interesting to understand the derivation of this relationship from first principles. It is interesting to note that if the multiplying factor were 1.00 rather than 1.09, the empirical relationship would be an expression for the contact potential between the two respective bulk metals. It is further noticed that a comparison of columns 4 and 6 of Table VI shows the average work function at the

apparent monolayer ϕ_o to be nearly equal to the average bulk work function ϕ_a of the adsorbate. It therefore follows that the average work function change at the monolayer $\Delta\phi_o$ is in fact nearly equal to the contact potential between the bulk metals of the adsorbate and substrate. Assuming the qualitative picture of metallic adsorption suggested by Gurney[22] and expanded by others[23-25] is essentially correct, the above results suggest the broadened valence level of the adsorbate at the monolayer condition becomes a band of electronic states with the uppermost filled level coinciding with what would be the Fermi level when further layers are added and three-dimensional bulk considerations become valid. This picture of the adsorbate at the monolayer condition also implies that the outer part of the work function of the adsorbate is not only formed with a near monolayer of adsorbate, but is unaffected by the underlying substrate, at least on the low work function planes which contribute most to the average work functions given in Table VI.

Comparison of Probe Tube Results with Theory

As mentioned previously, the likely explanation for the anisotropy in the coverage distribution is the greater site density and binding energy for cesium on the (110) plane. At high coverages the binding energy should become more uniform over the different crystallographic planes so that the coverage distribution should be largely determined by the local site density and lateral interactions. As will be shown below, there is some evidence to believe that the atom density at the minimum work function is identical on the two planes; to accomplish the latter a uniform shift of 0.2×10^{14} atoms/cm^2 in the proper direction throughout the coverage range for the curves both aligns the minimum work functions of the two curves and causes linear extrapolation to $\Delta\phi = 0$ as σ approaches zero, as mentioned above. This shift also leads to the occurrence of the work function minimum at $\sigma_m = 2.03 \times 10^{14}$ atoms/cm^2 for each curve. In addition, the monolayer coverage for the (110) and (100) planes occurs at 3.00 and 2.53×10^{14} atoms/cm^2 respectively. It is interesting to note that this amount of shifting yields a monolayer coverage on the (100) plane which is in agreement with a hard sphere geometric arrangement, whereas the monolayer coverage on a (110) plane is approximately 16% less than the geometric monolayer.

On the basis of the work function change data for the two planes with the above-mentioned corrections to the two curves an attempt will be made to fit the data to existing theories of work function change on adsorption. The basic Helmholtz equation relating $\Delta\phi$ and fractional monolayer coverage θ for a layer of adsorbate atoms with charge ze concentrated at a point d_o from the plane of electric neutrality is as follows:

$$\Delta\phi = 4\pi\, ze\, d_o\, \sigma_o\, \theta \tag{25}$$

In the above formulation the dipole moment μ is given by $2\, ze\, d_o$. The modification of Equation (25) most frequently utilized to analyze $\Delta\phi$ vs. σ

data allows for the de-polarization of the dipole moments by the dipole field of neighboring adsorbate atoms. For a square array of adsorbate atoms of polarizability α which expands uniformly as the coverage decreases, the modification of Equation (25) to include de-polarization effects according to the Topping model is as follows:

$$\Delta\phi = \frac{2\pi\mu\sigma_o\theta}{\epsilon} \tag{26}$$

where:

$$\epsilon = 1 + 9\alpha(\sigma_o\theta)^{3/2} \tag{27}$$

Equation (26) can be derived from application of Gauss' law to a Helmholtz dipole layer with a σ dependent dielectric constant ϵ. In the case of image dipoles $\Delta\phi$ is half the potential difference between the surface and free space at large distances from the surface. It can readily be shown that values of $\Delta\phi_m$ and θ_m at the maximum in the curve of $\Delta\phi$ vs. σ as given by Equation (26) are as follows:

$$\theta_m = \left(\frac{2}{9\alpha}\right)^{2/3} \frac{1}{\sigma_o} \tag{28}$$

$$\Delta\phi_m = 0.489\,\pi\mu\alpha^{-2/3} \tag{29}$$

Thus, Equations (28) and (29) permit calculations of α and μ for each plane from knowledge of the corresponding σ_m and $\Delta\phi_m$. Using the corrected curves of Figure 14, i.e., σ_m (100) = σ_m (110) the following values of α and μ are obtained:

$$\alpha(110) = \alpha(100) = 79\ A^3$$
$$\mu(110) = 15.8 \times 10^{-18}\ \text{esu (statcoulomb - cm)}$$
$$\mu(100) = 11.1 \times 10^{-18}\ \text{esu (statcoulomb - cm)}$$

Inserting the above values for α and μ into Equation (26), the data of Figure 14 can be tested throughout the coverage range according to the depolarization theory. Regardless of whether the corrected or uncorrected data of Figure 14 is utilized, the simple depolarization theory as outlined above fails to fit the experimental data throughout an appreciable part of the coverage range. It is possible to fit the experimental data between $\sigma = 0$ and σ_m reasonably well to Equation (26) if lower values of α (i.e., higher values of σ_m) are employed.

Although various modifications of Equation (25) to include depolarization effects have been given[35], a recent self-consistent treatment by

MacDonald and Barlow[36] appears to be most rigorous. They consider the depolarizing field at a given adsorbed element arising from the total polarization of all surrounding elements including the presence of average charge on the adsorbing surface. A distinction is made in their treatment between "natural" fields E_{nl} polarizing a single adsorbed element in the absence of neighboring elements, and of the self-consistent effective field leading to induced polarization perpendicular to the adsorbent surface. For image dipoles they obtained the following expression:

$$\Delta\phi = 4\pi\sigma_o\theta\left[\frac{2ze\,d_o}{\epsilon} - \frac{4\pi\theta\sigma_o\,ze\,a}{\epsilon} + \frac{a\,E_{nl}}{\epsilon} - ze\,d_o\right] \quad (30)$$

In the case of polarized atomic adsorption $z = 0$ and Equation (30) is identical to Equation (25) where $\mu = 2\,a\,E_{nl}$ (the factor 2 arises from the fact that μ is totally contained in the ad-atom). In the case of image dipoles with small a, $\epsilon \cong 1$ and aE_{nl} is small compared to the other terms throughout the range of θ and Equation (30) becomes:

$$\Delta\phi = 4\pi\theta\sigma_o\,ze\,d_o - (4\pi\theta\sigma_o)^2\,ze\,a \quad (31)$$

It can readily be shown that $\Delta\phi_m$ occurs at:

$$\theta_m = \frac{d_o}{8\pi\sigma_o a} \quad (32)$$

The corrected data of Figure 14 has been plotted in Figure 16 according to Equation (31) written in the form:

$$\frac{\Delta\phi}{\theta} = C_1 - C_2\,\theta \quad (33)$$

where

$$\frac{C_2}{C_1} = \frac{1}{2\,\theta_m} = \frac{4\pi\sigma_o\,a}{d_o} \quad (34)$$

The agreement of the experimental data with Equation (33) as shown in Figure 16 for the (110) and (100) results, lends support to MacDonald's theory of WFC. Using the data of Figure 14 and Equation(33) without any corrections to σ causes the low θ points to deviate upwards; however, the slope and intercept of the line drawn through the higher coverage points are

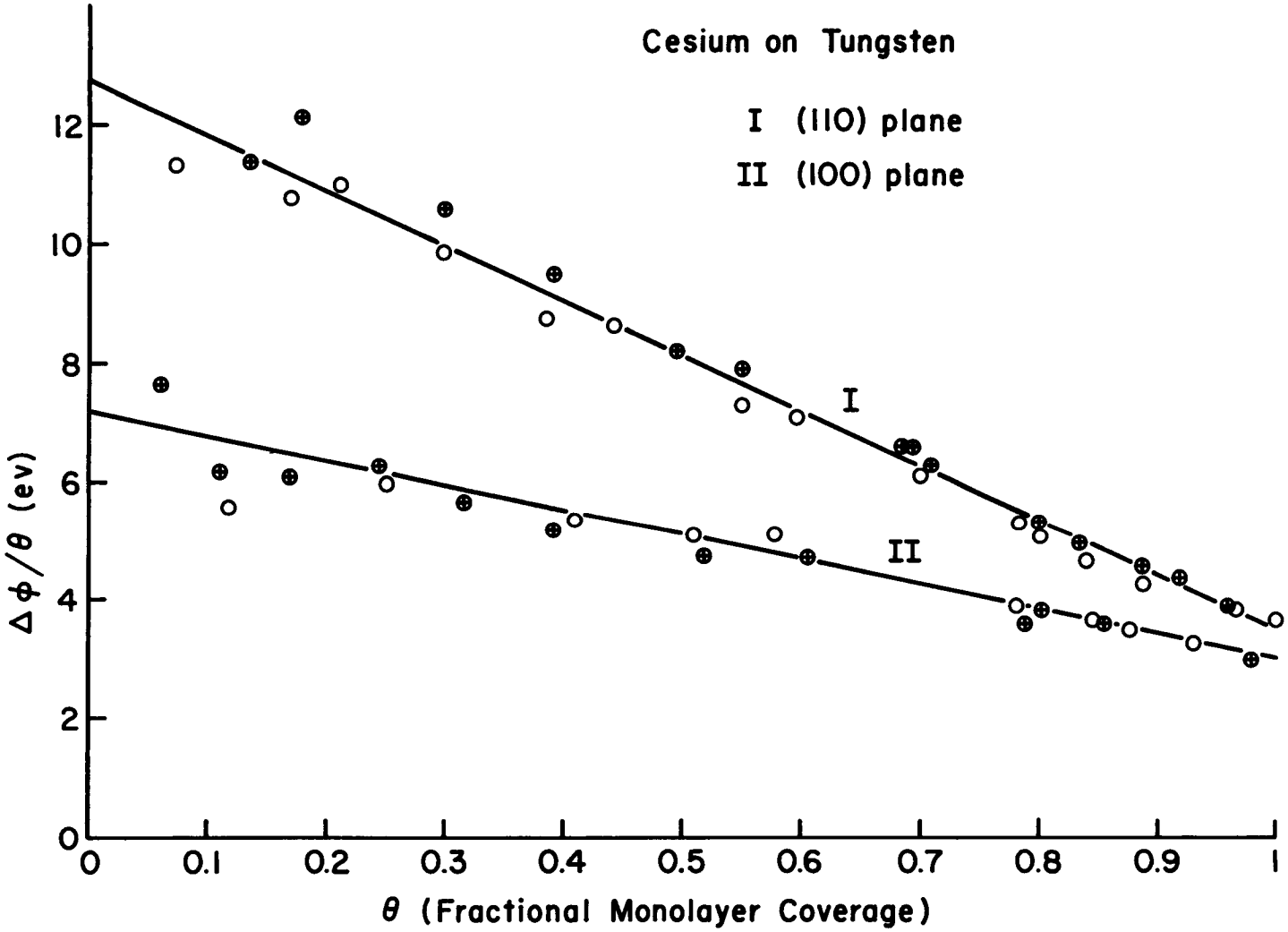

Figure 16. Analysis of the data of Figure 14 according to equation (34).

nearly unchanged from the corrected data used in Figure 16. Good agreement near $\theta = 1$ is somewhat fortuitous since the approximation that $\epsilon \cong 1$ becomes less valid. The various constants of Equation (31) obtained from the slopes and intercepts of Curve I and II of Figure 16 are given in Table VII.

TABLE VII

Constants of Equation (31) obtained from best fit to data of Figure 14

Plane	$ze\,d_o$ (esu)	$z\,d_o$(A)	α/d_o(A^2)	$\alpha\,z$ (A^3)
(110)	11.2×10^{-18}	2.34	1.95	4.56
(100)	7.6×10^{-18}	1.58	1.84	2.90

From Equations (31) and (32) one finds that $\Delta\phi_m$ is given as follows:

$$\Delta\phi_m = \frac{ze\,d_o^2}{4\,\alpha} = \frac{\mu\,d_o}{8\,\alpha} \tag{35}$$

In view of the following relation obtained from Table VII,

$$\frac{\alpha/d_{o\,(110)}}{\alpha/d_{o\,(100)}} = 1.06 \tag{36}$$

it appears that $\Delta\phi_m$ given by Equation (35) is proportional to μ. Although it is not totally justified with the limited probe data, let us assume the existence of a linear relationship between μ and ϕ_s of the form:

$$\mu = k_1\,\phi_s - k_2\,V_I \tag{37}$$

where V_I is the ionization potential of the adsorbate; one might then expect to observe the following relationship:

$$\Delta\phi_m = (k_1'\,\phi_s - k_2'\,V_I) \tag{38}$$

If the proportionality constant k_1' is near unity, then one obtains the prediction that ϕ_m depends only on the adsorbate properties, namely $k_2'\,V_I$ and

is independent of the substrate electrical and geometric properties. The latter is indeed observed experimentally for cesium on a variety of substrates and different crystallographic planes of a given substrate, as was shown previously, if $k_2' V_I \cong \phi_a$. It was also pointed out that Equation (38) seems to be approximately valid for a variety of substrate-adsorbate combinations.

In essence, the preceding discussions point out the likelihood of a linear relation between μ and ϕ_s for a given adsorbate which, when combined with the predictions of MacDonald's WFC (Equation 35), yields an expression (Equation 38) that is experimentally confirmed.

It is also interesting to compare the values of z and α on the (100) and (110) planes since they can give insight as to the electronic structure of the ad-atom. From Table VII it can be deduced that:

$$\frac{\alpha z_{(110)}}{\alpha z_{(100)}} = 1.57 \tag{39}$$

In view of the large value of ϕ_{110} it is likely that $z \cong 1$, thereby, according to Table VII, yielding a value of $\alpha_{110} = 4.56 A^3$ and $d_{110} = 2.34 A$. It also follows that $z_{100} = 0.634$ and $d_{100} = 2.48$ A if $\alpha_{110} = \alpha_{100}$. The nearly identical values of d_{100} and d_{110} may mean the image plane is further from the geometrical surface on the (100), but is compensated by the fact that cesium can "bury" itself further into a (100) than a (110) surface; thus, the larger value of μ on the (110) is primarily due to a larger z.

Table VIII compares the values of α, z, and d_o as obtained above on the (100) and (110) planes with atomic and ionic parameters of cesium. It seems somewhat paradoxical that α of the ad-atom is close to α of Cs^+ whereas d_o of the ad-atom is close to the metallic radius; furthermore, the results of Table VIII suggest a large variation in z of the ad-atom with crystal plane without concomitant variations in α or d_o. Although values of α, d_o and z given in Table VIII are based on equivocal assumptions, they do reflect the current ideas of metallic adsorption. For example, the strong overlap of the atomic orbital of cesium with metallic wave functions leads to a broadening of the valence level A in the adsorbed state. On the (110) plane the large value of $V_I - \phi$, where V_I is the ionization potential of the adsorbate, may cause the broadened valence level to lie wholly above the Fermi level of the substrate, so that a negligible part of the A band is filled, i.e., $z \cong 1$. For all other planes which possess relatively small $V_I - \phi$ the values of z are appreciably less than unity.

TABLE VIII

Various constants obtained from Table VII results assuming $z_{110} = 1$ and $\alpha_{110} = \alpha_{100}$

	$\alpha(A^3)$	d_o (A)	z
Cs	48[a]	2.62	0
Cs-W (100)	4.56	2.48	0.63
Cs^+	2.80[b]	1.69	1
Cs-W (110)	4.56	2.34	1

a. G. Chamberlain and J. Zorn, Phys. Rev. 129, 677 (1963).
b. R. Sternheimer, Phys. Rev. 115, 1198 (1959).

Adsorbate Polarizability

An independent method of estimating the value of α in the adsorbed state as a function of θ is possible by analysis of the variation of the pre-exponential factor of the Fowler-Nordheim equation. This stems from a field-induced WFC, which according to Equation (30) would involve an additional term:

$$\Delta\phi_F = \frac{4\pi\,\theta\sigma_o\,\alpha F}{\epsilon} \tag{40}$$

where the ratio of the effective field F_e to the external field F is $F/F_e = \epsilon$.

$$\ln\frac{I}{V^2} = \ln\frac{B}{\phi_F\,t^2(y)} - \frac{b\,\phi_F^{3/2}\,v(y)}{\beta V} \tag{41}$$

where $b = 6.8 \times 10^7$ when I is in amperes, F in volts/cm, and ϕ in ev. The functions t(y) are slowly varying tabulated[71] functions. B is a function of the geometric factor β where $F = \beta V$. Noting that $\phi_F^{3/2} = (\phi + \Delta\phi_F)^{3/2}$ can be expanded, since $\Delta\phi$ is normally small compared to ϕ, and using the empirical relation $v(y) = 0.943 - 0.146 \times 10^{-6}\,F/\phi^2$, we can rewrite Equation (41) as follows:

$$\ln\frac{I}{V^2} = \ln\frac{B}{\phi_F t^2(y)} + \frac{9.94}{\phi_F^{1/2}} - 5.66b\pi\sigma_o\,\theta\,\phi^{1/2}\alpha - 0.943\,\frac{b\phi^{3/2}}{\beta V} \tag{42}$$

Within limits of the above approximation the experimental intercept ln A of the Fowler-Nordheim plot ($\ln I/V^2$ vs. $1/V$) is given by:

$$\ln A = \frac{\ln B}{\phi_F t^2(y)} + \frac{9.94}{\phi_F^{1/2}} - 5.66 b \pi \sigma_o \phi^{1/2} \frac{a}{\epsilon} \tag{43}$$

It is now possible to obtain the following expression for a/ϵ:

$$\frac{a}{\epsilon} = \frac{\dfrac{\log \phi_s t_s^2(y)}{\phi_F t^2(y)} - \log \dfrac{A}{A_s} + 4.32 \left(\dfrac{1}{\phi_F^{1/2}} - \dfrac{1}{\phi_s^{1/2}} \right)}{1.67 \times 10^8 \pi \sigma_o \theta \phi^{1/2}} \tag{44}$$

where ϕ_s and A_s refer to the corresponding clean values. Values of a/ϵ and a are given in Table IX for the (110) and (100) as a function of σ. Since relatively large experimental errors are associated with the $\log A/A_s$ term in the numerator of Equation (44) along with the uncertainties in σ_o, θ, one must consider the values of a as a rough approximation. The two conclusions to be drawn from the results are: (1) the values of a appear relatively constant over the range of σ; and (2) the values of a are roughly similar for the two planes and in approximate agreement with the value 4.5 A^3 obtained in the preceding section by assuming $z_{110} = 1$.

TABLE IX

Polarizabilities of the adsorbed cesium atoms on two crystallographic planes of tungsten calculated according to Equation (44)

(100)					(110)				
$\sigma^*(\times 10^{14})$	ϕ(ev)	$\alpha/\epsilon(A^3)$	$\alpha(A^3)$	$\ln A/A_s$	$\sigma^*(\times 10^{14})$	ϕ(ev)	$\alpha/\epsilon(A^3)$	$\alpha(A^3)$	$\ln A/A_s$
2.35	1.65	6.0	7.4	0.65	3.00	2.19	6.0	8.4	-0.09
2.16	1.63	4.3	4.9	1.07	2.90	2.13	4.6	5.8	0.42
2.03	1.61	5.9	6.9	0.89	2.66	2.03	4.2	5.0	0.73
1.97	1.67	5.7	6.7	0.83	2.52	1.91	5.5	6.8	0.63
1.53	1.84	4.9	5.3	0.94	2.40	1.76	6.3	8.0	0.72
1.31	2.22	3.2	3.3	0.81	2.35	1.65	5.6	6.9	1.03
0.97	2.61	5.9	6.2	0.36	2.10	1.54	5.5	6.5	1.34
0.80	2.87	5.0	5.1	0.34	1.79	1.57	6.1	7.0	1.34
0.62	3.13	3.8	3.9	0.34	1.65	1.79	6.9	8.0	0.97
0.28	3.93	4.5	4.5	0.08	1.34	2.09	5.2	5.6	1.01
0.16	4.17	29.0	29.0	-0.41	1.16	2.42	8.1	8.9	0.46
					0.90	2.85	8.5	9.1	0.28
					0.64	3.46	5.6	5.8	0.35
					0.29	4.51	1.0	1.0	0.31

*corrected values of σ used

Summary

The variation of work function with cesium coverage for molybdenum and rhenium substrates are similar to that observed earlier for tungsten, but with a slight shift of the minimum toward lower coverages in the case of rhenium.

The variation of work function change with cesium coverage on single crystallographic planes has been completed on the (110) and (100) planes of tungsten. These results have been compared with some of the existing theories, although some problems were encountered when attempting to establish the absolute coverage since the results suggest a difference in coverage between the two planes. This variation in coverage is such that the (110) plane has greater than average coverage, whereas the (100) plane has less than average coverage. An empirical relationship between the maximum work function change and local substrate work function was formulated and appears to have validity for a variety of electro-positive adsorbate-substrate systems.

SURFACE MIGRATION OF CESIUM ON TUNGSTEN

In earlier work[1,3] it was shown that the temperature required for surface migration of a known amount of cesium over a previously partially covered surface reached a maximum when the underlying cesium covered surface corresponded to the coverage attained at the work function minimum. Also, it was observed that a single dose of cesium diffused across the field emitter by what appeared to be a separation into two sharply divided high and low concentration phases when initial coverage of the half-covered tip exceeded 0.7 monolayer.

A crude theoretical model[1,3] of the adsorbed cesium layer incorporating both attractive and repulsive lateral forces indicated the likelihood of a two-dimensional phase change or transition to a state of long-range order in which mutual correlation of the migrating cesium atoms became important. This model was partially substantiated by observing[3] that the variation of activation energy E_d for surface migration of cesium on a molybdenum substrate with varying concentrations of underlying cesium remained essentially constant over the coverage range, and that the variation of migration rates with cesium coverage was due primarily to a variation in the pre-exponential factor D_o when the data was analyzed according to the following expression:

$$t_s = \frac{y^2}{D_o} \exp (E_d/k T) \tag{45}$$

where t_s is the time required for the cesium to travel a distance y.

In order to further substantiate the results obtained with cesium on molybdenum substrates, similar studies were performed on tungsten utilizing more sophisticated methods for measuring the surface diffusion rates which will be described in the following section.

Recent Results on Tungsten

The measurements of the activation energy of surface migration for cesium on clean tungsten, rhenium and molybdenum surfaces have been described in earlier reports[1,3,21]. Results to be described here were performed on a tungsten substrate in different coverage ranges by first equilibrating the cesium layer at the desired coverage and then depositing a small dose onto one side of the emitter and measuring the time required to completely spread this dose at a particular temperature. The emitter was then heated in order to thermally desorb the excess cesium back to the original starting coverage, and the sequence repeated at several other temperatures. The data was then analyzed according to Equation (45) and the activation energy determined.

In the past experiments of this nature, the end points were determined visually by noting certain characteristic changes in the field emission pattern when the cesium dose was completely equilibrated. However, it is often difficult to accurately determine the end points in such experiments, particularly when small doses are used, because of the lack of contrast in the field emission pattern. This usually leads to Arrhenius plots with an undesirable scatter in the points and hence, a large degree of uncertainty in both the activation energy E_d and the pre-exponential factor y^2/D_o. A new method of establishing the end points as well as following the progress of the migration process was established by following variations in the pulsed field emission current.

Briefly, the method utilized involves measurement of average pulse field emission current as a function of time by utilizing circuitry diagrammed schematically in Figure 17. This circuit allows simultaneous measurement of both the average pulse field emission current I_p and the pulse voltage V_p. Since all these measurements are performed on the high voltage side of the tube, it is possible to simultaneously heat the emitter as well as observe the field emission pattern. During the course of equilibrating a small dose of cesium, I_p at constant V_p usually goes through one or two maxima or minima as a function of time. It happened that one of the latter corresponded to a nearly completely equilibrated pattern and thus could be used as a fairly accurate endpoint indicator. Alternatively, it would also be possible to hold I_p constant and observe the variation in V_p as a function of time; however, for the surface diffusion work the former method was used since variations in I_p were much larger because of the exponential dependence on work function according to the Fowler-Nordheim relationship.

To implement this method it was found useful to record the variations of I_p with time on a chart recorder, thus allowing analysis of the data at later times as well as providing a permanent record. Throughout most of the coverage range investigated, the variations of I_p with time were essentially the same, thereby allowing the utilization of the same current maximum or minimum throughout the coverage range as the end point. The Arrhenius plots obtained from this method are shown in Figure 18. In addition, this method can be used as a check on the reproducibility of the cesium source by monitoring the variation of I_p during the course of deposition. In this manner it is possible to reproduce exactly the dose amount for each run.

There are other areas of field emission investigation of adsorbed layers in which the above method will be useful. For example, it would be possible to follow rates of thermal desorption in an analogous manner by monitoring either V_p or I_p as a function of time, and choosing various initial and final points in order to establish the rate of desorption in a particular coverage range. The main complicating feature in the measurement of thermal desorption rates by this method is the fact that the work function of adsorbed layers often shows a strong temperature dependence, in addition

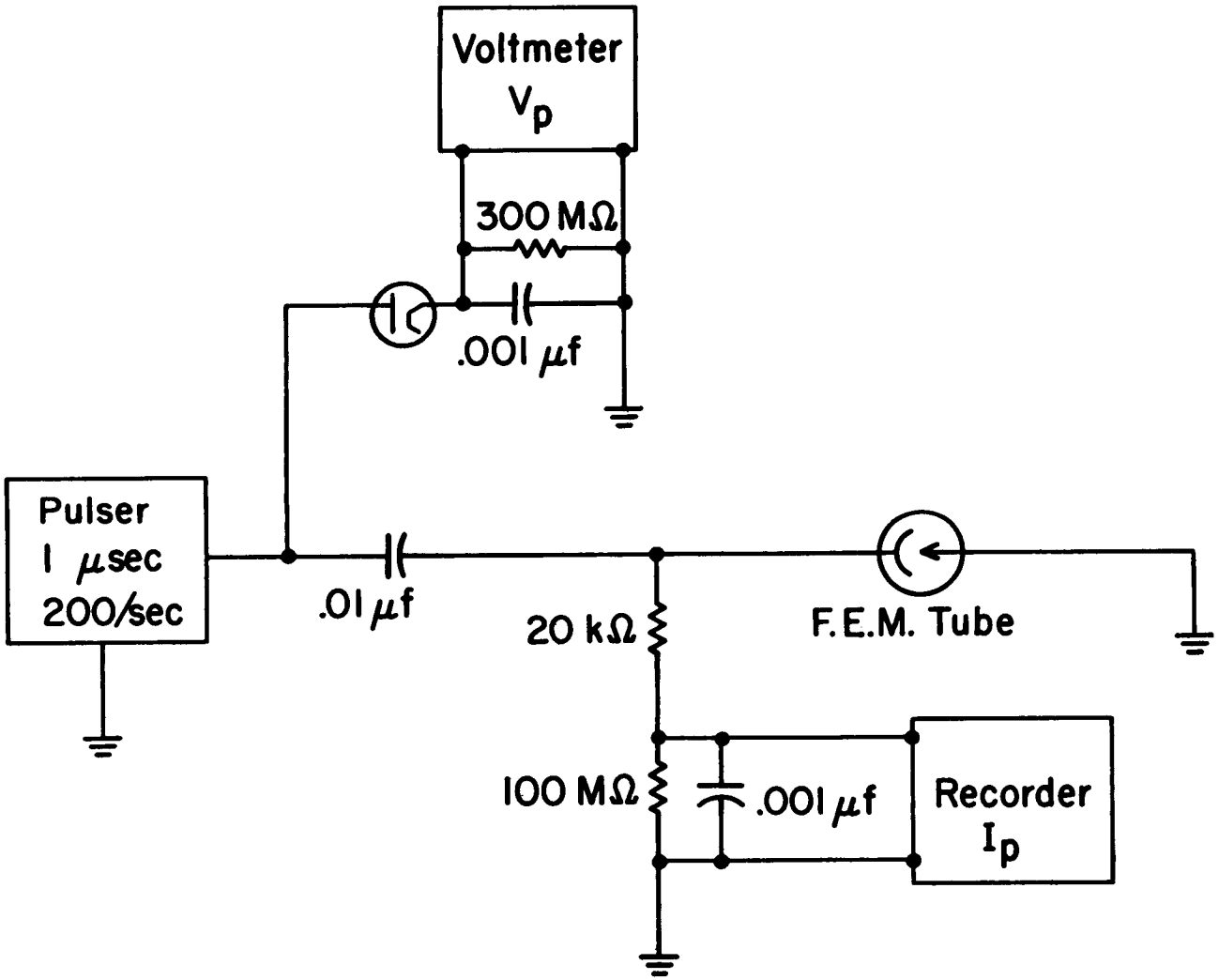

Figure 17. Block circuit diagram for measuring pulse voltage V_p and average pulse current I_p.

to the normal temperature dependence of field emission. In general, these effects do not greatly obscure the results when V_p is measured as a function of time at constant I_p, particularly over the temperature ranges normally encountered in establishing Arrhenius plots. It is also possible to use this technique to measure work functions of the heated emitter in order to establish their temperature dependence. For the latter use it is necessary that a nearly square voltage pulse be employed in order to obtain accurate current measurements, and also one must beware of space charge effects which occur, particularly when dealing with work functions less than 2.0 ev, because of the high peak pulse currents employed in pulsed field emission.

A further simplification and improvement in the temperature measurements was also made. As described previously[21], the tip temperature is controlled by a servo circuit which maintains a constant, pre-set resistance across a portion of the filament to which the emitter is spot welded. This resistance is then related to a temperature by a predetermined relationship between temperature and resistance for the particular tip assembly. In the past, resistance measurements were made by monitoring two meters, one which measured the current flowing through the filament, and the other which monitored the voltage across a small segment of the filament. The new method employed to measure the resistance consists of utilizing a recently acquired x-y recorder in a manner to allow the voltage developed on the filament to be recorded on one axis and the current developed measured on the other axis of the recorder, thus a single point is obtained on the x-y plot, in which the ratio of the ordinate to abscissa corresponds to the filament resistance. The advantage of this method is to allow instant read out of the resistance values and immediately display any drift in the temperature due to malfunctioning of the servo circuit.

Results and Discussion

The results of the Arrhenius plots shown in Figure 18 are tabulated in Table X along with the earlier results[3] obtained on molybdenum. The recent results obtained on tungsten thus appear to substantiate the trend noted in the earlier results on molybdenum, namely, the increase in the temperature required for equilibration of a cesium dose which has a maximum at the work function minimum is not due to an increase in the E_d, but rather to a decrease in the pre-exponential factor. The last column of Table X shows the variation of the diffusivity D_o with coverage by estimating the average value of y required for equilibration. Writing the diffusion coefficient $D(\sigma)$ in the following form:

$$D(\sigma) = D_o \exp(-E_d/kT) \tag{46}$$

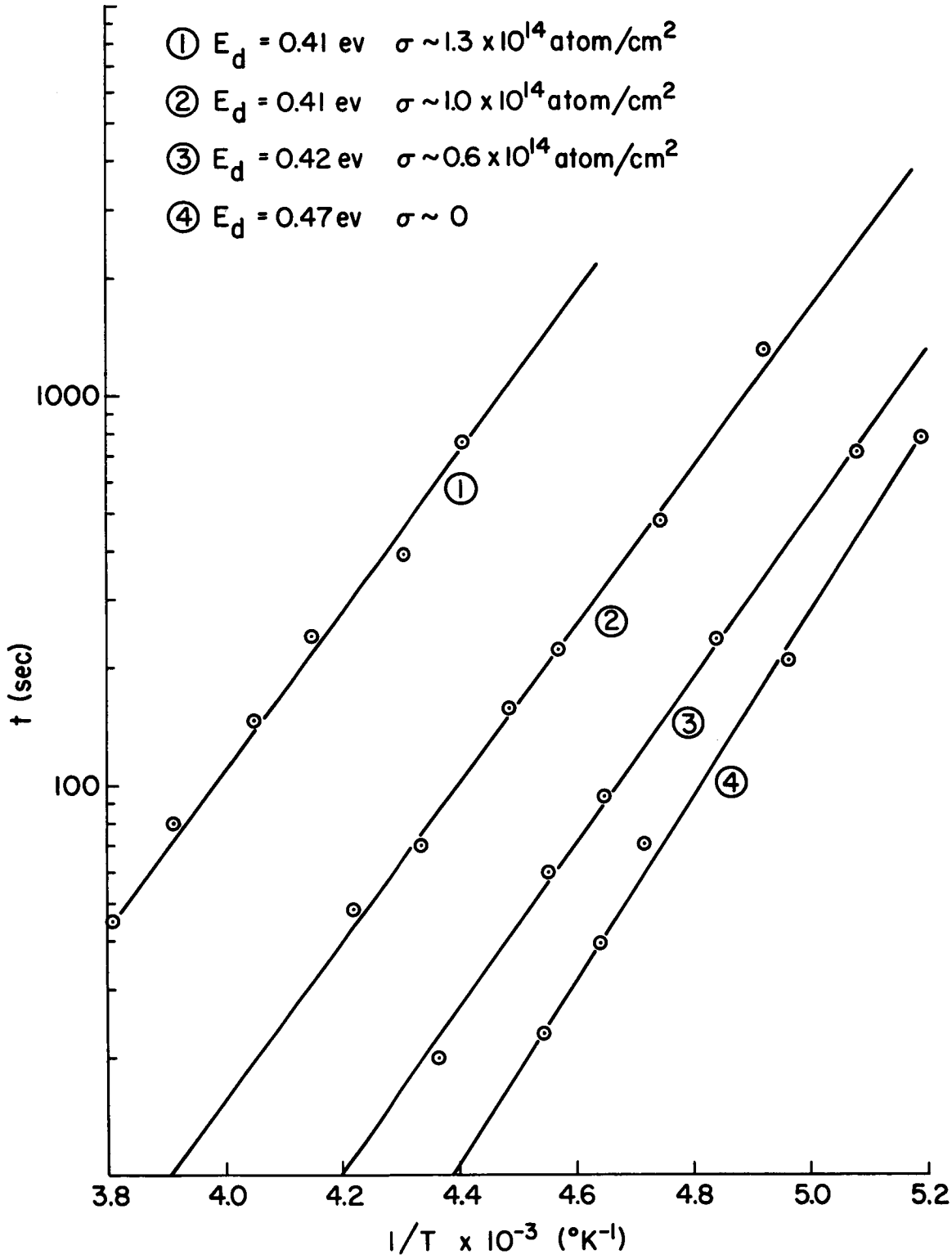

Figure 18. Arrhenius plots of the time required for equilibration of a small dose of cesium for the various underlying coverages of cesium where end points have been determined by the variations in pulse current with time according to the circuitry given in Figure 21.

TABLE X

Summary of surface migration data for Cs on tungsten and molybdenum

TUNGSTEN RESULTS

σ (atoms/cm^2) Initial	Final	E_d(ev)	E_d/E_a	$Log(y^2/D_o)$	D_o(cm^2/sec)*
0	0.08×10^{14}	0.47	0.16	-9.4	1.39×10^{-1}
0.61×10^{14}	0.71	0.42	0.21	-7.9	4.41×10^{-2}
0.98	1.09	0.41	0.24	-6.9	4.41×10^{-3}
1.32	1.45	0.41	0.28	-6.1	7.0×10^{-4}
--	>3.00	0.26	~ 0.31	--	---

MOLYBDENUM RESULTS

0	0.1	0.43		-6.6	2.2×10^{-3}
1.3	1.4	0.43		-5.2	8.8×10^{-5}
1.9	2.3	0.37		-5.9	4.41×10^{-4}

*Obtained by assuming $y \cong \frac{\pi R_c}{2}$, where R_c is approximate emitter radius

it is possible from the data of Table X to determine $D(\sigma)$ both as a function of temperature and coverage over the range in which the latter variables were investigated.

It should be emphasized that the values of E_d given in Table X correspond to migration over all the crystallographic planes of the substrate and, hence, are average values weighted heavily by those planes exhibiting the largest value of E_d. This means in the low coverage region the (100) planes, which exhibit the largest E_d, contribute strongly to the average E_d. The relatively small value of the ratio E_d/E_a (where E_a is the desorption activation energy) throughout the coverage range is indicative of a large adsorbate whose bonding mode with the substrate is rather delocalized. This is in contrast with the more electro-negative adsorbates which exhibit larger values of E_d/E_a in agreement with localized pair-wise type bonding to the substrate. In the latter case migration over the loosely packed planes of the substrate involves the breaking and reforming of a larger degree of the bonds to the substrate. This will be pointed out more clearly in a succeeding section on mercury surface migration on tungsten.

Summary

In summary, the results reported here for the variation of surface migration of cesium on tungsten with cesium coverage agrees with the earlier results obtained on a molybdenum substrate and generally support the semi-quantitative theory set forth earlier[3]. It is interesting to note that for the system potassium on tungsten, a similar variation of the surface migration rates with coverage was observed[34], but in this case it was found that the variation in rates with potassium coverage was primarily due to a variation in E_d, rather than a variation in the pre-exponential factor as observed here. At the moment, it is difficult to explain the difference in behavior of these two systems since in many other aspects they closely resemble each other.

MERCURY ADSORPTION ON MOLYBDENUM

The changes in field emission pattern detail and in work function for adsorption and desorption of thin mercury films on a molybdenum substrate have been investigated by field emission techniques. Also, the activation energies for thermal desorption and surface diffusion of a low coverage of mercury on molybdenum were obtained from Arrhenius plots.

The behavior of mercury on molybdenum is found to be considerably different from that of cesium on molybdenum: (1) adsorption of mercury on molybdenum increases the work function rather than decreasing it; (2) a heavy coverage of mercury on molybdenum is mobile even at 77°K; (3) the high fields required for pulsed field emission (about 40 Mv/cm in this case) cause arcs to occur in the region of the emitter tip when it is covered with several monolayers of mercury. In connection with this latter point an arc is found to remove some of the adsorbed mercury from the emitting portion of the tip even though the tip is at a temperature of 77°K. For this reason the field emission patterns for mercury on molybdenum were photographed using dc electric fields, which are not as high as those required for pulsed operation.

Adsorption and Diffusion

Adsorption of mercury on molybdenum has been studied by two different methods, the first consisting of a series of successive doses with no thermal equilibration, and the second being a series of successive doses each being thermally equilibrated. Field emission techniques used for this investigation were identical to those described earlier[1,21] for cesium adsorption and migration on tungsten.

The results of the first method are shown in Figure 19, which is a series of field emission patterns taken during evaporation of mercury onto a molybdenum field emitter held at a temperature of 77°K. Figure 19 (a) is the emission pattern of clean molybdenum; Figure 19 (b) identifies the principal planes in the emission pattern. Figure 19 (c) was taken after the tip had been dosed with an amount of mercury chosen to be a unit dose N = 1. The darkening of the upper portion of the pattern by the adsorbed mercury shows that (1) mercury adsorbed on molybdenum raises the work function, and (2) for this particular degree of coverage mercury is not mobile on molybdenum at 77°K. Figure 19 (d) indicates that doubling the amount of mercury does not change the basic behavior of the mercury film. The uniform appearance of the pattern in Figure 19 (e), taken after dosing the tip a total amount N = 4, shows that at this higher degree of coverage mercury is mobile, even at 77°K. From this it may be inferred that N = 4 corresponds to a coverage greater than a monolayer, since multilayer

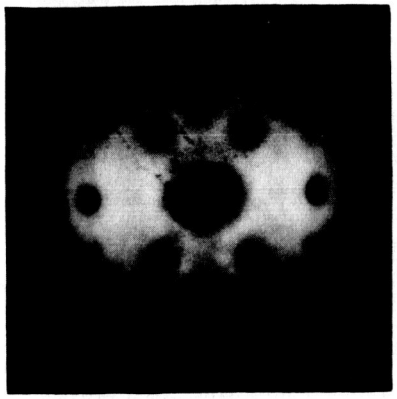

(a)
Clean Mo
ϕ = 4.20 ev

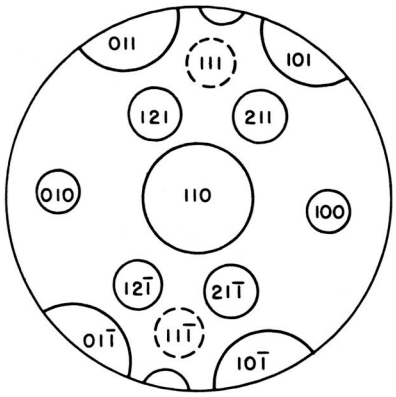

(b)
Principal planes of
(110)-oriented Mo

(c)
N = 1 (arbitrary units)

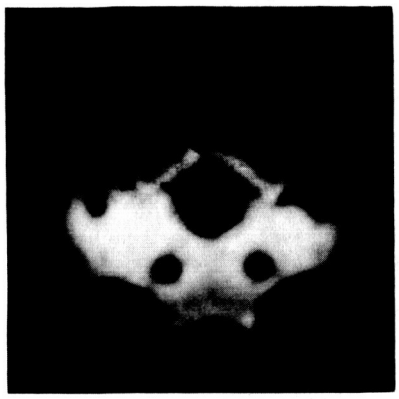

(d)
N = 2

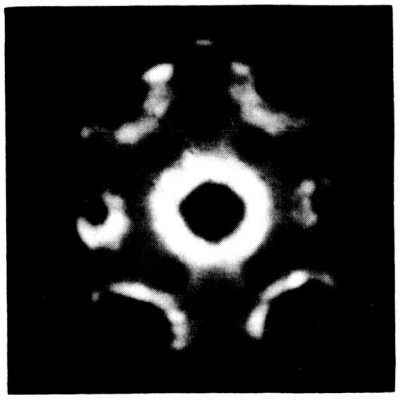

(e)
N = 4

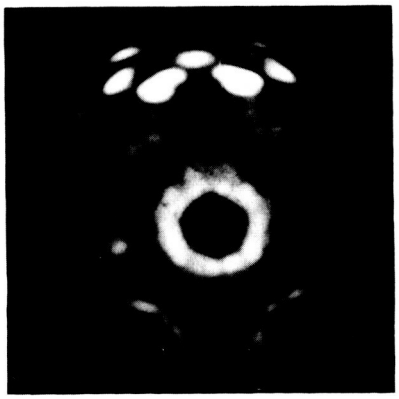

(f)
N = 6

Figure 19. Changes in the field emission pattern of a molybdenum emitter during adsorption of mercury. The relative amount of mercury on the emitter is given by the quantity N.

diffusion generally can occur at lower temperatures than first layer diffusion for most systems. The spots in the top of the pattern in Figure 19 (f), taken after dosing the tip a total amount N = 6, are indicative of mercury atom clustering, and suggest that epitaxial growth studies could be made on this system. Dosing a total amount N = 8 caused no further changes in the field emission pattern. Thus, mercury was found to raise the work function when adsorbed on molybdenum and to be mobile in the second layer but not in the first at 77°K.

In the second method, the molybdenum tip was dosed with a small amount of mercury, which was then equilibrated over both the emitter tip and shank by surface diffusion. A photograph of the resulting field emission pattern was taken and the work function of the surface was determined from a Fowler-Nordheim plot. The results are shown in Figures 20 and 21. In Figure 20 are plots of the change in work function and change in log A, the pre-exponential part of the Fowler-Nordheim equation, as functions of the relative amount of mercury coverage. The maximum work function change is 0.42 ev, and in the opposite direction from the change caused by cesium adsorption on molybdenum. It was stated earlier that an empirical relationship between ϕ_s the substrate work function, ϕ_a the adsorbate work function, and $\Delta\phi_m$ the maximum change in work function upon adsorption,

$$\Delta\phi_m = 1.09\,(\phi_s - \phi_a), \tag{47}$$

which was in good agreement with a number of electro-positive adsorbate-substrate combinations. For mercury on molybdenum the above equation would predict a work function increase of 0.35 ev, whereas 0.42 ev was actually measured; these two numbers are in reasonable agreement. However, for many other adsorbate-substrate combinations the work function change at the monolayer is very nearly equal to the contact potential between the bulk metals of the adsorbate and substrate, whereas it can be seen in Figure 20 that for mercury on molybdenum the work function drops below the average adsorbate work function (4.52 ev)[37] and continues to drop with increasing coverage (the last point on the graph is of questionable validity because of the growth of projections on the emitter tip). Moreover, on another contract[38] the work function changes of mercury on tungsten have been measured; whereas Equation (47) predicts zero change in work function for this system a work function change of 0.35 ev is actually measured. Thus the quantitative application of Equation (47) to electro-negative adsorbates appears questionable. Figure 21 shows the field emission pattern changes that occur during the adsorption run. In general the changes are quite small and the pattern looks rather similar to that of clean tungsten through most of the coverage range.

Also plotted in Figure 20 are the temperatures required for equilibration of the various coverages over both the emitter tip and shank. This

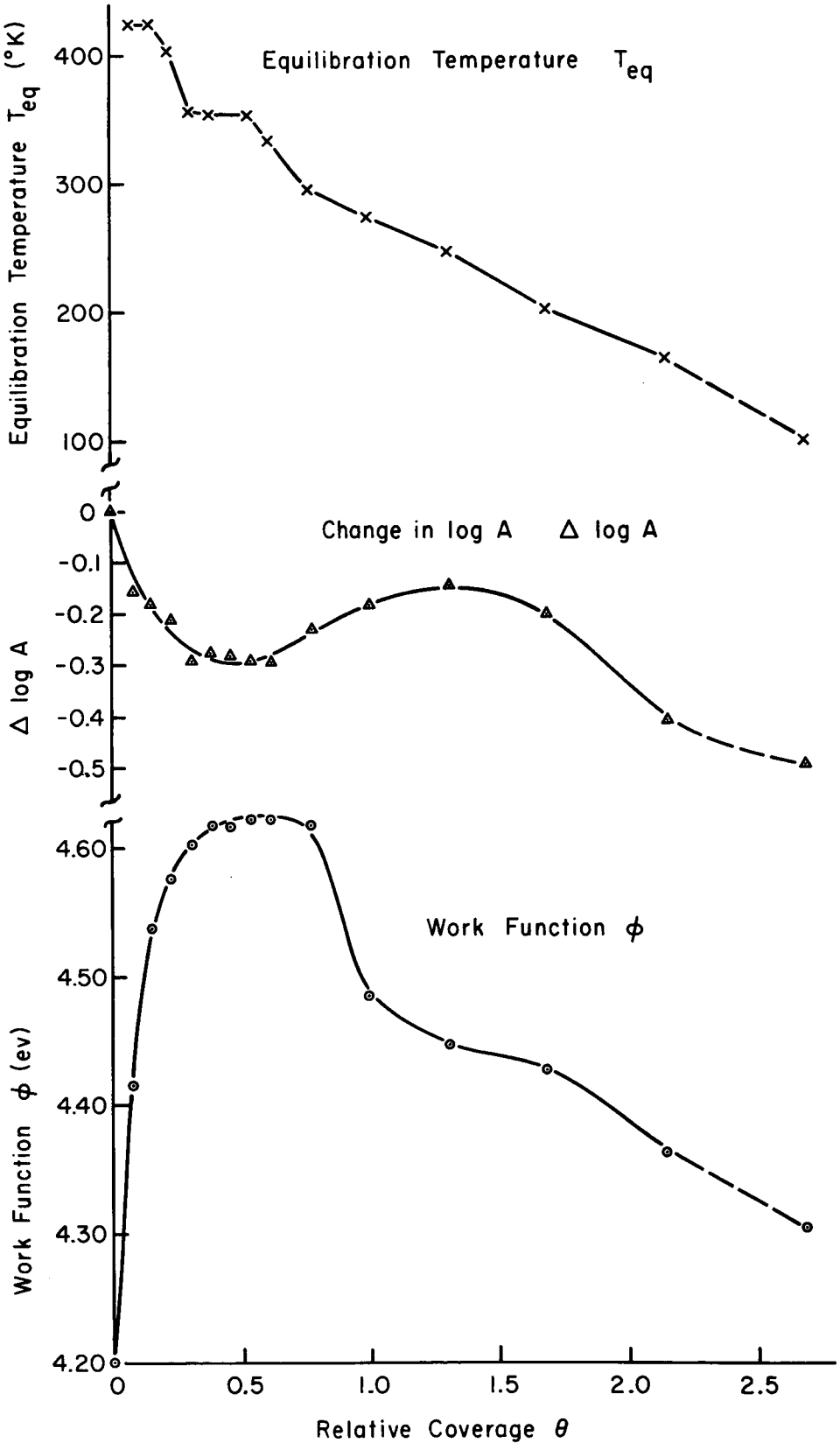

Figure 20. Changes in work function, the Fowler-Nordheim pre-exponential term A, and equilibration temperature as functions of the relative amount of mercury coverage for mercury on molybdenum.

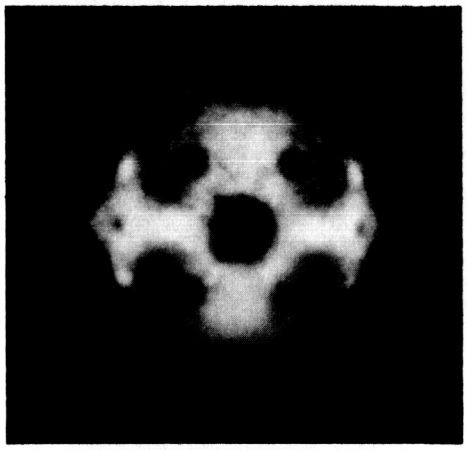

(a)
ϕ = 4.42 ev
θ = 0.08

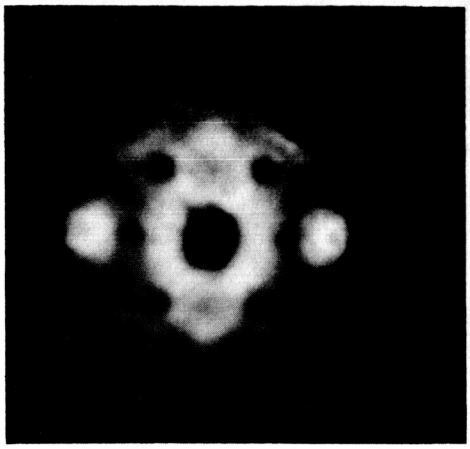

(b)
ϕ = 4.54 ev
θ = 0.15

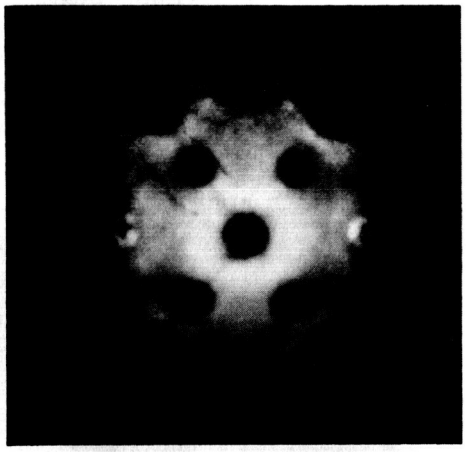

(c)
ϕ = 4.62 ev
θ = 0.77

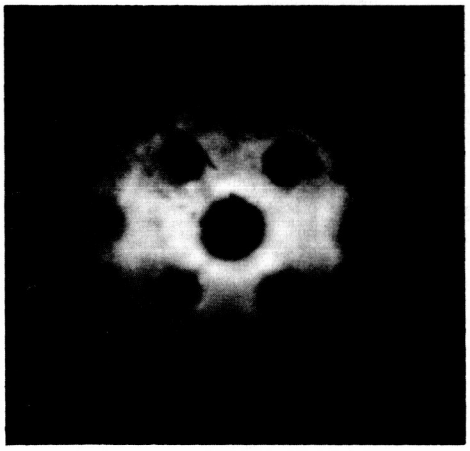

(d)
ϕ = 4.45 ev
θ = 1.31

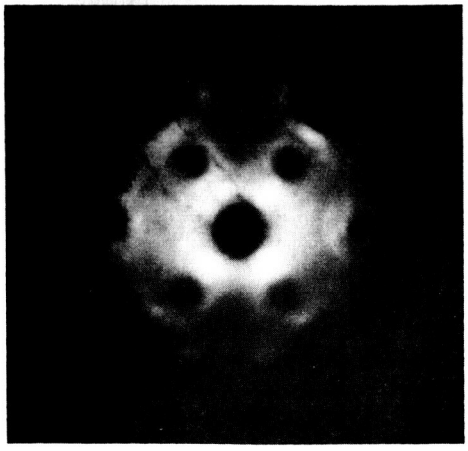

(e)
ϕ = 4.43 ev
θ = 1.69

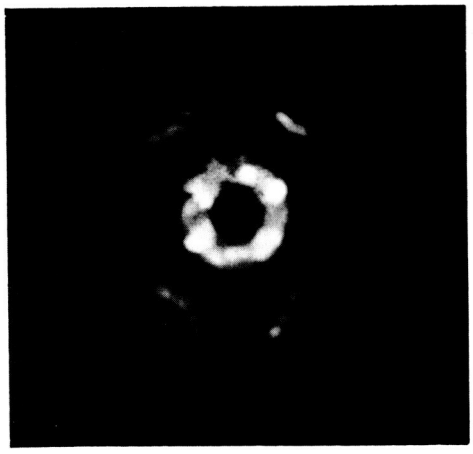

(f)
ϕ = unknown
θ 3.3

Figure 21. Field emission patterns for various coverages of mercury on molybdenum, after equilibration. The relative amount θ is based on the coverage scale of Figure 20.

graph of equilibration temperature vs. coverage gives a rough idea of the change in diffusion constant as a function of coverage.

At a high coverage (greater than 2.5 on the relative coverage scale of Figure 20) viewing fields of 25 Mv/cm or greater were observed to cause the growth of projections near the edges of the {110} planes (the bright spots in the bright rings surrounding the {110} planes in Figure 21 (f). When the viewing field was reduced to zero the projections (i.e., the bright spots in the emission pattern) disappeared, apparently due to the mobility of mercury at this coverage at 77°K. The projections could be made to grow and disappear many times by having the viewing field alternately above 25 Mv/cm or at zero. The growth of projections as in Figure 21 (f) is probably due to the electrostatic stress of the applied field acting upon the mobile mercury layer and pulling mercury atoms toward points of highest field.

Thermal Desorption

The thermal desorption characteristics of mercury on molybdenum were determined in the usual manner; that is, the emitter was heated for 60-second periods to successively higher temperatures, and after each heating period was returned to a temperature of 77°K at which a photograph of the emission pattern was taken and the work function determined from a Fowler-Nordheim plot. The changes in work function are plotted as a function of desorption temperature in Figure 22. By using the work-function vs. coverage curve of Figure 20 a relation between the desorption temperature and relative coverage may be obtained; this is plotted in Figure 23. The desorption temperature is roughly proportional to the desorption activation energy; thus Figure 23 is essentially a graph of the variation of the desorption activation energy with relative coverage. The sequence of patterns obtained during desorption are the same as for adsorption but reversed; this indicates that the adsorption and desorption processes are reversible.

Diffusion and Desorption at Low Coverage

The activation energies for surface diffusion and thermal desorption of mercury from molybdenum have been determined from Arrhenius plots for the coverage interval 0 - 0.07 relative monolayer (that is between the coverages indicated by Figures 19 (a) and 21 (a). The Arrhenius plots were obtained from measurements of the time required to go between two pulsed current measurements corresponding to the coverages indicated as a function of temperature. The results are shown in Figure 24. As would be expected, the desorption activation energy is less than the corresponding value for cesium on tungsten; however, the diffusion activation energy is higher than for cesium on tungsten[39]. From pattern detail it is found that this diffusion energy corresponds to diffusion across regions in the neighborhood of {110} and {211} planes, but not across the {100} regions.

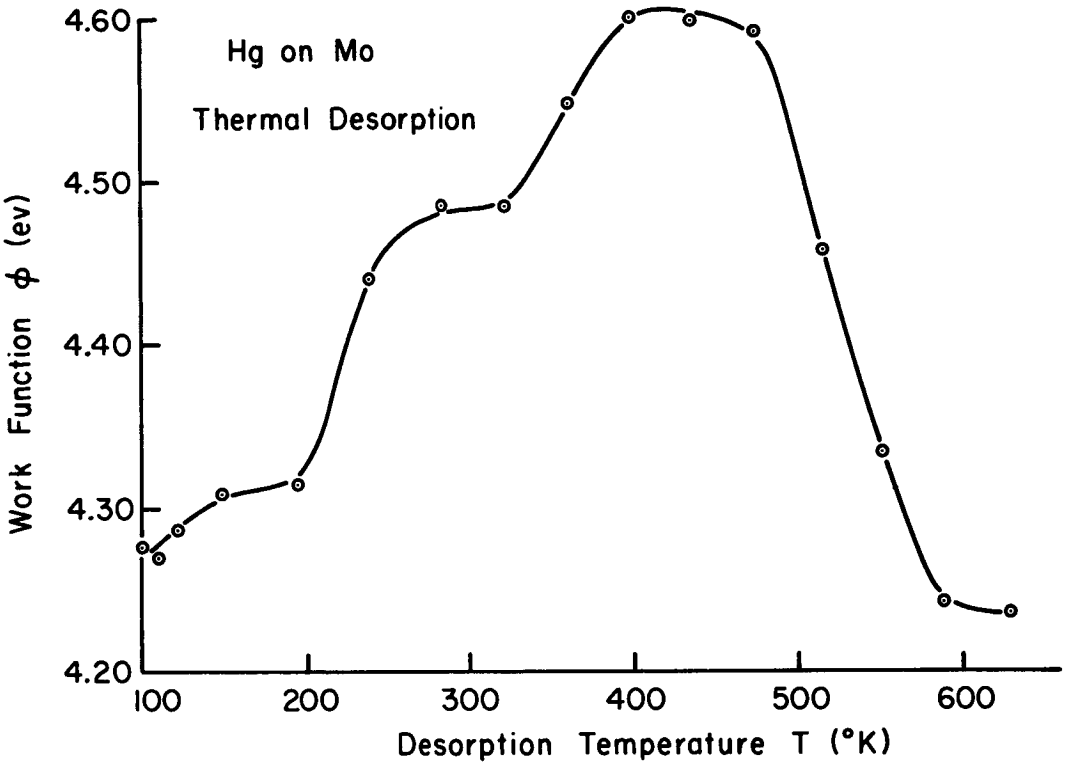

Figure 22. Work function of mercury on molybdenum as a function of desorption temperature to which the emitter had been heated for successive 60-second heating periods.

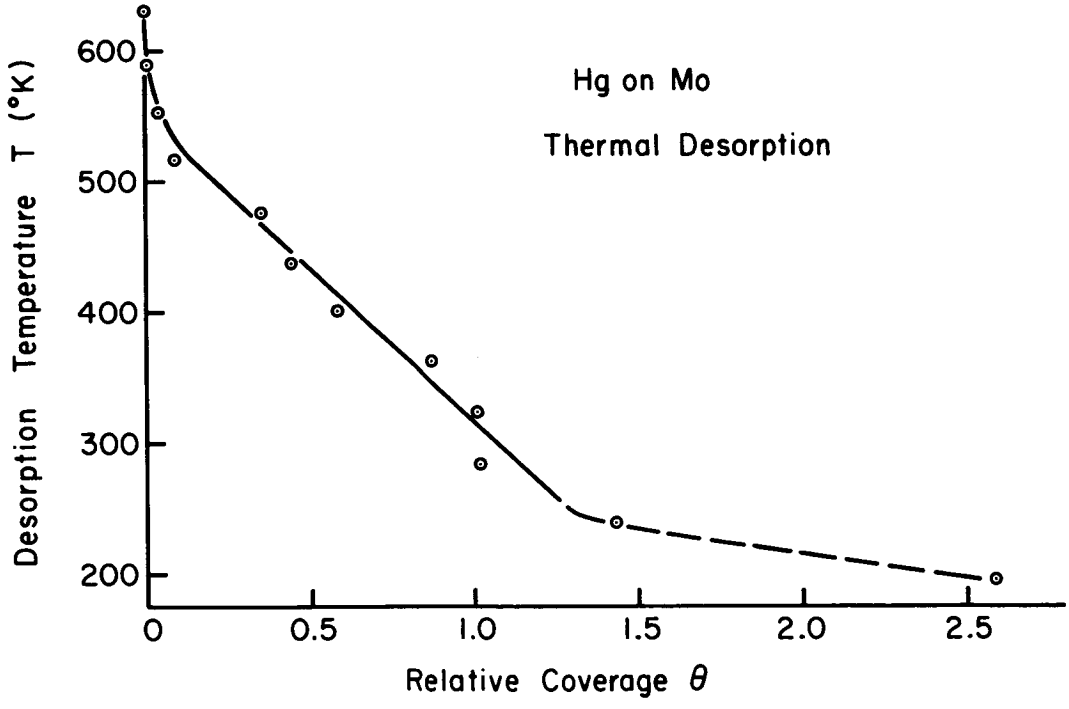

Figure 23. Desorption temperature for successive 60-second heating periods as a function of mercury coverage for mercury on molybdenum. The relative amount θ was obtained by means of Figure 20.

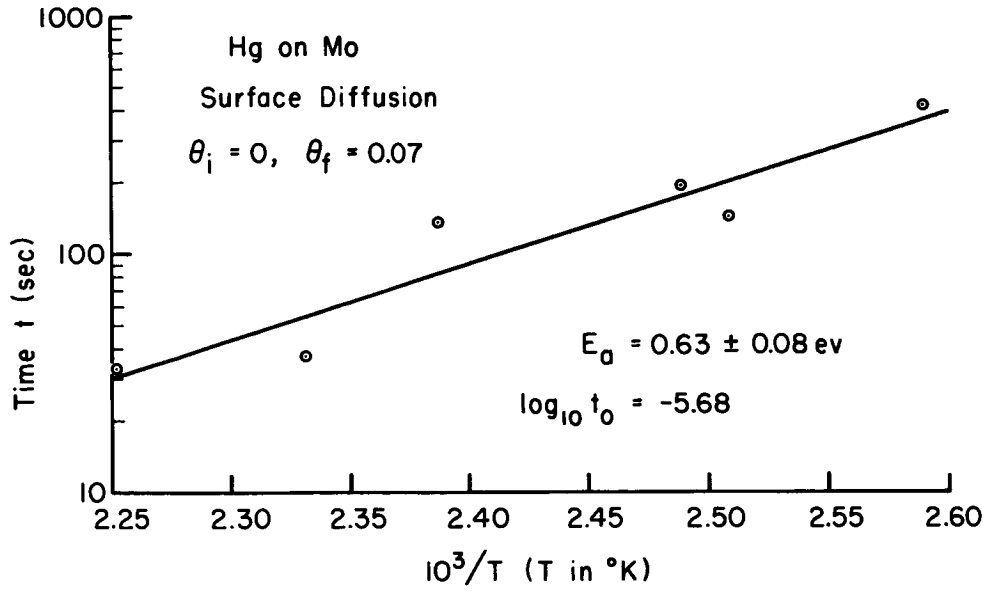

(a)

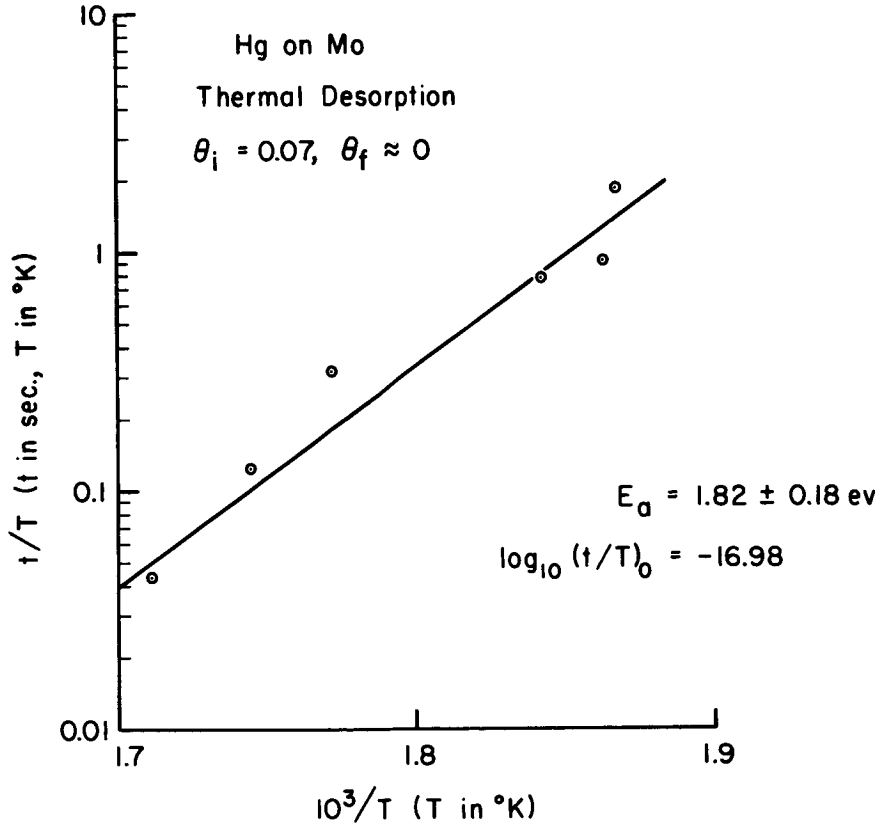

(b)

Figure 24. Arrhenius plots for a low coverage of mercury on molybdenum.
(a) Surface diffusion between coverages $\theta_i = 0$ and $\theta_f = 0.07$
(b) Thermal desorption between coverages $\theta_i = 0.07$ and $\theta_f \approx 0$.

As in the case of mercury-tungsten mentioned below, the energy for diffusion across the {100} regions is probably considerably higher.

A more detailed investigation[38] of the mercury-on-tungsten system revealed an unusually high value of $E_d = 1.33$ ev at $\theta = 0$ which could be attributed to diffusion into the {100} regions. This leads to a value of $E_d/E_a \cong 0.69$ considerably larger than those exhibited by electro-positive adsorbates. In many ways mercury adsorption bears closer resemblance to electro-negative adsorbates (e.g. CO, N_2, O_2, etc.) than to electro-positive metallic adsorption. Apparently the high value of the ionization potential ($V_I = 10.3$ v) for mercury causes a localized-pairwise type bonding to the substrate manifested, among other ways, by the high value of E_d/E_a.

In contrast to cesium, mercury diffused into the (100) plane at low coverages with a sharp boundary. On the basis of the importance of pairwise interactions and the close fit of mercury on this plane (the atomic diameter of mercury 3.10A is nearly equal to the lattice spacing of tungsten or molybdenum) it is likely that the (100) plane will exhibit the highest value of E_a as well. This may be examined in the future by single plane probe techniques.

COPPER, BERYLLIUM AND CHROMIUM ADSORPTION ON TUNGSTEN

The field emission studies of low melting metal adsorbates on refractory metals are being extended to cover adsorbates with higher melting points; in this report are given results for copper, beryllium and chromium on tungsten. Field emission techniques have been used previously to investigate copper coatings on tungsten,[2,40] but no such work has been reported for beryllium or chromium on tungsten.

Experimental Procedures

The experimental procedures used in these studies were the same as those described previously;[1] only details relating to the metal adsorbates and the sources used to evaporate them will be given here.

Copper was obtained from MRC Corporation in the form of 0.010'' D wire made from zone-melted material. A short piece of copper wire was wrapped around a V-shaped 0.010'' D tungsten filament and melted in vacuum to form a ball at the apex of the filament. The filament was then mounted in a standard field emission microscope (Figure 25(a))that also had a cesium source, so that co-adsorption of copper and cesium could be studied. The resistance of a segment of the filament supporting the copper ball was measured as a function of temperature, as determined by an optical pyrometer, so that the

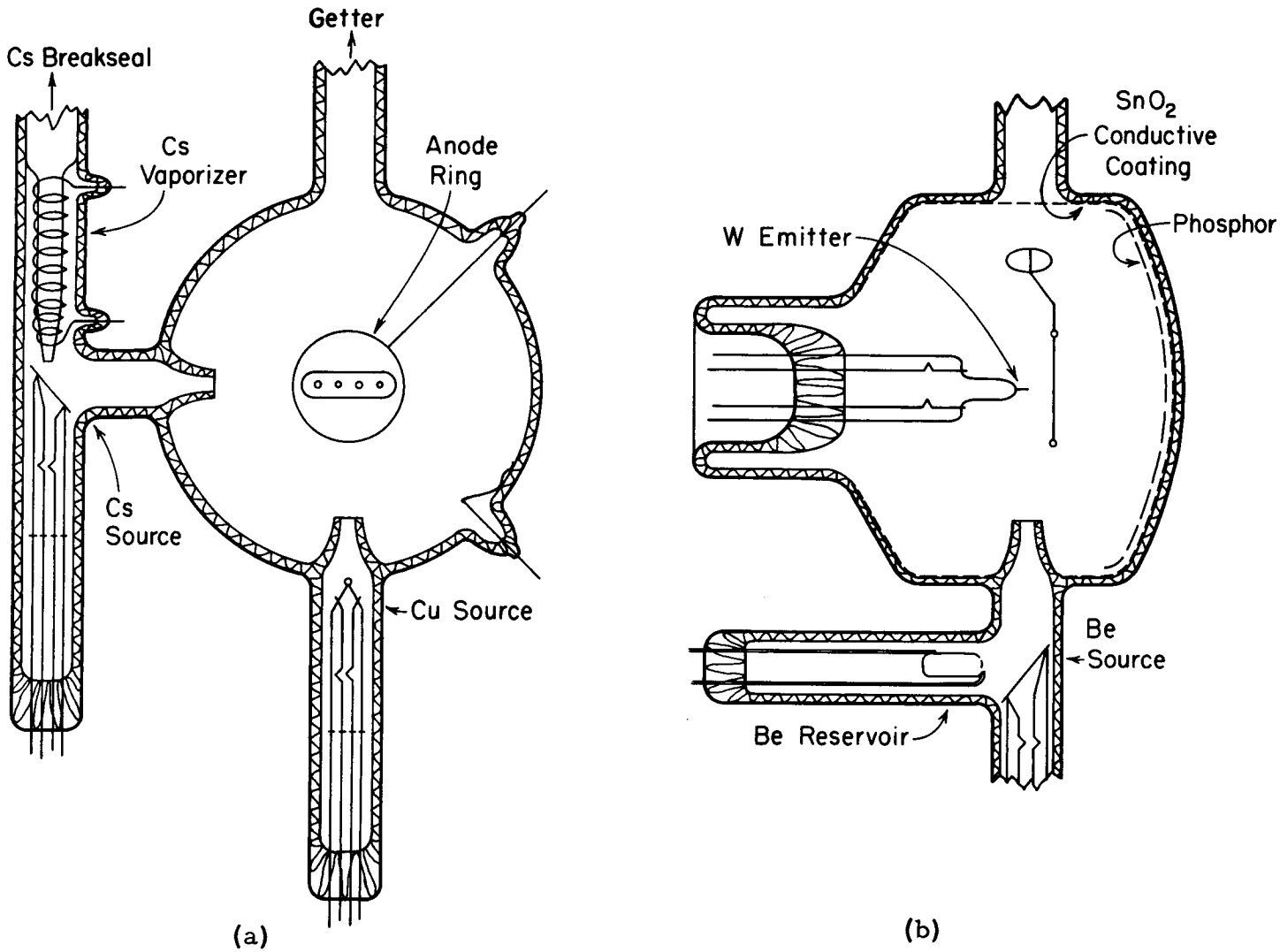

Figure 25. Diagrams of field emission microscopes used in the studies of (a) copper on tungsten and cesium on copper-covered tungsten, and (b) beryllium on tungsten.

temperature of the copper ball could be both controlled and measured by use of a temperature controller described previously[21].

The degree of copper coverage on the emitter was determined from the known geometry (the diameter of the copper ball was 0.666 $\pm$ 0.003 cm, and its distance from the tip was 4.0 cm), the temperature of the ball (1316 $\pm$ 10°K), the vapor pressure of copper at that temperature (1.65×10^{-4} torr, using Nesmayonoff's best estimate tables[41]), and the time that the source was at temperature (a change in coverage of 0.75×10^{14} atom/cm^2 was obtained for a 200 sec dose). Care was taken to obtain equilibration of the emitter shank as well as of the emitting area of the tip.

Beryllium of reasonable purity (1000 ppm of detectable impurities) was obtained from Bureau of Mines, Albany, Oregon, in the form of small flakes. The beryllium was placed in a platinum container which could be heated and thus used as a reservoir of beryllium. In the evacuated tube Figure 25 (b) beryllium was evaporated from the reservoir onto a platinum disk, which was used as a source of evaporation for beryllium onto the emitter tip. This arrangement turned out to be unsatisfactory because not enough beryllium could be deposited onto the platinum disk in a reasonable time to permit adequate dosing of the tip without burning out the reservoir.

Chromium adsorption on tungsten was accomplished by placing powdered chromium of high purity into a platinum crucible which could be heated resistively to $\sim$1300°K for evaporating chromium onto a tungsten field emitter. The tube design was similar to that shown in Figure 25 (b) except the platinum disk was omitted and evaporation from the crucible was directed at the emitter.

COPPER ON TUNGSTEN

Adsorption

The change in work function of the emitter with increasing copper coverage was obtained by evaporating onto the tip a series of small successive doses of copper each of which was equilibrated over both the emitter tip and shank by surface diffusion. The average work function of the surface was determined from a Fowler-Nordheim plot, and the emission distribution from the resulting field emission pattern. The results are shown in Figures 26 and 27.

In Figure 26 are plots of the change in work function, change in log A, the pre-exponential part of the Fowler-Nordheim equation, and change in the equilibration temperature as functions of the amount of copper coverage. As the copper coverage is increased the work function increases first to a maximum of 4.75 ev then decreases to a minimum of 4.18 ev and then increases again to approximately 4.30 ev for high copper coverages. (The work function of bulk copper is 4.47 ev). The field emission patterns (Figure 27) indicate that

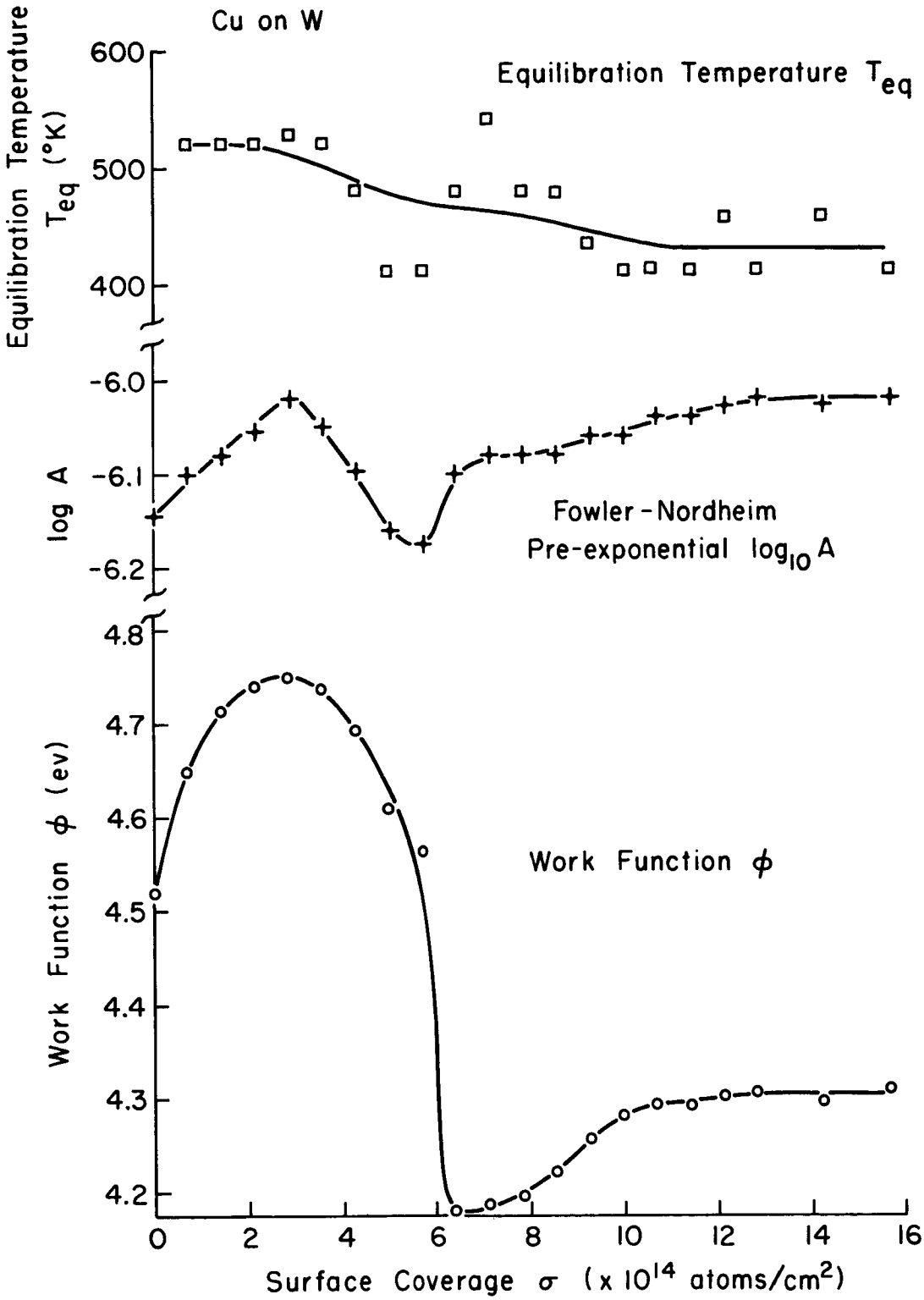

Figure 26. Changes in work function ϕ, the Fowler-Nordheim pre-exponential term A, and equilibration temperature T_{eq} as functions of copper atom surface coverage for copper on tungsten.

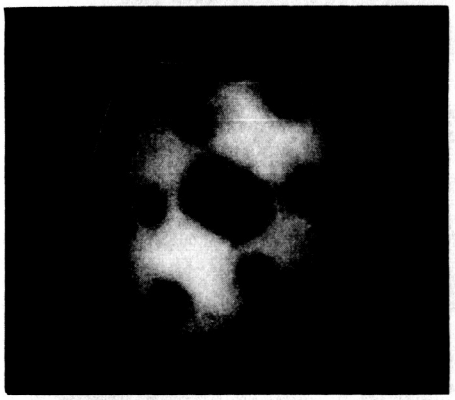

(a) Clean W
ϕ = 4.52 ev

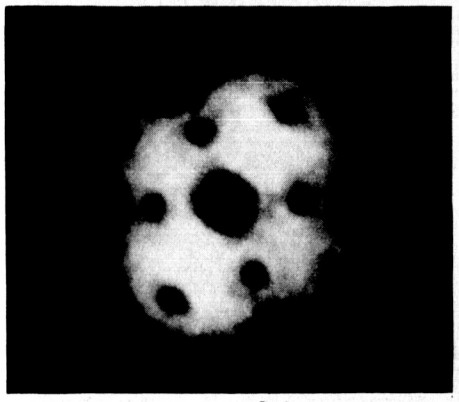

(b) $\sigma = 0.7 \times 10^{14}$ atoms/cm^2
ϕ = 4.65 ev

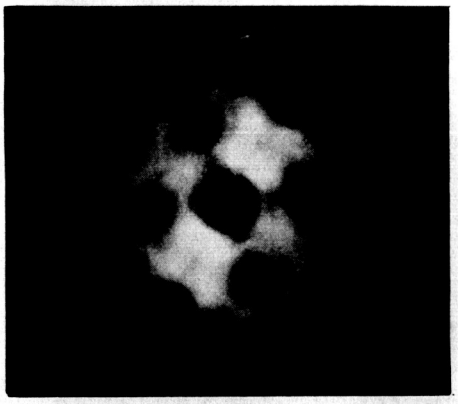

(c) $\sigma = 2.8 \times 10^{14}$ atoms/cm^2
ϕ = 4.75 ev

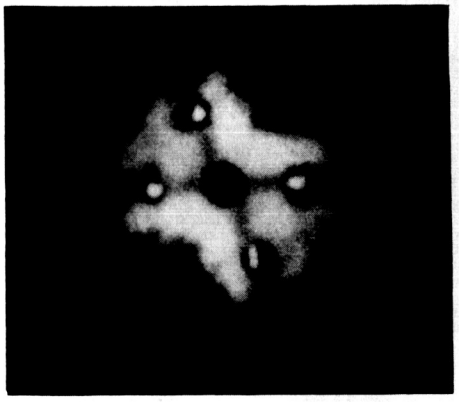

(d) $\sigma = 6.0 \times 10^{14}$ atoms/cm^2
ϕ = 4.40 ev

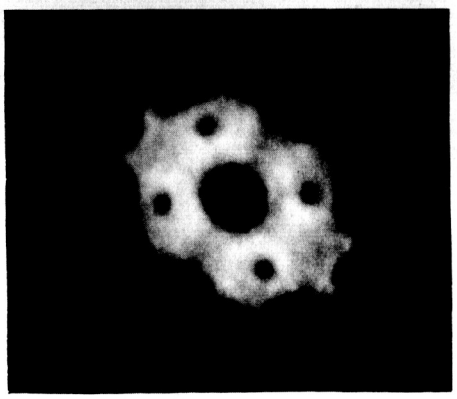

(e) $\sigma = 6.4 \times 10^{14}$ atoms/cm^2
ϕ = 4.18 ev

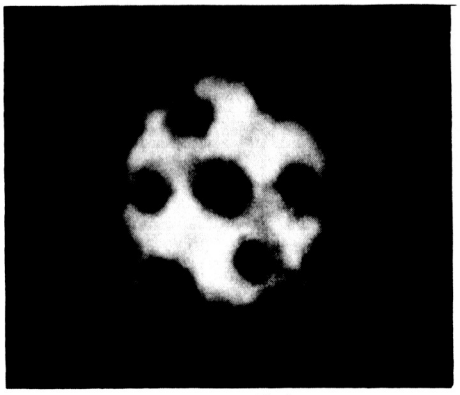

(f) $\sigma = 12.8 \times 10^{14}$ atoms/cm^2
ϕ = 4.31 ev

Figure 27. Field emission patterns for various coverage for copper on tungsten.

the initial work function changes are associated mainly with the {111} regions of the tip (Figure 27 (b)), and as the work function increases with the {100} and {211} planes (Figure 27 (c)). As the work function falls to its minimum value, emission in {111}, {211}, and {310} regions increases (Figure 27 (d) and (e)). It is interesting to note that for a very narrow coverage range about 6.0×10^{14} atom/cm^2 the {211} planes have bright spots, as shown in Figure 27 (d). Emission decreases in the same regions as the work function increases at higher coverages (Figure 27 (f)). The coverage at which the work function becomes independent of coverage is approximately the same atom density as that of the (110) plane of a copper crystal. The work function at this point (4.30 ev) is somewhat lower than the average work function for copper (4.47 ev), as one might expect since (110) plane is one of the higher emitting planes in a face-centered cubic crystal.

Diffusion

Figure 26 shows that the equilibration temperature was not greatly affected by the underlying copper coverage; this indicates that the diffusion constant D for surface diffusion does not have a strong dependence on coverage. The activation energy for surface diffusion of a small amount of copper was determined for the coverage interval, 0 to 0.3×10^{14} atom/cm^2, from an Arrhenius plot made from measurements of the time required to go between two pulsed current measurements corresponding to the coverages indicated as a function of temperature (Figure 28); the value obtained was 1.15 ± 0.08 ev/atom.

Field emission patterns indicate that at low coverage the diffusion occurs primarily around the (110) ledges (no diffusion or changes are seen in the {100} regions). At high coverages where changes are observed in the {100} regions diffusion into these regions occurs last.

Thermal Desorption

The activation energy for terminal thermal desorption of copper from tungsten for the coverage interval, 0.3 to 0×10^{14} atom/cm^2, was determined from an Arrhenius plot of the time required to go between two pulse current measurements corresponding to the coverages indicated as a function of temperature (Figure 29); the result was an activation energy of 3.07 ± 0.16 ev/atom for this coverage range and the pre-exponential factor of $\overline{16.0}$ (this corresponds to a frequency of approximately 10^{13} sec^{-1}). This result is below the heat of sublimation of copper. At the temperatures required for complete desorption of copper from tungsten, the tungsten atoms themselves are mobile; this may enter into the copper desorption process.

The general thermal desorption characteristics of copper on tungsten

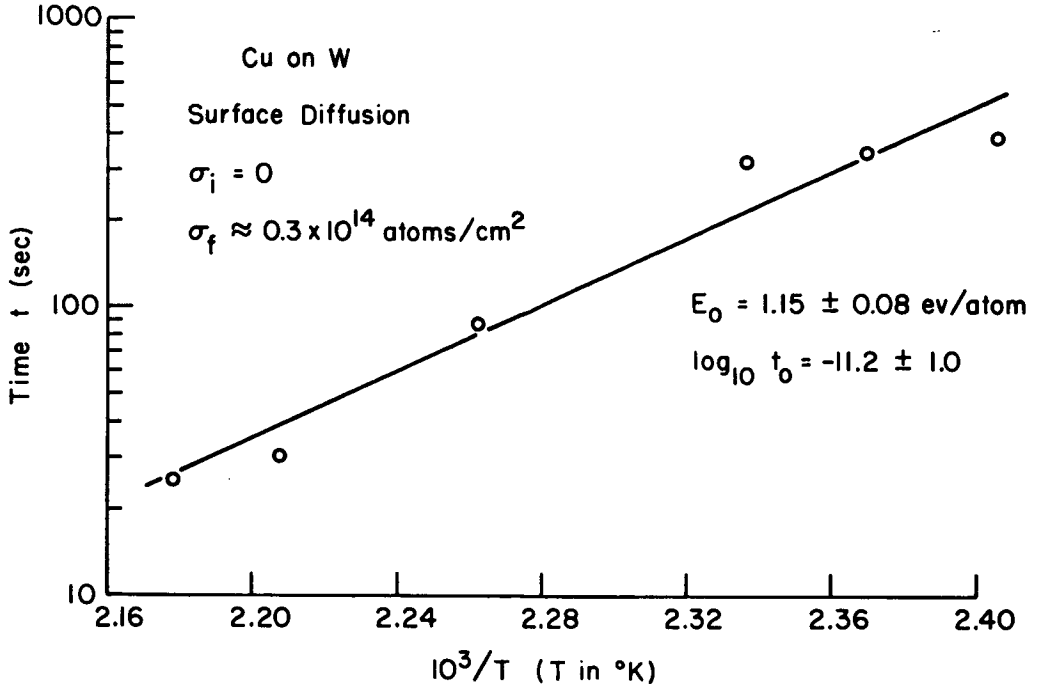

Figure 28. Arrhenius plot of copper on tungsten surface diffusion data for coverages between 0 and 0.3×10^{14} atoms/cm^2.

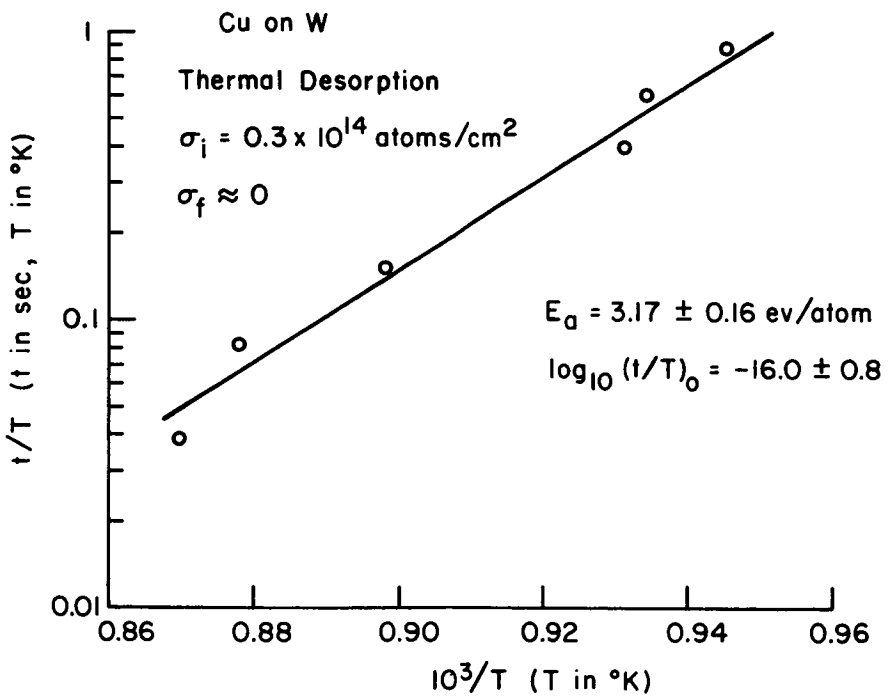

Figure 29. Arrhenius plot of copper on tungsten terminal thermal desorption data for coverages between 0.3×10^{14} atoms/cm^2 and 0.

were determined by dosing the tungsten emitter with a heavy coverage of copper and then heating the emitter for 60 sec periods to successively higher temperatures and determining the work function of the surface by a Fowler-Nordheim plot after each heating period. The results are shown in Figure 30. With the aid of the work function vs coverage curve of Figure 26 a relation between the desorption temperature and the copper coverage may be obtained; this is plotted in Figure 31. Since the desorption temperature is roughly proportional to the desorption activation energy, an approximate thermal desorption activation energy scale is plotted on the right hand side of Figure 31. It can be seen that the changes of activation energy with coverage are not nearly as great for copper as they are for cesium and mercury. The work function changes and field emission patterns obtained during the desorption process were the same as those obtained during adsorption, which indicates that the adsorption and desorption processes are essentially reversible.

Discussion

A rather complete study of copper on tungsten has just recently been published by J. P. Jones[2]; it is of interest to compare our data with his. The shape of the work function vs coverage curve and the magnitudes of the work function changes are in good agreement, but the coverage scale differs considerably. Jones considers the work function maximum to occur at one monolayer and the work function minimum to occur at three monolayers; Our data indicate that the monolayer condition is not approached until the work function becomes essentially independent of coverage. The latter seems more reasonable from the viewpoint that many adsorbates are known to exhibit work functions at the monolayer that approach the work function of the adsorbate in the bulk.

Jones designated the region of coverage up to the work function maximum as Region I, between the work function maximum and the work function minimum as Region II, and beyond the work function minimum as Region III. He obtained thermal desorption activation energies 4.13, 3.05, 2.76 ev/atom for Regions I, II and III respectively, as compared to the value of 3.17 ev/atom obtained here for terminal desorption. The reason for the disagreement is not known at this time, although somewhat different methods were used to obtain the activation energies. Jones measured the time required to change the voltage at a constant dc emission current by an amount that corresponded to a considerably larger coverage interval than was used here. Both experiments were done in the same temperature range and thus would be subject to the same possible errors resulting from the mobility of the tungsten atoms at that temperature.

In contrast the surface diffusion activation energies measured by Jones and here are in reasonable agreement although they were made over the same coverage interval. Jones obtained a value of 0.87 ev/atom in the Type II region of copper coverage.

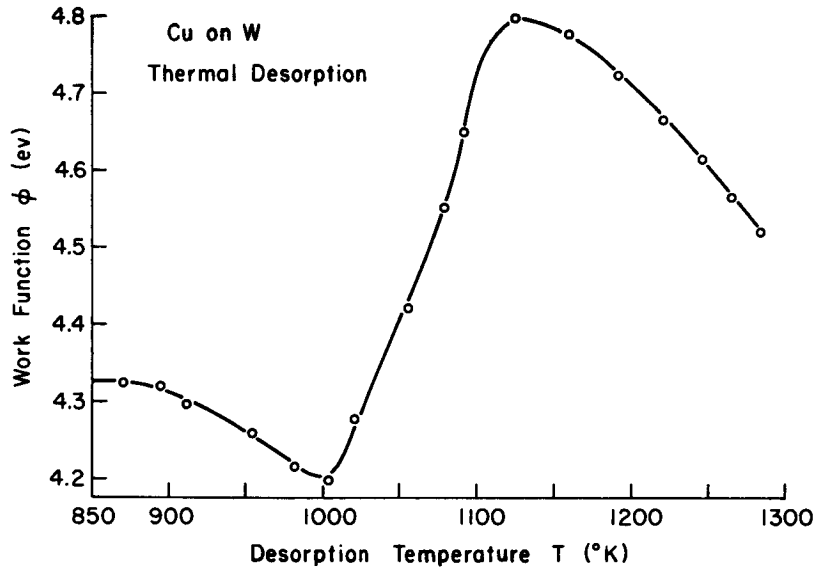

Figure 30. Work function of copper on tungsten as a function of desorption temperature to which the emitter had been heated for 60-second heating periods.

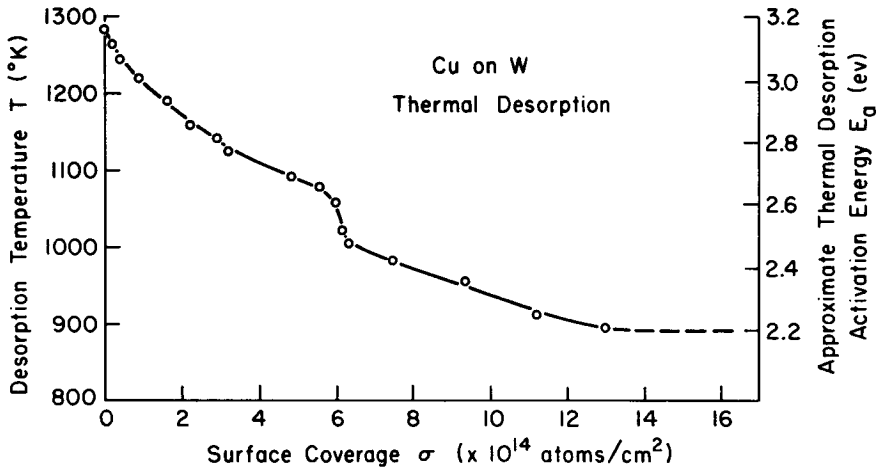

Figure 31. Thermal desorption temperature for successive 60-second heating periods as a function of copper-coverage for copper on tungsten. The scale on the right-hand side of the graph is obtained by assuming that the thermal desorption activation energy is proportional to desorption temperature.

CESIUM ON COPPER COVERED TUNGSTEN

Results

The thermal desorption of cesium on copper-covered tungsten has been studied as a function of underlying copper coverage. The resulting thermal desorption curves of changes in work function as a function of desorption temperature for 60-second heating periods were quite similar to the curves obtained for the case of cesium on clean tungsten. Pattern detail, however, showed considerable local changes as the copper coverage is increased, as is shown in the field emission patterns of Figure 32. In particular, at low cesium coverage, increasing copper coverage reverses the relative emission from the {100} planes as compared to the {110} and {211} planes (that is the {100} planes become more emitting while the {211} and {110} planes become less emitting). At higher cesium coverages, increasing copper coverage enhances emission of the {100} planes. In Figure 33 are plotted the values of the minimum and high coverage work functions of cesium at several underlying copper coverages on tungsten; also, terminal desorption temperatures for cesium is given with the copper work function as functions of the surface coverage of copper on tungsten. Throughout the range of copper coverage the temperature required to remove the cesium did not appear to alter the underlying copper. Although the changes in these quantities are small, the trends are significant. Both the minimum work function and the high coverage work function for cesium on copper-covered tungsten increase at high copper coverages. In all cases a positive voltage applied to the anode causes these measurements to refer to neutral cesium desorption. The terminal desorption temperature goes through a maximum at the copper coverage corresponding to a maximum in the copper work function vs coverage curve; this would be expected from consideration of an empirical relation derived earlier, which showed that the activation energy for thermal desorption increases with increasing substrate work function. These results suggest that a copper coverage 3×10^{14} atoms/cm^2 causes a minimum in the flux of neutral cesium atoms desorbing at any temperature from a tungsten substrate. Although, cesium ion desorption rates were not determined, it is likely that they will either be unaffected by the underlying copper or show a slight maximum.

Summary

In summary, copper exhibits a high degree of mobility above 500°K throughout the monolayer coverage range. Thermal desorption of copper from tungsten in vacuum is complete at 1300°K without any evidence of bulk alloying. These results suggest that contact ionization ion propulsion engines operating at, or above, 1300°K should not be greatly affected by a small vapor pressure of copper from accel electrodes. Also, since small amounts of copper increase the work function and, hence, the ionization efficiency of

σ_{Cu} (x 10^{14} atoms/cm^2) (a) (b)

0 - 1.5

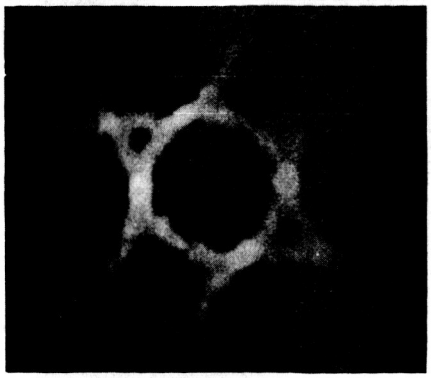

146°K, 1.82 ev

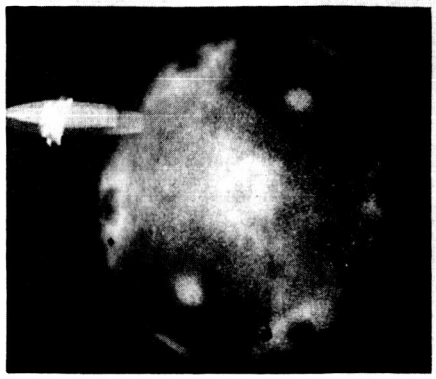

450°K, 1.49 ev

2.1

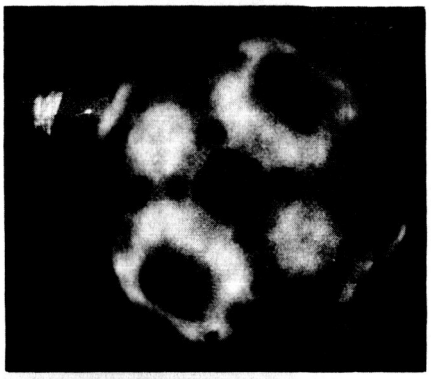

172°K, 1.82 ev

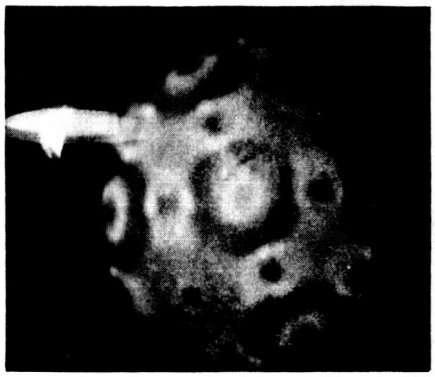

410°K, 1.48 ev

4.2

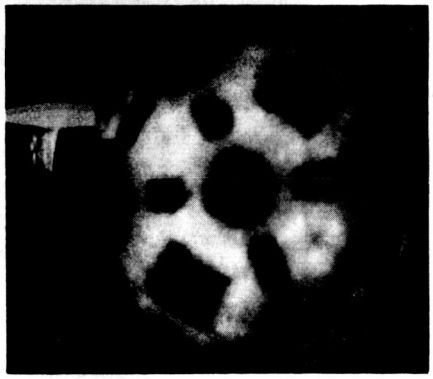

180°K, 1.91 ev

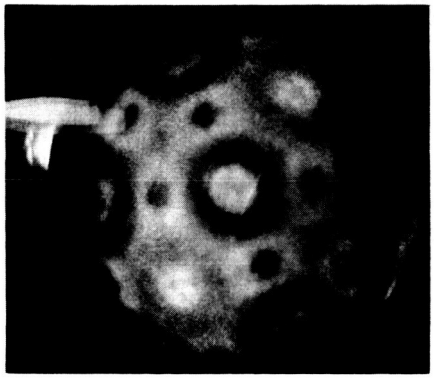

419°K, 1.52 ev

6.0

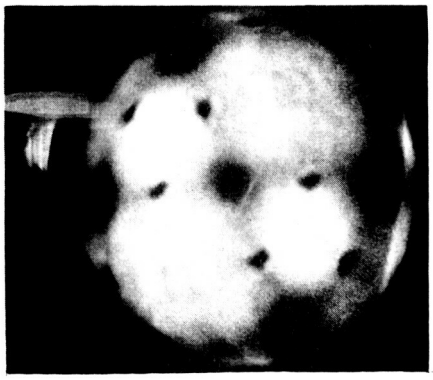

170°K, 1.95 ev

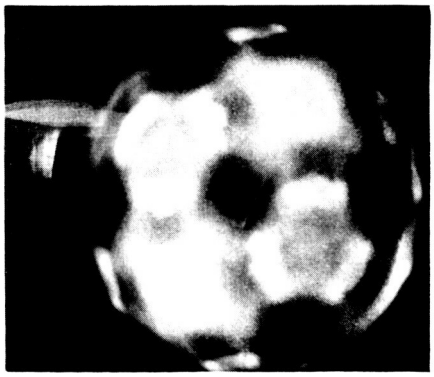

419°K, 1.57 ev

Figure 32. Field emission patterns of cesium on copper-covered tungsten for various copper coverages and desorption temperatures.

σ_{Cu} (x 10^{14} atoms/cm^2)	(c)	(d)
0 - 1.5	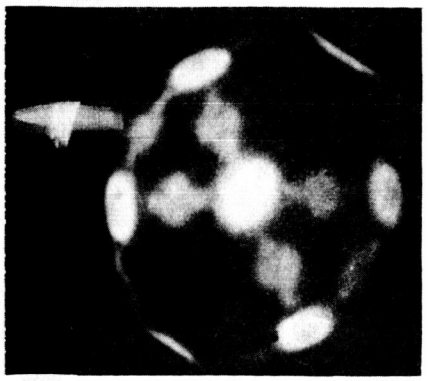	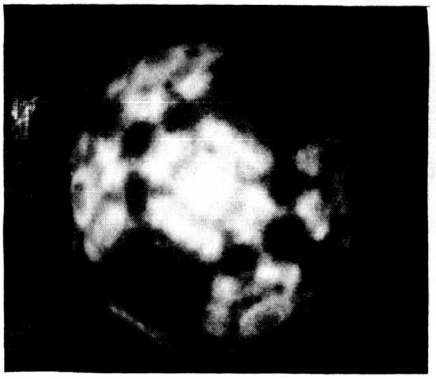
	493°K, 1.49 ev	698°K, 2.78 ev
2.1	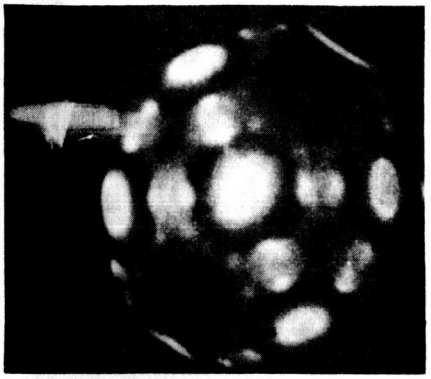	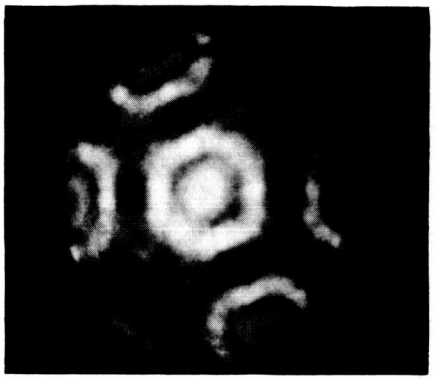
	465°K, 1.53 ev	691°K, 2.78 ev
4.2	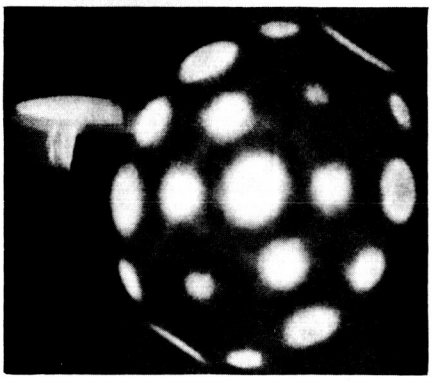	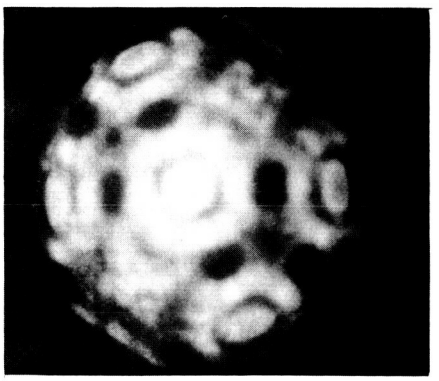
	476°K, 1.54 ev	690°K, 2.86 ev
6.0	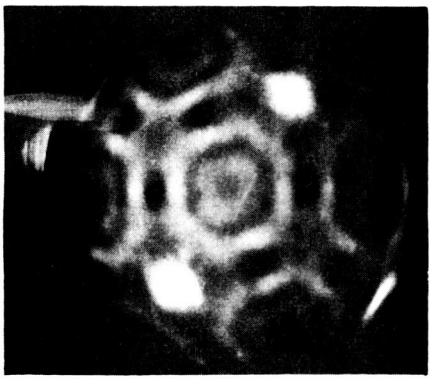	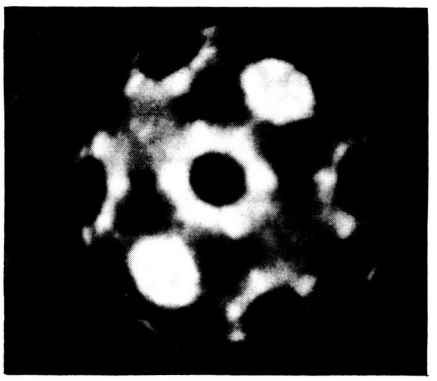
	476°K, 172 ev	686°K, 3.00 ev

Figure 32. (Continued)

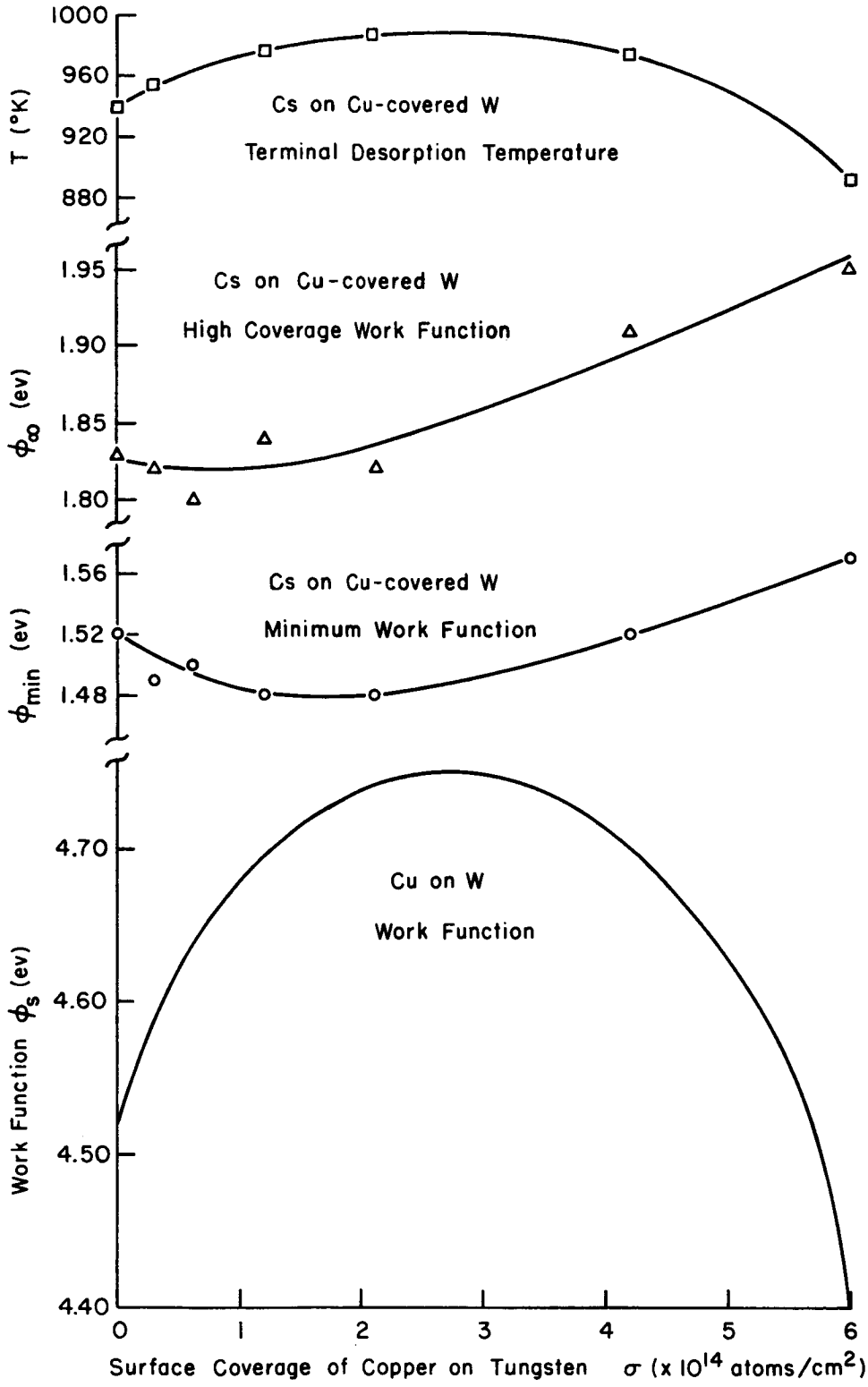

Figure 33. Terminal desorption temperature, heavy coverage cesium work function, and minimum cesium work function as functions of copper coverage. (For reference, the copper on tungsten work function is also graphed.)

the cesium-tungsten system, it follows that contact ionization engines operating at temperatures below 1300°K may not be adversely affected. The latter is certainly the case for underlying copper coverages on clean tungsten.

BERYLLIUM ON TUNGSTEN

An attempt was made to study the behavior of beryllium on tungsten, but due to the difficulty with the dosing arrangement mentioned earlier very little beryllium was ever deposited onto the tungsten tip. However, a small amount of beryllium was evaporated onto the tip and Figure 34 shows some of the pattern changes obtained by heating the emitter tip. Diffusion into the {111} and {211} regions occur at temperatures even below room temperature; in contrast diffusion into the {100} regions does not occur at temperatures below 400°K. At higher temperature most of the changes are noticed primarily in the {100} region. Nearly all of the beryllium is desorbed from the tip at 1250°K. The voltages given beneath each pattern in Figure 34 are the pulse voltages required to draw a constant pulsed field emission current and thus show the changes in field emission characteristic of the tip with beryllium desorption. Assuming that the changes in voltage are due to changes in work function and not in the pre-exponential term of the field emission equation, the surface work function has changed from 4.52 for clean tungsten to 4.65 for tungsten dosed with this small amount of beryllium. In contrast, a recent Russian article in which work function changes were measured by a retarding potential thermionic technique found no change in work function with adsorption of beryllium on tungsten up to several monolayers of beryllium.[30] It is planned to investigate this further in a tube with a re-designed beryllium source.

CHROMIUM ON TUNGSTEN

A preliminary study of chromium adsorption, migration and desorption on tungsten was carried out. The results obtained thus far are summarized in Figure 35 where patterns and work functions obtained from a thermal desorption sequence are given. Surface migration across the tungsten emitter is complete at approximately 380°K. The work function decreases slightly to a minimum of 3.83 ev at moderate coverages corresponding to a temperature of 450°K. Thermal desorption of chromium from tungsten occurs at higher temperatures and is completely removed at ~1200°K. No evidence of appreciable alloying with tungsten was observed.

It is interesting to note that chromium lowers the tungsten work function in contrast to copper which increases it. In many ways copper and chromium are similar - both being transition metals with similar atomic sizes. The major difference between the two adsorbates lies in their ionization potentials; for copper $V_I = 7.7$ ev, whereas for chromium $V_I = 6.7$ ev.[42] Apparently the 1 volt difference in ionization potential is sufficient to give copper a negative and chromium a positive dipole moment.

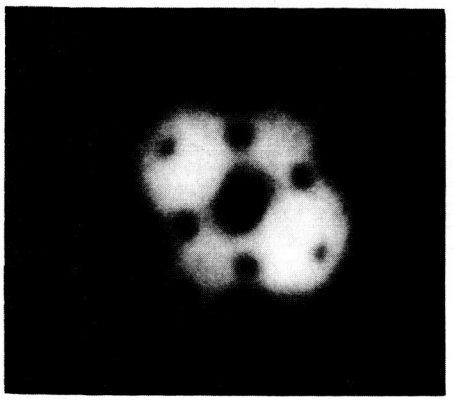

Clean W, V = 5.55 kv

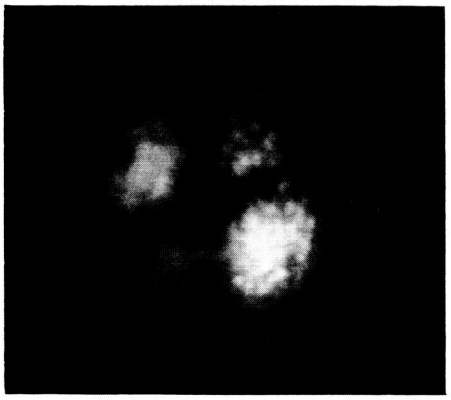

Small Be dose
T = 77°K, V = 5.93 kv

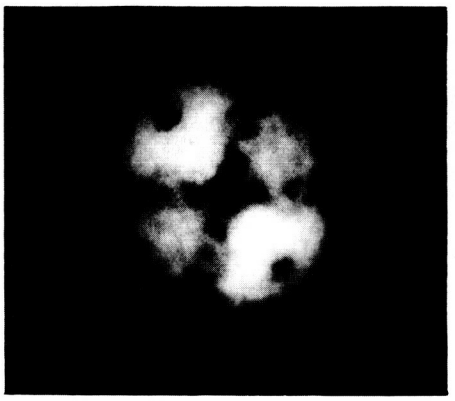

T = 291°K, V = 5.83 kv

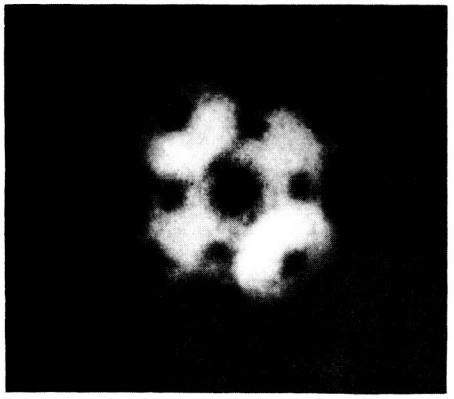

T = 419°K, V = 5.70 kv

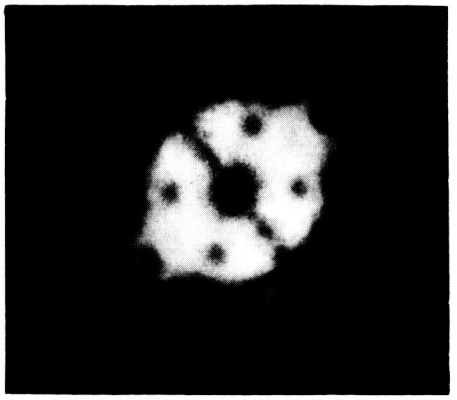

T = 850°K, V = 5.77 kv

Figure 34. Field emission patterns of a small amount of beryllium on tungsten for various emitter heating temperatures. Voltage required for obtaining pattern is given.

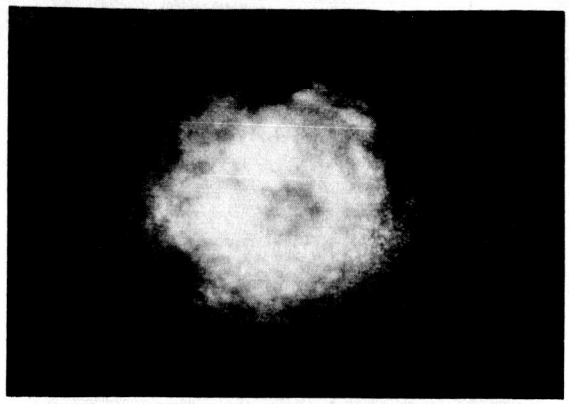

T = 388° K
Ø = 4.09 ev

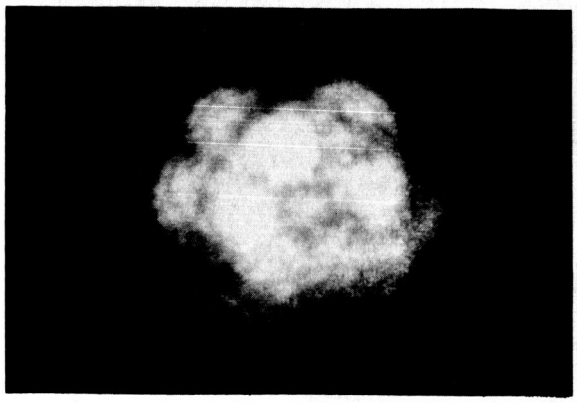

T = 455° K
Ø = 3.83 ev

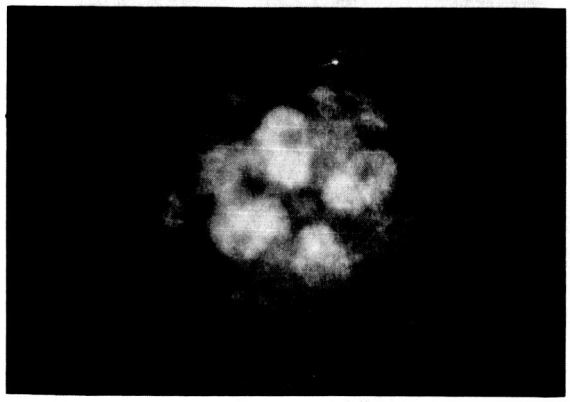

T = 733° K
Ø = 4.38 ev

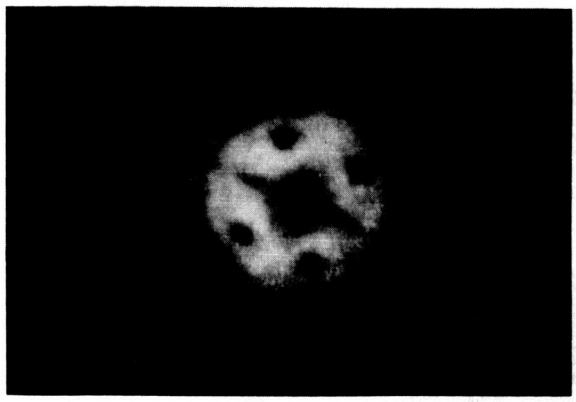

T = 942° K
Ø = 4.55 ev

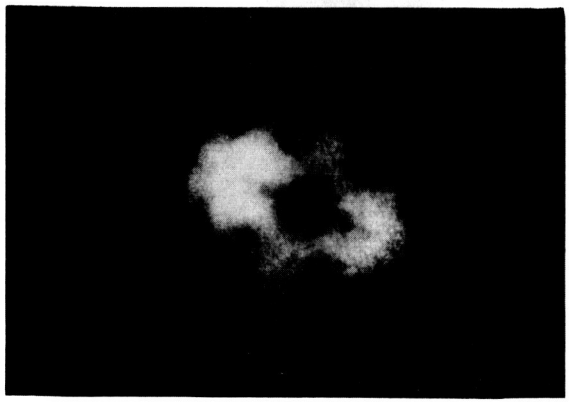

T = 1095° K
Ø = 4.51 ev

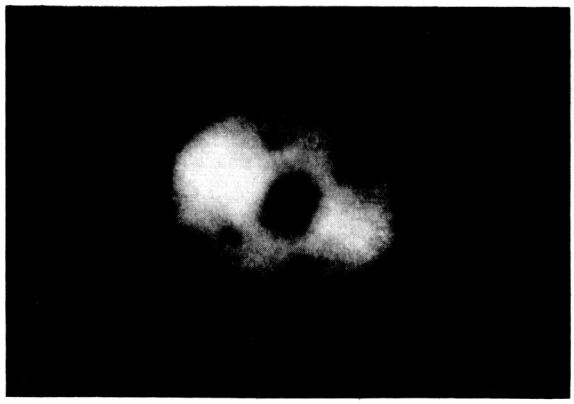

T = 1197° K
Ø = 4.54 ev

Figure 35. Field emission patterns for chromium on tungsten. The patterns were selected from a sequence obtained by heating the emitter to successively higher temperatures for 60 second heating periods.

STUDIES OF ELECTRONIC INTERACTIONS WITH ADSORBATES ON TUNGSTEN

Interest in the interaction of electrons with adsorbed layers is increasing at the present time due to such possible applications as electron-enhanced ion emission, production of clean surfaces by low energy electron bombardment, and others. So far, very few detailed studies in this area have been reported. Existing investigations of this nature have been performed primarily on electro-negative adsorbates[43-46]. For these systems electron-induced desorption is thought to be caused by electron excitation of the adsorbate into an ionic state, leading to desorption of the ad-atom as an ion (or as a neutral if electron interchange between the adsorbate and substrate is sufficiently rapid). Studies made thus far indicate that electron induced desorption of electro-positive adsorbates is not likely, because of very rapid transition of electrons between the ad-atoms and the Fermi sea of the substrate. One recent measurement of the system of barium on tungsten confirms this, since no measurable desorption was detected[46]. However, what happens when electrons bombard a system with both electro-negative and electro-positive adsorbates, such as cesium and oxygen on tungsten, is not clear and probably can be settled only by experiment.

EXPERIMENTAL PROCEDURES AND RESULTS

A tube for the study of electron interactions with cesium and/or oxygen adsorbed on tungsten has been designed. This tube, which is illustrated in Figure 36, is basically a probe tube arrangement which allows a work function change to be determined on a small portion of the emitter. In addition, a thermionic emitter in the Faraday collector can be used along with the suppressor electrode elements as a part of a lens system to focus electrons onto the emitter. In other words, the tube is designed so that the same set of electrodes are used, at different times, as the beam-forming electrodes for the bombardment beam and as Faraday collection electrodes for emission from a small portion of the emitter; this insures that the bombarding electrons hit nearly normal to the same plane from which the measured field emission current is obtained. The tube has side arms containing cesium and oxygen sources, so that the target can be dosed with either one or both adsorbates, and a phosphor screen so that the field emission pattern detail may be monitored.

The characteristics of the electron beam at the emitter have been determined over the wide range or accelerating voltages. This was performed by removing the tip assembly shown in Figure 36 and replacing the backup plate E with a Faraday collector arrangement consisting of a large plate with a small 15 mil diameter hole placed in the same position as the emitter and a Faraday cage and suppressor arrangement behind the hole to measure the transmitted current. Thus, knowing the total current I_t and

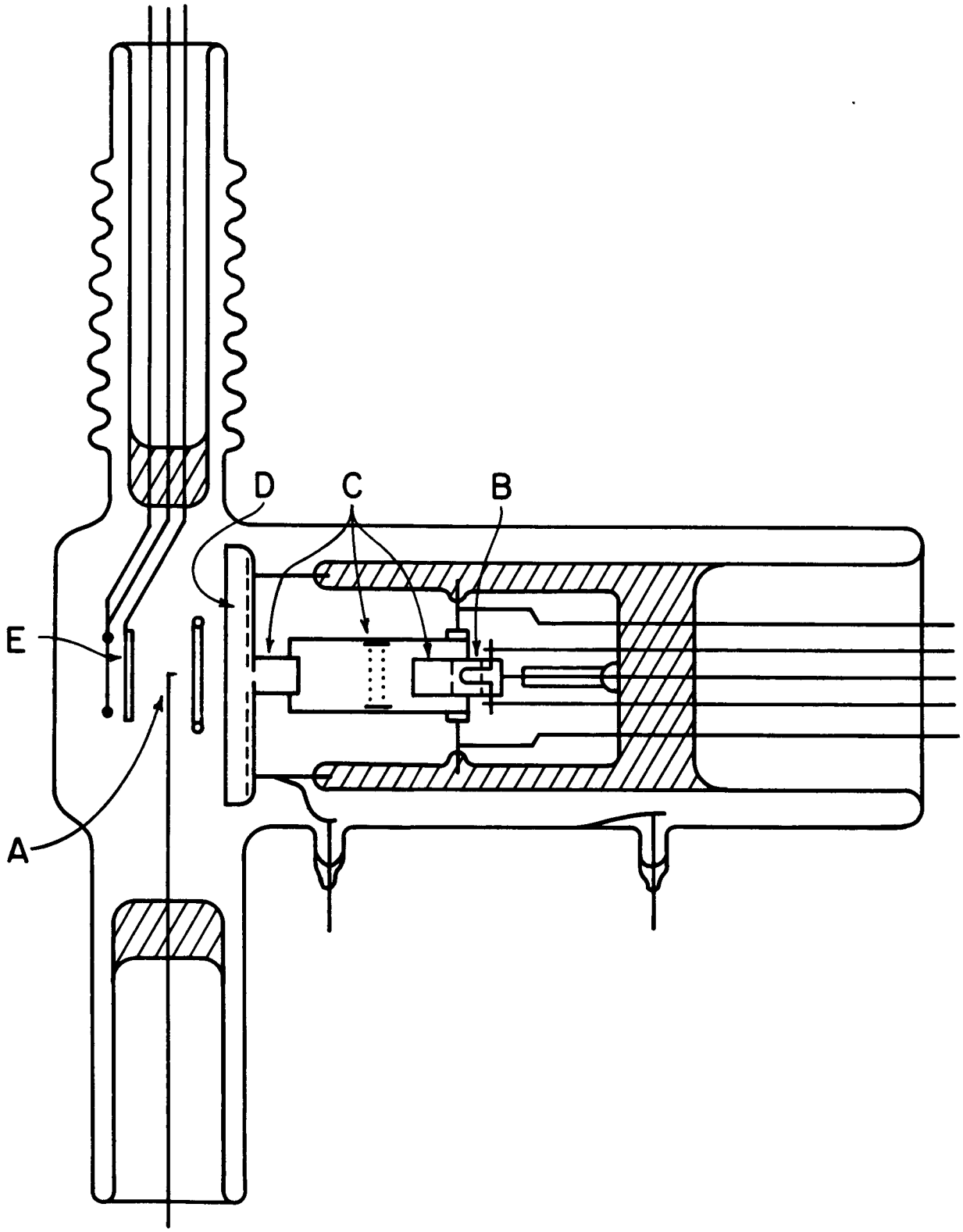

Figure 36. Electron desorption studies tube. A is a tungsten field emitter, B is a tungsten filament used as the electron source, C is a lens arrangement that can be used either to focus the electron beam or as a Faraday collector, D is a phosphor screen, and E is a collector.

the area of the hole, a measure of the current density at the same spatial position of the tip was obtained. Figure 37 shows a block diagram of the electronic circuit employed to measure the beam characteristics as a function of accelerating voltage V_1. The results of this calibration and the pertinent voltages on the electrodes are given in Table XI where the voltages are all measured relative to ground. The voltage V_1 is the total accelerating voltage, $V_2 - V_1$ represents the extraction voltage and V_3 is the lens voltage. For each accelerating voltage, V_2 and V_3 were adjusted to maximize the current density J_e at the collector. The voltage V_7 on the suppressor of the collector assembly shown in Figure 37 was operated between -40 and -20 volts to insure the return of all secondaries to the Faraday collector and the aperture plate. For each accelerating voltage the total current I_t was obtained from the sum of the current collected at all the elements including the conductive coating by operating these elements slightly positive in voltage relative to the final lens element in order to eliminate the return of secondaries to the lens element. As shown in Table XI, the current density J_e varies from approximately 30 to 7 ma/cm^2 over the accelerating voltage range of 500 to 23 volts. This should be ample current density for measuring electron-induced desorption of adsorbates with moderately low cross sections.

After the calibration run was completed the Faraday collector arrangement was replaced with a tip and backup plate as shown in Figure 36. The degree of accuracy needed in positioning the tip in the same spatial position as the probe hole of the collector can be seen from the results shown in Figure 38 which show the current distribution in the electron beam as a function of displacement from its center. The emitter could be placed within $\pm$ 5 mils of the original position of the aperture hole; this means that at high accelerating voltages there should be no error in the current density at the emitter as predetermined by the calibration run, whereas at low accelerating voltages the error is less than 10%.

Prior to dosing the tip with cesium, the gun was run for several minutes to establish the level of contamination of the tip due to operation of the gun alone. It was discovered that one of the lens elements aperturing the electron beam slowly liberated an electro-negative gas (presumed to be oxygen) which established a residual contamination rate of the emitter and hence, a minimum level of sensitivity for the detection of the electron-induced desorption of cesium. The contamination of the emitter by the electron-induced electro-negative gas is sufficiently slow that running the beam for 100 seconds caused no detectable work function change of the emitter. Thus it was assumed that any changes in work function of the cesium layer during electron bombardment in the space of 100 seconds should be due to electron-induced desorption of the cesium layer.

The procedure followed for this investigation was to dose the tip heavily and, after equilibration of the cesium dose, a work function measurement was obtained; this was followed by electron bombardment

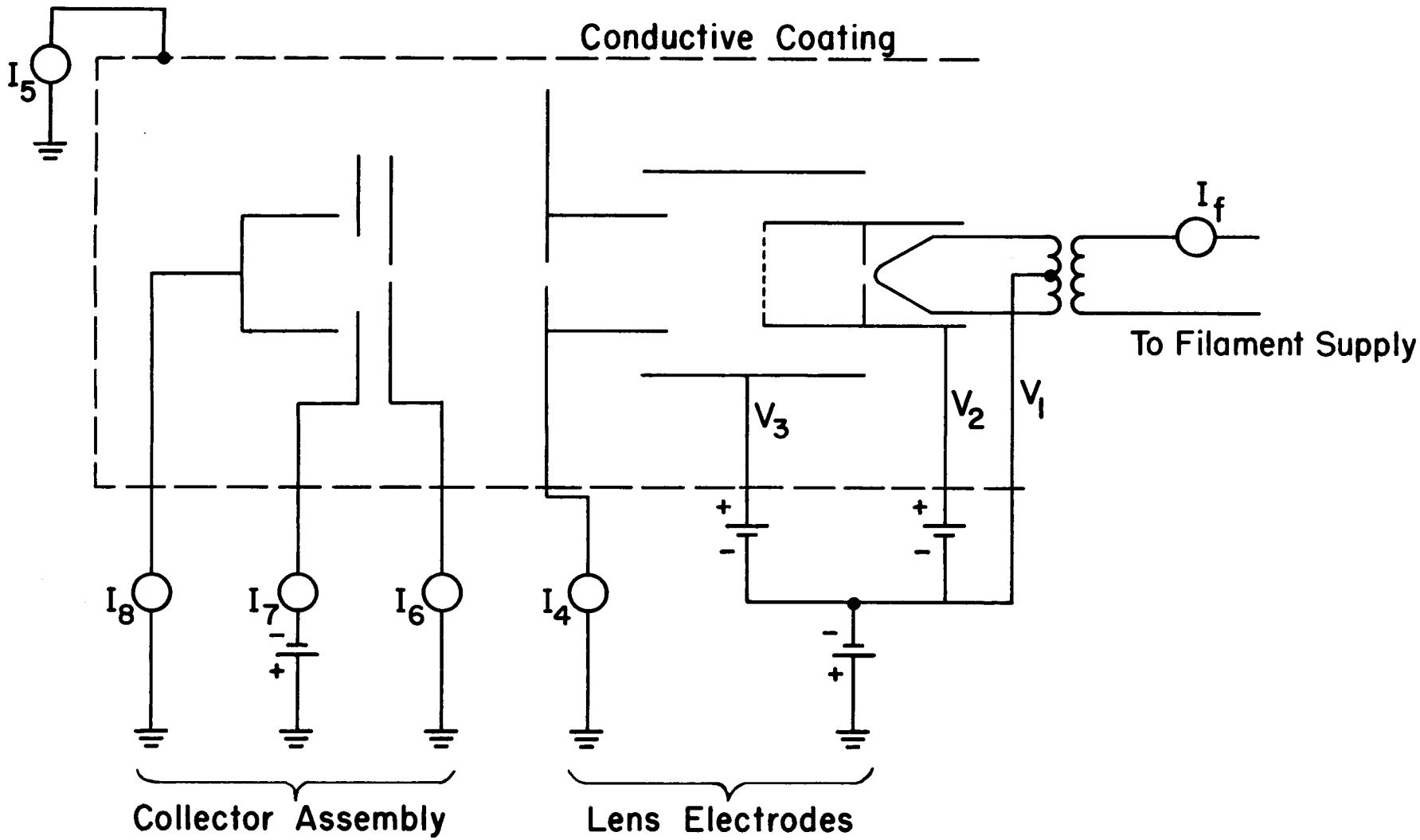

Figure 37. Block diagram of the circuitry employed for calibrating the beam characteristics of the electron desorption tube shown in Figure 36.

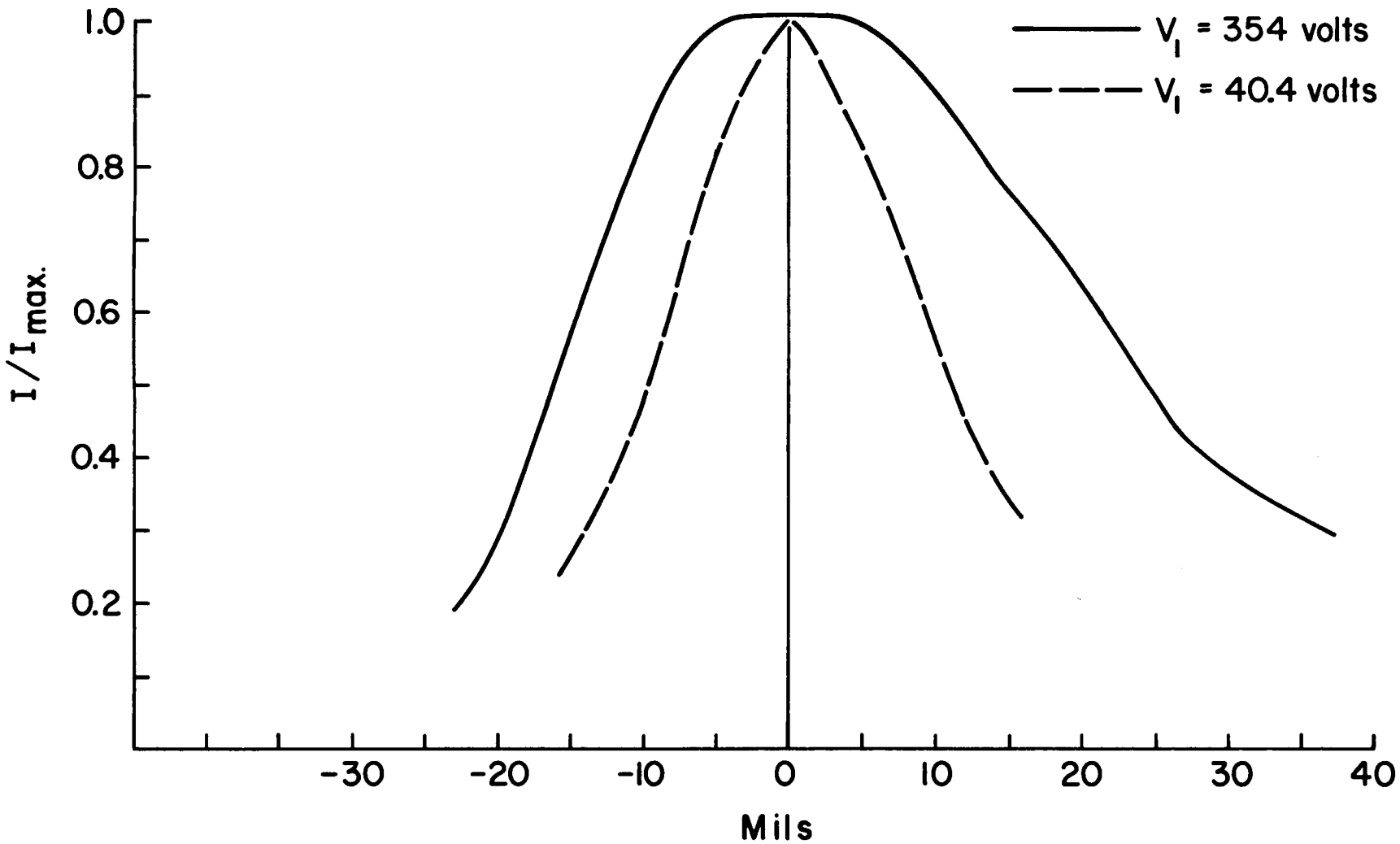

Figure 38. Results of the measured variation in the electron beam at the 15 mil aperture hole as the latter is moved on a line in either direction from its central position.

TABLE XI

Current-voltage relationships
for electron bombardment beam circuitry of Figure 37

V_1	V_2	V_3	$I_e(\mu a)$	$I_t(\mu a)$	$J_e(ma/cm^2)$
-497.0	-462.5	-377.3	3.20	35.13	30.81
-452.0	-418.3	-327.9	3.75	38.86	34.08
-401.7	-368.8	-281.3	3.55	33.09	29.02
-354.0	-323.2	-240.4	3.25	30.56	26.80
-294.0	-268.3	-198.2	2.78	27.40	24.03
-243.5	-219.2	-144.8	2.32	26.35	23.11
-199.2	-182.4	-137.2	2.66	15.30	13.40
-149.4	-127.1	- 53.4	2.77	18.30	16.05
- 98.9	- 76.1	+ 5.97	2.46	17.31	15.18
- 79.1	- 56.3	+ 27.05	2.05	16.44	14.42
- 59.5	- 35.66	+ 49.9	1.90	16.07	14.09
- 40.45	- 18.94	+ 62.45	1.03	15.87	13.92
- 29.54	- 7.70	+ 99.8	0.48	16.43	14.41
- 23.24	- 10.84	+ 46.01	0.10	8.73	7.66

for approximately 100 seconds and another work function measurement. The cesium layer was then thermally desorbed to a lower coverage and the operation repeated. At some of the lower coverages, the emitter temperature could be raised from 77°K to as high as 660°K during the electron bombardment to establish the presence of any temperature dependence of the yields of electron-induced desorption. The work function changes caused by the electron bombardment should be related to coverage changes from previously established relationships between work function and cesium coverage.

The results of this investigation are summarized in Table XII for a bombarding electron beam at 294 volts and a current density of 24.03×10^{-3} amps/cm^2.

TABLE XII

Summary of electron-induced desorption of Cs on W for 294-volt electrons at a current density of 24.0×10^{-3} amps/cm^2

Desorption Time (sec)	T(°K)	ϕ_i (ev)	ϕ_f(ev)	(atoms/cm^2 x 10^{-14}) σ_i	σ_f
106	77	1.77	1.78	1.41	1.41
100	77	1.82	1.82	1.35	1.35
100	416	2.08	2.10	1.15	1.13
100	77	2.10	2.13	1.13	1.11
100	77	3.66	3.65	0.25	0.25
100	663	3.72	3.74	0.23	0.22

DISCUSSION OF RESULTS

The results of Table XII show that throughout the coverage and temperature range, the interaction of 294-volt electrons with cesium layers for all intents and purposes is negligible. Maximum cross section for the electron-induced desorption of cesium from tungsten can be estimated from the following kinetic arguments. For a given cesium atom density σ, the following first order reaction for the rate of electron-induced desorption can be deduced

$$\frac{-d\sigma}{dt} = N_e b_c \sigma \tag{48}$$

where b_c is the desorption cross section in cm^2 and N_e the electron flux in electrons/cm^2/second. The above first order desorption equation can be integrated to yield the following expression for the cross section in cm^2:

$$b_c = \frac{3.68 \times 10^{-19}}{Jt} \log \frac{\sigma_i}{\sigma_f} \tag{49}$$

where J is the current density in amp/cm^2 and σ_i and σ_f are the coverage at times 0 and t, respectively.

From Equation (49) and Table XII it can be deduced that the cross section for electron-induced cesium desorption must be less than 6×10^{-22} cm^2. The somewhat larger change which occurred at 663°K is attributed to thermal desorption rather than electron-induced desorption. These results are in agreement with similar results obtained for barium on tungsten[46] and the general expectations of the existing theory of electron-induced desorption. In the case of metallic adsorption where $V_I - \emptyset$ is small, it has been postulated that binding involves almost wholly delocalized electrons[47]. In such systems, the barrier for tunneling to and from the adsorbate is highly transparent so that transition times are extremely short. In this case one would expect excited ionic or molecular states of the adsorbate bond formed by electron impact to be extremely short lived (less than vibrational frequencies) because of rapid electron exchange with the electrons within the Fermi sea. The results with cesium on tungsten seem to confirm this view since no desorption could be detected throughout the coverage and temperature range investigated.

It is not obvious from the existing knowledge what one might expect during electron bombardment in the case of cesium co-adsorbed with oxygen on tungsten. Experiments to investigate this system by the above described methods will be continued.

SPUTTERING OF TUNGSTEN BY CESIUM AND XENON IONS

Physical sputtering is an area of interest to workers in the field of space physics because it plays a role in such problems as the erosion of electrodes in electrical propulsion devices, erosion of rocket nozzles, ion bombardment of missiles and satellites in the space environment, and the state of the surface of the moon, as well as others. Although sputtering has been studied for over a hundred years, only recently have enough consistent and reliable data been collected to permit some insight into the mechanisms governing it. Despite recent theoretical and experimental progress in this field, many questions remain to be answered; field emission and field ion microscopy can shed light on some of these questions.

Most techniques used in studying sputtering examine in some fashion the sputtered particles emitted from the target and can therefore yield information concerning particle yield, angular distribution and energy. Field emission and field ion microscopy permit direct examination of the sputtered surface and thus may be expected to yield information on interactions between the bombarding ions and the target surfaces; consequently these techniques complement those in more general use.

In a previous report[1] are given a brief review of sputtering theories, references to previous applications of field ion microscopy to this area, and a report of an FIM investigation of gross damage in tungsten due to a large number of energetic xenon ions and/or neutrals. In this section are described an FIM investigation in atomic detail of the surface damage and interior damage in tungsten caused by bombardment of a few xenon ions, and an FEM investigation of the surface damage and changes in cesium coating due to cesium ion sputtering of cesium-coated tungsten.

FIELD ION MICROSCOPE STUDY OF XENON ION SPUTTERING OF TUNGSTEN

Xenon ion sputtering of clean tungsten has been investigated as a function of ion energy for three different energies, 100 volts, 500 volts, and 1300 volts. It seems pertinent to review the experimental tube design and procedure followed in this study before giving the results.

Experimental Tube and Procedure

The field ion microscope (FIM) used in this study was standard[48] except for the addition of a Xe ion gun and a Faraday cage ion collector assembly for measuring ion current density (Figure 39). The FIM was liquid N_2 cooled; thus the W anode tip used as the sputtering target was maintained

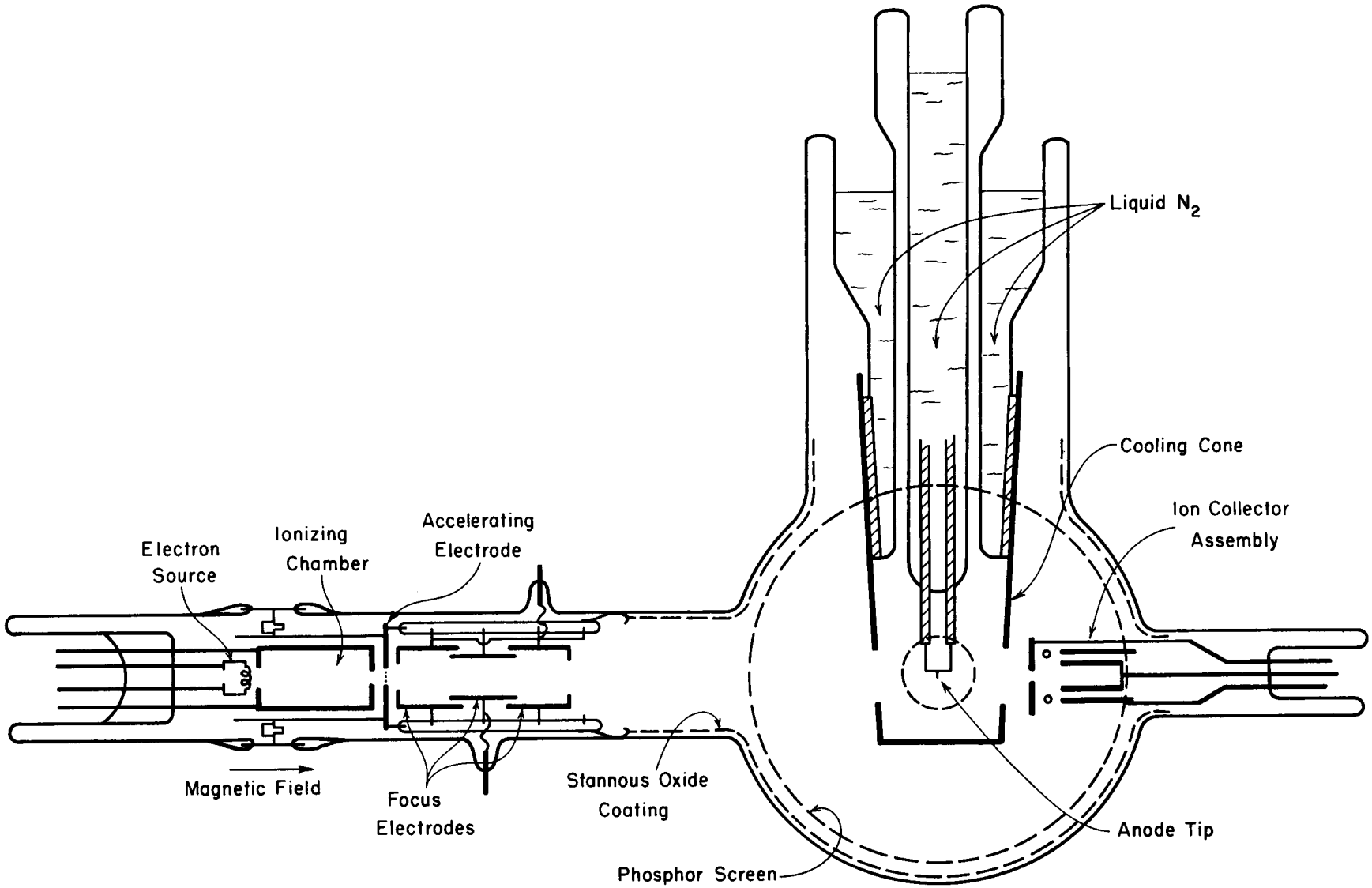

Figure 39. Schematic diagram of field ion microscope used for xenon ion sputtering of tungsten.

at a temperature of 77°K in this study. In the ion gun Xe gas was admitted to the ionizing chamber where it was ionized by electrons constrained axially by a magnetic field. The 14.0 v accelerating potential supplied to the electrons permitted ionization of Xe, but not of most other gases (e.g., N_2, CO, H_2, etc.) likely to be found in the system.

The tube was mounted on a liquid N_2 trapped, mercury diffusion, bakeable vacuum system capable of obtaining a pressure of 2×10^{-10} torr. The normal background pressure for the experiments described below was about 5×10^{-9} torr. Extremely pure He was admitted to the system through heated Vycor tubing; a He pressure of about 4×10^{-3} torr was used to obtain field ion patterns of the W tip. Xe was obtained from a flask of spectroscopically pure Xe gas (less than 100 ppm impurities) and admitted into the experimental tube through a liquid N_2 cooled, Ti gettered trap to remove active gases. The Xe pressure in the tube during ion gun operation was 6×10^{-5} torr, well below the pressure at which charge exchange effects became noticeable (about 3×10^{-4} torr for this tube geometry). The experimental tube was separated from the diffusion pump of the system by a ground glass valve, which permitted raising the He or Xe pressure in the tube to the necessary levels, and yet allowed rapid removal of the gas when desired.

The experimental procedure for this study was the following: (1) The tube was filled with He, the tip surface was cleaned by field evaporation at a field of approximately 500 Mv/cm, and a photograph was taken of the resulting field ion pattern of the clean W surface at a viewing field of about 450 Mv/cm (Figure 40 (a)). (2) The He was pumped out and Xe was admitted with the viewing field still being applied to the tip; this prevented any contaminating atoms from reaching the tip during this step. (3) When the ion gun was ready to operate, the field was reduced to zero and the tip was bombarded with Xe ions. During this step the region around the tip was field-free; thus the bombarding ions hit the tip on only one side and the ion current density could be determined accurately. Also this was the only step during which impurity atoms could reach the anode surface. (4) After raising the field to 450 Mv/cm, the Xe was pumped out and He admitted in order to photograph the field ion pattern of the sputtered surface.

Results

Figure 40 (a) is a typical field ion pattern of clean W; Figure 40 (b) identifies the major crystal planes and a few of the minor ones. The many rows of small net planes extending inward toward the central (110) plane indicate that the anode tip was formed of a highly pure and nearly perfect single crystal of W. There are a few edge vacancies and crystal imperfections visible in the pattern; this amount of disorder is very small compared to that created by the sputtering of a few hundred ions. The bright spots around the edge of the pattern result from the method of cleaning used, and are not significant.

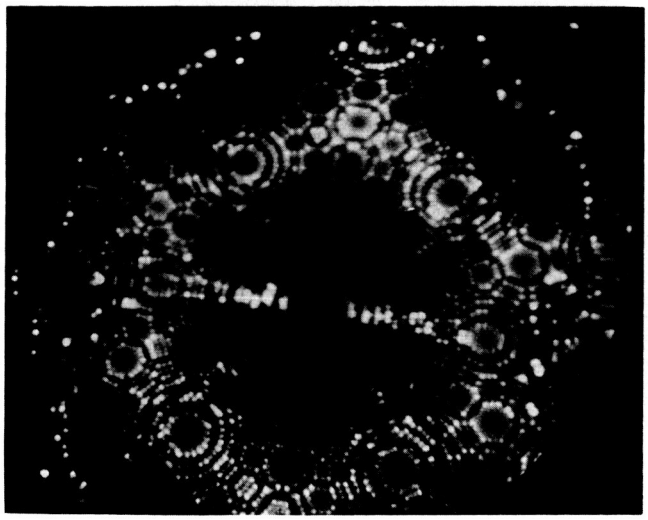

(a)

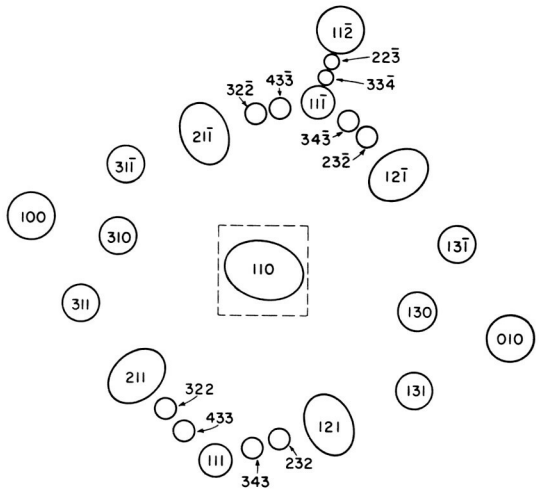

(b)

Figure 40. (a) Typical field ion pattern of a clean and nearly perfect tungsten surface.
(b) Principal planes of a (110)-oriented bcc crystal corresponding to (a).

Figure 41 (a) shows the surface in Figure 40 (a) after being sputtered by 1200 ions of 500 ev energy (the ion beam is incident on the left side of the tip). By direct comparison of Figure 41 (a) with Figure 40 (a), a wealth of sputtering detail may be discovered; for example, the (433) plane near the lower edge of the pattern contains 10 atoms in its top atom layer in Figure 40 (a), but in Figure 41 (a) only 5 atoms remain. Just below the (433) plane a two-atom chain is missing, and the small net plane to the lower left of the (433) has two new vacancies. (The location of new, displaced and missing atoms in two successive ion patterns is greatly facilitated by Müller's color comparison technique[49], which was used extensively in the present analysis.) In general it can be seen that very little sputtering occurs on the uppermost atom layers of the major planes (the {110}'s, the {100}'s and the {211}'s), and that most of the sputtering damage is visible in regions lying between two major planes. Surprisingly, slightly more atoms are missing or displaced on the side away from the ion beam than on the side upon which it is incident.

Not all of the changes between Figures 40 (a) and 41 (a) are due to sputtering; a few are the results of impurity atoms. Figure 41 (b) was taken under the same conditions that Figure 40 (a) was taken except that no ions were allowed to hit the tip; thus the changes in Figure 41 (b) are due to impurity atoms only. The color comparison technique reveals that impurities not only add a few atoms to the surface which remain at the best viewing field, but also remove some tungsten atoms, primarily from the edges of net planes, as the field is raised up to the best viewing field[50]. These effects were in general a small fraction of those due to sputtering, and were randomly distributed over the pattern.

Figure 41 (c) was taken after bombardment of the anode tip by 200 ions with 100 ev energy. Although not too clear in Figure 41 (c) (but made clear by the color comparison technique) most of the changed atoms on the beam-incident side are added atoms, while most of the displaced and missing atoms are on the opposite side. For the 1300-ev ions (Figure 41 (d)) far more damage is done on the beam-incident side than on the opposite side, and there is very little dependence of damage upon crystallographic direction. These results may be explained qualitatively on the basis of a computer study by Gibson, et al.[51], of radiation damage in Cu. This study shows, among other things, that (1) energy can be transmitted long distances along close-packed atom chains (as first suggested by Silsbee[52]), and (2) above a certain energy (for Cu, Gibson[51] calculates 30 ev, Thompson[53] calculates 60 ev) the atom chains begin to defocus the transmitted energy and become increasingly inefficient at transmitting energy as the input energy is raised. Since in a bcc crystal like W there are two {111} atom chains lying in the (110) plane, every point on the opposite side of a <110>-oriented tip (which can be regarded as a stacking of {110} planes parallel to the ion beam axis) is connected to the beam-incident side by a close-packed atom chain. Thus at low energy (100 ev) a large fraction of the energy is transmitted through the

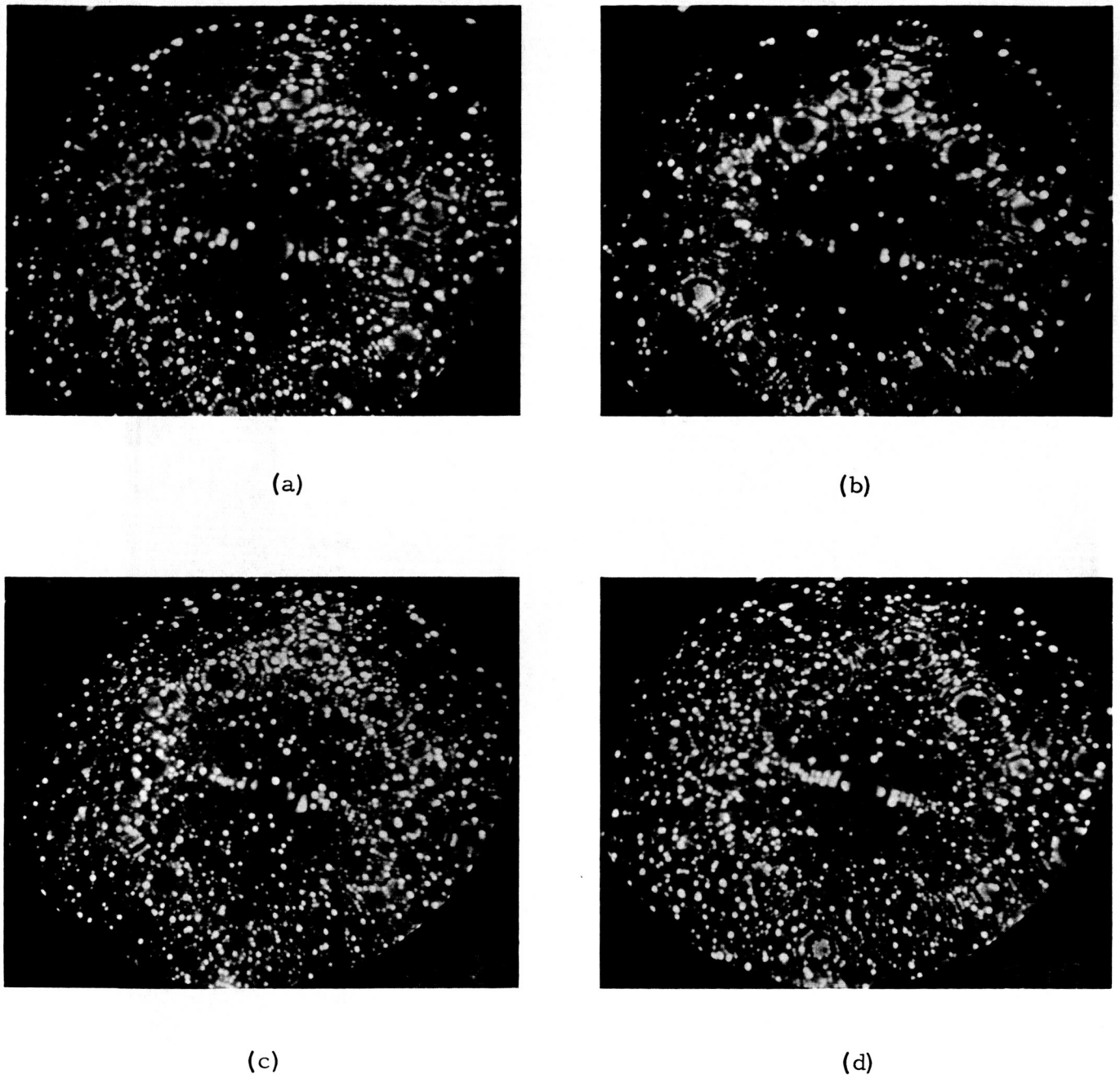

Figure 41. Field ion patterns of xenon ion sputtering of clean tungsten: (a) $N \approx 1200$ ions, $E_p = 500$ v; (b) Impurity pattern corresponding to (c); (c) $N \approx 200$ ions, $E_p = 100$ v; (d) $N \approx 1500$ ions, $E_p = 1300$ v. Ion beam is incident upon left side.

crystal and causes atom ejection or displacement on the opposite side, whereas at high energy (1300 ev) energy transmission becomes inefficient and sputtering occurs primarily on the beam-incident side.

The number of displaced and missing atoms in different regions of the sputtered patterns were determined by counting all such atoms in an area whose size is indicated by the dashed square in Figure 40 (b) and which was centered on a particular plane. (Missing and displaced atoms in the same region of the corresponding impurity pattern were subtracted.) The results are given in Table XIII and in general confirm the conclusions reached above. In addition the atom counts provide a rough estimate of the sputtering yield for each ion energy; these are also given in Table XIII. When these yields are compared with yields obtained by another method[48], it can be seen[54] that the 1300 ev yield is reasonable, the 500 ev yield is too low for reasons unknown, and the 100 ev yield is too high by an order of magnitude.

TABLE XIII

Atom count summary

Region	Bombardment Angle	Displaced and Missing Atoms at 100 ev	500 ev	1300 ev
110	90°	0	0	0
111	90	5	4	3
100	45	8	0	a
310	63	9	16	a
311	65	10	20	a
211	73	0	6	38
322-433	82	3	12	35
010	135[b]	5	1	1
130	117	13	8	11
$13\bar{1}$	115	21	19	3
$12\bar{1}$	107	14	12	18
$23\bar{2}$-$34\bar{3}$	98	15	24	15
Sputtering Yield (atom/ion)		0.7	0.25	>1

Notes: a Damage too great to permit atom counting in this region

b Angles greater than 90° indicate the region is on the side opposite to which ion beam is incident

The high yield obtained for 100 ev ions is attributed to the small size of the target: the distance between the (211) and (121) planes is approximately 300 atom diameters, a distance over which energy can readily be transmitted through the target and produce observable displacements on the far side, whereas the thickness of targets normally used for sputtering is sufficiently large that no energy is transmitted through to the back side.

The depth of sputtering damage has been examined by removing through field evaporation successive atom layers from the surface of the target; Figure 42 is a series of ion patterns taken while field evaporating atom layers from the tip sputtered by 1300-ev ions (Figure 41 (d)). It shows that the damage is primarily on the beam-incident side, and persists to a depth of approximately 6 (110) atom layers. In contrast, almost all of the damage due to 100-ev ions is removed by the field evaporation of one atom layer. An interesting feature of Figures 42 (b) and 42 (c) are the bright spots appearing at random over the central portions of the ion patterns; these bright spots are attributed to impurity atoms lying just below the surface[48]. In this case the impurity atoms are very likely to be Xe atoms; Kornelsen, et al.,[55], have shown that 1% of 1300-ev Xe ions can penetrate a depth greater than 8 atom diameters in W.

FIELD EMISSION INVESTIGATION OF CESIUM ION SPUTTERING OF CLEAN AND CESIUM-COATED TUNGSTEN

The basic approach to investigating sputtering by means of field emission microscopy is to use the emitter tip as the target for the bombarding ions. Sputtering of a clean tip surface is detected by changes in surface roughness which are visible in the field emission pattern of the tip and which are also discernable as changes in β, where β, the ratio of the electric field at the tip surface to the applied voltage, is a function of electrode geometry only, and depends mainly on emitter shape. Sputtering of a surface covered with an adsorbate such as cesium may be detected as a change in adsorbate coverage as shown by the field emission pattern and by the change in work function of the surface. These effects of sputtering may be measured as functions of target temperature, ion beam energy and density, and adsorbate coverage; more qualitatively the effects of ion beam angle of incidence and target crystallographic orientation can be investigated.

FEM Sputtering Tube Design

An easily constructed tube design was adopted first in order to determine the feasibility of using field emission techniques to investigate sputtering. The tube (Figure 43) consists of a standard FEM envelope incorporating two cesium vaporizer arrangements and a heatable tungsten filament for use as the cesium ionizer. Some of the cesium evaporated from the upper vaporizer hits the heated ionizer, becomes ionized, and bombards the emitter tip. The

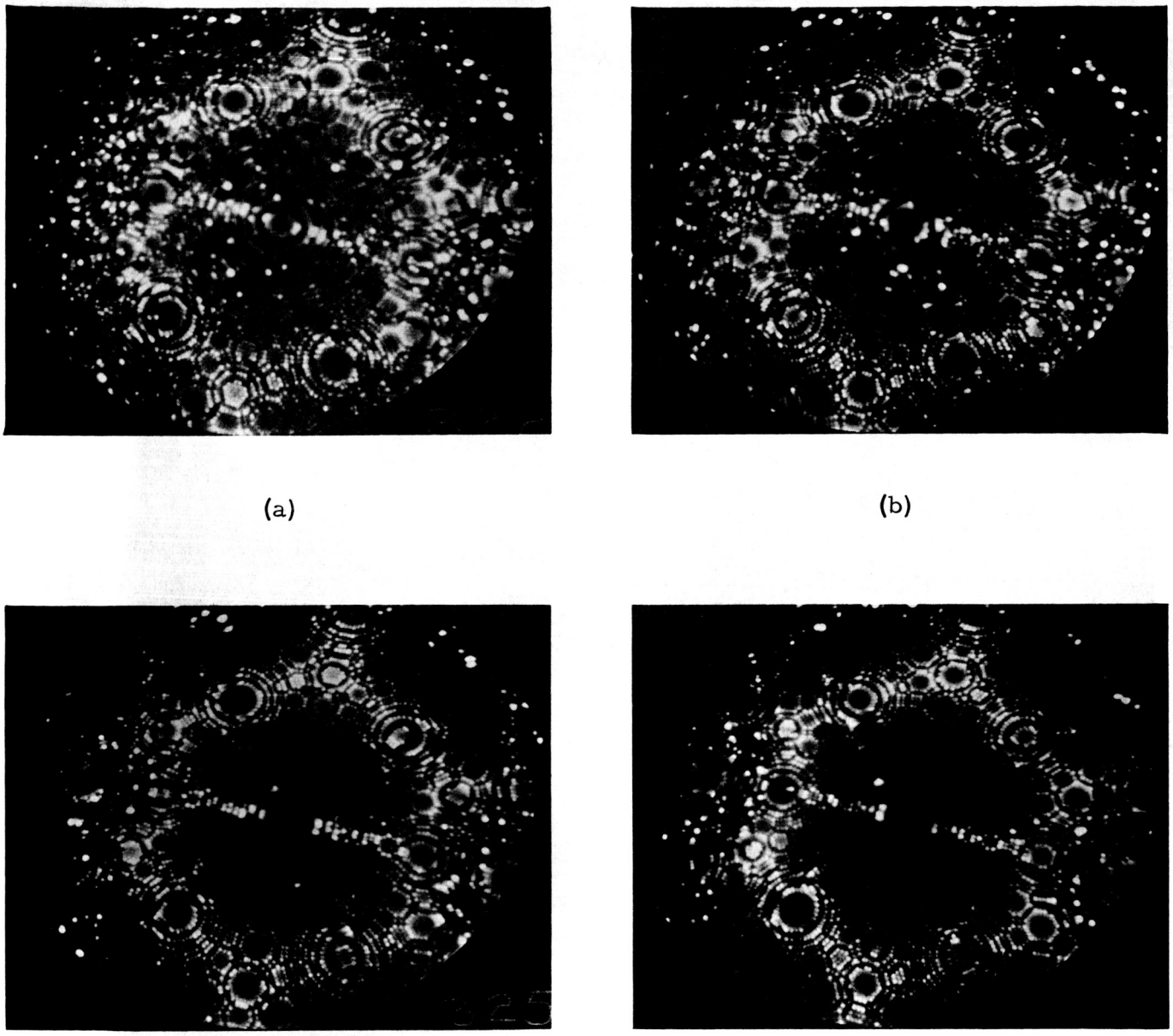

Figure 42. Field ion patterns illustrating the depth of damage due to 1300 v sputtering as revealed by the total number of (110) layers removed by field desorption: (a) one, (b) two, (c) four, (d) six.

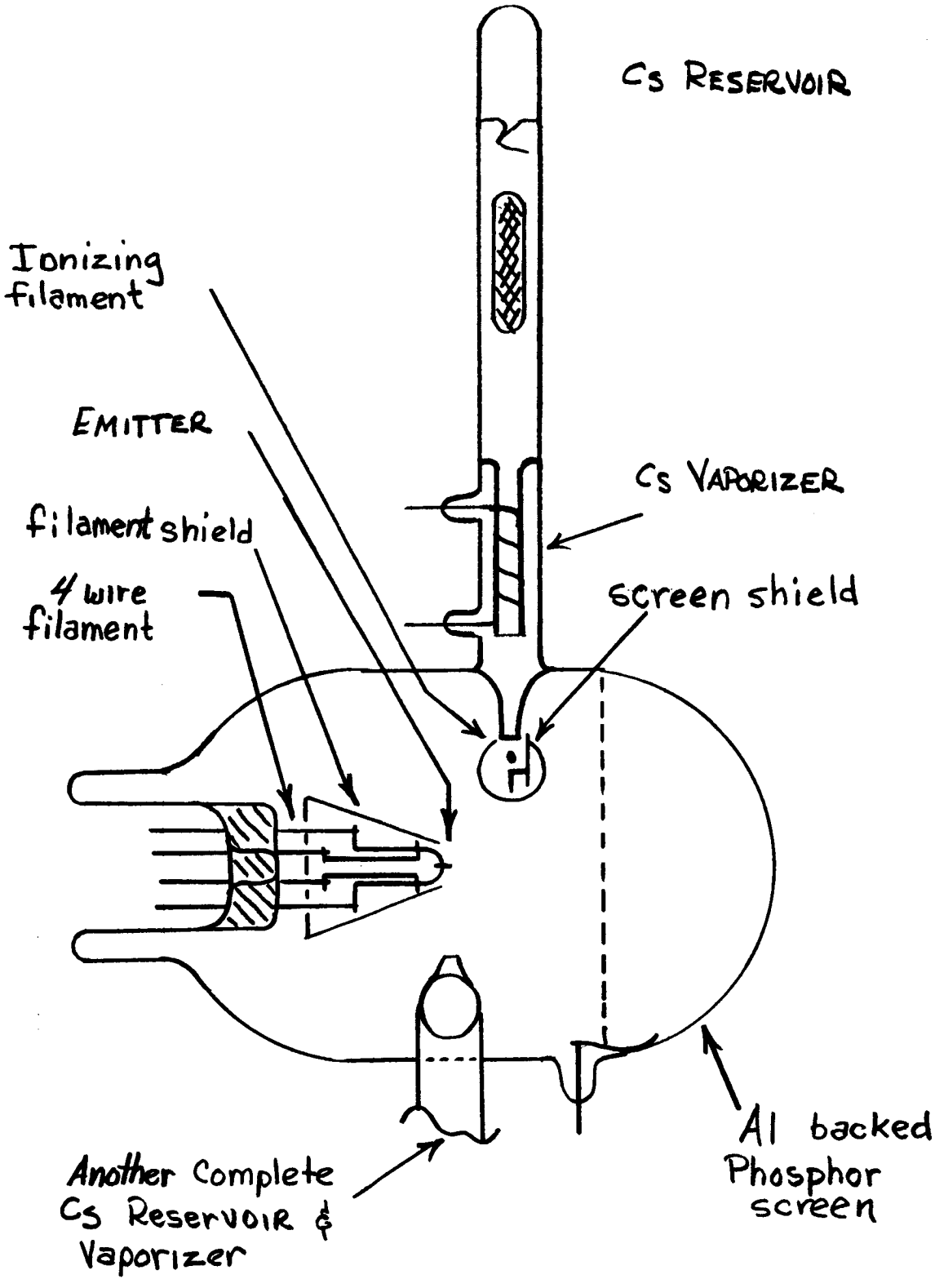

Figure 43. Schematic diagram of field emission microscope tube for the study of cesium-ion sputtering of cesium-covered tungsten.

lower vaporizer permits independent dosing of the emitter. A shield surrounds the emitter assembly, to reduce the number of ions hitting regions other than the tip.

During operation of the tube, the ion energies are determined by the difference in potential between the ionizer filament and the emitter assembly. The total number of ions hitting the emitter assembly is measured by the total charge Q collected by it. The number of ions hitting the emitting area of the tip cannot be determined accurately since the ion paths are not well-known in this particular tube. However, voltage ratios within the tube are kept constant whenever the ion accelerating voltage is changed, so that the ion paths remain the same. Thus the number of ions hitting the emitting area is always proportional to Q, and relative measurements can be made.

Sputtering of Clean Tungsten as a Function of Ion Energy

One question of interest is how much damage is done to a tungsten crystal by low energy cesium ions. It can be partially answered by measuring the increase in surface roughness as a function of ion energy; for this purpose the following technique was used: (1) The emitter was first cleaned and smoothed by flashing it to approximately 2400°K (the resulting field emission pattern is shown in Figure 44 (a), and β for the resulting surface was obtained from a Fowler-Nordheim plot; (2) The emitter assembly was bombarded by cesium ions of known energy and amount (resulting in a pattern of which Figure 44 (b) is typical); (3) Cesium adsorbed on the emitter during bombardment was removed by field desorption at 77°K (Figure 44 (c) was taken after a part of the cesium was removed, and Figure 44 (d) was taken after desorption was complete); (4) The amount of surface roughness due to sputtering was then determined from the change in β for the emitter, as obtained from a Fowler-Nordheim plot.

As Figure 44 (d) illustrates, surface damage due to sputtering can clearly be seen in the corresponding field emission pattern. No strong directional or crystallographic effects were noted in the present work, probably because the bombarding ion beam was not uni-directional. Although the amount of damage actually done to the surface in these experiments was quite striking in the field emission patterns, it was actually small and could be removed at rather low temperatures for tungsten. A typical case is indicated in Figure 45, a change in β of $\Delta\beta \approx 590\ cm^{-1}$ was produced by an amount $Q \approx 6.76\ \mu coul$ of 1073 ev ions striking the tip assembly. Heating the tip to a temperature of $T = 773°K$ reduced $\Delta\beta$ to zero and completely removed the roughening caused by ion bombardment.

The dependence of surface damage upon ion energy for cesium ion bombardment of clean tungsten is shown in Figure 46, which is a plot of $\Delta\beta/Q$ (i.e., the change in β normalized with respect to Q) as a function of ion energy. Figure 46 shows an increase in surface roughness with increasing

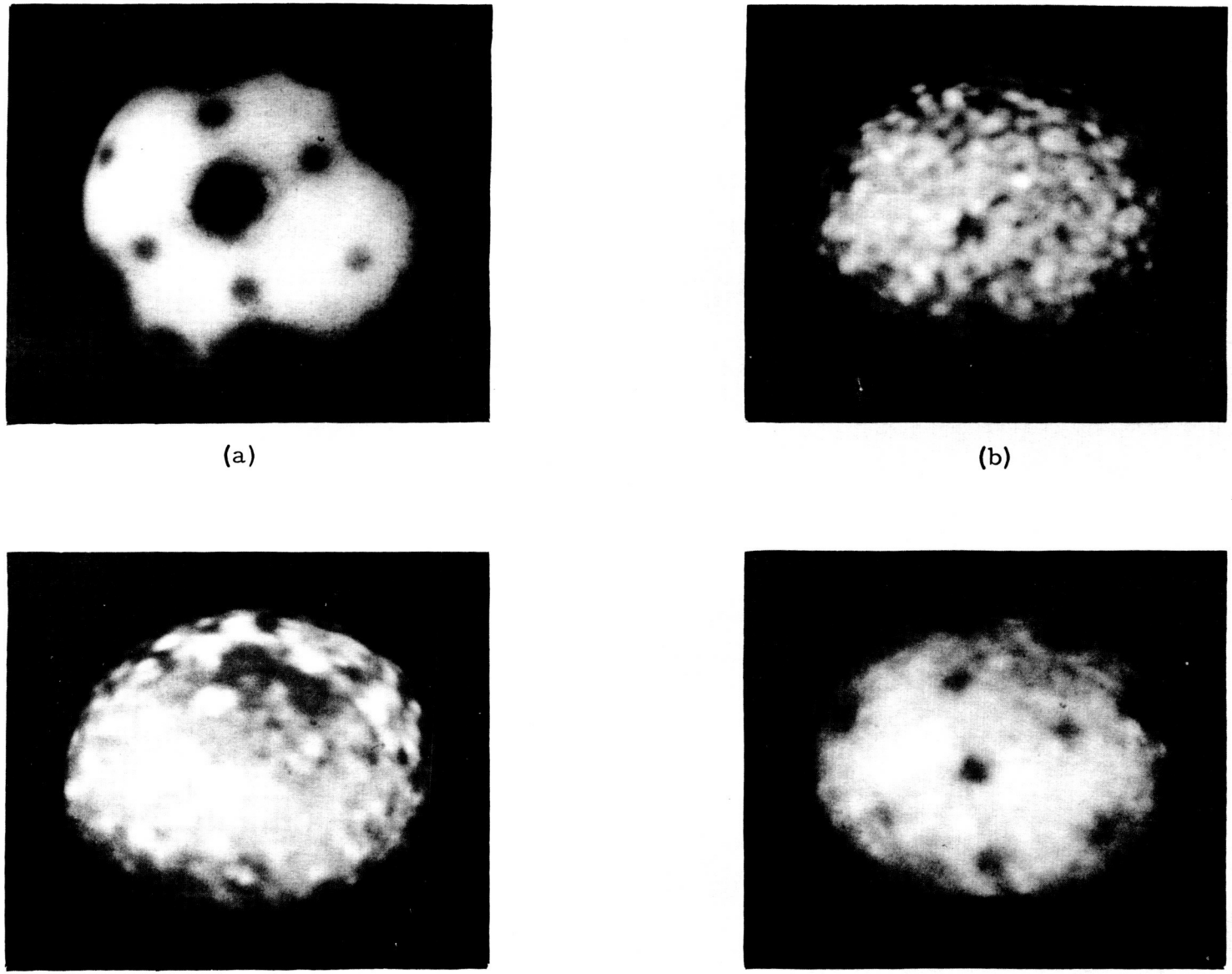

Figure 44. Cesium ion sputtering of clean tungsten ($Q = 6.76$ μcoul, $E_p = 1073$ ev)
(a) Clean and smooth tungsten pattern ($\beta = 10,530$ cm^{-1}, $\phi = 4.52$ ev)
(b) After sputtering ($\beta = 11,120$ cm^{-1}, $\phi = 3.89$ ev)
(c) After partial field desorption of adsorbed cesium layer ($T = 77^{\circ}$K, $F_d = 30$ Mv/cm)
(d) After complete field desorption of adsorbed cesium layer ($T = 77^{\circ}$K, $F_d = 39$ Mv/cm; $\beta = 11,120$ cm^{-1}, $\phi = 4.52$ ev). The spots in the pattern are due to surface roughness.

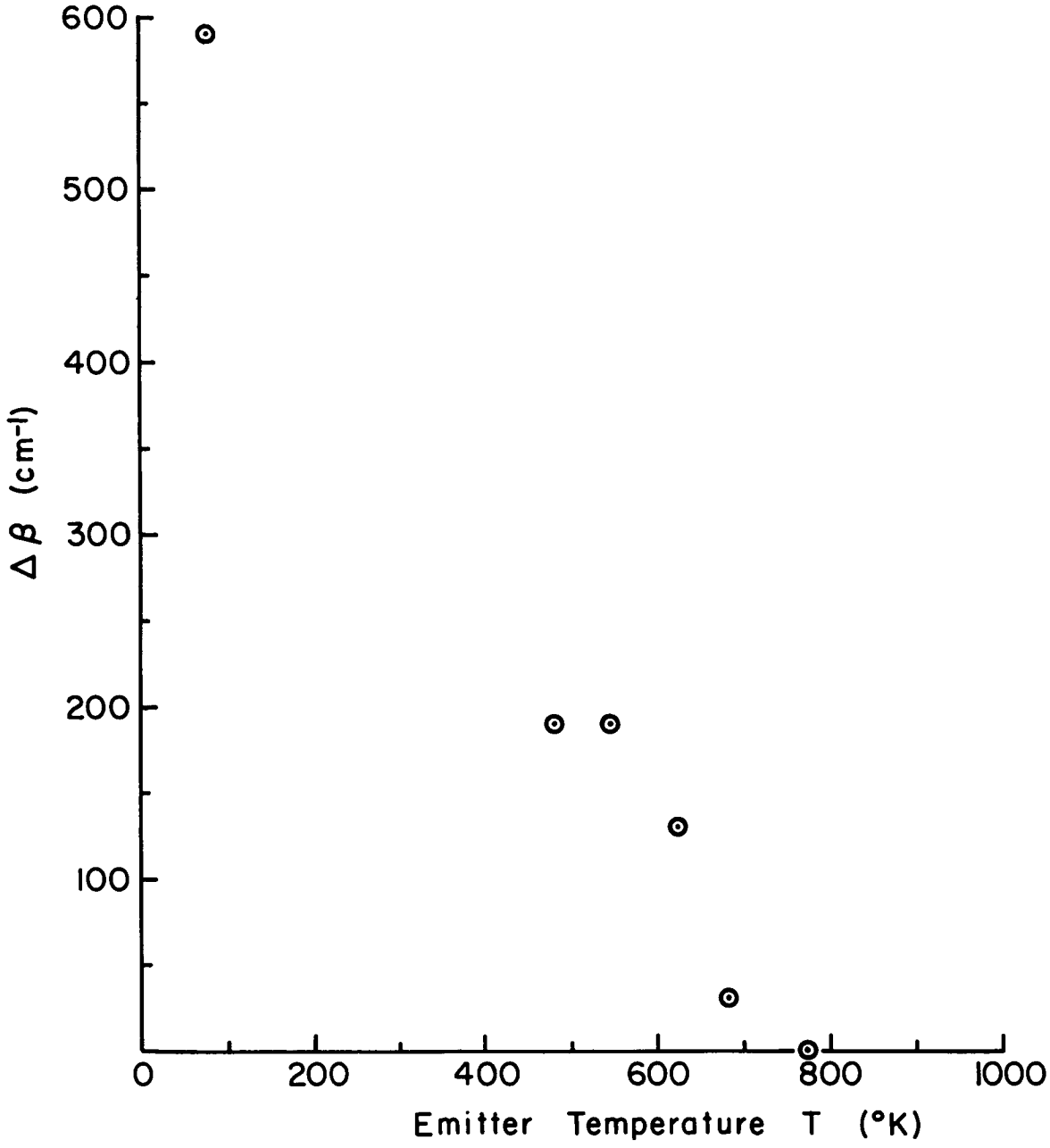

Figure 45. Reduction in surface roughness, as measured by change in β, as a function of emitter temperature. Heating time at each temperature was 60 sec.

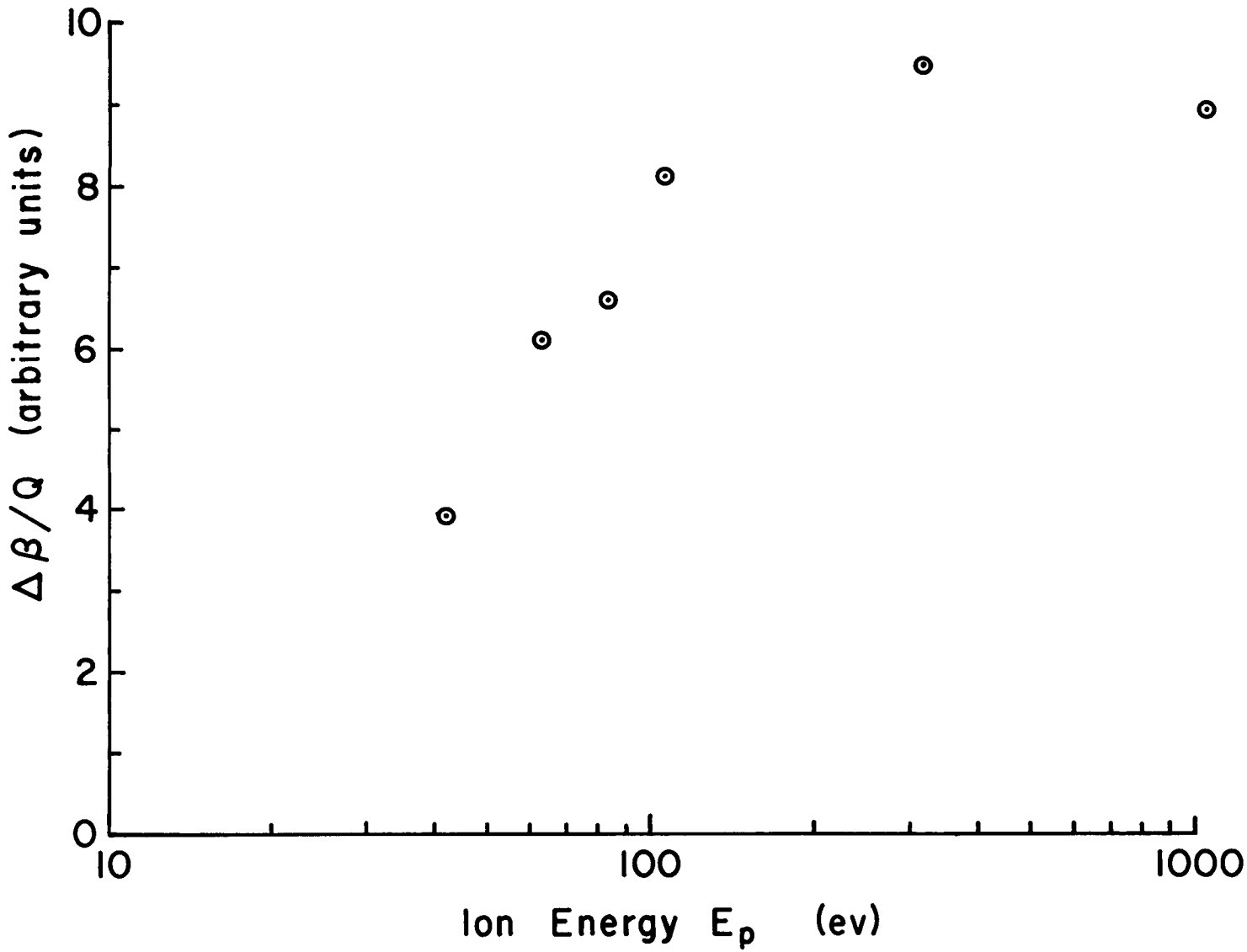

Figure 46. Surface roughness, as measured by a normalized change in β, as a function of cesium ion energy E_p.

ion energy up to an ion energy of about 300 ev, above which no further increase in roughening was observed. The higher energy ions probably sputter away new projections as fast as they are formed, preventing further increase in surface roughness. Extrapolation of the data in Figure 46 to $\Delta\beta = 0$ gives an ion threshold energy for surface roughening of about 20 ev, in reasonable agreement with the threshold sputtering value of 30 ev measured by Stuart and Wehner for xenon ion bombardment of tungsten[56].

Sputtering of Cesium-Coated Tungsten

An attempt was made to study sputtering of cesium-coated tungsten as a function of cesium coverage with the tube shown in Figure 43, but an unexpectedly large fraction of neutral atoms was able to strike the tip during ion bombardment, thus preventing accurate coverage measurements. However, some general trends could be noted. At coverages approaching a monolayer (such as shown in Figure 47 (a)), the main effect of low energy ion bombardment seemed to be to reduce the surface coverage (Figure 47 (b)). At low coverages (such as in Figure 47 (c)) ion bombardment also roughened the underlying tungsten surface; this can be seen in the pattern asymmetry of Figure 47 (d), which was taken after the sputtered cesium coating was re-equilibrated. These results will be made more quantitative with an improved design of the FEM sputtering tube.

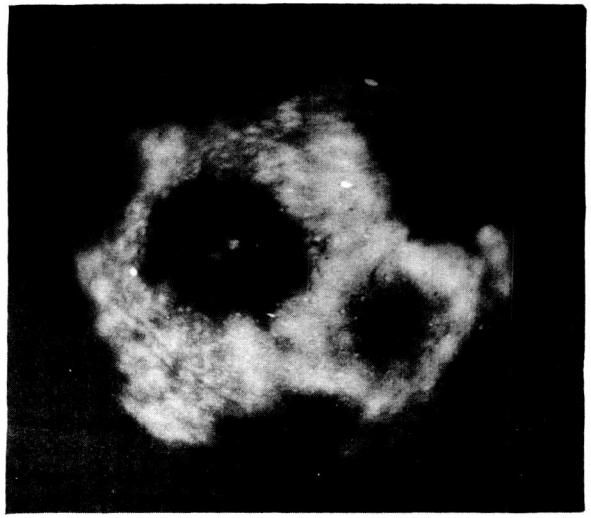

(a)

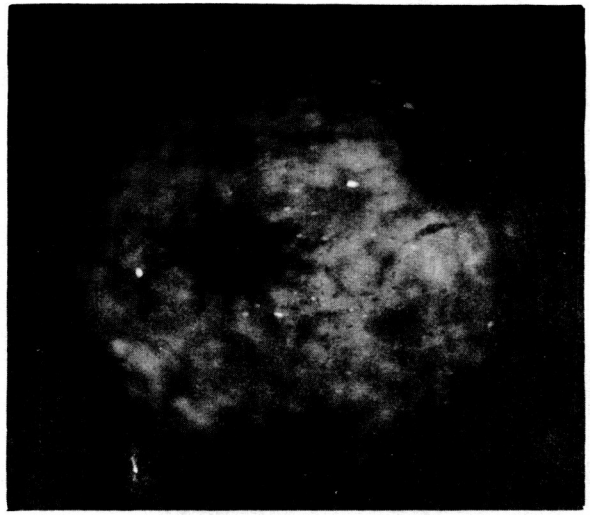

(b)

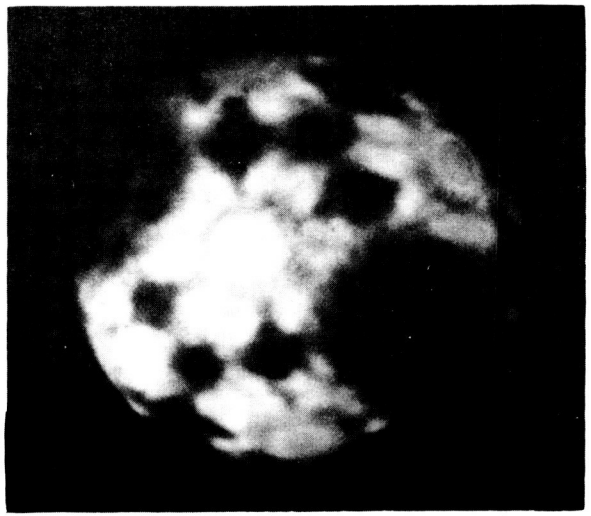

(c)

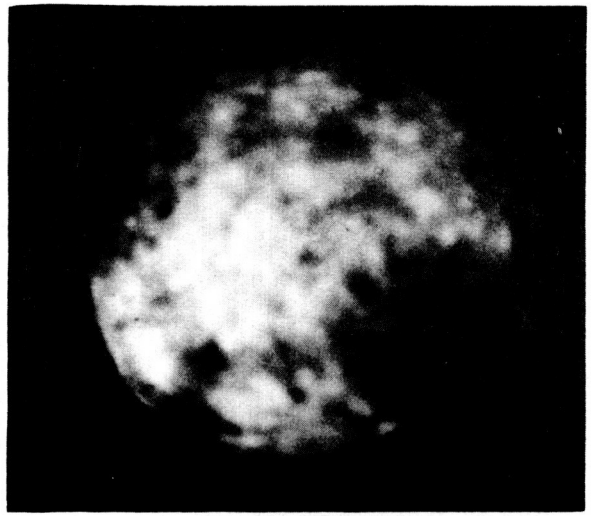

(d)

Figure 47. Cesium ion sputtering of cesium-coated tungsten. (a) Before sputtering ($\sigma = 2.3 \times 10^{14}$ Cs atom/cm^2); (b) After sputtering with Q = 2.5 μcoul, E_p = 535 ev ions and Cs re-equilibration ($\sigma = 2.0 \times 10^{14}$ Cs atom/cm^2); (c) Before sputtering ($\sigma = 0.47 \times 10^{14}$ atom/cm^2); (d) After sputtering with Q = 2.9 μcoul, E_p = 1073 ev ions and Cs re-equilibration. Note roughness is still visible underneath Cs layer.

SURFACE IONIZATION OF CESIUM ON TUNGSTEN ALLOYS

INTRODUCTION

The purpose of this portion of the overall program is to provide information helpful in the evaluation of various tungsten alloys in terms of their potential usefulness as substrates for the surface ionization of cesium. Although the surface ionization of cesium (and other alkali metals) on various metal surfaces has been studied for many decades, no systematic studies using alloys as substrates have been made, probably because of difficulties anticipated in comparing results with theory. However, tungsten alloys, in the form of porous ionizers for cesium, may have metallurgical properties superior to those of the pure metals, and thus their surface ionization properties are of interest.

The quantities of significance in this study are the thermal desorption activation energy E_p for cesium ions, the desorption activation energy E_a for neutral cesium atoms, and the work function ϕ of the ionizing surface. From consideration of an energy cycle it can be shown that these quantities are related by

$$E_p = E_a + V_I - \phi , \tag{50}$$

where V_I is the ionization potential of the adsorbate. The quantity E_p is essentially a measure of the amount of energy required to form an adsorbate ion; the quantity $E_a - E_p = \phi - V_I$ determines the neutral atom to ion ratio, as given by the Langmuir-Saha equation:

$$\frac{n_p}{n_a} = \frac{g_p}{g_a} \exp\left(\frac{\phi - V_I}{kT}\right) , \tag{51}$$

where n_p and n_a are the number of ions and atoms, respectively, desorbed from a unit area in a unit time, and g_p/g_a is the ratio of the statistical weights of the ionic and atomic states of the adatom (for monovalent atoms like cesium, $g_p/g_a = 1/2$). Thus, for a given surface temperature it is desired that E_a be as small as possible, in order to achieve a high rate of ion production, and that $E_a - E_p$ be as large as possible, in order to reduce the neutral atom to ion ratio. Both of these considerations suggest the use of a substrate with a high work function, as is shown in Equation (50).

Equation (50) is strictly valid only for the case of electropositive adatoms desorbed from a uniform surface such as a single crystallographic plane. For an electropositive adsorbate the high rate of electronic transitions between the substrate metal and the adsorbate make it impossible to distinguish between the atomic and ionic states of the adatom; for electronegative adsorbates this is not true and an energy difference between the atomic and ionic states at the surface must be considered. For polycrystalline surfaces the average work function as determined by electron emission is not the same as the average work function for the same surface as determined by positive ion emission, since electron emission comes predominantly from low work function areas while positive ion emission comes from high work function areas. Also, it is likely that the relative ion and atom desorption rates vary from plane to plane; little accurate information is known in this regard. Thus the quantities E_p, E_a and $\emptyset$ in Equation (50) must be separately measured, and Equation (50) used as a guide to the numbers expected.

FIELD EMISSION MEASUREMENTS OF DESORPTION ACTIVATION ENERGIES

Formation of Field Emission Cathodes from Tungsten Alloys

A necessary step in a determination of adsorbate desorption energies from a particular substrate material by field emission methods is the formation of a field emission cathode from that material. For the tungsten alloys of interest here, namely W - Ta, W - Ir, W - Os and W - Re, this had not been done previously, and thus etching techniques had to be developed for this purpose.

The etching of W - Ta alloys may be used as an example. The usual dc etching techniques used in making field emission cathodes from W material were not successful in producing emitters of W - Ta alloys, because during the etching process tungsten only was removed, leaving on the surface of the emitter blank an increasing amount of tantalum residue which in turn interfered with further etching. W - Ta alloy emitters were made successfully by an ac etching technique which caused the formation of bubbles of hydrogen on the surface of the emitter blank; the rapid gas evolution removed the tantalum residue by physical agitation.

The steps involved in the process of making field emission cathodes from W - Ta alloys are as follows: (1) A small bar of material is formed into a rectangular bar with square cross section approximately 0.250 x 0.020 x 0.020 inch by etching away excess material with a 2 inch D rotating electrolytic cylinder[57] (etching solution is 0.5N NaOH, etching voltage and current are 8 v ac and 250-300 ma). (2) The rectangular blank is changed into a cylinder by etching at 50 v dc to remove the corners. The cylinder is then an emitter blank and is spot-welded onto a tungsten filament used as the emitter support. (3) The emitter blank is then etched into the form of a sharp needle in 2N NaOH with 12 v ac applied to the electrolytic cell. The resulting emitters made from W - Ta alloys are shown in Figure 48.

EXPERIMENTAL PROCEDURES AND RESULTS

For this particular investigation terminal neutral and ionic desorption rates were studied, that is, the clean alloy surface was used as the end point. The coverage increment over which the measurements were made was normally confined to a 4 to 8 percent change in work function; for clean tungsten this corresponds to a change in the fractional monolayer coverage $\Delta\theta$ of 1.8 to 3.6 percent. Because of the variation of both the neutral and

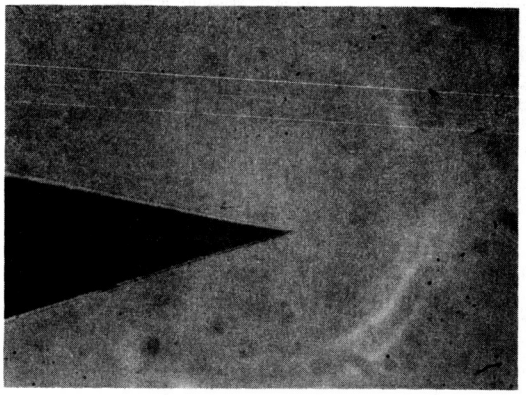

A

B

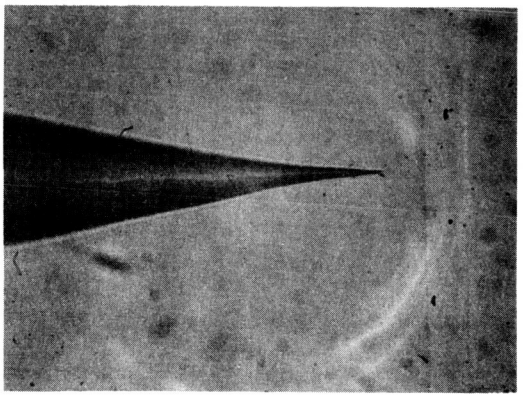

C

Figure 48. Shapes of emitters made from W-Ta alloys at 215x magnification. A, W-5%Ta; B, W-10%Ta; C, W-20%Ta.

ionic desorption energies with adsorbate coverages it is highly desirable to confine the measurement to a small $\Delta\theta$ in order to more nearly localize the values of E_a and E_p to a given coverage and work function.

Activation energies E_{des} of neutral and ionic desorption were determined from Arrhenius plots of the rate-temperature data. Assuming first order kinetics and an average frequency factor the rate equation

$$\frac{-d\theta}{dt} = \theta \quad \exp\left(-E_{des}/kT\right) \tag{52}$$

can be integrated over the coverage increment θ_i to θ_f to yield

$$\ln t = \ln\left[\ln(\theta_i/\theta_f)\right] - \ln \nu + E_{des}/kT \tag{53}$$

where θ_i and θ_f are initial and final coverages and t is the time.

In the present case where $\theta_f = 0$ and $\Delta\theta \sim \theta$ Equation (53) is not applicable, and the differential expression Equation (52) leads directly to the working equation

$$\ln t = -\ln \nu + E_{des}/kT \tag{54}$$

where $d\theta/\theta\ dt$ is replaced by $\Delta\theta/\theta\Delta t \approx 1/\Delta t$.

The experimental procedures followed for obtaining the desorption energies were as follows:

(1) The emitter surface was cleaned by flashing the emitter to successively higher temperatures until a stable, symmetrical field emission pattern was obtained which did not undergo further change when the emitter was flashed at a slightly higher temperature. For most alloys employed the pattern obtained by this procedure was similar to that of clean tungsten; however, this was not the case for the iridium and osmium alloys.

(2) After obtaining a Fowler-Nordheim plot of this surface the alloy was then heated for specified intervals at successively increasing temperatures from 800 to 1500°K. In this way the temperature which caused the maximum change in work function was determined. After equilibrating the surface at the latter temperature another Fowler-Nordheim plot was obtained. To check that the surface thus obtained was stable for cesium desorption measurements, the emitter was heated for a long period at temperatures between 700 and 1000°K (the temperature range required for terminal cesium desorption). In those cases where surface changes seemed to occur at these lower temperatures

the emitter was heated for sufficient time to bring the surface to an equilibrium condition at the lower temperature.

(3) The emitter was then dosed with a partial monolayer of cesium which was equilibrated and desorbed by heating to the coverage chosen for the initial point of the desorption study. For the investigation of neutral desorption a negative field of 5 Mv/cm was applied in order to return ions to their respective adsorption sites. Superimposed on the dc bias voltage was a field emission pulse voltage (duty factor 10^{-4}) in order to draw a measurable pulse field emission current I_p. In this manner the progress of the desorption could be followed without relaxing the temperature. The attainment of a clean surface was manifested by a sharp break in the I_p vs t curve such that I_p no longer varied with time. In a similar fashion ionic desorption was investigated by replacing the negative field with a small positive field. This allowed both ions and neutrals to be desorbed simultaneously. Since $E_a > E_p$ in the coverage range investigated concomitant neutral desorption during ionic desorption was negligible. Typical I_p vs t curves are given in Figure 49 for both neutral and ionic desorption.

The results of this work are summarized in Table XIV. The first four columns of data give the experimental values of the neutral and ion desorption energies and Arrhenius plot intercepts (i.e., $\ln t$ vs $1/T$ obtained from least squares analysis of the time-temperature data according to Equation (54). The fifth column gives the ratio of the initial cesium covered average work function ϕ_i to the clean alloy average work function ϕ_o equilibrated for several minutes at the indicated temperature T_o.

Initial cleaning of the alloys was accomplished by high temperature flashing (above 2200°K). For most alloy samples a pseudo clean tungsten pattern was obtained on flashing (see Figures 50 through 54). The latter was not true, however, for the iridium and osmium samples. In the case of the 5 percent rhenium and 20 percent tantalum samples initial flashing produced pseudo clean tungsten patterns which could not be reproduced by subsequent flashing after the emitter had been equilibrated at lower temperatures. The sixth column of Table XIV, which gives the ratio of the average work function after the high temperature flash ϕ_o/ϕ_c, should be an indication of the fractional change in average work function due to the presence of the alloy. It was noticed that all those samples which exhibited a change did so in a direction to decrease the pseudo clean tungsten work function.

After initial flashing to obtain a pseudo clean tungsten pattern subsequent heating at lower temperatures produced gradual changes in the field electron patterns. This behavior is illustrated in the pattern pictures

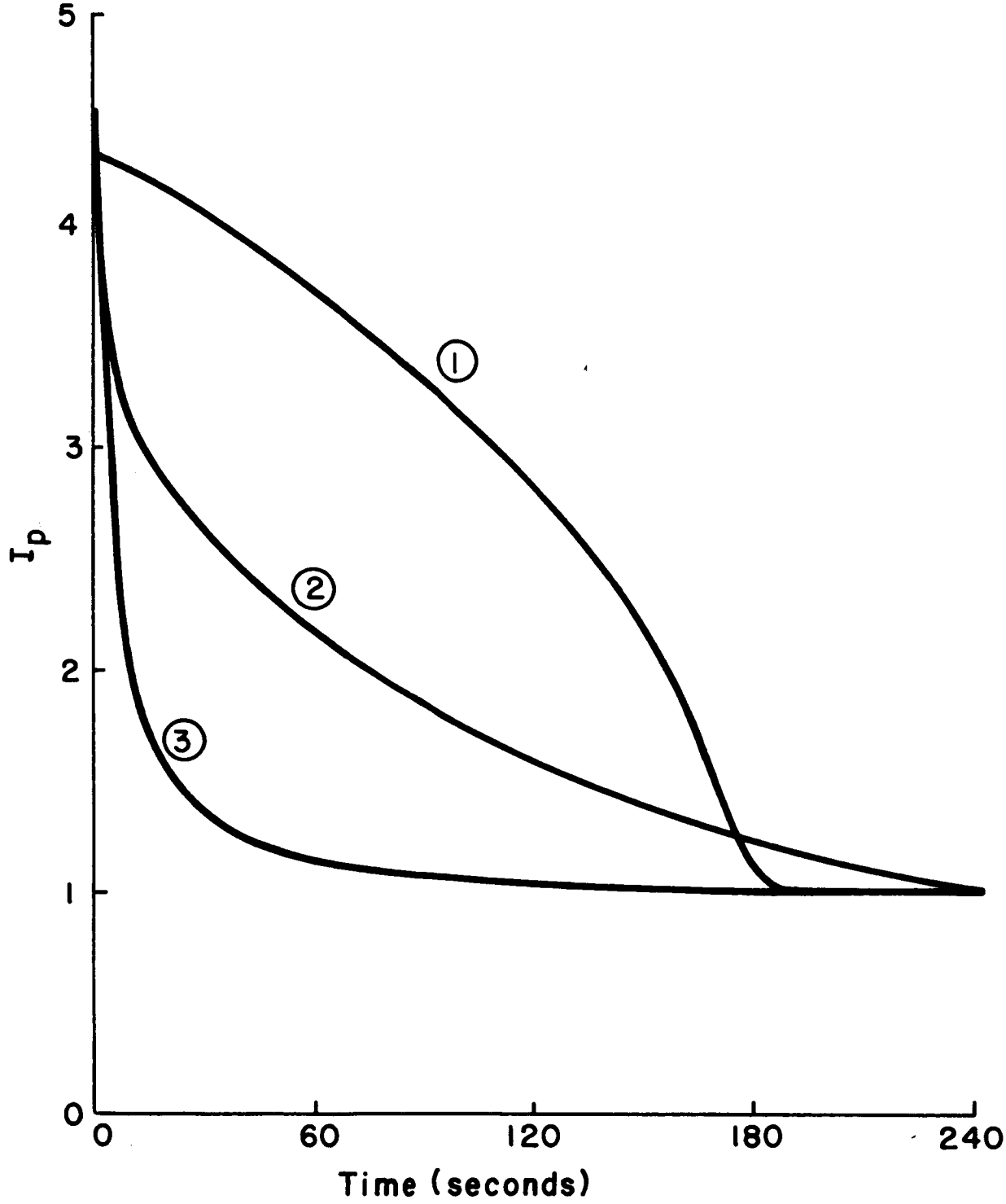

Figure 49 Chart recorder output showing variation of I_p with time at constant V_p. Three types of curve were recorded - (1) ion desorption from W - 20 Ta, W - 1 Ir, and W - 23 Re - (2) ion desorption from remaining alloy surfaces, and (3) neutral desorption.

TABLE XIV

Data obtained from tungsten alloy study by field emission microscopy techniques

Alloy	E_a (ev)	E_p (ev)	Log ν_a	Log ν_p	ϕ_i/ϕ_o	ϕ_o/ϕ_C	T_o (°K)	ϕ_o(ev)*
5 TA	2.06 ± 0.14	1.71 ± 0.03	9.56 ± 0.79	9.68 ± 0.24	0.965	0.89	1230	$4.22 \pm .14$
10 TA	2.61 ± 0.04	2.11 ± 0.13	10.76 ± 0.22	12.33 ± 0.87	0.97	0.91	1573	$4.37 \pm .14$
20 TA	2.22 ± 0.04	1.62 ± 0.08	9.78 ± 0.21	8.65 ± 0.58	0.93	0.97	1517	$4.47 \pm .09$
1 Ir	2.47 ± 0.24	2.44 ± 0.20	9.22 ± 1.13	13.67 ± 1.33	0.91	1.0	No chg	$4.00 \pm .31$
2 Ir	2.96 ± 0.18	2.20 ± 0.18	13.07 ± 0.93	12.81 ± 1.23	0.96	1.0	No chg	$4.63 \pm .26$
2.5 Os	2.71 ± 0.07	2.18 ± 0.05	10.27 ± 0.30	11.87 ± 0.31	0.965	0.92	1403	$4.40 \pm .09$
5.0 Os	3.07 ± 0.15	2.29 ± 0.08	12.29 ± 0.71	13.07 ± 0.54	1.015	0.94	1500	$4.65 \pm .17$
5 Re	2.86 ± 0.10	2.10 ± 0.11	12.21 ± 0.50	12.20 ± 0.74	0.94	0.98	1610	$4.63 \pm .15$
15 Re						1.0	No chg below 1350	
23 Re	3.31 ± 0.10	3.28 ± 0.71	12.29 ± 0.43	16.36 ± 4.02	0.965	1.0	No chg below 1350	$4.00 \pm .72$
W	3.30	2.0	14	12				5.3

* Calculated from Equation (50)

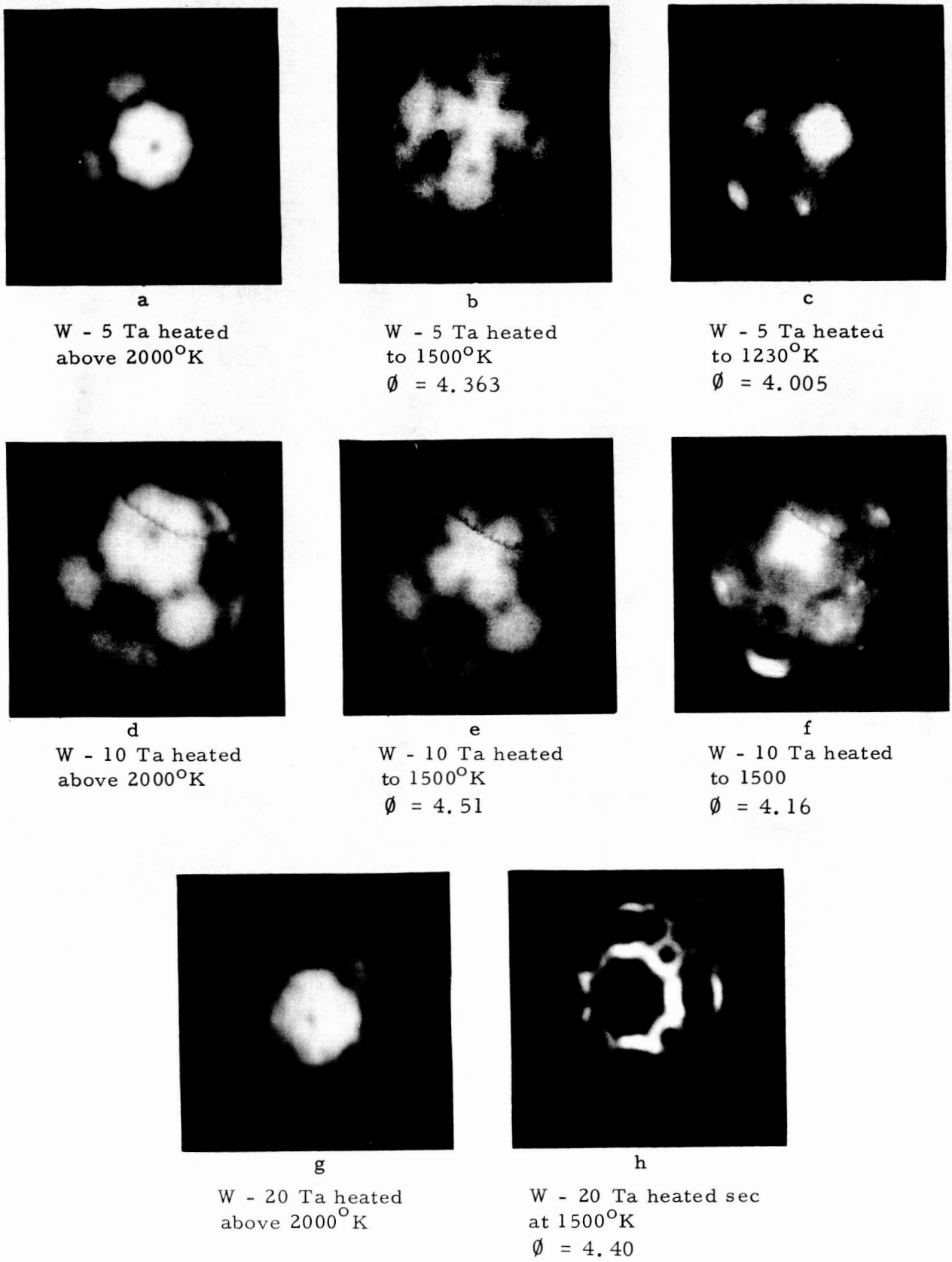

Figure 50 Patterns (a), (d) and (g) are psuedo clean tungsten patterns obtained by flash heating; patterns (c), (f) and (h) are obtained by equilibrating at the indicated temperatures.

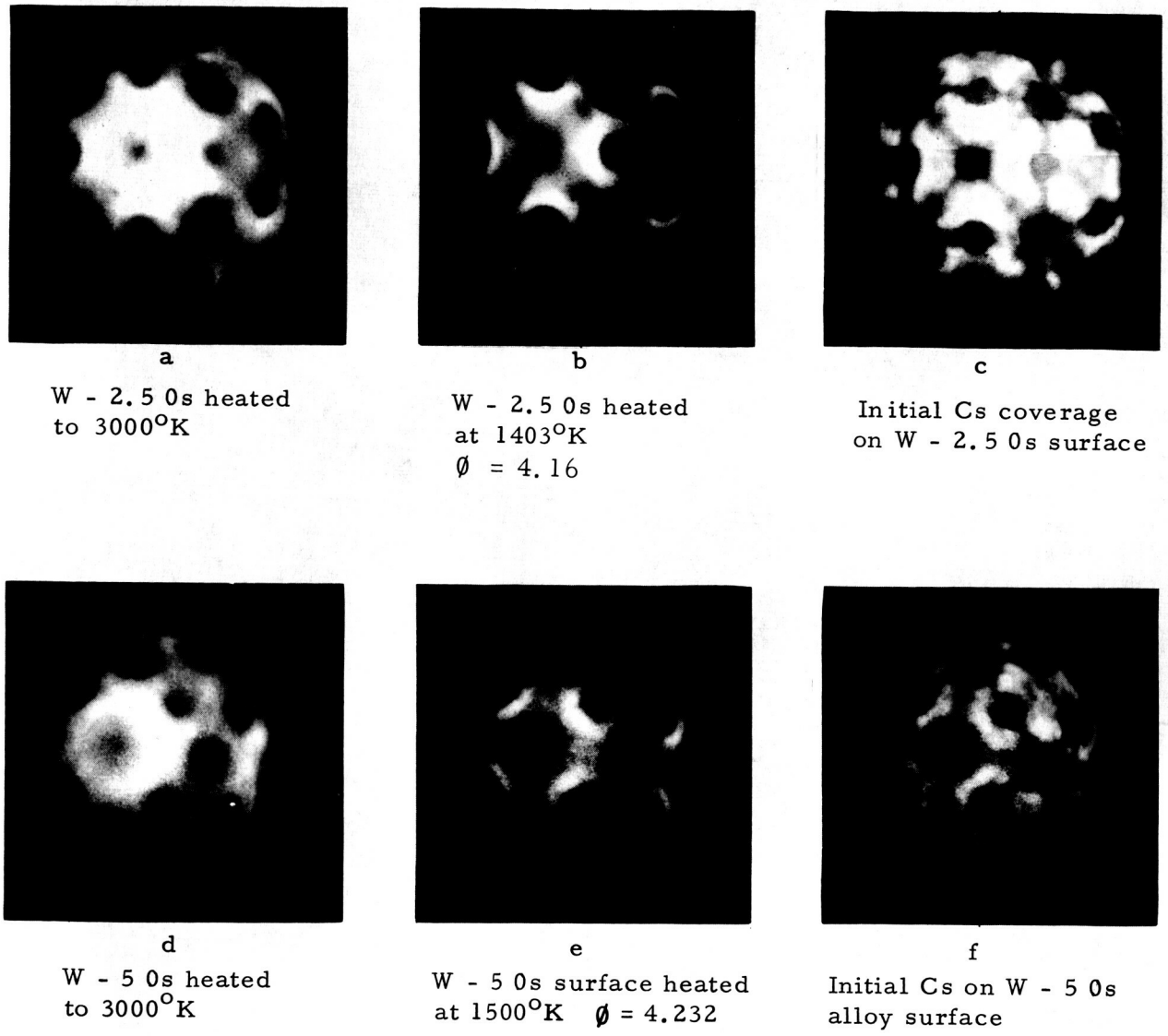

Figure 51 Principal pattern changes of $(3\bar{1}0)$ oriented osmium alloys.

a

W - 1 Ir surface heated near 3000° K

b

W - 1 Ir surface

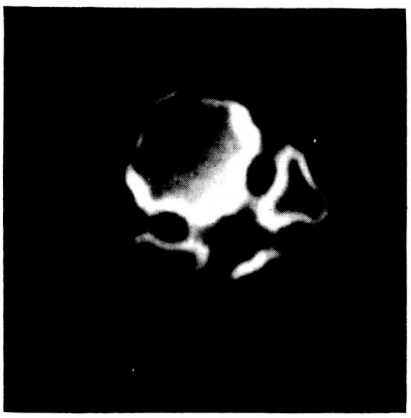

c

W - 2 Ir surface

Figure 52 Field emission patterns of $(4\bar{1}1)$ oriented W - 1 Ir alloy and (310) oriented W - 2 Ir alloy.

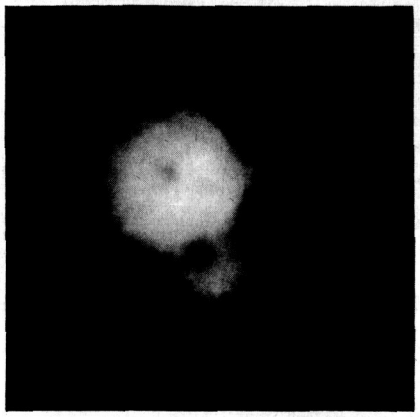

a

W - 5 Re surface after heating above 2000°K

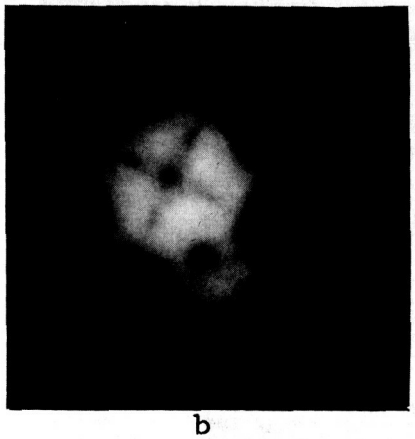

b

W - 5 Re Surface after heating for 300 sec at 1122°K

ϕ = 4.505

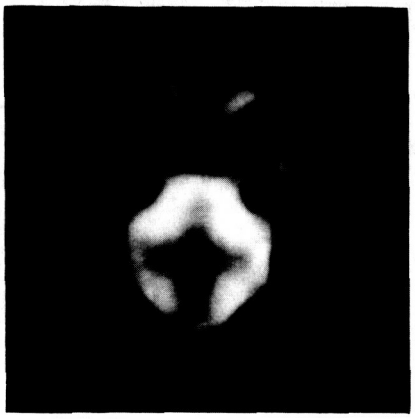

c

W - 5 Re surface after heating for 300 sec at 1620°K

ϕ = 4.42

Figure 53 Principal pattern changes of W - 5 Re alloy. (a) and (b) are $(4\bar{1}1)$ oriented. The (530) oriented equilibrated alloy shown in (c) was the surface used for the desorption work.

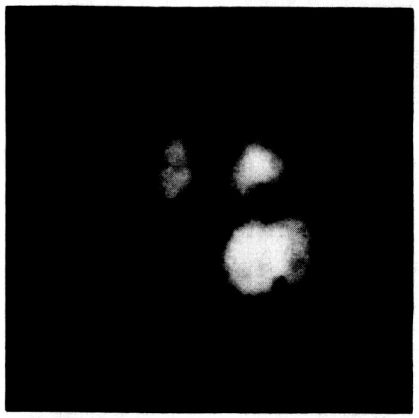

a

W - 23 Re surface flashed clean above 2000°K

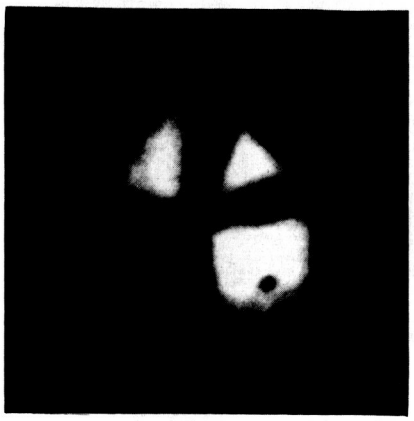

b

Tip heated for 300 sec at 1417°K

$\emptyset$ = 4.49

c

Tip heated for 600 sec at 1434°K

d

Tip heated for 1200 sec at 1434°K

$\emptyset$ = 4.76

Figure 54 Pattern changes in a (110) oriented W - 23 Re alloy caused by oxygen diffusing onto the surface from the bulk when the tip is heated at the indicated temperatures.

of tantalum shown in Figure 50. Excluding the iridium and the 15 and 23 percent rhenium samples, most samples showed a slight change in ϕ_o with temperature in the range 800 to 1500°K. For the most part, changes in ϕ_o were sufficiently small so as not to adversely affect the cesium desorption measurements which cover the temperature range 690 to 1175°K for the various alloy samples.

Figure 51(c) and (f) are typical of the initial cesium covered surfaces from which the desorption runs were made. As can be seen from column 5, Table XIV the variation in work function over which the cesium desorption measurements were made did not exceed 9 percent which corresponds approximately to a coverage of $\theta = 0.05$ (assuming pure tungsten ϕ vs θ characteristics).

The 15 and 23 percent rhenium samples exhibited a special behavior not apparent in any other samples. This is illustrated in Figure 54 which gives pattern pictures and average work functions (based on a 4.52 ev value for the pseudo clean surface) after flashing (Figure 54 (a) and after heating for several minutes at the indicated temperatures. What seemed to be occurring for both the 15 and 23 percent rhenium samples was the slow release of an absorbed electro-negative gas from the bulk upon heating above 1350°K. That the absorbed gas was oxygen was confirmed by (1) comparing the pattern changes of Figure 54 with previous work[1] on oxygen adsorption reported elsewhere and (2) observing that the temperature of approximately 2000°K required for returning to a clean tungsten pattern was approximately the temperature required to clean adsorbed oxygen from pure tungsten.

No evidence of oxygen absorption was obtained from the 5 percent rhenium sample. The cesium desorption data from the 23 percent rhenium was obtained on the pseudo clean tungsten equilibrated at a sufficiently low temperature to preclude oxygen diffusion to the surface. Fortunately, the cesium desorption temperature was also sufficiently low to preclude significant oxygen diffusion to the surface. Because of the difficulty with the oxygen contamination from the bulk, no cesium desorption data was obtained from the 15 percent rhenium sample. The effect of oxygen on the desorption characteristics of cesium from tungsten has been given in an earlier report.[1]

General Discussion of Results

An indication as to the variation of E_{des} with θ can be obtained from I_p vs t curves given in Figure 49. The difference in shape of the curves reflects the differing variations of E_{des} with θ over the coverage increment investigated. In the case of cesium desorption from pure tungsten $dE_a/d\theta$ is negative over the entire coverage range whereas $dE_p/d\theta$ is positive for $0 \leqslant \theta < 0.02$ and negative over the range $0.02 < \theta \leqslant 0.70$.[21]

The above can be better understood by recalling from Equation (50) that

$$\frac{dE_p}{d\theta} = \frac{dE_a}{d\theta} - \frac{d\phi}{d\theta} \tag{55}$$

It is known from previous work[21, 58] on pure tungsten that both $\frac{d\phi}{d\theta}$ and $\frac{dE_a}{d\theta}$ are negative in the range $0 < \theta < 0.70$ and that the average values in the coverage range $0 \leq \theta \leq 0.02$ are such that $|dE_a/d\theta| > |d\phi/d\theta|$; which predicts the observed negative $dE_p/d\theta$ in the latter coverage range. On the other hand throughout the coverage range $0.02 < \theta < 0.70$ $|dE_a/d\theta| < |d\phi/d\theta|$ so that here a positive $dE_p/d\theta$ is predicted. Accordingly, the E_p vs θ curve possesses a minimum near 0.02 as shown originally by Langmuir[58] and recently confirmed by field electron microscopy techniques.[59]

In order to analyze the I_p vs t data further it is necessary to determine the variation of θ with t. This cannot be accomplished easily from I_p vs t data because of the complex relationship between I_p and θ via the Fowler-Nordheim relationship. The three curves given in Figure 49 are typical of the variation of I_p with t. Those ion desorption rates whose I_p vs t relationships were similar to Curve (1) of Figure 49 were the 1 percent iridium, 20 percent tantalum and 23 percent rhenium alloys; the ion desorption characteristics of the remaining alloy samples were analgous to Curve (2) of Figure 49. The neutral desorption rates behave similarly to Curve (3) for all alloy samples, indicating a rate which decreases with decreasing coverage. This is in accord with the known sharp increase in E_a as θ approaches zero. The ion desorption rates do not appear to decrease as rapidly as the neutrals and, in the case of Curve (1), may even remain constant. We therefore conclude that $dE_p/d\theta$ is probably negative for most samples so that a minimum in the E_p vs θ curve is expected near zero coverage as observed in the pure tungsten results.

Inasmuch as E_p, E_a and ϕ are averaged over the exposed crystal faces there is some uncertainty as to the regions of the crystal contributing to these values. Earlier cesium desorption studies[21] on pure tungsten suggested that the final stage of cesium desorption occurred primarily from the (110) region. Recently, careful measurements of E_p and E_a values are weighted toward the high work function $\{110\}$ planes.

There are two possible explanations why the calculated values of ϕ_o for the alloy samples are all appreciably lower than the pure tungsten value. First, it is possible that the presence of the alloy lowers the work function of tungsten significantly; some proof of this is the several values of ϕ_o/ϕ_c that are less than unity. Secondly, both E_a and E_p are averaged over

various crystal faces and over the coverage increment $\Delta\theta$;[74] it is possible that the averaging is altered by the presence of the alloy or by the slightly larger coverage increment used in this work such that lower values of ϕ are obtained.

It is interesting to note that the trends observed in the calculated ϕ_o values of tantalum agree with the trends suggested by the ϕ_o/ϕ_c. This sort of agreement is most likely to occur with the tantalum samples since ϕ_c refers to what appeared to be a nearly clean tungsten surface. It is somewhat surprising that the 20 percent tantalum sample exhibited a value of ϕ_o closer to that of pure tungsten than either the 5 or the 10 percent samples. We also note a similar trend in the iridium and osmium samples both of which suggest values of ϕ_o closer to the pure tungsten value for the higher percentage alloy sample. It will be noticed in the following section that most of these observations are confirmed by the thermionic work function measurements.

The 5 percent rhenium, 2 percent iridium and 5 percent osmium samples exhibited the highest values of ϕ_o. This is a desirable characteristic for possible application of these alloys as ionizers in contact ionization electric propulsion engines since according to Equation (51) a higher ratio of n_p/n_a is expected. Of equal importance are the values of E_p and log $_p$ which, for these samples, do not differ greatly from the pure tungsten values. This means that the rate of ion desorption is not significantly reduced from that of pure tungsten at a given temperature.

Of perhaps even greater interest for application to contact ionization engines is the results of the 15 and 23 percent rhenium samples. Observing that repeated high temperature flashing and long-term heating did not exhaust the low temperature oxygen diffusion to the surface we conclude that these alloys can absorb a remarkably large supply of oxygen. The higher work function surface of a partial oxygen layer on tungsten is generally believed to be beneficial to contact ionization engines through increased ionization efficiency. The results given in Table XIV refer to a tungsten-rhenium surface free of oxygen, but work has been reported earlier on the effect of oxygen on E_a and E_p for the pure tungsten system.

WORK FUNCTIONS OF TUNGSTEN ALLOYS

Method of Approach

The absolute work functions of the tungsten alloys of interest in this work were determined by a thermionic retarding potential method instead of by a field emission method, because the latter involves a considerably more complicated tube design and more sophisticated measuring techniques. A brief description of the thermionic retarding potential method of determining work function and of the experimental tube design considerations will be

given in this section; following sections will discuss the experimental procedures followed and the results.

Thermionic Retarding Potential Method of Measuring Work Function. - Consider a plane parallel two electrode system consisting of a cathode and an anode with the cathode heated to a temperature T and possessing a uniform work function ϕ_K, and the anode at a low temperature and having a uniform work function ϕ_A. If voltage is applied to this system such that a small accelerating field exists at the cathode surface, the emission current density is given by the well-known Richardson equation

$$J_o = A_{th} T^2 \exp -\left(\frac{\phi_K}{kT}\right), \tag{56}$$

where $A_{th} = 120$ amp/cm^{2}deg^2. In this case the barrier to emission is simply the cathode work function ϕ_K (Figure 55(a)). However, if a negative potential V of sufficient magnitude is applied to the anode the barrier to emission becomes, as shown in Figure 55(b), $\phi_A - V$, and it can be readily shown[23] that the emission current density is given by

$$J = A_{th} T^2 \exp\left[(-\phi_A + V)/kT\right] = J_o \exp\left[(\phi_K - \phi_A + V)/kT\right] \tag{57}$$

(it should be mentioned that implicit in the derivation of Equation (57) is the conservation of the Maxwellian normal energy distribution.) Thus a plot of log J, or more conveniently log I, as a function of anode voltage V results (a) in a straight line independent of V for $V \gg \phi_A$, or (b) in a straight line with a slope 2.30/kT for $V \leq \phi_K - \phi_A$ (see Figure 56). The voltage at the point of intersection of these two straight lines, the so-called "knee" of the curve, is just equal to the difference in the work functions of the two surfaces (their contact potential). Increasing the temperature of the cathode increases the current at any value of V. Plotting the current as a function of temperature in the form of a Richardson plot (log I/T^2 versus $1/T$) permits determination of the work function of the cathode for case (a) and of the anode for case (b) from the slopes of the resulting straight lines.

The simple picture presented above is in practice complicated by a large number of effects, among which are space charge, the Schottky effect, nonuniform work functions, variation of work function with temperature, as well as others [60, 27]. For the plane parallel diode space charge is a serious limitation; it can be shown [23] that space charge causes deviations in the expected I(V) curve for low values of V of either sign, and that the range of V affected increases with increasing I_o, the current corresponding to the saturation current density J_o. This limitation can be overcome by placing a third electrode with a small aperture in it between the cathode and the anode and with sufficient potential to reduce space charge

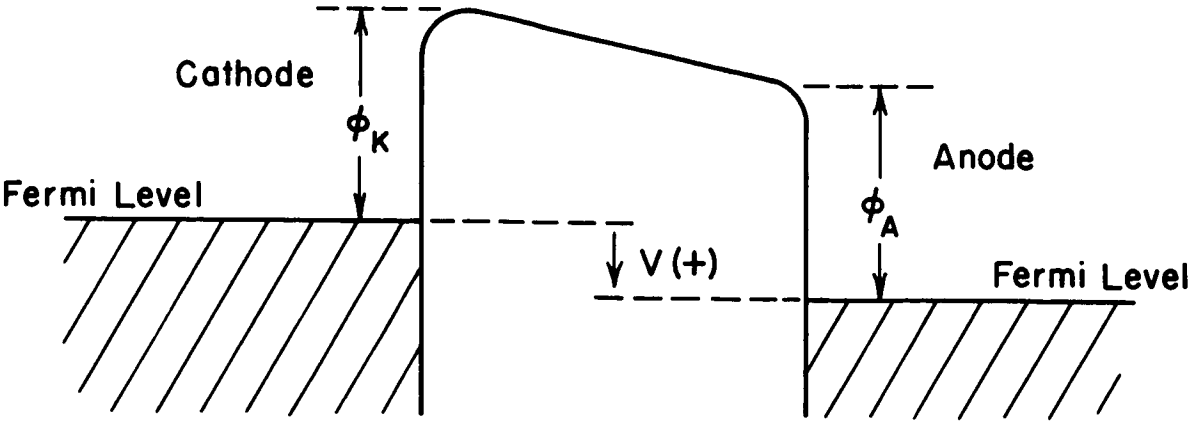

(a) $V \geq \phi_K - \phi_A$

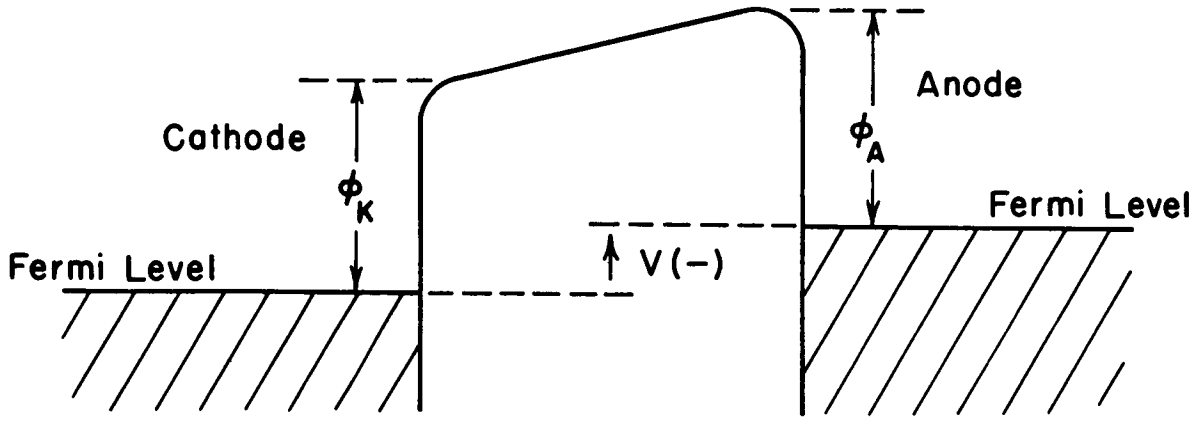

(b) $V \leq \phi_K - \phi_A$

Figure 55. Energy barrier to thermionic emission when the current is (a) cathode-limited, or (b) anode-limited.

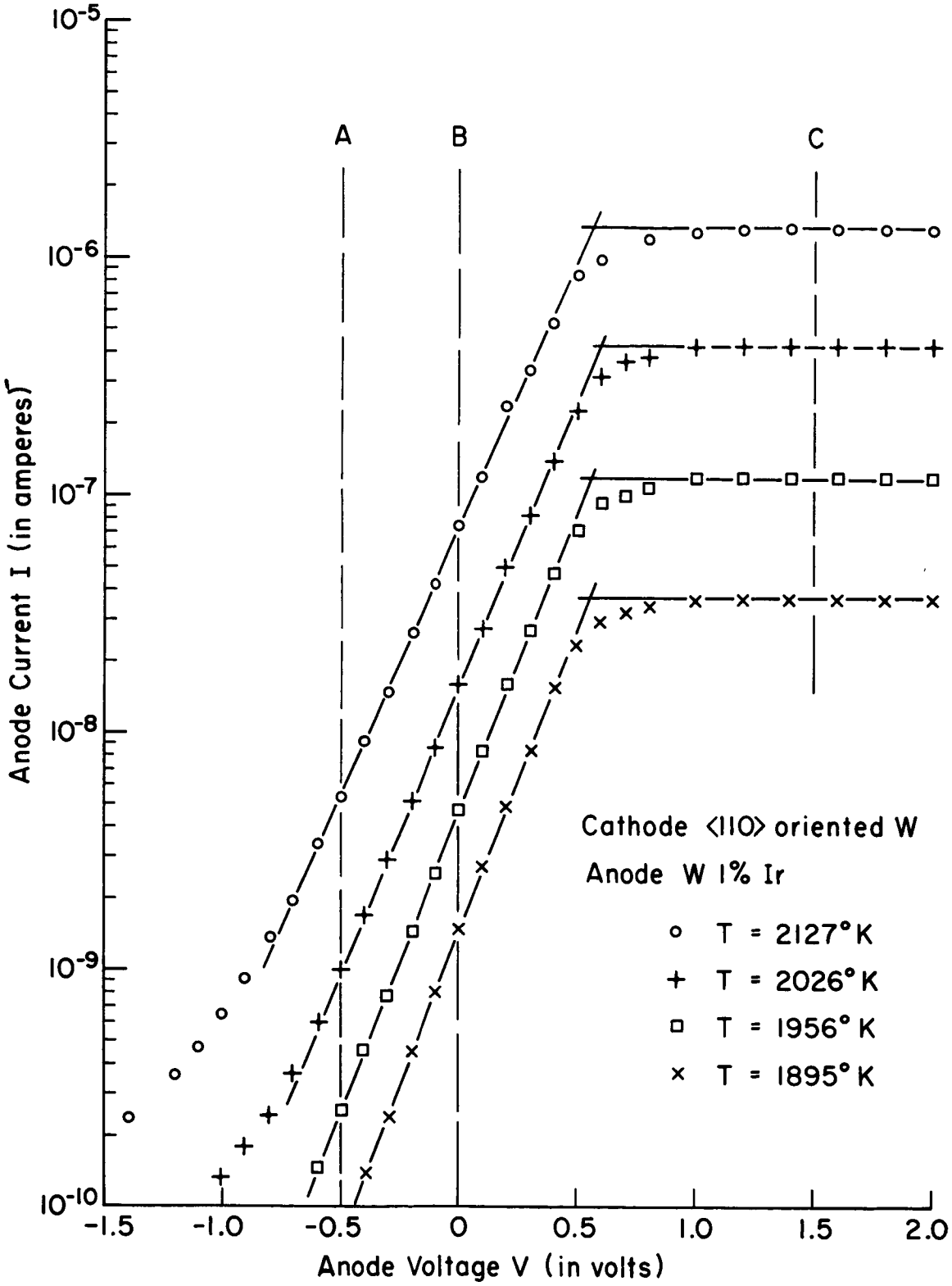

Figure 56. Typical plots of the anode current as a function of anode voltage for selected cathode temperatures. The temperatures are obtained from the slopes of the semi-logarithmic portions of the curves.

to a negligible amount. In this case, however, the current collected at the anode passes through an aperture which has a divergent lens effect on the beam, and thus will affect the I(V) curve [61]. This effect can be reduced to a negligible amount by use of an axial magnetic field of sufficiently high strength such that the maximum possible radius a_M of the helical path traveled by any electron is less than the radius of the aperture a[61]:

$$a_M = 3.37\ V_c^{1/2}/H < a \tag{58}$$

where a_M is in cm, V_c is the voltage of the center electrode in volts, and H is the magnetic field in gauss.

Nonuniform work functions and deviations in geometry from the plane parallel case (i.e., effects which disturb the conservation of normal energy) affect the I(V) curve primarily by rounding the knee. The position of the knee under these circumstances may be obtained by extrapolation of the two straight lines of cases (a) and (b) until they intersect.

A variation of work function with temperature affects the I(V) curves in two ways: (1) the position of the knee is shifted with respect to the V axis; (2) the measured thermionic constants A_R and ϕ_R for the heated cathode will differ from the constants A_{th} and ϕ_K in Equation (56). If we assume $\phi_K = \phi_{Ko} + \alpha_{wf}T$, then $\alpha_{wf} = \Delta V/\Delta T$, where ΔV is the shift in the knee for a temperature change ΔT. Also Equation (56) becomes

$$J_o = A_{th}\ T^2\ \exp\left[-(\phi_{Ko} + \alpha_{wf}T)/kT\right]$$

$$= A_{th}\ T^2 \exp(-\alpha_{wf}/k) \exp(-\phi_{Ko}/kT) \tag{59}$$

assuming other complications such as reflection are negligible in comparison with the temperature effect. Thus $\phi_R = \phi_{Ko}$, and the temperature coefficient of the work function α_{wf} may be obtained from

$$A_R = A_{th} \exp(-\alpha_{wf}/k) \tag{60}$$

Experimental tube design. - The work function triode design used in the present work is shown in schematic form in Figure 57. The cathode C of the tube is heated by bombardment of electrons from filament B. (The backplate A prevents electrons emitted by B from hitting the glass walls of the tube.) A few of the electrons emitted by C pass through a small aperture in the center electrode D and are collected by the anode E A magnetic field constrains the size of the electron beam striking E to the size of the aperture in D and preserves the transverse energy components of the electrons. Since the electrodes are symmetrical about the center

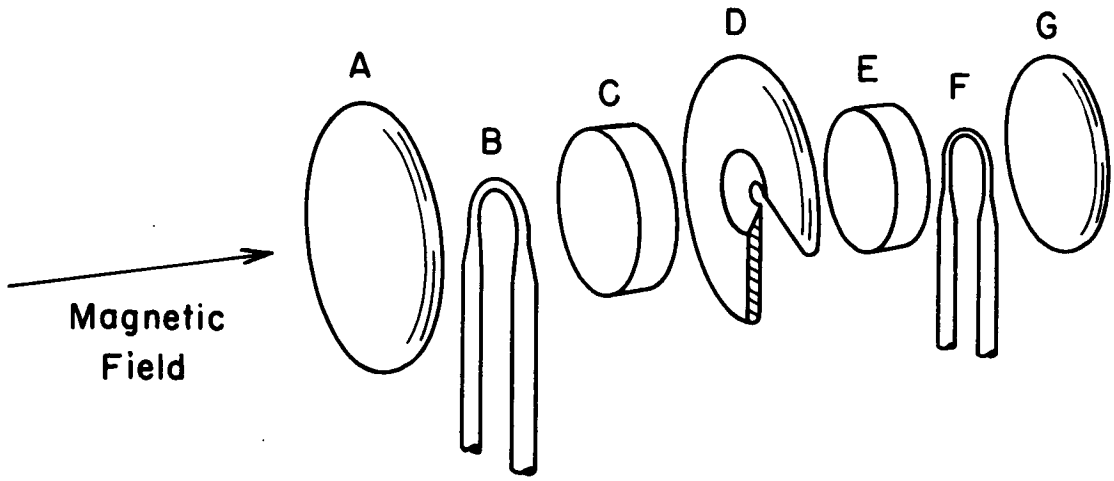

Figure 57. Diagram of the electrodes in the work function triode tube. A and G, backplates to prevent electrons from bombarding tube wells; B and F, bombarding filaments; C, cathode; D, center electrode with beam-defining aperture; E, anode.

electrode, the anode and cathode can be interchanged and thus both the true work function and the Richardson constants for a particular alloy sample may be obtained.

This design differs from the more usual work function triode design[62] in that the cathode and the anode are heated by electron bombardment instead of resistively. This choice was dictated by the alloy sample size and shape, but it has some additional advantages: (1) The resistively heated cathode has a magnetic field associated with the filament current which the indirectly heated cathode does not; (2) the resistively heated cathode has a drop in potential across the emitting area (which means that electrons emitted from different points on the cathode encounter different retarding potentials) whereas the indirectly heated cathode is unipotential; and (3) the resistively heated cathode may have geometry changes associated with the filament current, while any changes that occur on the indirectly heated cathode are just those due to temperature alone[63]. A disadvantage of the design illustrated in Figure 57 showed up during operation; some of the electrons emitted by B miss the cathode C and strike D where they release secondary electrons, a few of which may find their way through the aperture in D and contribute to the measured anode current. In practice this depended upon actual tube geometry and was minimized by proper choice of tube operating voltages.

The experimental tube was made for each alloy sample. It was quite small in overall dimensions (0.750 inch OD x 5 inches L) so that it could be placed in a liquid-nitrogen filled dewar that was positioned between the poles of a 4200 $\pm$ 200 gauss magnet with 1.75 inch D pole pieces and a 1.75 inch gap. The electrode arrangement of Figure 57 was mounted in one end of the tube and a combination magnetron-type ion gauge and molybdenum getter in the other. The anode was an alloy block approximately 0.120 inch x 0.120 inch x 0.040 inch and the cathode was a zone-melted <100>-oriented tungsten disk 0.110 inch D x 0.040 inch. Each was spaced approximately 0.050 inch from the center electrode, which contained an 0.011 inch D knife-edged (to reduce secondary electron production) aperture. The bombarding filaments were made of 0.030 inch tungsten wire etched down to 0.005 inch at the filament apex. The glass wall surrounding the electrode was coated with a conductive stannous oxide coating so that its potential could be controlled.

Experimental Procedures and Results

After evacuation each tube was placed in a liquid nitrogen filled dewar in order to maintain good vacuum within the tube during operation. The rate at which the anode contaminated was measured by noting the change in voltage required to maintain a constant current in the semilogarithmic portion of the I(V) curve: in most cases the rate was too small to affect the data.

The tube operating conditions were the following: the bombardment voltage was 800 volts, the bombardment current was between 7 and 14 ma (depending upon the temperature and size of the particular target being bombarded), the wall potential was 0 volts, and the voltage on the center electrode was between 120 and 330 volts (chosen for best operating characteristics and dependent upon exact tube geometry). This latter voltage was high enough to minimize space charge, yet low enough to keep the Schottky effect negligible. In order to obtain good reproducibility of the data it was found necessary to emission-regulate the bombarding current to the cathode.

Determination of the Alloy Work Function. - For this measurement the alloy sample was the anode in the tube, and the following procedure was used:

(1) The anode was heated by electron bombardment to a temperature of about 2300°K for a few seconds to remove any possible contamination, then cooled to 77°K;

(2) The cathode was heated to a temperature T by electron bombardment;

(3) The anode current I was measured as a function of the voltage difference V between the anode and the cathode;

(4) Steps (1) to (3) were repeated at different cathode temperatures.

Typical plots of the resulting data are shown in Figure 56 for the W - one percent Ir sample. The work function of the anode is determined from a Richardson plot of the I(T) data at constant V in the semilogarithmic portions of the I(V) curves. For example, data from constant voltage lines A and B in Figure 56 are graphed in the form of a Richardson plot for the W-1 percent Ir anode in Figure 58. (Using data from two or more constant voltage lines provided a check on the work function so obtained.) The theoretical value of A_{th} is assumed in obtaining the anode work function. The work functions obtained in this manner for the various alloys are listed in the first column of Table XV.

Determination of the Alloy Richardson Constants. - The same procedure is followed as in the previous measurement, but for this case the alloy sample is the cathode of the tube. A Richardson plot is made of data from the temperature-limited portion of the I(V) curves (for example, line C in Figure 56), and ϕ_R and A_R are obtained from the slope and intercept of the resulting straight line. The Richardson constants for the various alloys are listed in the second and third columns of Table XV. The temperature coefficients of the work function for the various alloys

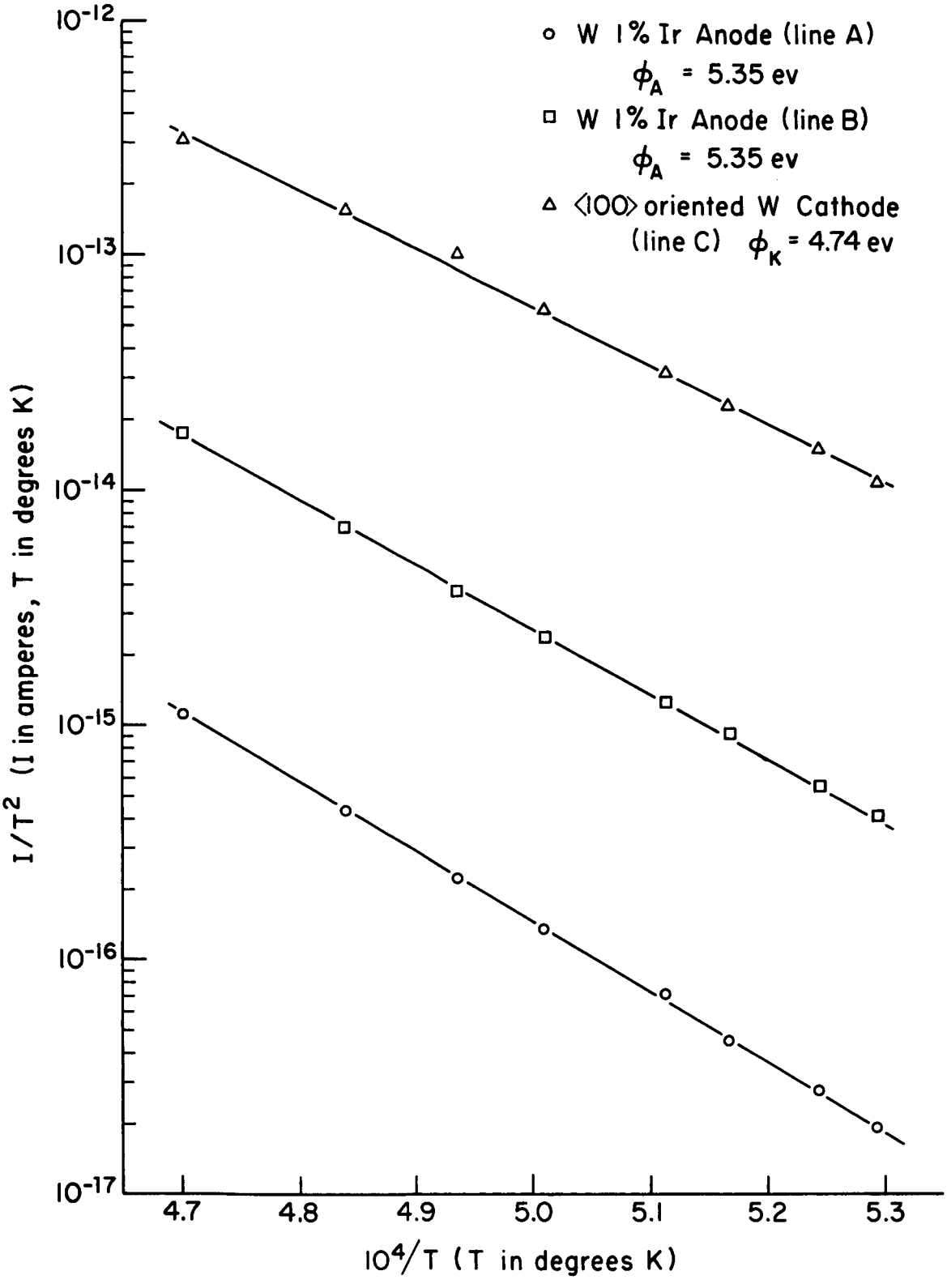

Figure 58. Richardson plots of data from lines A, B (both anode-limited emission), and C (cathode-limited emission) of Figure 56.

TABLE XV

Work functions and emission constants of the alloys

Alloy	ϕ (ev)	ϕ_R(ev)	A_R(amp/cm^{2}deg^2)	α(x10^{-5}ev/deg)	$\Delta\phi$eq(ev)	ϕeq(ev)
W-1% Ir	5.35	-	-		-0.07	5.28
W-2% Ir	4.77	4.77	28.1	+12.9	+0.03	4.80
W-2.5% Os	4.97	4.97	184	-3.67	-	-
W-5% Os	5.08	5.15	355	-9.35	-0.27	4.81
W-5% Ta	5.30	5.31	121	-0.07	+0.02	5.32
W-10% Ta	4.74	-	-	-	$>$-0.24	$<$4.50
W-20% Ta	4.66	4.70	142	-1.50	0	4.66
W-5% Re	4.98	5.00	194	-4.26	-0.50	4.48
W-15% Re	5.22	-	-	-	-0.41	4.81
W-23% Re (with O_2)	5.50	-	-	-	+0.07	5.57
W-23% Re (without O_2)	5.01	4.97	120	0	0	5.01
(100) W	4.73 $\pm$ 0.06	4.73 $\pm$ 0.04	122 $\pm$ 23	-0.49 $\pm$ 0.49	-	-

are obtained from the A_R's by means of Equation (6), and are listed in the fourth column of Table XV.

Each tube contained a <100> - oriented tungsten electrode, so that several measurements of the emission constants for the (100) face of tungsten were obtained; the averages of these measurements and the corresponding probable errors are listed in Table XV. Since the knees of the I(V) curves give the difference in cathode and anode work functions, the alloy work functions may be obtained from these data and the values for <100> -oriented tungsten. The values of work functions so obtained differ from those listed in Table XV by 1 percent or less, which is about the same as the probable error obtained for the work function of <100> - oriented tungsten.

Determination of the Work Function of the Equilibrated Alloy Surface. - An alloy flashed at 2300°K, as was done for the above measurements, may have its surface somewhat depleted of the minor constituent, and thus not be typical of the alloy surface operated at temperatures necessary for contact ionization. Therefore, after flashing the alloy (which was the anode for these measurements) to 2300°K to remove any possible contamination, it was heated at 1500°K (as determined by an optical pyrometer) for successive 10 minute periods until equilibrium was established. (This was done ahead of the measurements above to avoid any effects due to long-term depletion.) The change in the work function due to this treatment was obtained from the shift along the V axis of the semilogarithmic straight line portion of the I(V) curve with the cathode held at constant temperature. Contamination rates were checked by running the tube under the same conditions for similar times with the anode at 77°K. The data thus obtained is tabulated in the fifth column of Table XV and the work function of the alloy surface equilibrated at 1500°K is listed in the sixth column.

Determination of Crystal Direction and Size. - In order to relate the work functions of the alloy samples to their crystallography both backscattered Laué patterns and optical photographs were taken of the surfaces examined; these are illustrated in Figures 59 to 62. The crystallographic face of the alloy surface was obtained by direct comparison of its Laué pattern with those of the prominent planes of zone-melted tungsten, as given in Figures 59 (a) to (c). Also of interest is the number of crystals sampled by the 0.011 inch D electron beam in the work function triode for the work function determination. This cannot be determined directly, but the number of crystals within the 0.020 inch D X-ray spot can be estimated from the appearance of the Laué patterns and from the average crystal size as seen in the optical photographs. The pertinent results are listed in Table XVI.

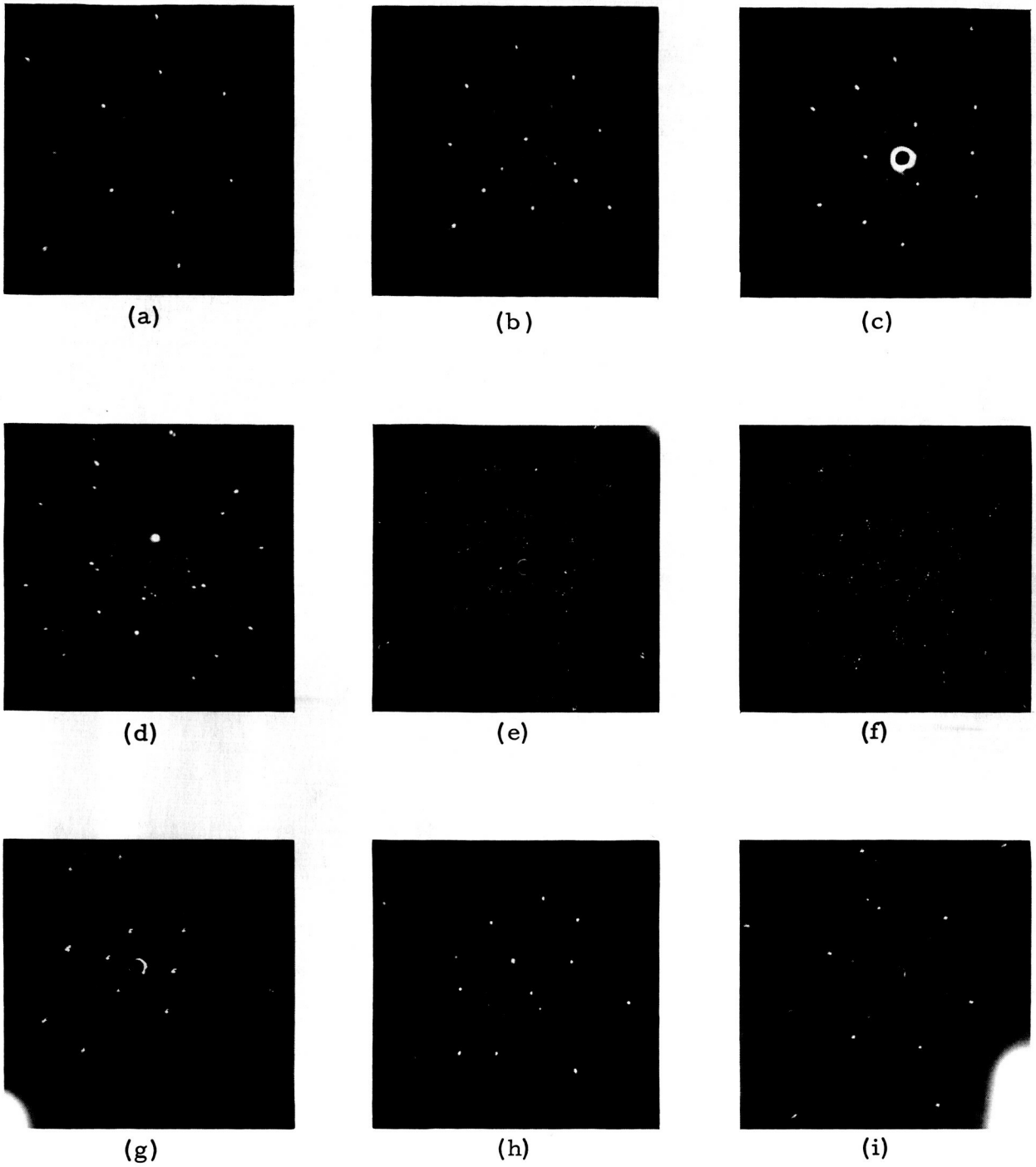

Figure 59. Back-scattered Laué patterns of the major low-index planes of tungsten and of the alloy surfaces examined in the work function triode. (a) (110) W, (b) (100) W, (c) (111) W, (d) W-1% Ir before operation in triode, (e) W-1% Ir after, (f) W-2% Ir (g) W-2.5% Os, (h) W-5% Os, (i) W-5% Ta.

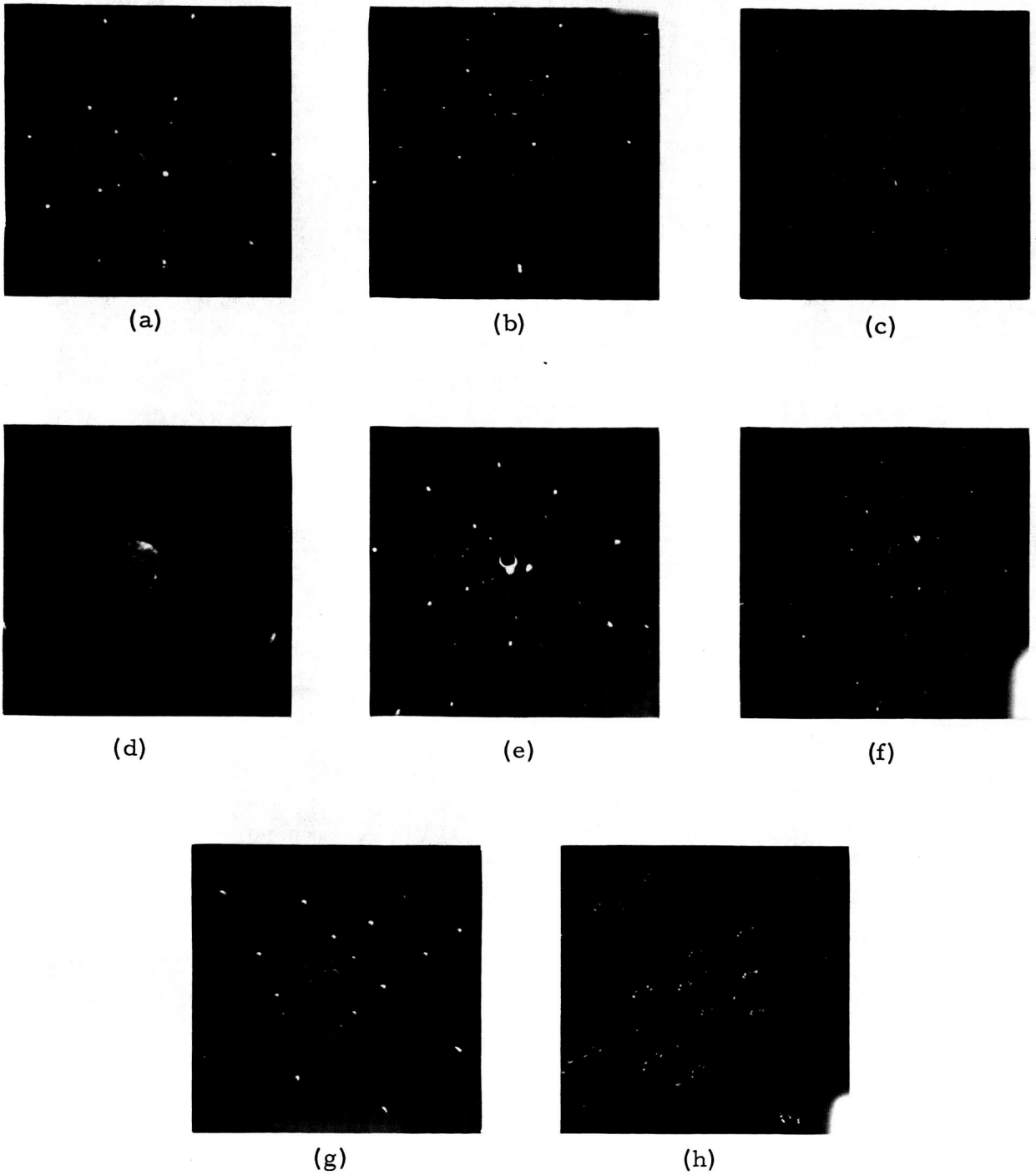

Figure 60. Back-scattered Laue patterns of the alloy surfaces examined in the work function triode. (a) W-10% Ta, (b) W-20% Ta, (c) W-5% Re, (d) W-15% Re before electrolytic etching, (e) W-15% Re before operation in triode, (f) W-15% Re after (g) W-23% Re before operation, (h) W-23% Re after.

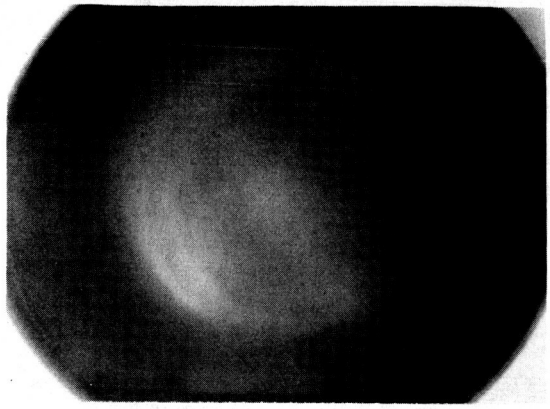

(a)

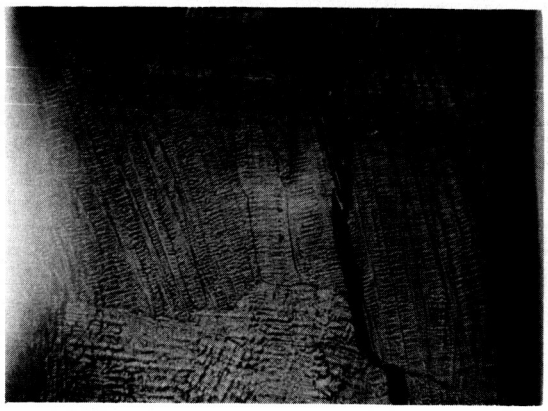

(b)

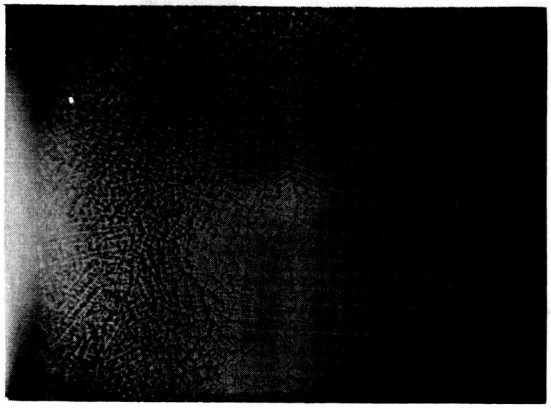

(c)

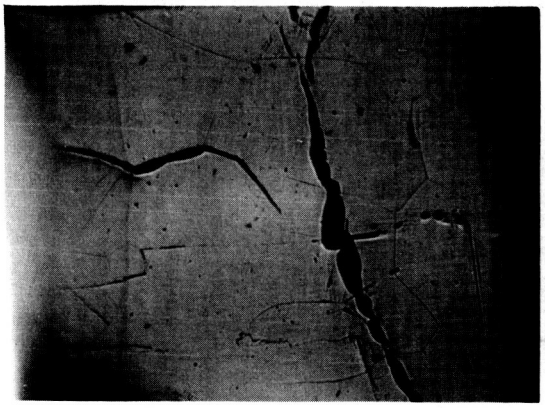

(d)

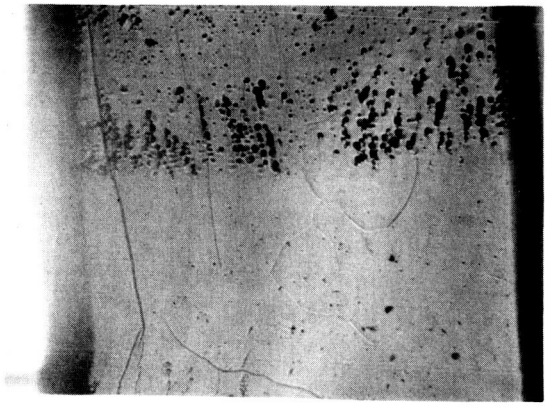

(e)

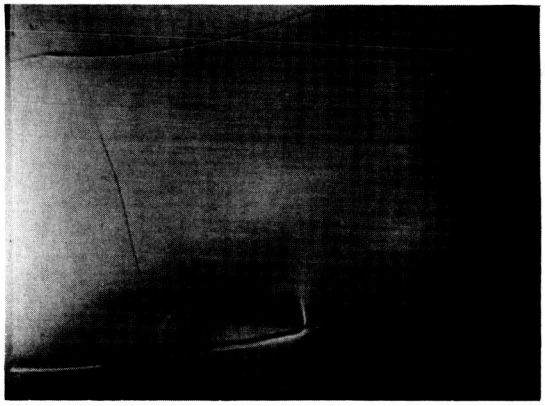

(f)

Figure 61. Optical micrographs of electrode surfaces used in work function triodes. (a) (100) W, (b) W-1% Ir, (c) W-2% Ir, (d) W-2.5% Os, (e) W-5% Os, (f) W-5% Ta. Magnification 25x.

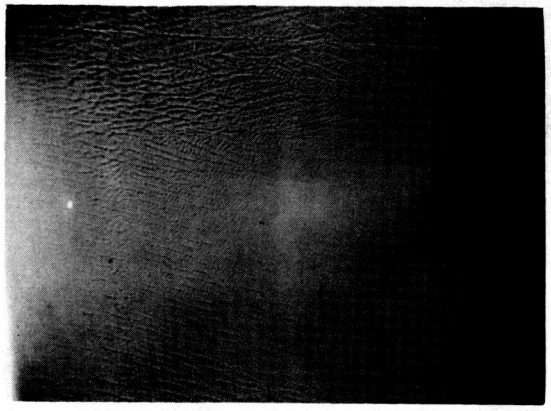

(a)

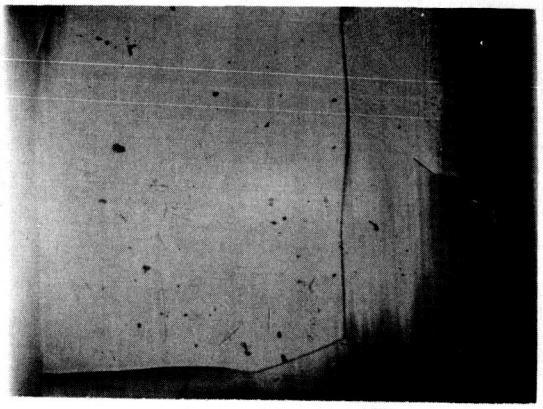

(b)

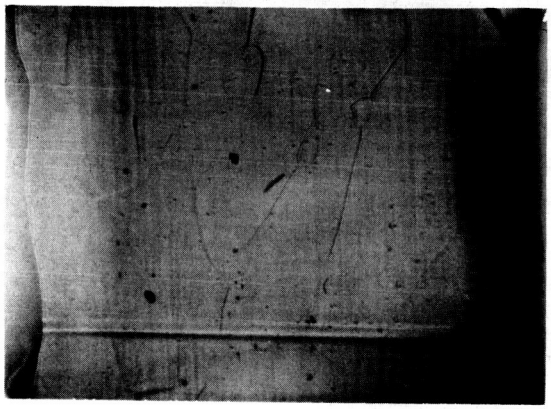

(c)

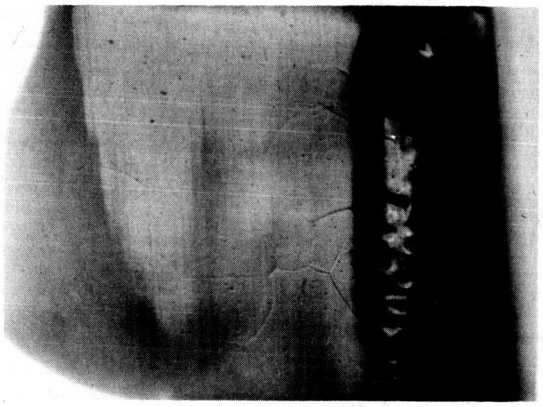

(d)

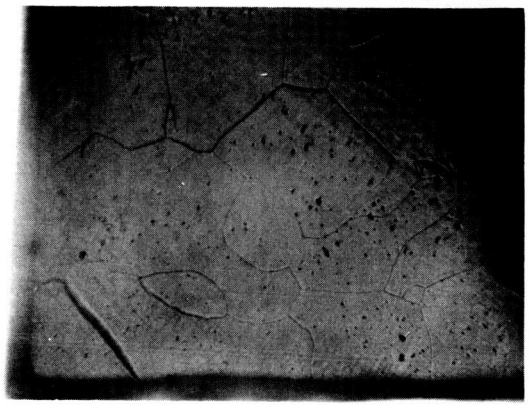

(e)

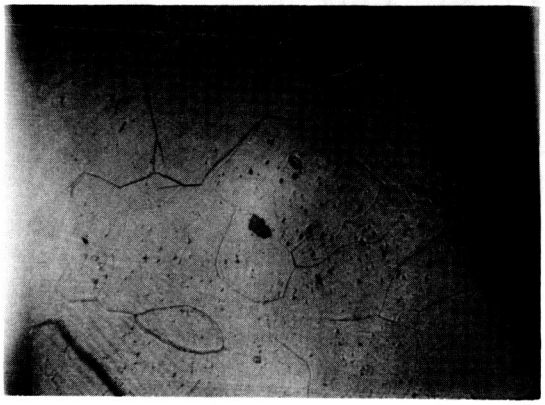

(f)

Figure 62. Optical micrographs of alloy surfaces used in work function triodes. (a) W-10% Ta, (b) W-20% Ta, (c) W-5% Re, (d) W-15% Re, (e) W-23% Re before operation in triode, (f) W-23% Re after. Magnification 25x.

TABLE XVI

Crystallographic data of the alloys

Alloy	Laue pattern taken Before	After	Face Examined	Number of Crystals in 0.020" D Spot	Changes in Crystal Structure
W-1%Ir	x		(340), 8° from(110)	2	not evident in photographs
		x	polycrystalline	many	
W-2%Ir	x	x	polycrystalline	many	No
W-2.5% Os		x	(334), 8° from (111)	≥ 2	No
W-5% Os	x	x	(250), 22° from (010) (one crystal only)	2	No
W-5%Ta		x	(110)	1	No
W-10%Ta	x	x	near (340), 8° from (110)	1	No
W-20%Ta		x	near (230), from (110)	1	No
W-5%Re		x	near (230), 13° from (110)	many	Yes (smaller crystals)
W-15%Re	x		near (340), 6° from (110)	1	not evident in photographs
		x	polycrystalline	many	
W-23%Re	x		near (221), 14° from (111)	≥ 2	Yes(more pits in crystals)
		x	" " " "	many	

Discussion of Results

Crystalline Structure. - Most of the alloy samples had surfaces whose crystal directions could be determined from the Laue patterns and are given in Table XVI. For some alloys, W-1 percent Ir, W-5 percent Re and W-15 percent Re, the Laue patterns or photographs indicated changes in crystal structure during operation, the final surfaces being made of smaller crystals than the initial ones. The reasons why heating the alloys should cause this are unknown. The single-crystal tungsten surfaces showed no changes during operation.

Emission Constants for (100) Tungsten. - The work function obtained here for the (100) face of tungsten agrees well with values obtained previously[64, 65]. The temperature coefficient of the work function is of the same sign but considerably lower in magnitude than that obtained by field emission techniques [64]. This may be due to the measurements being taken over different temperature ranges.

Emission Constants for the Flashed Alloy Surfaces. - The work functions of the flashed alloy surfaces differ at most by a few tenths of an electron volt from what one obtains for clean tungsten on the same faces, being about the same or somewhat higher. The alloy minor constituents may be listed in order of decreasing alloy work function as follows: iridium, osmium, rhenium, and tantalum. The highest work functions obtained for clean alloy surfaces are 5.35 ev for (340) W-1 percent Ir and 5.30 ev for (110) W-5 percent Ta. It is interesting to note that none of these values approach the 5.8 to 6.1 ev obtained by field emission techniques on (110) tungsten,[66, 67] but are instead much closer to the value of 5.2 to 5.3 ev obtained by thermionic and retarding potential techniques [68, 69]. This may indicate that the corrections for differences in electric field in the field emission case are greater than originally thought.[67]

Work Functions of the Equilibrated Alloy Surfaces. - Only on four of the alloy samples do appreciable work function changes occur when the alloy surface is equilibrated by heating at 1500°K. The majority of the results agree essentially with those obtained by the field emission techniques (i.e., W-1 percent Ir, W-2 percent Ir, W-5 percent Os, W-10 percent Ta, and W-20 percent Ta). The results for W-5 percent Ta are actually in agreement because in this case the measurement was taken on a plane which, because of its high work function, does not contribute to the total field emission current. Substantial disagreement is obtained only for W-5 percent Re and W-15 percent Re, where large unexplained decreases in work function occur upon equilibration.

Oxygen in Tungsten - Rhenium Alloys. - Effects due to absorbed oxygen were observed in the tube containing W-23 percent Re alloy, although

not for the other rhenium alloys. The effect consisted of desorption of oxygen whenever the alloy sample was heated, causing a slight change in the alloy work function and a considerable change in the (100) W work function. After approximately 3 hours heating at temperatures between 2000 and 2300°K, the oxygen reservoir was exhausted, and both electrodes, upon further heating, attained their final work function values. Examination of the alloy surface crystals afterwards showed no change in the size or shape of surface crystals, but did show an increase in the number of pits on the surface, with one large pitted area in the center region of which the work function was determined (Figures 62 (e) and (f). It is interesting to speculate whether or not the pits are associated with the release of oxygen.

SUMMARY AND CONCLUSIONS

In this section we summarize the pertinent features of the tungsten alloy work and the correlation between the field electron microscope and retarding potential methods. The ability to effectively reduce the alloy concentration at the surface of some samples by flash heating provided an internal reference for establishing a semiquantitative measure of the work function change on equilibrating, which could be utilized by both methods.

Tantalum-Tungsten Alloy

The values of E_p and E_a are below those of clean tungsten for all three tantalum alloy mixtures. The trends in both the calculated values of ϕ_o from Equation (50) and the field electron measured ratios from ϕ_o/ϕ_c suggest that the lowering of ϕ_o is inversely proportional to the alloy concentration. This observation is substantiated in the retarding potential measurements of work function for the 10 and 20 percent tantalum-tungsten alloy mixtures, but not in the case of the 5 percent mixture. In the latter case, the retarding potential method suggests no change in the work function on flash heating and equilibrating for a longer time period at 1500°K. Since the high work function (110) plane does not contribute to the averaging in field electron microscopy, it is conceivable that the lower work function planes do experience a large work function lowering in the case of the 5 percent tantalum-tungsten alloy, whereas the high work function (110) plane is essentially unchanged.

Iridium-Tungsten Alloy

Both the 1 percent and 2 percent iridium-tungsten alloys exhibit values of E_p which are slightly larger than the corresponding value for clean tungsten; the experimentally determined value of E_a for the 1 percent sample is less than the corresponding value for clean tungsten, whereas the 2 percent sample shows a value only slightly below that of clean tungsten. Both methods suggest no work function change between flash heating and equilibration at lower temperatures. This was also substantiated by the field electron patterns which also exhibited no change on flash heating and subsequent equilibration at lower temperatures. We conclude that iridium is tenaciously adsorbed at the surface of tungsten and not greatly affected by heating. The calculated values of ϕ_o for the iridium-tungsten alloy samples have a sufficiently large error associated with them that it is difficult to establish whether the average work function of tungsten is substantially altered by the presence of bulk iridium. The retarding

potential measurements yield a value for the 1 percent sample that is identical to the 5 percent tantalum sample, both measurements being made along a nearly identical crystallographic direction. By comparison with the 5 percent tantalum results, we conclude that iridium does not greatly alter the (110) work function; the retarding potential work function of the 2 percent alloy could not be identified to a particular crystallographic direction, and therefore we cannot ascertain the magnitude of the work function change in this case.

Osmium-Tungsten Alloy

The values of E_p for the 2.5 and 5.0 percent osmium-tungsten alloys were nearly identical and slightly greater than the corresponding value for clean tungsten. The value of E_a for the 2.5 percent alloy was below that of the clean tungsten value, whereas the 5.0 percent sample exhibited a value of E_a nearly identical to that of pure tungsten. Both methods of measuring the work function change on equilibrating after a high temperature flash suggest that osmium reduces the average work function of clean tungsten. The field electron patterns of the equilibrated surface of the osmium alloy exhibited some similarities to those observed from the iridium alloy; also, flashing to the osmium alloy required unusually higher temperature attain a psuedo clean field electron pattern.

Rhenium-Tungsten Alloy

The value of E_p for the 5 percent rhenium-tungsten alloy was nearly identical to that of clean tungsten, while the value of E_a was slightly lower than that of clean tungsten. On equilibrating the alloy sample, after high temperature flashing very little change was noted in the average electron work function as measured by the field emission method; in contrast, the thermionic method gave a large decrease in ϕ on equilibrating. Both the 15 and 23 percent alloy samples were able to absorb oxygen; heating a previously flashed sample at $\sim 1350^{\circ}K$ caused the formation of an oxide layer at the surface. After removing all absorbed oxygen by repeated flash heating the 15 percent rhenium alloy showed a decreasing work function on heating, whereas the 23 percent rhenium alloy showed no change. Values of E_a and E_p measured on the 23 percent rhenium-tungsten alloy were the largest of all the alloy samples. The ability of the 15 and 23 percent alloys to liberate oxygen near operating temperature of the porous ionizers may be useful in increasing the efficiency of contact ionization sources.

ERRATA

It has recently been pointed out to us that the derivation of Equation (30) by MacDonald and Barlow [36] is incorrect. The details of the correction and further developments of the theory of work function change on absorption of polarizable ions will appear in a future publication. The immediate result is to produce a basic change in Equation (31) which eliminates the second term. Retaining ϵ, this changes the working Equation (33) to the following:

$$\theta^{3/2} = \frac{\theta}{\Delta\phi} \quad \frac{4\pi\,\mu_o}{9\,a\,\sigma_o^{\,1/2}} - \frac{1}{9\,a\,\sigma_o^{\,3/2}} \qquad (33)$$

which is identical to Equation (26), based on the Topping model. Thus, parts of the discussion on pages 52 to 55 and the Table VII and Table VIII results, which are based on the validity of Equation (33), must be omitted. The empirical relationship in Equations (37) and (38) still holds, since both the Topping equation and MacDonald's incorrect derivation predict $\Delta\phi_m \propto \mu$.

Upon analyzing the "corrected" (i.e. shifted to cause linear extrapolation to $\sigma = 0$) probe tube results of Figure 14 by the Topping model (Equation 26), we can obtain a close fit between $0 \leq \sigma \leq \sigma_m$. Interestingly, we obtain values of $\mu = ze\,d_o$ identical to those given in Table VII based on the incorrect equation; however, values of a are a factor of 10 larger than those given in Table VIII.

More recent experiments [70] show that unequilibrated (i.e. localized random) absorption of potassium on tungsten yields results on various planes which fit the Topping model between $0 \leq \sigma \leq \sigma_m$, whereas equilibration causes redistribution of the potassium between adjacent crystal faces similar to that noted in the Figure 14 results. Yet, it is interesting that the "corrected" equilibrated results of Figure 14 obey a functional relationship of the form of the incorrectly derived Equation (33).

Thus it appears that both the experimental and theoretical picture of work function change on adsorption still remains somewhat clouded. What appears to be needed in the way of experimental results is σ vs ϕ data on a large single crystal face so that equilibration does not lead to redistribution between crystal faces. In this way, both localized and equilibrated adsorption can be compared directly on a single crystal face.

REFERENCES

1. L. W. Swanson et al., NASA CR-54106 (Field Emission Corporation, 1964).

2. J. P. Jones, Proc. Royal Soc. 284A, 469 (1964).

3. L. W. Swanson, et al., Final Report for NASA Contract NASw-458 (Field Emission Corporation, 1963).

4. G. E. Vibrans, "Field Emission in Vacuum Voltage Breakdown", Lincoln Laboratory Technical Report No. 353, 8 May 1964.

5. P. H. Levine, J. Appl. Phys. 33, 582 (1962).

6. H. S. Carslaw and J. C. Jaeger, Conduction of Heat in Solids, second ed. (Clarendon Press, Oxford, 1959) p. 264.

7. G. E. Vibrans, "Calculation of the Surface Temperature of a Solid Under Electron Bombardment", Lincoln Laboratory Technical Report No. 268, 16 November 1962.

8. G. E. Vibrans, Technical Report 308, Lincoln Laboratory, M.I.T. (18 April 1963).

9. J. P. Barbour, et. al., Phys. Rev. 117, 1452 (1960)

10. C. J. Bennette, et al., J. Appl. Phys. 35, 3054 (1964).

11. D. D. Eley and P. R. Wilkinson in Structure and Properties of Thin Films (John Wiley and Sons, Inc., New York, 1959), Proceedings of International Conference, p. 508ff.

12. Linfield Research Institute, Quarterly Report No. 6, Contract No. NObsr 72697, Index No. NE-110000, 1 August 1958 to 31 October 1958.

13. W. P. Dyke, et al., Phys. Rev. 91, 1043 (1953).

14. W. W. Dolan, et al., Phys. Rev. 91, 1054 (1953).

15. J. Franzen and K. D. Schuy, Z Naturforsch, 20a, 176 (1965).

16. L. W. Swanson, et al., Proceedings of the 25th annual conference on Physical Electronics, (Massachusettes Institute of Technology, Cambridge, Mass., 1965).

17. R. P. Little and W. T. Whitney, J. Appl. Phys. 34, 3141 (1963).

18. H. E. Tomaschke, Coordinated Science Laboratory Report R-192 (University of Illinois, January 1964).

19. Barry Singer and H. D. Doolittle, J. Appl. Phys. 36, 2002 (1965).

20. E. Müller, J. Appl. Phys. 26, 732 (1955).

21. L. W. Swanson, et al., Final Report NASA Contract NASr-19 (1962).

22. R. Gurney, Phys. Rev. 47, 479 (1 935).

23. L. Dobretsov, "Electronic and Ionic Emission", (NASA Technical Translation F-73, 1963).

24. R. Gomer and L. Swanson, J. Chem. Phys. 38, 1613 (1963).

25. N. Rasor and C. Warner, J. Appl. Phys. 35, 2589 (1964).

26. H. Utsugi and R. Gomer, J. Chem. Phys. 37, 1707 (1962).

27. C. Herring, Rev. Mod. Phys. 21, 185 (1949).

28. W. Brattain and J. Becker, Phys. Rev. 43, 428 (1933).

29. AIP Handbook, ed. by D. W. Gray (McGraw-Hill Book Co., Inc., New York, 1963), 2nd ed., Sec. 9, pp. 149-151.

30. Y. Zingerman, V. Ishchuk and V. Morozovskii, Soviet Phys. - Solid State 3, 760 (1961).

31. R. Bosworth, Proc. Roy. Soc. 162, 1 (1937).

32. Unpublished work from this Laboratory.

33. J. Anderson, W. Danforth and A. Williams, J. Appl. Phys. 34, 2260 (1963).

34. L. Schmidt and R. Gomer, J. Chem. Phys. 42 3573 (1965).

35. E. Gyftopoulos and J. Levine, J. Appl. Phys. 33, 67 (1962).

36. J. MacDonald and C. Barlow, J. Chem. Phys. 39, 412 (1963).

37. AIP Handbook, ed. by D. W. Gray (McGraw-Hill Book Co., Inc., New York, 1963), 2nd ed., Sec 9, p. 149.

38. Quarterly Report No. 3, Contract PH 43-64-71 (NIH), Field Emission Corporation, 26 January 1965) p 7.

39. L. W. Swanson, et al., NASA CR-22 (1964).

40. A. J. Melmed, J. Chem. Phys. 38, 1444 (1963).

41. A. N. Nesmeyanov, Vapor Pressure of the Chemical Elements (Elsevier Publ. Co., Amsterdam, 1963), p. 424.

42. R. B. Leighton, Principles of Modern Physics (McGraw - Hill Book Co., Inc., New York, 1959), p. 727.

43. A. Redhead, Vacuum 13, 253 (1963).

44. D. Menzel and R. Gomer, J. Chem. Phys. 40, 1164 (1964).

45. D. Menzel and R. Gomer, J. Chem. Phys. 41, 3329 (1964).

46. D. Menzel and R. Gomer, J. Chem. Phys. 41, 3311 (1964).

47. R. Gomer and L. Swanson, J. Chem. Phys. 38, 1613 (1963).

48. E. W. Müller, in Direct Observations of Imperfections in Crystals, ed. by J. B. Newkirk and J. W. Wernich (Interscience Publishers, New York, 1962) 77.

49. E. W. Müller, J. Appl. Phys. 28, 1 (1957).

50. J. F. Mulson and E. W. Müller, J. Chem. Phys. 38, 2615 (1963).

51. J. B. Gibson, et al., Phys. Rev. 120, 1229 (1960).

52. R. H. Silsbee, J. Appl. Phys. 28, 1246 (1957).

53. M. W. Thompson, Proc. 5th International Symposium of Ionization of Gases, Munich, 85 (October 1961).

54. D. Rosenberg and G. K. Wehner, J. Appl. Phys. 33, 1842 (1962).

55. E. V. Kornelsen, et al., Phys. Rev. 136, A849 (1964).

56. R. V. Stuart and G. K. Wehner, J. Appl. Phys. 33, 2345 (1962).

57. P. R. Strutt, Rev. Sci. Instr. 32, 411 (1961).

60. W. B. Nottingham, Handbuch der Physik XXI (Springer-Verlag, Berlin, 1956), p. 1.

61. J. A. Simpson, Rev. Sci. Instr. 32, 1283 (1961).

62. H. Shelton, Phys. Rev. 107, 1553 (1957).

63. D. O'Boyle, J. Appl. Phys. 36, 2849 (1965).

64. L. W. Swanson and L. C. Crouser, Quarterly Report No. 3 for NASA Contract NASw-1082 (Field Emission Corp., 1965).

65. E. P. Sytaya, et. al., Sov. Phys. - Sol. State 4, 750 (1962).

66. R. D. Young and E. W. Müller, J. Appl. Phys. 33, 91 (1962).

67. E. W. Müller, J. Appl. Phys. 26, 732 (1955).

68. G. F. Smith, Phys. Rev. 94, 295 (1954).

69. J. Fine, et. al., Surf. Sci. 3, 227 (1965).

70. L. D. Schmidt and R. Gomer, J. Chem. Phys. 42, 3573 (1965).

71. R. H. Good and E. W. Müller, Handbuch der Physik 21, 176 (1956).

72. W. J. Ooster Kamp, Philips Res. Rep. 3, 49 (1948).

73. W. J. Ooster Kamp, Philips Res. Rep. 3, 303 (1948).

74. L. W. Swanson and R. Gomer, J. Chem. Phys. 39, 2813 (1963).

LIST OF SYMBOLS

Symbol		Equation No.	Page No.
A	intercept with vertical axis at $10^4/V = 0$ in a Fowler-Nordheim plot	43	57
A_c	effective emitting area		23
A_R	experimentally determined, pre-exponential of Richardson equation	60	1[illegible]
A_s	intercept of Fowler-Nordheim plot for a clean substrate	44	57
A_{th}	pre-exponential term in Richardson equation	56	130
a	aperture radius of the electrostatic lens	58	133
a_M	maximum radius of the helical path of an electron in a magnetic field	58	133
B	geometrical factor in Fowler-Nordheim equation	41	56
b	constant in the Fowler-Nordheim equation	41	56
b_c	desorption cross section	48	96
C_1, C_2	constants defined by Equation (34)	34	52
c	specific heat	9	10
D	diffusion coefficient		79
$D(\sigma)$	diffusion coefficient as a function of coverage	46	62
D_o	pre-exponential term in diffusion equation	45	59
d	electrode spacing	1	6
d_o	dipole length of adsorbate atom	25	50
E_a	activation energy for atomic desorption		65

LIST OF SYMBOLS (Cont'd)

Symbol		Equation No.	Page No.
E_{aM}	maximum energy related to power input at anode	17	12
E_d	surface diffusion activation energy	45	59
E_{des}	desorption activation energy	52	118
E_{nl}	field polarizing a single adsorbed atom in the absence of neighboring atoms	30	52
E_p	activation energy for ionic desorption	50	114
e	electronic charge	25	50
F	electric field at an emitting surface	3	6
F_c	critical field corresponding to that current density at which an emitter will heat regeneratively	8	9
F_e	effective field at the adsorbate due to the applied external field	40	56
F_o	gross electric field on the surface of an electrode	2	6
F_s	electrostatic stress equal to the yield point of a material		39
G	defined as equal to the emitted current density times the apex radius		39
g_a	statistical weight of the atomic state of an ad-atom	51	114
g_p	statistical weight of the ionic state of an ad-atom	51	114
H	magnetic field	58	133
H_{100}	binding energy of the atoms on the (100) plane	22	47
H_{110}	binding energy of the atoms on the (110) plane	22	47

LIST OF SYMBOLS (Cont'd)

Symbol		Equation No.	Page No.
k	Boltzmann constant	20	26
k_1, k_2	constants in Equation (37)	37	54
k_1', k_2'	constants defined by Equation (38)	38	54
k_{des}	first order rate constant	58	133
N	adsorbate dose number		66
N_e	electron flux	48	96
n_a	number of atoms per unit area per unit time	51	114
n_p	number of ions per unit area per unit time	51	114
p	temperature dependent field emission parameter	20	26
Q	total charge		108
R_a	radius of the anode spot	1	6
R_c	emitter apex radius	1	6
r	radius of electron beam expanded by electron space charge repulsion		13
r_o	initial radius of an electron beam		13
S	surface tension	19	14
T	temperature of a surface	11	11
T_o	alloy equilibration temperature		
ΔT	change in temperature	13	11
ΔT_a	temperature change at the anode		26

LIST OF SYMBOLS (Cont'd)

Symbol		Equation No.	Page No.
ΔT_c	temperature change at the cathode	20	26
ΔT_{Max}	maximum temperature change	14	11
t	time	9	10
t_c	thermal time constant		10
t_1	thermal time constant defined by Equation (9)	9	10
t_2	thermal time constant defined by Equation (10)	10	10
t_o	voltage pulse length		11
t_s	time required for adsorbate atoms to move a certain distance	45	59
$t(y)$	tabulated function in the Fowler-Nordheim equation, taking into account image corrections	41	56
$t_s(y)$	the $t(y)$ corresponding to the clean substrate	44	57
V	applied voltage	2	6
V_c	voltage on central electrode	58	133
V_I	ionization potential	37	54
V_p	pulse voltage		60
$v(y)$	tabulated function in the Fowler-Nordheim equation, taking into account image corrections	41	56
W_a	beam power density at the anode	2	6
W_{aM}	maximum beam power density for a given anode to be heated sufficiently to initiate an arc	8	9

LIST OF SYMBOLS (Cont'd)

Symbol		Equation No.	Page No.
x	variable name used to define a function		10
y	diffusion distance on the surface	45	59
z	number of electronic charges associated with each ad-atom	25	50
z_{100}	number of electronic charges associated with each ad-atom on the (100) plane		56
z_{110}	number of electronic charges associated with each ad-atom on the (110) plane		56
α	ad-atom polarizability	27	51
α_{100}	ad-stom polarizability on the (100) plane		56
α_{110}	ad-atom polarizability on the (110) plane		56
α_{wf}	temperature coefficient of work function	59	133
β	geometric ratio of electric field F at the surface to the applied voltage		13
$\Delta\beta$	change in β due to roughening of the emitter surface		108
γ	electric field enhancement factor due to surface roughness		5
γ_o	boundary value of surface enhancement factor separating surfaces for which the cathode will initiate the arc from those for which the anode will initiate the arc	8	9
γ_o'	boundary value of surface enhancement factor related to a copper-tungsten diode	21	30
δ	electron effective penetration depth	10	10
ϵ	effective dielectric constant of the adsorbate layer	26	51

LIST OF SYMBOLS (Cont'd)

Symbol		Equation No.	Page No.
η	electrical resistivity	20	26
θ	fractional monolayer coverage	25	50
θ_o	fractional monolayer over which I_p vs t data extends	58	133
θ_m	fractional monolayer coverage at minimum work function	28	51
θ_i	initial fractional coverage	53	118
θ_f	final fractional coverage	53	118
λ	field dependent factor used in determining emitting area		23
μ	effective dipole moment of the adsorbate		50
ν	frequency factor	52	118
ρ	density	9	10
σ	adsorbate surface density		41
σ_m	adsorbate surface density for which the change in work function is maximum		44
σ_o	monolayer coverage of adsorbate	42	56
σ_{100}	adsorbate surface density on the (100) plane		46
σ_{110}	adsorbate surface density on the (110) plane		46
σ_m^{100}	adsorbate surface density on the (100) plane for which the change in work function is maximum		51
σ_m^{110}	adsorbate surface density on the (110) plane for which the change in work function is maximum		51

LIST OF SYMBOLS (Cont'd)

Symbol		Equation No.	Page No.
σ_o^{100}	monolayer coverage of adsorbate on the (100) plane		47
σ_0^{110}	monolayer coverage of adsorbate on the (110) plane		47
Δ	change in coverage		46
σ_i	initial adsorbate coverage	49	97
σ_f	final adsorbate coverage	49	97
ϕ	work function		23
$\Delta\phi$	work function change		44
ϕ_a	average work function of bulk adsorbate	24	47
ϕ_A	work function of the anode	56	130
ϕ_i	initial work function before desorption		96
ϕ_c	average work function of alloy after high temperature flash		119
ϕ_f	final work function after desorption		96
ϕ_F	field dependent work function	41	56
ϕ_o	average work function of alloy according to Equation 50		119
$\Delta\phi_F$	field induced work function change	40	56
ϕ_K	work function of the cathode	56	130
ϕ_{Ko}	work function of the cathode at T = 0		126
ϕ_m	minimum value of work function		43

LIST OF SYMBOLS (Cont'd)

Symbol		Equation No.	Page No.
$\overline{\phi}_m$	minimum value of average work function		44
$\Delta\phi_m$	maximum change in work function	23	47
$\overline{\Delta\phi}_m$	maximum change in average work function		44
ϕ_o	apparent monolayer coverage	23	47
$\overline{\phi}_o$	work function at highest coverage investigated experimentally		44
$\Delta\phi_o$	average work function change at the monolayer coverage		50
$\overline{\phi}_s$	average substrate work function		44
$\Delta\phi_{100}$	change in work function on the (100) plane		46
$\Delta\phi_{110}$	change in work function on the (110) plane		46
ϕ_R	experimentally determined thermionic work function		133